LARGE SCALE SPECIMEN DESIGN AND CREEP ANALYSIS FOR NUCLEAR CONTAINMENT CONCRETE WALLS

A Thesis

by

LAUREN ELIZABETH KELLEY

Submitted to the Office of Graduate and Professional Studies of
Texas A&M University
in partial fulfillment of the requirements for the degree of

MASTER OF SCIENCE

Chair of Committee,	Joseph M. Bracci
Committee Members,	Zachary C. Grasley
	Harry H. Hogan
Head of Department,	Robin Autenrieth

May 2018

Major Subject: Civil Engineering

ABSTRACT

Nuclear containment facilities in the US are quickly approaching the end of their design lives. However, due to the need for energy and the staggering cost of constructing new facilities, the industry is hoping to push the service lives of existing structures upwards of 80 years. Therefore, it is necessary to identify the risks associated with long term use of such facilities. Since these structures are typically post-tensioned concrete containment vessels, one of the main concerns is the phenomenon known as concrete creep.

This study focuses on observing the effects of concrete creep by constructing three large scale reinforced concrete wall sections to model variable contributing factors to the creep phenomenon. Concrete strains and temperatures through the thicknesses of the specimens, as well as the strain in select post-tensioning bars used to apply specimen stresses, are measured.

From six months of measured data since post-tensioning, there were noticeable changes in the post-tensioning bar strains and concrete strains, which is most likely the result of changes in ambient temperature in the winter months, and possibly creep. To confirm the field data values, a simple, static finite element model was developed to simulate concrete strain changes as a result of post-tensioning. The model confirmed the preliminary field data was closely related to the numerical estimations, with deviations stemming from the lack of complexity of the model. The model can be easily modified in the future to include concrete creep and other important physical occurrences that the specimens undergo in practical applications.

This research, in conjunction with materials tests being conducted in the lab by other students, will provide the framework for a powerful predictive creep model to be developed to analyze the expected lifespans of such existing structures.

ACKNOWLEDGEMENTS

I would like to thank my thesis advisor Dr. Joseph Bracci of the Zachary Department of Civil Engineering at Texas A&M University for his unparalleled support and guidance in not only my research endeavors, but my professional life as well. He was always the first person to offer help in my difficulties and he trusted in my work ethic and skills to make the right engineering judgements.

I would also like to thank the multitude of students and faculty who helped me with all aspects of this project. Mary Beth Keating, Matthew Waltman, Ricardo Espinoza, and Nick Danney endured the summer heat assisting me with the construction of the specimens. Matt Potter taught me all about instrumentation and made it possible for the data acquisition to work properly. Tevfik Terzioglu and Christa Torrence assisted me in the development of the finite elements models. Without each and every one of these people, this project would have never been a success.

I would also like to acknowledge Dr. Zachary Grasley in Civil Engineering and Dr. Harry Hogan in Mechanical Engineering at Texas A&M University for their input and commentary on my thesis. I am grateful for their expertise and valuable comments.

Finally, I would like to thank my wonderful parents, my fiancé, and my friends for providing me with continuous encouragement and support throughout my years of studying here at Texas A&M and through my research.

CONTRIBUTORS AND FUNDING SOURCES

Contributors

This work was supervised by a thesis committee consisting of Dr. Joseph Bracci and Dr. Zachary Grasley in the Department of Civil Engineering and Dr. Harry Hogan of the Department of Mechanical Engineering.

The data for Sections 2.4.1 and 2.5.4 was provided by Aishwarya Baranikumar of the Department of Civil Engineering.

The remainder of the work conducted for the thesis was completed by the student independently.

Funding Sources

Graduate study was supported by a research grant provided by the U.S. Department of Energy in support of Project 16-10457, “Experimentally Validated Computational Modeling of Creep and Creep-Cracking for Nuclear Concrete Structures”.

TABLE OF CONTENTS

Page

Page

Page

LIST OF FIGURES

Page

Page

Page

Page

Page

Page

Page

Page

Page

Page

Page

Page

Page

Page

Page

Page

Page

Page

Page

Page

Page

Page

LIST OF TABLES

Page

1. INTRODUCTION

1.1. Problem Statement

Most concrete nuclear containment facilities in the United States have a licensed design life of 40 years, with the ability to renew the license an additional 20 years (U.S. Energy Information Administration 2017). Today, the average age of nuclear containment facilities in the US is around 36 years. The industry's leaders are pushing to extend the commissioned life of such facilities upwards of 80 years due to the demand for energy and for economic reasons (Schwitters et al. 2013). With this elongation of plant operation, many structural features of the containment facilities could be at risk and could potentially be dangerous if not researched thoroughly. One of the time dependent impacts of concern is the influence of concrete creep, a viscoelastic deformation mechanism that causes concrete in compression to deform over long periods of time, resulting in unintended stress concentrations, prestress losses, and probable concrete cracking.

Due to the possible impacts of concrete creep, the nuclear containment structure, which is the final barrier between the nuclear reactor mechanism and the environment, may be put at risk. An example of this can be observed in an article describing the incident that caused the Crystal River 3 Nuclear Power Plant in Crystal River, Florida to be decommissioned (Georgia Institute of Technology 2015). Crystal River 3 was receiving a protocol refueling where post-tensioned tendons were cut and cracks propagated through the structure, causing it to be permanently shut down. It was speculated that concrete creep may have been one of the contributing factors in this incident due to the deformations in the concrete that eventually lead to the tension force on the post-tensioning strands to be less than originally designed. In order to fully understand the

influence of concrete creep on the performance of nuclear containment facility walls, it is necessary to identify what variables contribute to creep and model their effects.

In this study, concrete creep will be evaluated in the simulated wall specimens of post-tensioned nuclear containment facilities over an extended period of time based on large scale specimen testing, accompanied by complementary small-scale materials testing. Three concrete wall specimens, containing instrumentation to measure concrete strain, temperature, and strains in post-tensioning bars, will be constructed with varying wall reinforcement ratios, thicknesses, and post-tensioning load to model the effects of creep. The data that is collected will be compared against a finite element model for verification purposes. Ultimately, a finite element model will be developed that can predict the effect of creep over time for these structures to assist in future design and repair plans for nuclear containment facilities.

1.2. Factors Contributing to Creep

To fully define the scope of the project, it is necessary to decompose concrete creep by identifying what are the contributing factors and how each influences creep propagation. First and foremost, concrete creep is broken down into two components, basic creep and drying creep. To define drying creep, shrinkage is an important concept that must be considered as well. Basic creep is the time-dependent change in strain due to sustained loading, not considering internal moisture movement (Kovler 1997). Shrinkage is the time-dependent change in strain in concrete in the absence of applied load as a result of moisture loss. Creep and shrinkage are not independent mechanisms. Therefore, the principle of superposition does not apply. Drying creep is the deviation from the idea of superposition of creep and shrinkage and can be defined as the difference between total creep at drying and basic creep. Other factors that influence creep are humidity, external temperature, concrete mix design parameters, and curing method. The contributing factors

that will be focused on in this study are the level of concrete prestress, environmental conditions, wall thickness, wall reinforcement ratio, and the combined effects of creep and stress redistribution.

1.2.1. Level of Stress

The level of applied stress on the concrete is a factor that contributes to the basic creep mechanism. If the level of stress is high with respect to the concrete compressive strength f'_c, then a non-linear creep curve is assumed, whereas low levels of concrete stress, including typical service stresses, are assumed to follow a linear creep model (Bazant 1988). ACI 318-14 limits the compressive stress at service loads of prestressed concrete to 0.45f'c to prevent excessive creep deformations (American Concrete Institute 2014). Above this limit, the creep behavior is presumed to be non-linear.

Creep can be broken down into three stages when a concrete specimen is subjected to a constant level of stress (Usibe et al. 2012). In the first stage, known as primary creep, the rate of strain is high. But as time passes, the strain rate decreases. The second stage is known as the steady-state creep stage. During the second stage, there is no change to the microstructure of the specimen. In both the first and second stages, the material strength remains unchanged. Typically, the second stage of creep is referred to in materials studies as steady-state creep, characterizing the constant rate of strain as the creep strain rate. The creep strain rate in this stage depends on the creep mechanism. During the third stage, known as tertiary creep, the strain rate increases exponentially due to the development of internal cracks and the decrease of the effective cross-sectional area of the specimen. As the material's shape is morphed in this stage, the strength of the material is reduced permanently.

1.2.2. Environmental Conditions

Environmental conditions typically influence the drying creep mechanism due to the varying external humidity, precipitation, and temperature. Since drying creep depends on the relative humidity of the concrete, the humidity of the environment, precipitation, and temperature fluctuations, differential creep can develop through the thickness of a specimen resulting in a stress gradient from the surface of the specimen that is directly in contact with the environment to the inside of the specimen. Another important environmental condition is the temperature of the specimen when the specimen is loaded. If the temperature during loading is relatively high, then there can be more creep induced by the load (Marques and Barbosa 2013).

1.2.3. Reinforcement Ratio

The longitudinal and transverse reinforcement ratios of a concrete specimen are important parameters in studying creep because of the ability of the steel to carry compressive loading and to potentially confine the concrete, resulting in enhanced triaxial stress-strain behavior. As concrete creeps over time, the reinforcing steel within the concrete can be forced to carry additional loading due to the redistribution of forces, which could potentially yield the steel. In addition, as the concrete can be confined by both longitudinal and transverse reinforcement, there can be less air voids inside the concrete where moisture would migrate, leading to less creep strain and less shrinkage (Lin et al. 2014).

1.2.4. Redistribution of Stress

For repair and maintenance purposes of nuclear containment concrete walls, it is important to identify the combined effects of concrete creep and stress redistribution. In post-tensioned nuclear containment walls, post-tensioning strands must undergo maintenance and repairs to keep the facility safe and operable, therefore there may be a need to retighten or even cut tendons

periodically. Cutting tendons leads to instantaneous stress redistribution through the structure, adding more load to the other strands as well as the concrete in the surrounding area. Creep on its own leads to stress redistribution between the concrete, reinforcing steel, and post-tensioning strands, which can overstress the structure when a post-tensioning tendon is cut, potentially causing failure (Stefanou 1981). Long term concrete creep is the leading cause of prestress losses in a structure as well (Song et al. 2002), therefore it is important to have a method of tightening tendons periodically over time, if necessary, to keep the structure safe and operable.

1.3. Research Objectives

The purpose of this research is to determine how creep influences the long-term life span of nuclear containment structures by determining the creep induced strain in the concrete and the loss of post-tensioning force as a result of creep in the concrete. Different design parameters will be adjusted for each specimen to determine how the structural detailing can directly influence creep propagation as well, including varying vertical and circumferential reinforcement ratios and wall thicknesses. Sensors will carefully be selected and tested to ensure compatibility with the environmental conditions and strain demands of the specimens. A sustainable data acquisition system (DAQ) will be developed to capture data associated with strains and temperatures in the concrete and strains in the post-tensioning bars, ensuring long-term monitoring capabilities. A finite element model will be developed to verify the large-scale specimen strains resulting from post-tensioning operations. Complementary material tests by others involved in this research program will be conducted to develop a nuclear concrete database that will then be embedded in a finite element model that has the capability of predicting the influence of long-term creep as a result of structural design, stress conditions, material type, and environmental conditions so that a nuclear containment vessel design can be evaluated over extended periods of time.

1.4. Research Methodology

Three concrete wall specimens will be constructed, each with different wall thicknesses, levels of reinforcement, and applied post-tensioning steel forces, to analyze the influence of varying structural parameters on concrete creep propagation. Each specimen will be equipped with full bridge concrete strain gages and thermocouples at varying depths in three directions to measure concrete strain and temperature over time.

Specimens 1 and 2 will contain steel reinforcement and will be stressed with unbonded post-tensioning steel bars equipped with strain gages to measure the strains in the post-tensioning steel bars over time. Specimen 3 will act as a control specimen, containing only concrete with no reinforcement and no applied post-tensioning forces.

The design of Specimen 1 is based on a previous study conducted by Sandia National Laboratory (Hessheimer et al. 2003) in which a 1:4 scale prestressed concrete containment vessel was constructed and tested for overpressurization. The prototype used in Sandia's study was based on an actual nuclear power plant in Japan called Ohi-3. Sandia constructed a thin-walled cylindrical concrete structure with a dome top and an internal steel liner. The prototype was stressed with unbonded post-tensioning steel cables running both vertically and circumferentially through the structure.

Given the large diameter of typical prototype containment vessels, the actual wall stresses in such curved sections are similar to that in straight walls, exhibiting a biaxial state of stress. Thus, for experimental ease, the specimens for this study were designed and constructed as straight wall segments.

1.5. Scope of Thesis

This research will focus on the design decisions, construction, instrumentation, data collection, preliminary finite element modeling, and early measured data obtained in the three large-scale specimens. This research will serve as a link between small-scale specimens currently being tested for creep in the lab by other students and the large-scale, realistic structures that are going to be constructed in the future.

2. SPECIMEN DESIGN AND CONSTRUCTION

2.1. Design of Large Scale Specimens

In order to model the long-term behavior of concrete creep in the walls of nuclear containment facilities, three large-scale straight wall concrete specimens were designed and constructed (Figs. 1-27). It is worth noting that the middle 91 cm by 91 cm (3 ft by 3 ft) of each specimen was the focus of the data collection and design decisions. In order to ensure structural stability and resistance to overstress around the edges of each specimen as a result of post-tensioning forces, the outside perimeters of the two loaded specimens had doubly reinforced longitudinal steel and confined transverse steel. The middle 91 cm by 91 cm (3 ft by 3 ft) of each specimen, consisting of 2 wall face mesh layers of steel near the wall cover, were constructed to represent the conditions designed for this study.

The design of Specimen 1 (Figs. 1–10) was based on Sandia's 1:4 experimental specimen (Hessheimer et al. 2003). The wall thickness of Sandia's model was about 33 cm (13 in), which was the thickness used in Specimen 1 of this research. The height of the Sandia model (excluding the dome top) was approximately 10.8 m (35.3 ft) tall. However, due to cost, construction, and materials transportation limitations, a height and width of 2.4 m (8 ft) were adopted in the design of Specimen 1. Based on strut and tie theory, which assumes stress propagation at 45º from the loading point, it was determined that the height and width of Specimen 1 was sufficient to create a similar biaxial state of stress in portions of the full Sandia model. An additional 30 cm (1 ft) clearance at the bottom of Specimen 1 was required to provide space for the post-tensioning steel bars, so a 2.4 m by 2.4 m (8 ft by 8 ft) wall was designed with 30 cm by 46 cm (1 ft by 1.5 ft) feet on both sides, resulting in a 2.7 m (9 ft) wall height.

The reinforcement ratio of the Sandia model was 6 to 10 times larger than the minimum reinforcement ratio according to ACI 318-14, Chapter 11 (American Concrete Institute 2014). In the vertical direction, the reinforcement ratio was 0.0098, with 2 mats of #5 bars and #6 bars (grade 60) alternating every 15 cm (6 in) on center, where the minimum reinforcement ratio according to ACI is between 0.0012 and 0.0015. In the circumferential direction, the Sandia model had a reinforcement ratio of 0.0212, with 2 mats of #7 bars (grade 60) spaced every 11 cm (4.4 in), where the minimum reinforcement ratio is between 0.0020 and 0.0025, according to ACI. In the radial direction (through the thickness of the wall), the reinforcement ratio was 0.0021 with #3 bars (grade 60) with 90° bends in two planes spaced every 30 cm (12 in) horizontally and 11 cm (4.4 in) vertically. Since Sandia's model was a scaled version of an actual concrete nuclear containment vessel, the reinforcement ratios were directly adopted in the design of Specimen 1 (Figs. 6–10).

The Sandia model contained unbonded post-tensioning strands in both the vertical and circumferential directions. In the circumferential direction, post-tensioning strands were spaced every 11 cm (4.4 in), each with about 445 kN (100 kips) of applied force, resulting in a circumferential stress in the concrete of about 12 MPa (1.8 ksi), ignoring Poissons effect. In the vertical direction, the strands were spaced every 61 cm (2 ft), each with about 445 kN (100 kips) of applied force, resulting in a vertical stress in the concrete of 2.3 MPa (0.3 ksi), ignoring the gravity load and Poissons effect. To mimic the stress field that is modeled in Sandia's test structure, Specimen 1 was loaded in a similar manner (Figs. 3–5). However, rather than utilizing unbonded post tensioning strands, unbonded steel DYWIDAG bars with an ultimate stress of 1030 MPa (150 ksi) were used, which allowed larger spacing between post-tensioning bars to accommodate anchor plate clearances. In order to mimic the level of stress used in the Sandia

specimen, Specimen 1 had nine 36 mm (1.4 in) diameter DYWIDAG bars in the circumferential direction, spaced at 18 cm (7 in), each with about 670 kN (150 kips) of applied force, resulting in a circumferential stress of about 11.5 MPa (1.7 ksi), ignoring Poissons effect. In the vertical direction, Specimen 1 had three 33 mm (1.3 in) diameter DYWIDAG bars spaced at 61 cm (2 ft), each with about 445 kN (100 kips) of applied force, resulting in a vertical stress of about 2.2 MPa (0.3 ksi), ignoring the gravity load and Poissons effect. Specimen 1 contained 9 concrete gages with thermocouples to measure concrete strain and temperature over time at three locations through the wall thickness. In addition, 7 of the DYWIDAG post-tensioning steel bars in Specimen 1 were equipped with strain gages to monitor the bar strains over time.

To capture the effects of changing the geometry and reinforcement ratios (since compression steel is known to reduce the overall influence of concrete creep) in the vertical and circumferential directions on creep propagation, Specimen 2 was designed with 3 times the thickness (Figs. 11–12) of Specimen 1 and about 1/3 of the steel reinforcing ratios (Figs. 16–20). The reinforcement ratios used in Specimen 2 were also a more practicable ratio as used in typical concrete building construction. The level of applied stress was approximately the same for Specimens 1 and 2 with bar placement shown in Figs. 13–15. The comparison of creep between Specimens 1 and 2 may vary due to differential drying creep through the different thicknesses of the specimens. Thus Specimen 2 was equipped with 9 concrete gages to measure strain and temperature at varying thicknesses of the wall to capture any through thickness differentials. In addition, 14 of the DYWIDAG bars in Specimen 2 were equipped with strain gages to monitor the bar strains over time.

Specimen 3 (Figs. 21–22) was constructed to serve as a control specimen, containing no reinforcing steel and no post-tensioning bars, in order to identify how the concrete behaves

independent of applied loading and reinforcement. Specimen 3 was about 1.5 m (5 ft) tall and 1.5 m (5 ft) wide, with the same thickness as Specimen 2. The dimensions of Specimen 3 were selected to be representative of the larger wall thickness in Specimen 2 and were also limited to the capacity of the crane and the ability to safely lift and move the specimen. Specimen 3 contained 6 concrete gages with thermocouples at varying thicknesses of the wall to measure concrete strain and temperature over time.

One side of each of the three wall specimens was sealed by attaching water resistant wrapping such to mimic typical US containment structures.

As mentioned before, each specimen was equipped with internal gages to measure the strain in the concrete in 3-dimensions at varying depths through the wall thickness, as well as thermocouples attached to the internal gages to measure the temperature of the concrete through the thickness (Figs. 23–25). A thermocouple was also added externally to the specimens to measure daily ambient temperatures. Strain gages were attached to select post-tensioning bars used to apply the specimen prestressing to measure the bar strains as well as the changes in strain over time as stress is redistributed from creep and other mechanisms such as temperature changes (Figs. 26–27). Several humidity sensors were also embedded in Specimen 2 to observe the relative humidity as a function of depth through the thickness of the wall, in an attempt to distinguish the influence of drying creep. All sensors were located in the middle 91 cm by 91 cm (3 ft by 3 ft) of each specimen where the uniform biaxial stress distribution from the post-tensioning bars existed.

Measured sensor data was, and continues to be, collected into a data logger (Figs. 28–29) for the lifespan of the project and analyzed periodically to observe concrete and post-tensioning strains and temperatures. Data is post-processed and plotted over time to illustrate the trends in each of the sensors as well as the specimens as a whole. This data is presented in Section 3.

2.2. Instrumentation

The instrumentation used for the three specimens was selected carefully based on the demands and expected range of strain and temperature for each wall.

2.2.1. Sign Convention

The sign convention used for the instrumentation was defined as the x-axis running parallel to the ground, the y-axis running parallel to the vertical post-tensioning steel bars, and the z-axis running through the wall thickness of the specimens. All compression measurements are negative and all tension measurements are positive. Mentions of circumferential, vertical, and radial directions correspond to the x, y, and z directions, respectively.

2.2.2. Full Bridge Concrete Strain Measurements

The full bridge embedded concrete gages used in this study were KM-100BT, manufactured by Tokyo Sokki Kenkyujo Co., Ltd. The gages had an approximate rated output of ±5000 με at 2.5 mV/V within a temperature range of -20 °C to 80 °C, a gage length of 100 mm (3.9 in), and a resistance of 350 Ω (Tokyo Sokki Kenkyujo Co., Ltd. 2017b). These gages are designed with a self-temperature compensated transducer that has a coefficient of thermal expansion similar to that of concrete. To verify the temperature dependence from the manufacturer's specifications, a concrete gage was left to sit unloaded for about 4 and half days and the strains were plotted (Fig. 30) along with the expected thermal strains (calculated by multiplying the change in temperature by the thermal coefficient of expansion for concrete, estimated to be $10x10^{-6}$ ε /°C or $6x10^{-6}$ ε/°F, which falls within the range provided by the Federal Highway Administration 2016). The plot confirmed a correlation between the strain in the concrete gage and the change in temperature, closely related to the coefficient of thermal expansion of concrete.

These gages were chosen because the loadings designed for Specimens 1 and 2 were expected to produce strains that fell well within the output range. Each gage had an individual offset value that was provided in the product data when the gages were delivered. In order to ensure that each concrete gage remained within its functioning range (±5000 με), the gages were sorted and labeled based on the offset values to determine optimal location within the specimens (Table 1). For example, a gage with an existing compressive offset would not be installed in the compression direction of a specimen because the functioning range in compression (-5000 με) could potentially be exceeded.

The raw data read from the full-bridge concrete strain gages into the data acquisition was in mV/V and converted to με by multiplying by the excitation voltage of 2.5 V and multiplying by 1000 to convert units from mε to με. In summary, the conversion of raw data from the concrete gages in mV/V to με is:

$$Concrete\ gage\ strain\ [\mu\varepsilon] = Raw\ data\left[\frac{mV}{V}\right] * Excitation\ voltage[2.5\ V] * \left[1000\ \frac{\mu\varepsilon}{m\varepsilon}\right] \ldots (1)$$

A total of 24 concrete gages were installed in the 3 specimens, measuring the strain in the concrete in the x, y, and z directions at various depths of the wall thicknesses (Figs. 23–25).

2.2.3. Half Bridge Strain Measurements on Post-Tensioning Steel

Strain gages attached to the post-tensioning steel bars were type FCA-6-11, manufactured by Tokyo Sokki Kenkyujo Co, Ltd. The gages had a gage length of 5 mm (0.2 in), a gage width of 2.3 mm (0.09 in), a backing diameter of 14 mm (0.6 in), a resistance of 120 Ω, a gage factor of 2.1, and were composed of 2 stacked elements 90° from each other (Tokyo Sokki Kenkyujo Co., Ltd. 2017a). Each strain gage had a strain limit of ±5% or 50,000 με. The maximum strain

expected to be induced in the post-tensioning bars was about 4200 με, therefore these gages were deemed appropriate.

The raw data read from the half-bridge strain gages into the data acquisition was in με, therefore no conversion was required in the post-processing. However, some data offsets developed during the installation of the post-tensioning bars and were corrected during post-processing. This is discussed further in Section 2.4.6.

2.2.4. Thermocouple Measurements

The thermocouples were housed within the KM-100BT full bridge concrete gages, allowing for the simultaneous measurement of strain and temperature at a point (Tokyo Sokki Kenkyujo Co., Ltd. 2017b). The thermocouples were type T with an operating range of -20°C to 80°C. As per Japanese manufacturing convention, the thermocouples contained a white (-) and a red (+) wire. The wires needed to be extended due to the distance between the data acquisition and the specimens. The extension wire used in this project was United States grade, conventionally blue wire (+) and red wire (-). The data read from the thermocouples into the data acquisition was in °C.

An additional thermocouple was added to the outside of Specimen 2 to monitor ambient temperature as a means for comparing outside temperature fluctuations (daily and seasonally) with internal concrete temperature fluctuations.

2.3. Data Acquisition

The data acquisition system (Figs. 28-29) that was developed for this project was a Campbell Scientific system composed of a CR1000 data logger, three AM16/32B multiplexers for the concrete gages and post-tensioning bar strain gages, and an AM25T multiplexer for the

thermocouples. The system was designed with a solar panel connected to a backup battery for continuous power. The data logger was programmed to collect a data point for all of the gages once per hour. The program can be found in Appendix C. Figure 31 shows a representation of the data acquisition set up.

2.4. Materials of Construction

The materials used to construct the specimens were carefully selected to mimic those used in actual containment vessels.

2.4.1. Concrete Mix Quantities

In the smaller scale materials portion of this research conducted by PhD student Aishwarya Baranikumar (email, 2017), a design mix for the concrete was established based on a mix design provided by Electricité de France. The concrete used in the large-scale specimens, with an estimated 28-day compressive strength of about 38 MPa (5.5 ksi) and a design slump of about 150 mm (6 in), was designed saturated-surface-dry (SSD) with the following quantities:

1. Cement type I/II - 320.0 kg/m^3 (539 lb/yd^3)
2. Fine aggregate 0/4 mm (0/0.16 in) river sand – 835 kg/m^3 (1407 lb/yd^3)
3. Intermediate aggregate 4/11 mm (0.16/0.43 in) river gravel – 457 kg/m^3 (770 lb/yd^3)
4. Coarse aggregate 8/16 mm (0.31/0.63 in) limestone – 563 kg/m^3 (949 lb/yd^3)
5. Water – 166 kg/m^3 (280 lb/yd^3),
6. Water to cement ratio - 0.52
7. Admixture pozzolith 80 - 1350 mL (46 oz)

2.4.2. Reinforcement Steel

The large-scale specimens were fabricated with Grade 60 side face mesh reinforcement steel in accordance with ASTM A615 specifications (American Society for Testing and Materials 2016).

2.4.3. Post-Tensioning System

The unbonded post-tensioning steel bars used in the stressing procedures of Specimens 1 and 2 were threadbars manufactured by DYWIDAG-Systems International, conforming to ASTM A722 with an ultimate stress of 1034 MPa (150 ksi) (Dywidag-Systems International 2016). The circumferential bars were about 35 mm (1.4 in) diameter, with a cross sectional area, A_{ps}, of about 1,020 mm^2 (1.6 in^2), and an ultimate stress, f_{pu}, of 1030 MPa (150 ksi). The vertical bars were about 33 mm (1.3 in) diameter, with a cross sectional area, A_{ps}, of about 806 mm^2 (1.3 in^2), and an ultimate stress, f_{pu}, of 1030 MPa (150 ksi).

Both the circumferential bars and vertical bars were initially pulled to a stress of about 0.65 f_{pu}, resulting in a force of about 667 kN (150 kips) for the horizontal bars, and about 534 kN (120 kips) in the vertical bars. After anchoring and lock off, the stress in the bars dropped to about 0.53 f_{pu}, resulting in about 534 kN (120 kips) of force in the horizontal bars, and about 445 kN (100 kips) of force in the vertical bars.

2.5. Fabrication Procedure

Fabrication of the specimens started in the end of May, 2017 and concrete was poured in early July, 2017. The specimens were left to cure until post-tensioning operations started on August 22, 2017. Post-tensioning was completed on September 7, 2017 and the specimens were lifted and moved into their final positions on September 12, 2017.

2.5.1. Reinforcement Cage Assembly

Specimen 1 was the first specimen to be assembled (Figs. 6–10, 32–33) beginning in the end of May 2017. First, the two perimeter vertical cages of Specimen 1 were assembled, composed of 2 rows of 3 #6 longitudinal bars running vertically, spaced at about 16.5 cm (6.5 in). The vertical #6 bars were tied transversely by #4 closed hoops, spaced at about 11 cm (4.5 in) from the top and mid-height of the specimen and about 10 cm (4 in) near the feet of the specimen. Next, the upper and lower horizontal perimeter cages were assembled, which consisted of 2 rows of 3 #7 longitudinal bars spaced at about 10 cm (3.8 in) and tied transversely by #4 closed hoops spaced at about 15 cm (6 in). The horizontal cages bent inwards to tie into the vertical cages. Next, the two layers of wall face mesh steel were connected to the horizontal and vertical perimeter cages, composed of alternating #5 and #6 vertical bars spaced at about 15 cm (6 in), and tied directly to the horizontal #7 bars spaced at about 11 cm (4.4 in). Finally, the radial ties were installed through the wall thickness, providing a connection between the two mats of steel on both faces of the wall. Due to very tight spacing and constructing the walls flat on the ground, some of the radial ties were left out of the assembly in non-critical locations. However, the center 91 cm by 91 cm (3 ft by 3 ft) section was constructed per design. The circumferential reinforcement ratio for Specimen 1 was about 0.0212 and the vertical reinforcement ratio was about 0.0098, similar to the Sandia test specimen.

Specimen 2 was constructed next (Figs. 16–20, 34–35). Similar to the assembly of Specimen 1, the vertical perimeter cages were assembled first, then the horizontal perimeter cages were assembled and connected to the vertical cages, and finally the wall face mesh steel was connected to the perimeter cages with radial ties running through the thickness to connect the two mats of steel. The vertical perimeter cages consisted of 8 #9 bars, enclosed in #6 closed

hoops spaced vertically at about 11 cm (4.5 in). The horizontal perimeter cages consisted of 8 #10 bars enclosed in #6 closed hoops spaced horizontally at about 20 cm (8 in). The wall face mesh steel consisted of #9 vertical bars spaced at about 0.41 m (16 in) tied directly to #10 horizontal bars spaced at about 23 cm (9 in). #5 radial ties (with 90°and 135° hooked ends) were installed to provide a connection between the two mats of steel. The reinforcement ratio was about 0.0078 in the circumferential direction and 0.0035 in the vertical direction.

Specimen 3 had no steel reinforcement.

Once the steel reinforcement was assembled for Specimens 1 and 2, the plastic post-tensioning ducts were installed through the cages to provide hollow holes for the post-tensioning bars to be inserted after the concrete was poured (Figs. 36–39).

2.5.2. Formwork Assembly

Formwork assembly began in mid-June 2017. Specimens 1 and 2 were built on the ground for ease of formwork construction, concrete pouring, and post-tensioning, and were later lifted upright and into place (Figs. 40–41). Formwork bases and walls consisted of 20 mm (0.8 in) plywood supported by 50 mm by 152 mm (2 in by 6 in) boards at a spacing of about 31 cm (12 in) center to center and braced with 50 mm by 152 mm (2 in by 6 in) boards for lateral support.

2.5.3. Concrete Gage Installation

Once the formwork was assembled and the reinforcing steel cages were lifted into the formwork, the concrete gages were attached to the reinforcing steel of Specimen 1 and 2 and to a smooth steel support in Specimen 3 (Fig. 42–45). The concrete gage locations are summarized in Table 1.

9 concrete gages were installed in Specimen 1 with 3 bundles of 3 gages (x, y, and z-directions) at 3 different depths, all located within the center 91 cm by 91 cm (3 ft by 3 ft) of the specimen (Figs. 23 and 43). Gages 1 through 3 (1 corresponding to the x-direction, 2 corresponding to the y-direction, and 3 corresponding to the z-direction) were installed in the cover at about 5 cm (2 in) from the surface of the side of Specimen 1 without weatherproofing. Gages 4 through 6 were installed in the center depth of Specimen 1 at about 17 cm (6.5 in). Finally, gages 7 through 9 were installed in the cover of the face of Specimen 1 that had the weatherproofing. All gages were attached to reinforcing steel with zip ties and tie wire to ensure alignment in the correct direction and to ensure maximum contact with concrete on all sides of the gages. Some initial strains were induced in the concrete gages because of the way they were attached to the reinforcing steel cage for proper alignment in their respective directions. These initial strains and offsets were accounted for in post-processing and the gages were zeroed just prior to when the concrete was poured.

9 concrete gages were installed in Specimen 2, similar to the layout of Specimen 1. However due to the depth of Specimen 2 (91 cm, 36 in), it was impossible to reach into the bottom of the reinforcing steel cage to install gages in the cover of the face of the specimen that was not weatherproofed (Figs. 24 and 44). Therefore, gages 10 through 12 were installed in the cover of the face with weatherproofing, gages 13 through 15 were installed at the quarter point of the depth (about 23 cm, 9 in) and gages 16 through 18 were installed at the center of the depth (about 46 cm, 18 in).

6 concrete gages were installed in Specimen 3 with 2 bundles of 3 gages in the x, y, and z-directions (Figs. 25 and 45). Gages 19 through 21 were installed in the center depth of Specimen 3 at about 46 cm (18 in) and gages 22 through 24 were installed in the cover Specimen

3 without weatherproofing. Since there was no reinforcing steel to attach the gages to in Specimen 3, the gages were attached to a smooth steel support.

Before pouring the concrete, the gages were connected to the data acquisition (DAQ) (Fig. 46) to ensure that they responded to daily temperature changes. When the concrete was poured, care was taken to ensure that concrete was not poured directly on top of the gages to avoid shifting them in any direction.

2.5.4. Batching and Mixing Concrete

Concrete for all specimens was poured on July 7, 2017 (Figs. 47–53). Two trucks were used to pour all three specimens. In addition, several cylinder samples (101 mm (4 in) diameter and 203 mm (8 in) tall) were made from the concrete of both trucks to ensure concrete mix was consistent. The first truck, which arrived at 11:45 am, contained 6.5 m^3 (8.5 yd^3) of concrete and was used to pour Specimen 2. The second truck, which contained 5.0 m^3 (6.5 yd^3) of concrete, arrived at 12:30 pm and was first used to pour Specimen 3. At 12:50 pm, the rest of the concrete from the second truck was used to pour Specimen 1. The outside temperature during the pours was about 32 ℃ (90 ℉).

The concrete slump from truck 1 was approximately 25 cm (10 in) and the slump from truck 2 was approximately 28 cm (11 in). The slump values were more than expected from previous smaller scale materials testing, but the concrete was judged to be consistent and not separating.

The strains induced in the concrete gages during the concrete pour are recorded in Table 2.

After the concrete was poured, the specimens and cylinder samples were covered with plastic tarps to allow for minimal moisture loss during curing. The concrete specimens were not subjected to any additional moisture while the tarps were installed. The tarps were removed about one month after the concrete was poured.

28-day compressive strength tests were conducted on 3 cylinder samples from each truck. The samples from truck 1 (Specimen 2) had an average compressive strength of 37.9 MPa (5.5 ksi) and the samples from truck 2 (Specimens 1 and 3) had an average compressive strength of 32.3 MPa (4.7 ksi) (Baranikumar, email, 2017). Both strengths were slightly lower than the anticipated values from the smaller scale materials testing. However, the concrete was judged to be sufficient for this research.

28 day split tensile tests were also conducted on 3 cylinder samples from each truck. The samples from truck 1 (Specimen 2) had an average splitting tensile strength of 2.9 MPa (426 psi) and the samples from truck 2 (Specimens 1 and 3) had an average splitting tensile strength of 2.6 MPa (377 psi).

2.5.5. Strain Gage Installation on Post-Tensioning Steel

21 half bridge strain gages were attached to 21 post-tensioning steel bars in the climate controlled High Bay Lab at Texas A&M. The first step in the procedure was to grind down a 15 cm by 5 cm (about 6 in by 2 in) rectangular strip located about 60 cm (24 in) from the end of the bar until the surface was free of ridges. The area was then sanded down until the strip was shiny and smooth (Fig. 54). Then, the area was thoroughly cleaned with a cloth and alcohol to remove dust and residue left over from sanding. Next, the strip was wiped down with a lint free Q-Tip and Vishay M-Prep Conditioner A to remove finer particles from the surface. Next, Vishay M-Prep Neutralizer 5A was applied to neutralize the left-over Conditioner A on the strip of metal

and give it a final cleanse. A coat of Vishay M-Bond GA-2 adhesive was then applied to the smooth surface and the strain gage was carefully applied with the bottom element in line with the longitudinal axis of the bar. A strip of terminals was then glued down about 13 mm (0.5 in) below the gage wires. The gages and terminals were wrapped with tape to apply uniform pressure on the gage to ensure a strong bond between the gage and the steel bar (Fig. 55). The glue was left to dry for 24 hours and then an additional coat of Vishay M-Bond GA-2 adhesive was applied to the top of the gages and terminals, encasing the circumference of the bar with a thin layer of glue (Fig. 56). This layer was left to dry for another 24 hours. The next day, the gage wires were soldered to the terminals. Extension wires were then soldered to the terminals that would connect to the data acquisition (Fig. 57). Next, a thick layer of Vishay M-Coat J was applied to the bar, covering the strain gage and the circumference the bar to provide water resistance to the gage and the exposed ends of the extension wires. This layer was left to dry for 24 hours. To minimize damage, the extension wires were zip tied to the bar in multiple locations to prevent snagging. On the day that post-tensioning commenced, the bars were shipped out to Rellis Campus, where the specimens were located.

2.5.6. Post-Tension Installation

When the post-tensioning bars arrived to the site, the bars were placed into the ducts with the thinner diameter bars (about 33 mm, 1.3 in) running through the vertical ducts and the thicker diameter bars (about 36 mm, 1.4 in) running through the horizontal ducts. Due to the high concentration of reinforcing steel in the specimens, some of the ducts were slightly curved after concrete placement and some of the post-tensioning bars had to be forced into the ducts with a sledgehammer, which resulted in damage to some of the strain gages. Once all of the post-tensioning bars were placed in the ducts (Figs. 58–59), the anchor plates were slipped on both

ends of the bars and the nuts were loosely screwed onto the bars thereafter (Figs. 60–61). Finally, the extension wires that were attached to the bars with strain gages were connected into the data acquisition (Fig. 62).

Post-tensioning operations began on August 22, 2017 (about 46 days after the concrete was poured), beginning with the vertical bars of Specimen 2. It was later found that at the time that post-tensioning began the data acquisition was not properly reading the bar strain gage values due to a wire connection issue. In order to capture the amount of strain being applied to the post-tensioning bars, an external strain gage box was used to measure the bar strain under load. The strain gage box reading was zeroed initially for each bar. Once the bar was pulled and locked-off, the strain from post-tensioning was recorded. These values were recorded by hand and were accounted for in post-processing as the initial values for the bar strain gages (Table 3). The vertical bars were loaded with a hydraulic jack (Fig. 63) to about 534 kN (120 kips), about 15% more than the desired force of about 445 kN (100 kips) to account for losses from lock-off. Once the desired strain was attained, the nut was tightened by hand on the side of the bar where the jack was located and then the hydraulic jack was unloaded. As a result of unloading the hydraulic jack, the strain in the bar fell slightly due to anchoring and seating of the bar at the specimen ends. Next, the circumferential bars of Specimen 2 were loaded. It was initially planned to pull the circumferential bars with 800 kN (180 kips). However, the force capacity of the jack made it dangerous to exceed 667 kN (150 kips). Therefore, the circumferential bars were pulled with about 667 kN (150 kips), which resulted in a force of about 534 kN (120 kips) once the bars were unloaded and locked-off. Specimen 1 vertical bars were loaded next to the same force as the vertical bars in Specimen 2. Finally, the circumferential bars in Specimen 1 were loaded to the same level of force as the circumferential bars in Specimen 2.

For Specimen 1, the amount of stress on the concrete from the post-tensioning in the x-direction was approximately 11.5 MPa (1.7 ksi) and was about 2.2 MPa (0.3 ksi) in the y-direction, neglecting biaxial loading effects and gravity load. For Specimen 2, the stress on the concrete in the x-direction was close to 14 MPa (2 ksi) and was about 3.5 MPa (0.5 ksi) in the y-direction, neglecting biaxial loading effects and gravity load.

It was initially planned to post-tension all bars in the same week. However, the threaded couplers used in the stressing operations eventually were damaged and became stuck to some of the bars, so more couplers had to be ordered. All post-tensioning operations took place within three weeks, concluding on September 7, 2017. By the end of the three weeks, the data acquisition was corrected and was functioning properly. The specimens were moved and lifted upright (Figs. 64–68) later that week causing the data acquisition to be disconnected temporarily. The data acquisition was in its final location with all gages reconnected as of September 12, 2017.

Once the gages were reconnected to the data acquisition, the external strain gage box was used to verify the strain values on the bars against the data acquisition readings. As expected, the data acquisition was reading different strains than the external strain gage box because the strain values in the data acquisition were not zeroed prior to post-tensioning. At least two data points for each bar were captured with the strain gage box prior to the data acquisition functioning properly. The initial values were the values associated with the bars being pulled at the time of lock-off. Since the initial values were consistently recorded with the strain gage box, the difference between the box readings on September 12, 2017 and the data acquisition readings on the same date were recorded as the calibration constant (Table 3). The calibration constant for

each bar was added to the data acquisition values so that they matched the strain gage box values thereafter. All of the calibrating operations were done in post-processing.

Out of the 21 strain gages that were originally attached to the post-tensioning bars, only 10 survived the post-tensioning operations. The gages that were not functioning were excluded in the results section of this study.

2.6. Summary

The design process for the three specimens began in October 2016 at the project initiation. The reinforcing steel cages, formwork, and concrete gage and thermocouple instrumentation installation was completed, and the concrete was poured on July 7, 2017. The data acquisition collected hourly after the pour, collecting concrete strain and temperature information. Post-tensioning operations began on August 22, 2017, about a month and a half after the concrete was poured. All post-tensioning was complete by September 7, 2017. During the post-tensioning operations, about half of the strain gages on the post-tensioning bars were damaged. The damaged strain gages were excluded from the results section of this study. All data acquisition sensors (excluding the damaged sensors) were functioning properly after the specimens were lifted into their final positions on September 12, 2017. Since then, the data acquisition was, and continues to be, collecting data hourly for all functioning sensors. The collected data is analyzed in the results section of this study. All initial values and offsets can be found in Appendix II and are automatically accounted for in post-processing (Tables 2–3).

3. PRELIMINARY MEASURED DATA

3.1. Overview

All data collected for the functioning gages over the span of the project can be found in Figures 69–127. The instrumentation data for the specimens is broken down into three convenient sections to identify the behavior of the concrete and the post-tensioning bars during significant events in the project: pouring and curing of the concrete (Figs. 128–176), post-tensioning of the specimens (Figs. 177–222), and post-tensioning of the specimens to the February 16, 2018, which was the last day data was collected for this publication (Figs. 223–281).

3.2. Instrumentation Data Just Prior to Concrete Pour through Curing

Data for the 24 internal concrete gages (Figs. 128–151) and 25 thermocouples (Figs. 152–176) was collected and post-processed between the morning of the concrete pour (July 7, 2017) up to the about a month after the concrete pour (August 8, 2017), to identify the behavior of the concrete during curing. The concrete gages were zeroed the morning of the pour to identify the amount of strain induced during the pour and throughout curing.

3.2.1. Specimen 1

Specimen 1 contained 9 concrete gages (CG 1 through CG 9, Figs. 128–136) and 9 thermocouples (TC 1 through TC 9, Figs. 152–160). At the time the concrete was poured, the concrete gages immediately picked up either tensile or compressive strains, based on their orientation and connection to the reinforcing steel in the specimen. After the concrete was poured, the gages stabilized and their fluctuations reflected the strain induced by the changes of the internal temperature of the concrete throughout curing. Specimen 1 experienced a maximum curing temperature of nearly 70 ºC (158 ºF). After about a week of curing, the thermocouples in Specimen 1 stabilized to mimic the fluctuations of the ambient temperature.

3.2.2. Specimen 2

Specimen 2 contained 9 concrete gages (CG 10 through CG 18, Figs. 137–145) and 9 thermocouples (TC 10 through TC 18, Figs. 161–169). The behavior of the concrete gages in Specimen 2 were similar to Specimen 1. Concrete gage 11 malfunctioned when the concrete was poured and was unrepairable. The induced strains in the concrete from post-tensioning are summarized in Table 4. Specimen 2 experienced a maximum curing temperature of nearly 75 ºC (167 ºF). Similar to Specimen 1, the thermocouples stabilized after about a week of curing.

3.2.3. Specimen 3

Specimen 3 contained 6 concrete gages (CG 19 through CG 24, Figs. 146–151) and 6 thermocouples (TC 19 through TC 24, Figs. 170–175) Concrete gage 21 showed malfunctioning behavior early during the curing process and remained unresponsive to internal temperature changes. The other concrete gages behaved similarly to those in Specimens 1 and 2. The thermocouples in the middle of Specimen 3 read the highest temperature during curing of about 74 ºC (165 ºF).

3.3. Instrumentation Data as a result of Post-Tensioning Operations

Data for 18 internal concrete gages (Figs. 177–194), 18 thermocouples (Figs. 195–212), and the 10 functioning post-tensioning bar strain gages (Figs. 213–222) located in Specimens 1 and 2 was collected and post-processed between about 3 days before post-tensioning began (August 18, 2017) up to about two weeks after all post-tensioning operations concluded (September 20, 2017). The concrete gages were zeroed on August 18, 2017 to show the relative change in strains as a result of post-tensioning, as represented in Table 4. This data is presented for each specimen below.

3.3.1. Specimen 1

The concrete gages (CG 1 through 9, Figs. 177–185) remained relatively stable up to the day of post-tensioning (between August 22, 2017 and September 7, 2017), reflecting only the strains induced from temperature changes. For most of the concrete gages embedded in Specimen 1, there was an evident spike in strain when post-tensioning operations took place on August 22, 2017 and September 7, 2017. The induced strains in the concrete as a result of post-tensioning are summarized in Table 4.

On average in the x-direction (CG 1, 4, and 7), there was a total compressive strain of approximately -600 με as a result of post-tensioning operations. With the applied loading, the concrete gages in the x-direction were expected to notice an induced strain of about -423 με. The estimated strain was calculated based on the following formula, where the total applied force per bar is divided by the approximated modulus of elasticity (27.8 GPa, 4030 ksi, estimated based off of American Concrete Institute 2014), the net area (area of the wall in between the post-tensioning bars minus the area of the post-tensioning duct) and multiplied by 1,000,000 to convert strain to microstrain:

$$Est.\,Concrete\ Strain\ [\mu\varepsilon] = \frac{Jacking\ Force}{[Area\ between\ PT\ bars\ -\ Area\ duct] * E} * \left[1{,}000{,}000\ \frac{\mu\varepsilon}{\varepsilon}\right] \ldots (2)$$

In the y-direction, CG 2 (in the cover of the specimen on the face of the wall without weatherproofing) read a slightly compressive strain, whereas CG 5 (in the middle thickness of the specimen) and CG 8 (in the opposite cover of the specimen) read tensile strains. Thus, the sign difference reduced the average strain in the y-direction to a lesser value of about 63 με. With the applied loading, the concrete gages in the y-direction were expected to notice an

induced strain of about -80 με from Equation 2. However, the strain estimations did not take into consideration the effects of the 3D stress field and Poissons effect. In the z-direction (CG 3, 6, and 9), CG 3 (in the cover of the specimen on the face of the wall without weatherproofing), CG 6 (in the middle thickness of the specimen) and CG 9 (in the opposite cover of the specimen) read tensile strains. The average strain in the concrete in the z-direction as a result of post-tensioning was about 180 με.

Specimen 1 was first post-tensioned in the y-direction (with the post-tensioning bars aligned at about the center of the thickness of the specimen) and then it was later post-tensioned in the x-direction with a larger jacking force, resulting in an increase of compressive stress in the x-direction. Therefore, it makes sense that the strains in the x-direction were all compressive, and that there was a variation of smaller compressive and tensile strains in the y-direction and z-direction due to Poissons effect. As the specimen was post-tensioned, it was laying on its face with gage bundles CG 1-3 at the top, CG 4-6 in the middle, and CG 7-9 at the bottom, nearest to the base formwork. Thus, when Specimen 1 was post-tensioned in the y-direction, CG 2, 5, and 7 all went into compression until post-tensioning force was applied in the x-direction. It makes sense that CG 2 (in the cover and above the post-tensioning bars) went into compression and stayed in compression when the x-direction bars were pulled because the face of the concrete at the top was free. Whereas in the center of the specimen where CG 5 ran in the y-direction and CG 6 ran in the z-direction, it follows that the concrete experienced a tensile change in strain when the x-direction bars were pulled because the stress in the x-direction was larger (a result of the Poissons effect). Similarly, CG 8 and CG 9 experienced a tensile change in strain after the x-direction bars were pulled, most likely because the face of the concrete where the gages were

located was not free and was subjected to the weight of the concrete itself, along with the larger stress induced in the x-direction from the post-tensioning operations.

After post-tensioning operations were completed on September 7, 2017, the concrete gages experienced strain variations due to daily temperature fluctuations. The thermocouple readings (Figs. 195–203) indicated the temperature in the concrete in the same location as each respective concrete gage. The average temperature of the concrete between when post-tensioning was finalized and September 20, 2017 was approximately 28 ºC (82 ºF). The thermocouples in Specimen 1 did not show a strong relationship between the temperatures of the concrete and depth of embedment through the thickness of the wall, most likely because the wall was relatively thin compared to Specimen 2. Many data points for the thermocouples were missing due to a wiring issue that was resolved on September 8, 2017.

The strain gages on the post-tensioning bars (Figs. 213–217) in Specimen 1 (SG 2, 3, and 5 in the x-direction, and SG 6 and 7 in the y-direction) each exhibited similar behavior to one another. Each bar was pulled to a certain force, and because of losses during the lock-off and anchoring, the resulting force was reduced on average by about 25%. Strain gage 2 indicated a maximum strain about 1000 με less than that of strain gages 3 and 5, therefore there may have been some malfunctioning occurring in the sensor. Excluding strain gage 2, in the x-direction the strain gages on the post-tensioning bars indicated an average maximum strain of about 2700 με, where the expected value for the maximum strains induced on the horizontal bars was about 3400 με, obtained from the following equation:

$$Est.PT\ Bar\ Strain\ [\mu\varepsilon] = \frac{Jacking\ Force}{Area\ of\ Bar * E} * \left[1{,}000{,}000\ \frac{\mu\varepsilon}{\varepsilon}\right] \ldots (3)$$

where the jacking force in the x-direction was about 667 kN (150 kips), the area of the bar was about 1020 mm^2 (1.6 in^2) and the modulus of elasticity was about 205 MPa (29700 ksi). In the y-direction the strain gages on the post-tensioning bars indicated an average maximum strain of about 2900 με, where the expected value was about 3200 με, obtained from Equation 3, assuming a jacking force of 534 kN (120 kips) and a bar area of 806 mm^2 (1.3 in^2).

3.3.2. Specimen 2

Similar to Specimen 1, the concrete gages in Specimen 2 (CG 10 through 18, Fig. 186–194) remained relatively stable up to the day of post-tensioning. The induced strains in the concrete from post-tensioning are summarized in Table 4.

On average in the x-direction (CG 10, 13, and 16), there was a compressive strain of approximately -360 με induced by the post-tensioning operations with each gage reading a compressive value. With the applied loading, the concrete gages in the x-direction were expected to experience an induced strain of about -510 με from Equation 2. In the y-direction CG 11 (in the cover of the specimen on the face of the wall without weatherproofing) malfunctioned and is thus neglected in the analysis. CG 17 (located in the middle of the specimen) read a tensile change in strain, whereas CG 14 (located 23 cm, 9 in into the thickness of the specimen) read a compressive change in strain. Thus, the sign difference reduced the average strain in the y-direction to a lesser value of -10 με. With the applied loading, the concrete gages in the y-direction were expected to experience an induced strain of about -130 με from Equation 2. However, similar to the estimation made for Specimen 1, these strain predictions did not consider the effects of the 3D stress field and Poissons effect. All of the concrete gages in the z-direction (CG 12, 15, and 18) read tensile changes in strain, averaging to about 125 με as a result of post-tensioning.

Specimen 2 was first post-tensioned in the y-direction (with three layers of post-tensioning bars) and then it was later post-tensioned in the x-direction with a larger jacking force, resulting in an increase of compressive stress in the x-direction, causing compressive strains for all of the gages running in the x-direction. Similar to Specimen 1, there was a strain sign variation in the y-direction, most likely due to the fact that CG 14 was located in between the center of the thickness of the specimen and the top cover, where a high level of compressive stress was induced. CG 17 was strained in tension as the x-direction bars were pulled, indicating that the stress in the x-direction overcame that of the y-direction, and inducing a tensile strain because of the Poissons effect. As the specimen was post-tensioned, it was laying on its face with gage bundles CG 10-12 at the top, CG 13-15 in the quarter point (23 cm or 9 in), and CG 16-19 at the center thickness of the specimen, about 46 cm (18 in) below the top bundle. Similar to Specimen 1, all of the z-direction gages (CG 12, 15, 18) in Specimen 2 had induced tensile strains when the post-tensioning stresses were applied.

The thermocouples in Specimen 2 (Figs. 204–212) also captured temperature data from August 18, 2017 to September 20, 2017. There was clearly less movement in the temperature data associated with increased embedment depth of the gages associated with Specimen 2 than compared to Specimen 1. The average temperature in the concrete of Specimen 2 between when the post-tensioning was completed on September 7, 2017 and September 20, 2018 was similar than that of Specimen 1, approximately 28 ºC (82 ºF). There was a more obvious trend with the thermocouples in Specimen 2 showing less temperature variation for the gages that were embedded deeper in the thickness of the specimen.

The strain gages on the post-tensioning bars (Figs. 218–222) in Specimen 2 (SG 8, 10, 15, and 16 in the x-direction, and SG 18 in the y-direction) each exhibited similar behavior as the

post-tensioning bar strain gages in Specimen 1. Each bar was pulled to a certain force, and because of losses during the lock-off and anchoring, the resulting force was reduced on average by about 32%. Strain gages 8 and 15 indicated about 50% losses from the maximum strain, therefore there may have been some malfunctioning occurring in the sensors. In the x-direction the strain gages on the post-tensioning bars indicated an average maximum strain of about 2800 με, where the expected value for the maximum strains induced on the horizontal bars was about 3400 με, obtained from Equation 3, where the jacking force in the x-direction was about 667 kN (150 kips), the area of the bar was about 1020 mm^2 (1.6 in^2) and the modulus of elasticity was about 205 MPa (29700 ksi). In the y-direction the strain gages on the post-tensioning bars indicated an average maximum strain of about 2600 με, where the expected value was about 3200 με, obtained Equation 3, assuming a jacking force of 534 kN (120 kips) and a bar area of 806 mm^2 (1.3 in^2).

3.4. Instrumentation Data from Post-Tensioning to February 16, 2018

The data from the August 18, 2017 (4 days prior to post-tensioning) to February 16, 2018 was collected and post-processed (Figs. 223–281). Since about 26 weeks passed in between when post-tensioning operations commenced and the final data collection on February 16, 2018, the changes in measured data were relatively small, and possibly a function of ambient temperature change during the winter. The data associated with the overall change in strain the concrete gages over the 26-week time period is located in Table 5 and the data associated with the overall change in strain in the post-tensioning strain gages over the 26 weeks is located in Table 6.

3.4.1. Specimen 1

As indicated above, Specimen 1 contained 9 concrete gages (Figs. 223–231), 9 thermocouples (Figs. 247–255), and 5 properly functioning post-tensioning bar strain gages (Figs. 272–276). TC

8 began to malfunction after post-tensioning took place and was thus neglected in the following analysis of Specimen 1.

In the x-direction, the average change in concrete strain over the 26-week period was approximately -100 με (from to -600 με to -700 με), indicating that the concrete was becoming more compressive in the x-direction. This compressive behavior may be attributed to the seasonal temperature variations since the outside temperature (Fig. 271) started at approximately 35 ºC (95 ºF) in September and fell down to around 5 ºC (41 ºF) during the winter months, with a minimum temperature of -5 ºC (23 ºF) in the middle of January 2018. The strain gages attached to the post-tensioning bars in the x-direction (Figs. 272–274, SG 2, SG 3, and SG 5) experienced an average change in strain of about -370 με (from 1770 με to 1440 με), indicating that the tensile forces in the post-tensioning bars were reducing as time passed. SG 2 and SG 3 both experienced a compressive change in strain, whereas SG 5 malfunctioned and was not included in the average strain change formulation. Before SG 5 malfunctioned, it appeared to pick up more tensile strain. This pattern could be attributed to the fact that SG 2 and SG 3 were located on interior bars, whereas SG 5 was located on an exterior bar in Specimen 1. Therefore, as SG 2 and SG 3 relaxed, SG 5 picked up more tension to compensate for the change in stress.

In the y-direction, the average change in concrete strain over the 26-week period was approximately 55 με (from 60 με to 115 με), indicating a slight increase in tensile strain. The strain gages attached to the post-tensioning bars in the y-direction (Figs. 275–276) experienced an average change in strain of about -700 με (from 2358 με to 1658 με), indicating that the bars were losing some of the initial post-tensioning force. The change in strain in the y-direction on the post-tensioning bars seemed quite large and possibly indicated an error. Since the bars in the

y-direction were relaxing, the concrete in the y-direction would be put in tension to balance the change in stress, as is confirmed by the tensile strain increase in CG 2, 5, and 8.

In the z-direction, the average change in concrete strain was about 30 με (from 180 με to 210 με), indicating negligible strain changes through the thickness of the specimen.

There were obvious strain losses in the post-tensioning bars in Specimen 1 (disregarding SG 5) immediately after the bars were post-tensioned, most likely associated with the first and second stages of concrete creep. However, the changes in strain since the final placement of the specimens show the need to more carefully investigate the influence of seasonal temperature fluctuations and induced strain and decouple that response from creep response.

3.4.2. Specimen 2

As mentioned before, Specimen 2 contained 9 concrete gages (Figs. 232–240), 9 thermocouples (Figs. 256–264) and 5 properly functioning post-tensioning bar strain gages (Figs. 277–281).

In the x-direction, the concrete gages experienced an average change in strain of only about -55 με (from -355 με to -410 με) in the 26-weeks between post-tensioning and February 16, 2018. The strains measured with CG 10 and CG 16 became more compressive, whereas CG 13 picked up slight tensile strain. The strain gages on the post-tensioning bars in the x-direction endured an average change of strain of about -25 με (from 1875 με to 1850 με), indicating that the bars were slightly losing their tensile force over time, which was expected with the change in temperature and as a result of relaxation and primary and secondary creep. The compressive behavior in the x-direction concrete gages could again be associated with the temperature change, however the effect was much less than that associated with Specimen 1 because Specimen 2 had much larger volume.

In the y-direction, the average change in strain in the concrete was approximately 60 με (from 65 με to 120 με), indicating that the concrete in the y-direction was experiencing more tension over time. The only properly functioning strain gage in the y-direction was SG 18, which underwent a change in strain of about -400 με (from 1966 με to 1566 με) over the 26 weeks. As the y-direction bars lost some tensile force, the concrete in the y-direction had to compensate, putting CG 14, and 17 into tension, as confirmed by the data.

In the z-direction, the average change in concrete strain was about 125 με (from 125 με to 250 με), indicating an increase in tensile strain through the thickness of the specimen. This average change in strain was much more than that found in the z-direction in Specimen 1 and may be attributed to the larger thickness of Specimen 2.

Overall, the post-tensioning bar strain gages in Specimen 2 remained mostly stable, without dramatic losses immediately after post-tensioning was completed. However, over time, many of the bars lost small percentages of tensile force. The losses of the bars may be a result of purely seasonal temperature fluctuations or perhaps creep.

3.4.3. Specimen 3

Specimen 3 contained 6 concrete gages (Figs. 241–246) and 6 thermocouples (Figs. 265–270). Of the 6 concrete gages, CG 19, 21, and 23 continued to malfunction and were thus ignored in the analysis of Specimen 3. Specimen 3 experienced an average change in concrete strain of approximately 125 με in the x-direction (from 0 με to 125 με), 175 με in the y-direction (from 0 με to 175 με), and 125 με in the z-direction (from 0 με to 125 με). Since only one gage was functioning properly in each direction, it was difficult to identify the relationship between concrete depth and strain variation. It was unexpected that the purely concrete block experienced an overall tensile strain increase as the outside temperature dropped during the winter. Generally,

Specimen 3 experienced larger magnitudes of strain change over time compared to Specimens 1 and 2. However, since half of the gages in Specimen 3 malfunctioned, it is difficult to confirm the validity of the results.

3.4.4. Strains Induced by Seasonal Temperature Change

On average, the temperature change from when post-tensioning was completed to February 2018 was about -15 ºC (-27 ºF). Assuming the coefficient of thermal expansion of concrete is $10x10^{-6}$/ºC ($6x10^{-6}$/ºF) (falling within the range provided by the Federal Highway Administration 2016), the concrete would have been expected to experience an induced thermal strain of approximately -150 με between September 2017 and February 2018. Since the coefficient of thermal expansion for concrete is based on many factors including the mix design and aggregate type (Federal Highway Administration 2016), the associated value may vary, resulting in a variable thermal strain. The compressive change in strains in the concrete between September 2017 and February 2018 was most likely a result of the temperature change and thermal properties of the concrete. However, it is possible that some changes in strain result from creep.

3.5. Summary

Data was collected from the day concrete was poured on July 7, 2017 up to February 16, 2018, for a total of about 7 months. The concrete gages and thermocouples collected data from the concrete pour up to about one month after the pour to capture the strains and temperatures in the concrete during curing. All concrete gages experienced a sharp increase in strain (tensile and compressive) as a result of the concrete pour. Over the month of curing, the gages stabilized, reflecting strains induced from the temperature changes internally. Next, the data resulting from post-tensioning was presented. The x-direction concrete gages generally measured compressive strains, whereas the y-direction and z-direction gages varied in compression and tension and had

much smaller strain magnitudes. There were significant changes in the strain readings during post-tensioning steel seating and also some changes due to probable early age creep of the concrete. Finally, data was presented from 4 days before post-tensioning began up to February 16, 2018 to quantify strain changes in the concrete and post-tensioning bars, as well as seasonal temperature variations. Generally, the concrete gages in the x-direction experienced more compressive strains, whereas the y-direction gages picked up more tensile strains. The z-direction concrete gages in Specimen 1 did not pick up much strain difference over the 26-weeks, whereas Specimen 2 z-direction concrete gages picked up a larger amount. Generally, the strain gages on the post-tensioning bars lost tensile strain over time. More data is needed to attribute the behavior of the concrete and post-tensioning bars to creep since much of the collected data correlated to the seasonal temperature changes directly.

4. FINITE ELEMENT ANALYSIS OF SPECIMENS

4.1. Introduction

Two different finite element models were produced in ABAQUS to determine the expected induced strains as a result of post-tensioning operations and to verify the field data measured concrete strains. A creep model was not introduced into the finite element models at this time since the field data was still relatively young. However, the finite element models were designed to be easily modified, allowing the addition of a creep model in the future.

The two different models provided simplified methods for inducing post-tensioning stresses into the reinforced concrete wall structure, modeled after experimental Specimen 1. The first model introduces post-tensioning stresses into the concrete with compressive point (nodal) loads at the locations where the post-tensioning bars were anchored in Specimen 1. The second model introduces post-tensioning stresses as distributed loads over rectangular surface elements on the wall edges that mimicked the geometry of the anchor plates on the actual specimen.

For the future development of the finite element models of these types of structures, it is important to determine which idealization best matches the results attained from the measured sensors in the specimens.

4.2. Modeling Assumptions

In ABAQUS, a system of 8 node brick elements was used to represent the concrete of the wall specimen and linear spring elements were used to represent the side face reinforcing steel meshes. The concrete wall was idealized to be a solid extrusion with dimensions of about 2.4 m by 2.4 m by 33 cm (96 in by 96 in by 13 in) with side face meshing reinforcing steel. The concrete was assigned elastic material properties with a compressive strength of 34.5 MPa (5

ksi), a modulus of elasticity of about 27.8 GPa (4030 ksi), and a Poissons ratio of 0.2. Each component of the reinforcing steel assembly was modeled, including the #6 and #5 vertical bars, the #7 circumferential bars, the #3 radial ties, and the #4 stirrups. The reinforcing steel bars were modeled as 2-node truss elements, where each bars' cross-sectional area was defined. The material used for the reinforcing steel was elastic with a modulus of elasticity of about 199 GPa (29000 ksi) and a Poisson ratio of 0.3.

The reinforcing steel cage was meshed using 3D 2-node truss elements, with a node once about every 10 cm (4 in). The concrete wall was meshed using 8 node brick elements, without reduced integration, with nodes placed once about every 10 cm (4 in).

The reinforcing steel was constrained to the concrete wall as an embedded element, requiring the steel reinforcement to remain inside the wall at all times. The boundary conditions used on the wall were fixed supports on the outer two edges of the base of the wall. Only two analysis steps were defined: the first step was the initial step where the boundary conditions were defined and no external loads were present and the second step was the loading step where the compressive loads were assigned for each model.

4.3. Results

In comparison of the two models, the main focuses were the maximum strains induced by the post-tensioning loads in the x, y, and z directions at the center element of the wall in comparison with actual field data obtained and expected values from hand calculations.

4.3.1. Model 1: Point Loads

The first model simply had point loads applied to each location where a post-tensioning bar was anchored in the actual specimen. There were 9 horizontal compressive point loads on both sides

of the wall in Model 1 (equal and opposite directions), each with a magnitude of about 68 tons (150 kips), spaced every 18 cm (7 in). There were 3 vertical compressive point loads on the top and bottom of the wall in Model 1 (equal and opposite directions), each with a magnitude of about 45 tons (100 kips), spaced every 61 cm (24 in). The loads were applied directly to nodes of the concrete wall mesh at the center of the wall.

The analysis results for this model (Figs. 282–284) provided data for the maximum strains induced in the x, y and z directions, respectively. The maximum strain in the center element in the x-direction was approximately -290 με. From the data obtained in the field, the x-direction concrete gages picked up an average strain of -600 με. From hand calculations (Eq. 2), the expected value for strain in the x-direction as a result of post-tensioning was about -422 με (disregarding the influences of 3D stress fields). In the y-direction, the model output a strain in the center element of about 50 με. The field data indicated an average strain of about 65 με in the y-direction. From hand calculations (Eq. 2), the expected value for strain in the y-direction as a result of post-tensioning was about -480 με (again disregarding the influences of 3D stress fields). In the z-direction, the model output a strain of about 55 με, whereas the field data indicated an average strain value close to 180 με. Model 1 produced similar results to the data observed in the field data and the expected values. However, there was deviation from the model and the actual specimen data. The model did not consider many aspects that were realistic in the field, including the eccentricity of the load. In addition, the measured concrete strain had offsets due to the curing of the concrete that were not accounted for in this model. Another source of error arises from the estimation of the modulus of elasticity of the concrete which could have been determined experimentally but was instead estimated based off of ACI 318-14 Chapter 19 (American Concrete Institute 2014). Therefore, deviation was expected.

A stress-strain relationship is shown in Fig. 285. The relationship was linear because there were only two time steps taken into consideration and all materials were modeled linearly. In the future, the model can be modified to include a time series, with creep properties taken into consideration and time-dependent loads in place of the concentrated loads to simulate post-tensioning bar stress losses over time from creep, as well as temperature data and load eccentricity.

4.3.2. Model 2: Distributed Loads

The second model simulated post-tensioning by utilizing distributed forces where the anchor plates were installed on the specimen. Nine horizontal area loads with a magnitude of about 21 MPa (3.1 ksi) covered 178 mm by 178 mm (7 in by 7 in) squares that were spaced at 18 cm (7 in) down both sides of the specimen. In the vertical direction, 3 area loads with a magnitude of about 17 MPa (2.5 ksi) were placed on 13 cm by 20 cm (5 in by 8 in) rectangles spaced at 61 cm (24 in) on the top and bottom faces of the specimen.

The analysis results for this model (Figs. 286–288) provided data for the maximum strains in the x, y, and z directions, respectively. Model 2 produced almost the exact results as Model 1, showing about -290 με in the x-direction, 50 με in the y-direction, and 55 με in the z-direction. The stress-strain relationship for Model 2 is shown in Figure 289 and matches that produced in Model 1. Model 2 was slightly more complicated to develop than Model 1. Since the two models produced the same results, Model 1 is the desired model to continue developing in the future.

4.4. Conclusion

It can be concluded that Models 1 and 2 produced comparable results when observing the middle section of Specimen 1. There were stress and strain deviations, specifically around the edges of the specimen in the models where stress concentrations were present. However, the area of

interest in this study was the middle section of the specimen, which for both models produced reasonably close data as predicted by calculation (Eq. 2) and as seen in the field data. Model 1 provided a simpler, more flexible model and would be the easiest to modify for future developments.

4.5. Summary

The simpler of the two models was Model 1 that utilized point loads to simulate post-tensioning forces. For future analysis, Model 1 would be the easiest to modify while still producing the same results as the more complicated loading in Model 2. Creep properties and time dependent loading scenarios can be added to Model 1 in the future to simulate the concrete and post-tensioning steel bar behavior over time. Although deviations existed between the model data and the field data, more information (like a time-dependent temperature series) can be added to the model to better match the specimen construction and conditions in the field. The point loads in Model 1 can also be easily offset from the center of the specimen to mimic the real layout of the post-tensioning bars in Specimen 1, which would induce more stress and possibly make the model a better estimation of the actual stresses in the field specimen.

5. SUMMARY AND FUTURE TESTING

5.1. Summary

In this study, three different simulated wall specimens were designed to mimic the behavior of post-tensioned concrete nuclear containment facility vessel walls over time as a result of concrete creep. The specimens were designed with different thicknesses, transverse and longitudinal reinforcement ratios, and level of post-tensioning stress. This study focused on tracking the behavior of the concrete and post-tensioning steel over time to highlight the relationship between concrete creep propagation and different structural design parameters. Each specimen contained various instrumentation to measure internal concrete temperature, concrete strain, and post-tensioning strain hourly for 7 months.

Construction of the specimens began in the beginning of June 2017. The concrete was poured on July 7, 2017 approximately 46 days before the post-tensioning operations began on August 22, 2017. When post-tensioning occurred, the concrete gages in the specimens picked up high levels of strain, which correlated to their respective orientations and depths in the thicknesses of the walls. The highest compressive strains were identified in the x-direction of each specimen, where the highest level of post-tensioning force was applied. The concrete gages oriented in the y- and z-directions picked up strain, but on average balanced out to a total strain close to 0 με.

After post-tensioning was completed on September 7, 2017, the specimens were lifted and moved into their final locations. Data was collected and post-processed between August 18, 2017, 4 days before post-tensioning began, and February 16, 2018 to determine how much strain in the concrete and post-tensioning bars changed over time, in an attempt to correlate the trends

with concrete creep. Generally, the post-tensioning bars in the x-direction lost tensile strain over time. In the y-direction, the post-tensioning bars generally picked up compressive strains over time, to compensate for the stress fluctuations of the horizontal bars. The concrete gages in the x-direction generally gained more compressive strains over the 26-week period. Most of the concrete in the y- and z- directions and post-tensioning bars in the y-direction remained relatively stable and did not change dramatically over the 26-week period. It is anticipated that most of the strain deviations are due to temperature changes during the winter months.

The largest post-tensioning bar losses occurred immediately after post-tensioning operations ended as a result of anchorage seat losses and primary and secondary creep. It is impossible to attribute the total changes in strain to creep only, due to the outside temperature changing seasonally. With more data collection over at least a year, the seasonal temperature changes can be decoupled from the creep strains and a more reliable conclusion can be made about the influence of creep on the post-tensioned concrete wall specimens.

Two finite element models were designed to simulate stresses and strains induced by the post-tensioning steel bars on Specimen 1. The intention of the finite element model study was to determine the simplest method that could be used to model the specimen accurately, and that could later be added onto to develop a more complicated model. It was determined that a simple finite element model which used point loads to simulate post-tensioning forces gave the same results as a more complicated model that utilized distributed loads. Both models gave reasonable values for stresses and strains in the concrete after post-tensioning when compared to field data. The models did not include creep properties, time-dependent temperature data, and many more complexities that were physically experienced in the field specimens. However, the models are easily modifiable to include these parameters in the future.

5.2. Future Work

The instrumentation in the specimens will continue to collect data (until the project is concluded, and possibly thereafter) so that more strain data can be post-processed to highlight creep on a large scale. The simple point load finite element model will be modified to eventually include concrete creep, post-tensioning force reduction as a result of creep, temperature data, and specimens with different geometry to simulate more accurately the field conditions and serve as a verification of the data obtained out in the field. If the model is accurate in its predictions, it can be developed into a powerful tool for designers who are concerned with long-term concrete creep in concrete post-tensioned nuclear containment vessel structures.

REFERENCES

American Society for Testing and Materials (2016). *ASTM A615/A615M-16 Standard Specification for Deformed and Plain Carbon-Steel Bars for Concrete Reinforcement*.

Bazant, Z. (1988). "Creep Analysis of Structures." *Mathematical Modeling of Creep and Shrinkage of Concrete,* Wiley, Chichester, 217-219.

American Concrete Institute (2014). *Building Code Requirements for Structural Concrete (ACI 318-14) and Commentary (ACI 318R-14).*

Dywidag-Systems International (2016). "Dywidag Post-Tensioning Systems." *Dywidag Post-Tensioning Systems*, Dywidag Systems International, Bolingbrook, IL.

Georgia Institute of Technology School of Civil and Environmental Engineering (2015). "PhD Student Bradley Dolphyn Studying the Concrete Cracks that Shut Down Crystal River Nuclear Power Plant." *Georgia Tech School of Civil and Environmental Engineering,* <https://ce.gatech.edu/news/phd-student-bradley-dolphyn-studying-concrete-cracks-shut-down-crystal-river-nuclear-power> (Dec. 19, 2017).

Hessheimer, M. F., Klamerus E. W., Lambert, L. D., Rightley, G. S., and Dameron, R. A. (2003). "Design and Construction of the PCCV Model." *Overpressurization Test of 1:4 Scale Prestressed Concrete Containment Vessel Model,* Albuquerque, NM, 1-12.

Kovler, K. (1997). "Drying Creep of Concrete in Terms of Age-Adjusted Effective Modulus Method." *Magazine of Concrete Research,* 49(181), 345-351.

Lin, W., Liu, J. P., and Liu, J. Z. (2014). “Influence of Reinforcement Placement on the Creep of Concrete.” *Key Engineering Materials*, Trans Tech Publications, Switzerland, 130-135, 629-630.

Marques, A. C., Bittencourt, T. N., and Barbosa, M. P. (2013). “Influence of Ambient Conditions and Loading Age on CAA Drying Influence.” *IBRACON Journal of Structures and Materials*, *6* (2), 227-245.

Schwitters, R., Allen, T., Black, C., Barletta, W., Dahlburg, J., Slakey, F., Hosemann, P., Remer, J., Rosner, R., Teter, D., Was, G., Yang, R., and Zinkle, S. (2013). “Renewing Licenses for the Nation’s Nuclear Power Plants.”. *American Physics Society*, <http://www.aps.org/policy/reports/popa-reports/upload/nuclear-power.pdf> (Dec. 19, 2017).

Song, H. -W., Kim, S. -H., Byun, K. -J., and Song, Y. -C. (2002). “Creep prediction of concrete for reactor containment structures.” *Nuclear Engineering and Design*, 217(3), 225–236.

Stefanou, G. D. (1981). “A General Method of Calculating Stress Redistribution Due to Differential Creep in Concrete Structures.” *Computers & Structures*, 14(3-4), 231–245.

Federal Highway Administration (2016). “Thermal Coefficient of Portland Cement Concrete.” *U.S. Department of Transportation: Federal Highway Administration*, https://www.fhwa.dot.gov/publications/research/infrastructure/pavements/pccp/thermal.cfm (Dec. 19, 2017).

Tokyo Sokki Kenkyujo Co., Ltd. (2017). “Strain Gauges 2017.” *Strain Gauges 2017*, Tokyo Sokki Kenkyujo Co., Ltd., Tokyo, Japan.

Tokyo Sokki Kenkyujo Co., Ltd. (2017). “Transducers 2017.” *Transducers 2017*, Tokyo Sokki Kenkyujo Co., Ltd., Tokyo, Japan.

U.S. Energy Information Administration - EIA - Independent Statistics and Analysis (2017). “How Old Are U.S. Nuclear Power Plants, and When Was the Newest One Built?”. *U.S. Energy Information Administration*, <https://www.eia.gov/tools/faqs/faq.php?id=228&t=21> (Dec. 19, 2017).

Usibe, B. E., Etim, I. P., and Ushie, J. O. (2012). “Prediction of Creep Deformation in Concrete Using Some Design Code Models.” *IOSR Journal of Mechanical and Civil Engineering*, 4(3), 49–53.

APPENDIX A FIGURES

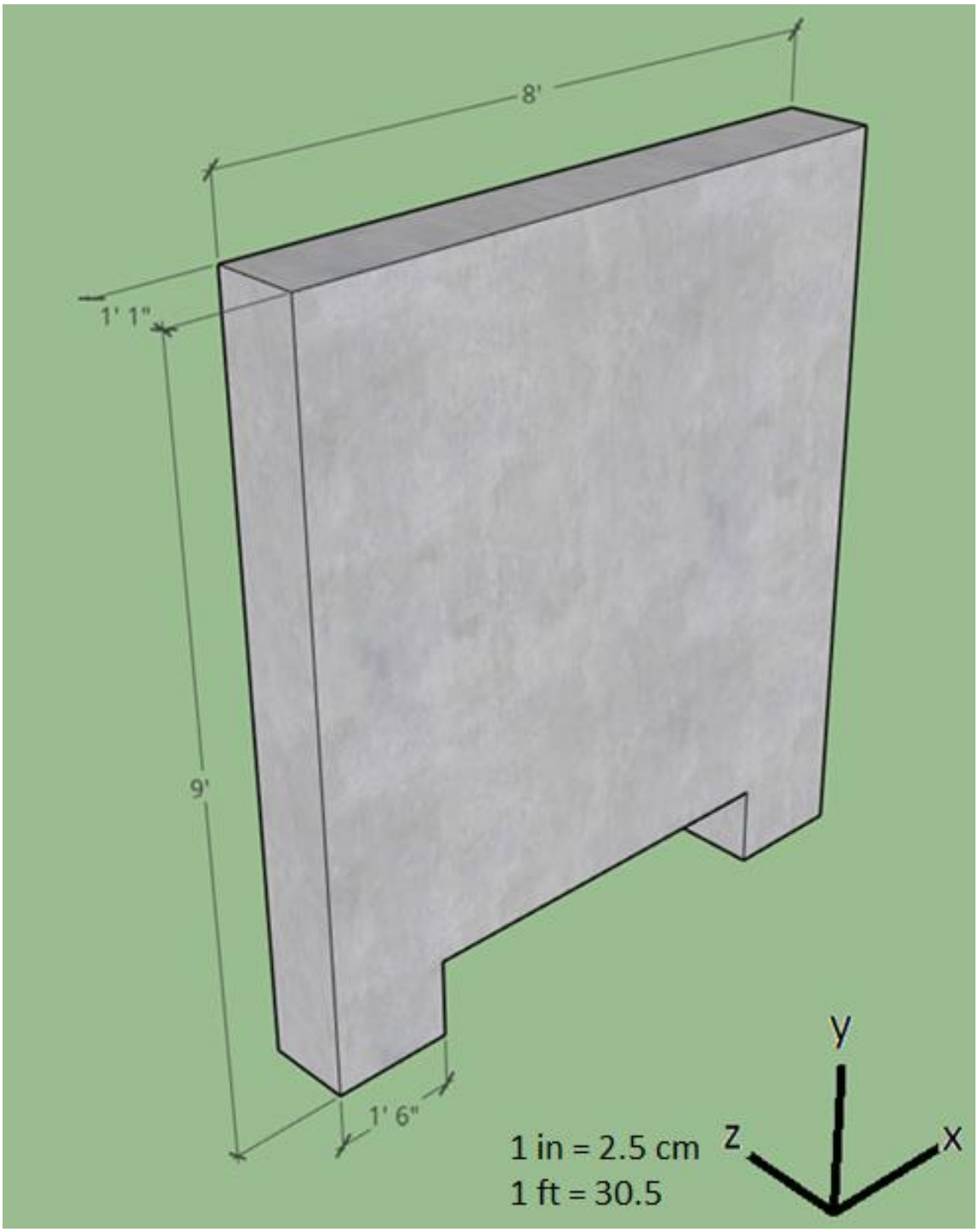

Figure 1 Specimen 1- Dimensions

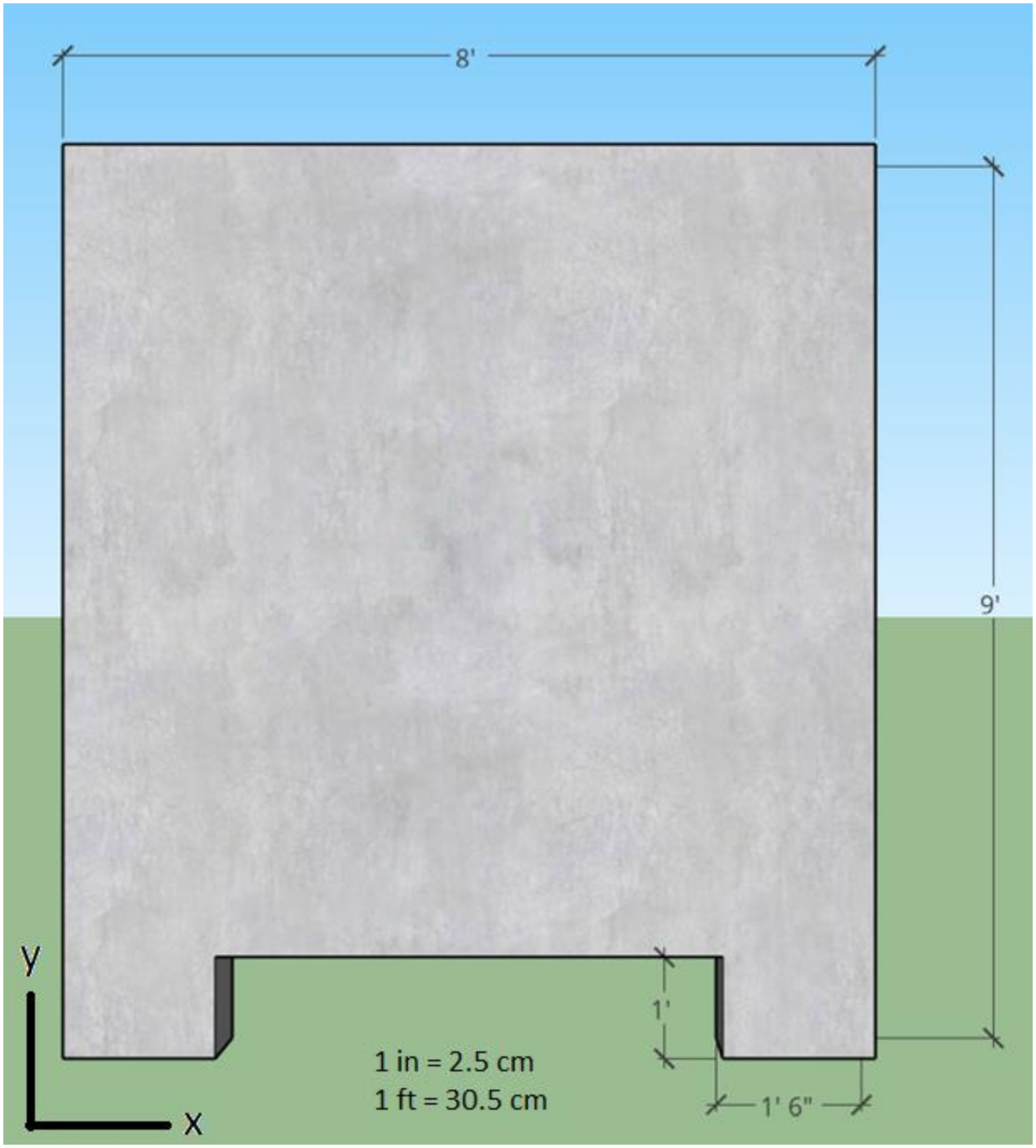

Figure 2 Specimen 1- Elevation View

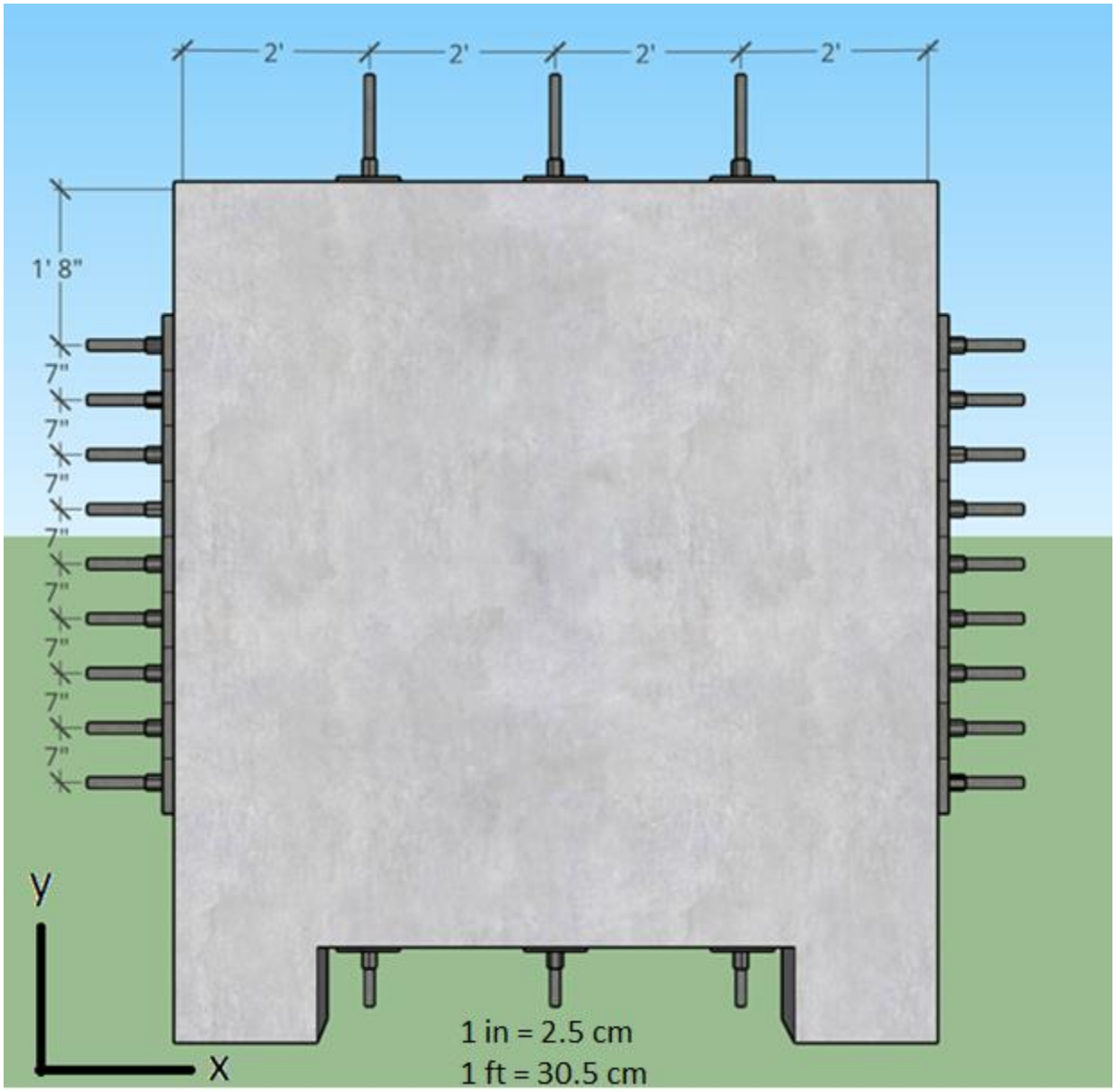

Figure 3 Specimen 1-Post-Tension Bar Layout Elevation View

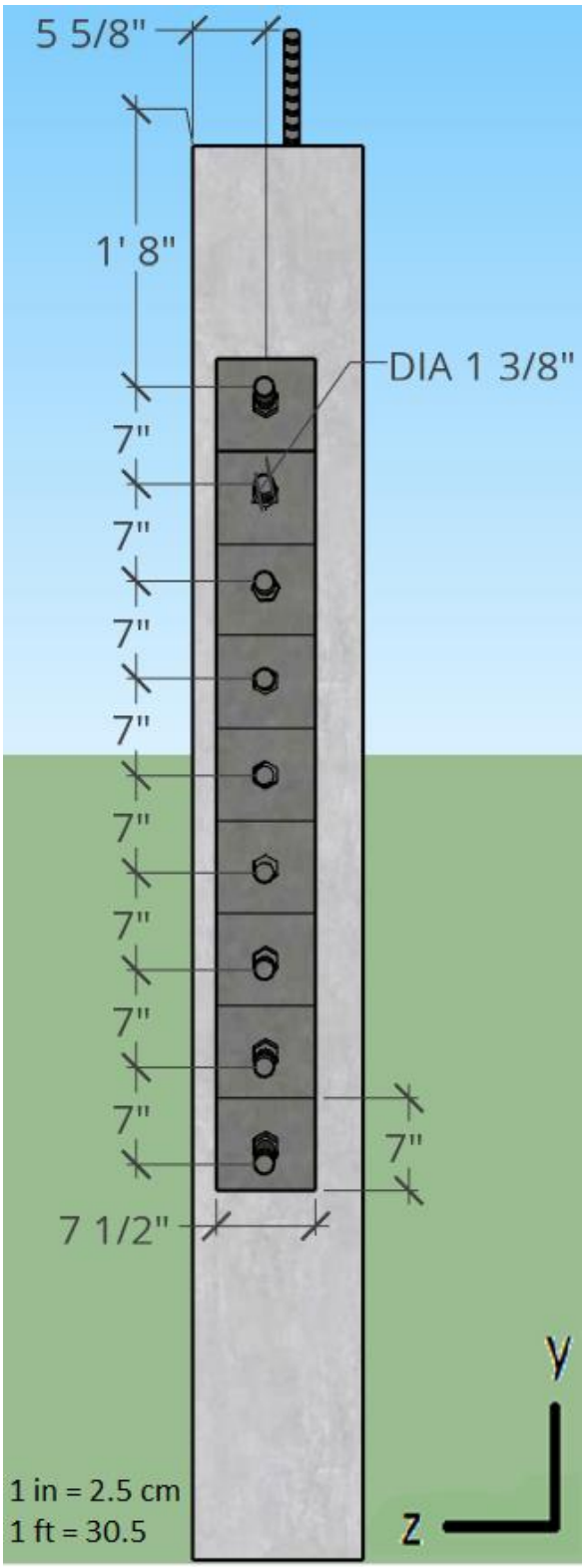

Figure 4 Specimen 1- Post-Tension Bar Layout Side View

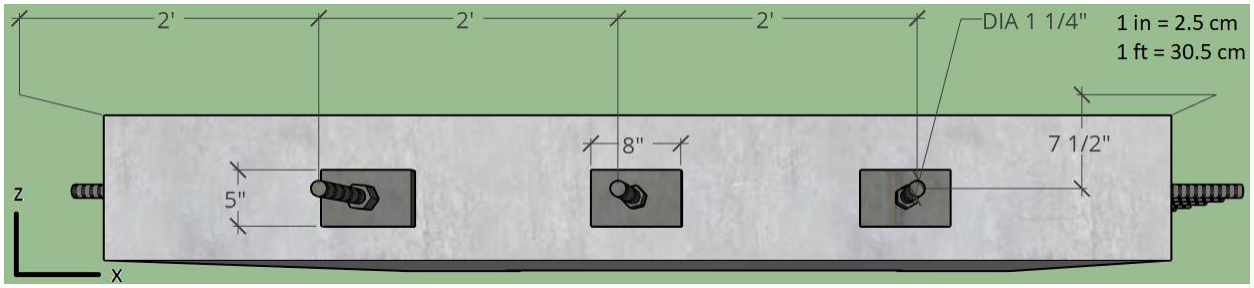

Figure 5 Specimen 1- Post-Tension Bar Layout Top View

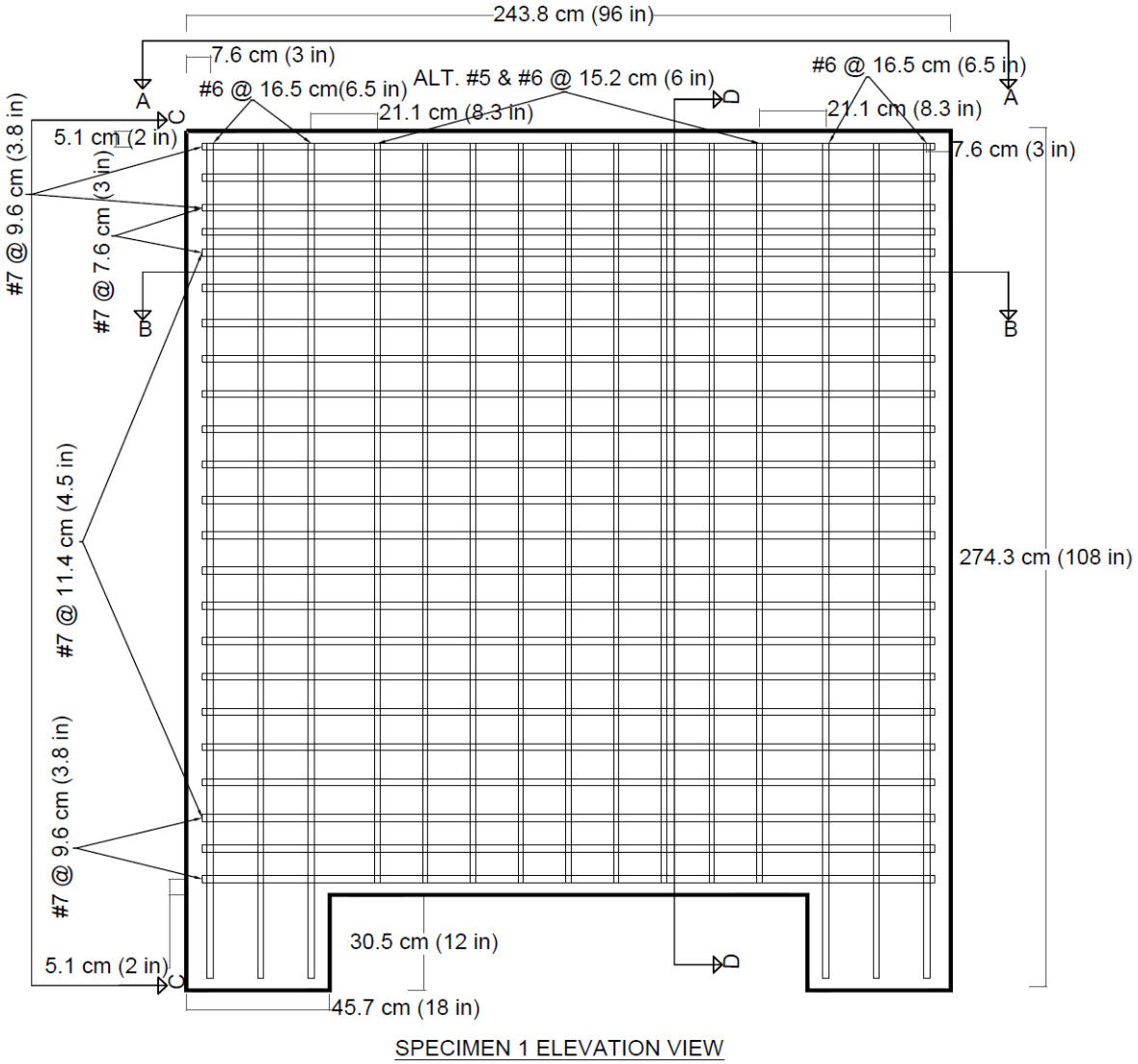

Figure 6 Specimen 1- Reinforcing Steel Layout Elevation View

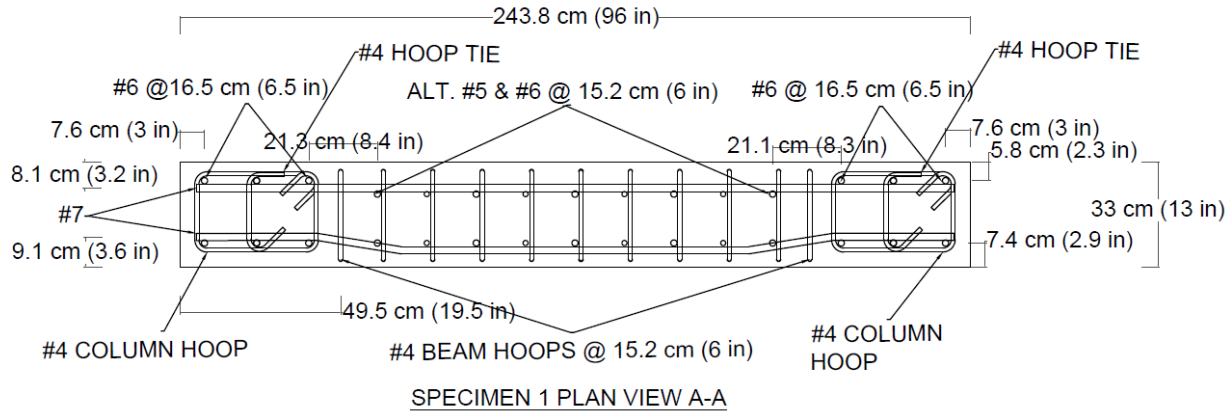

Figure 7 Specimen 1- Reinforcing Steel Layout Plan View A-A

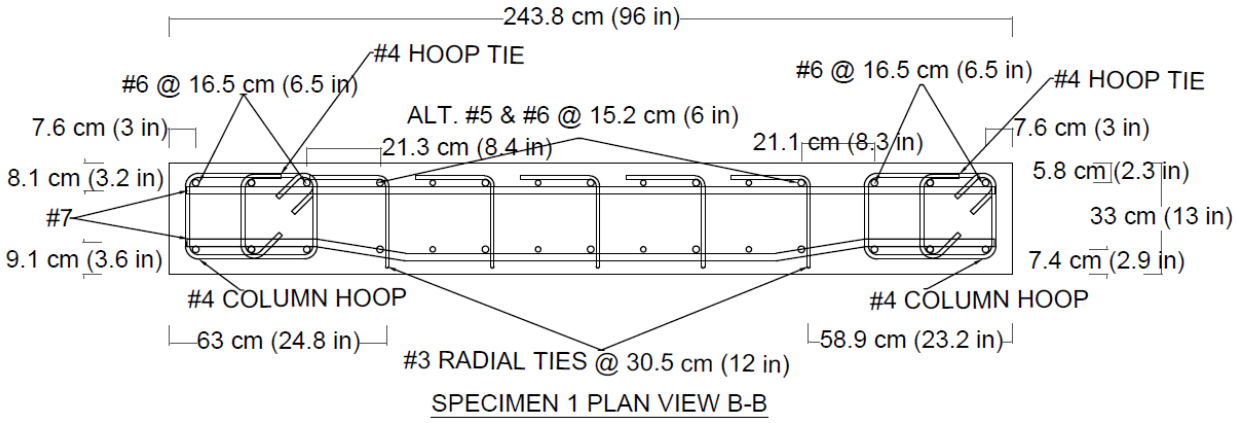

Figure 8 Specimen 1- Reinforcing Steel Layout Plan View B-B

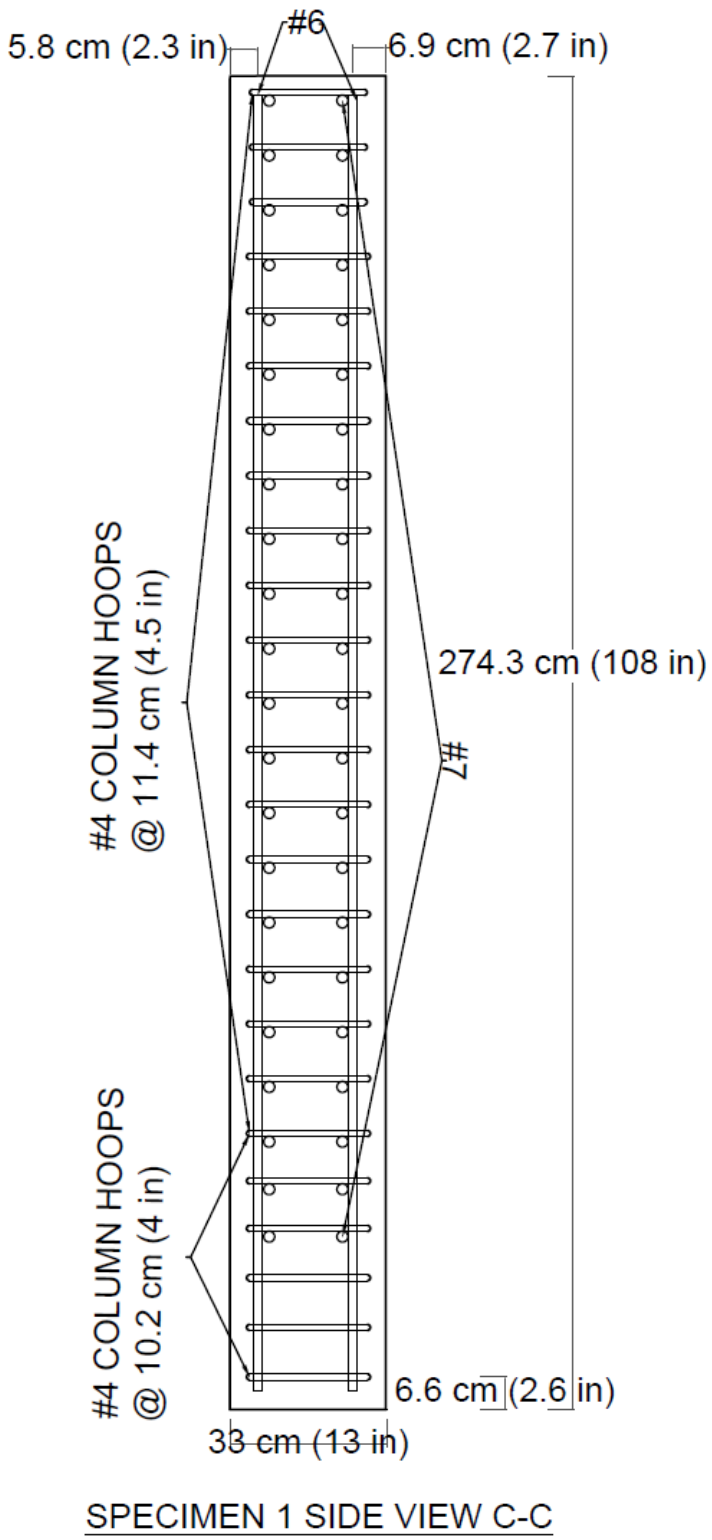

Figure 9 Specimen 1- Reinforcing Steel Layout Side View C-C

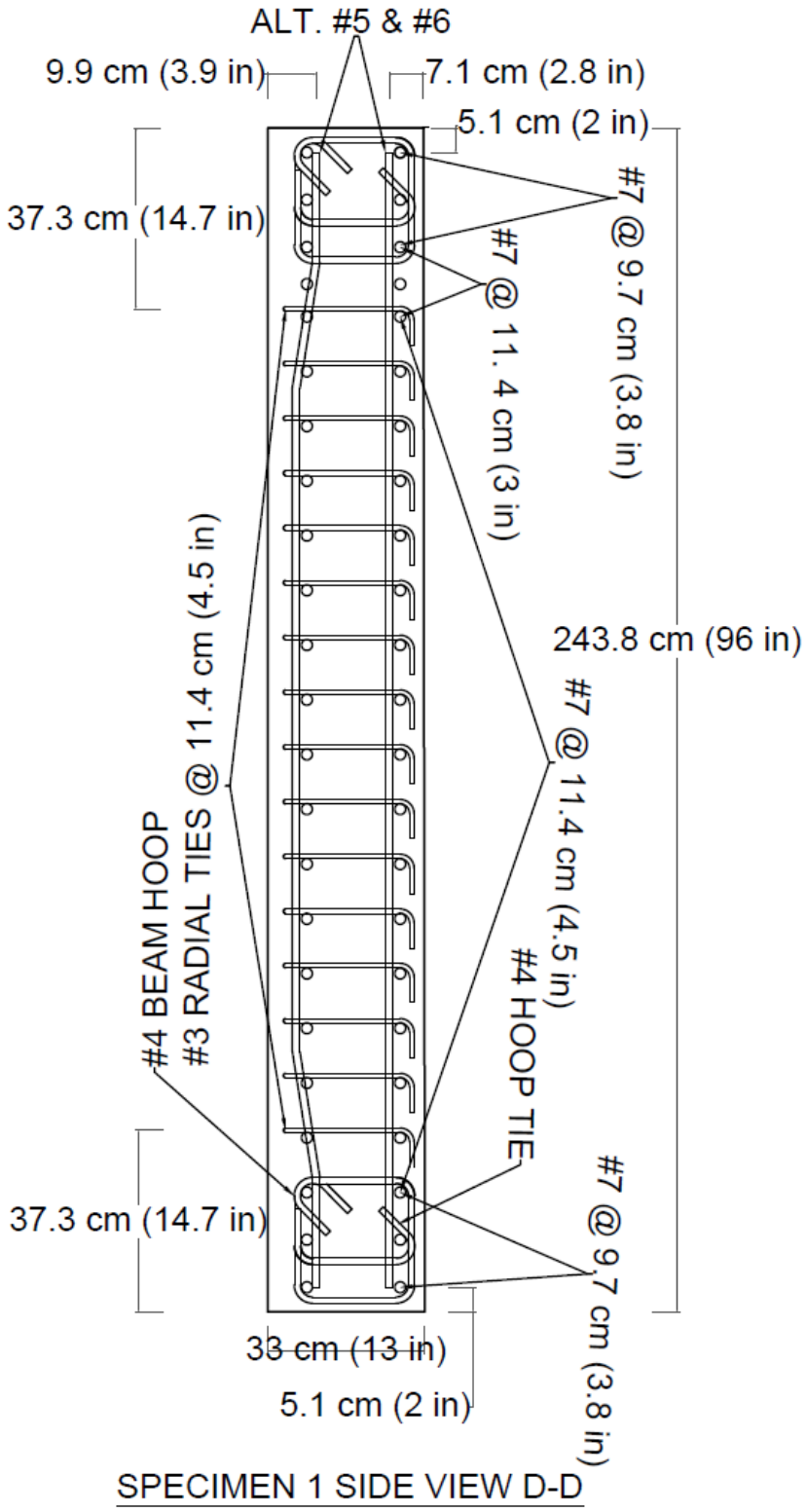

Figure 10 Specimen 1- Reinforcing Steel Layout Side View D-D

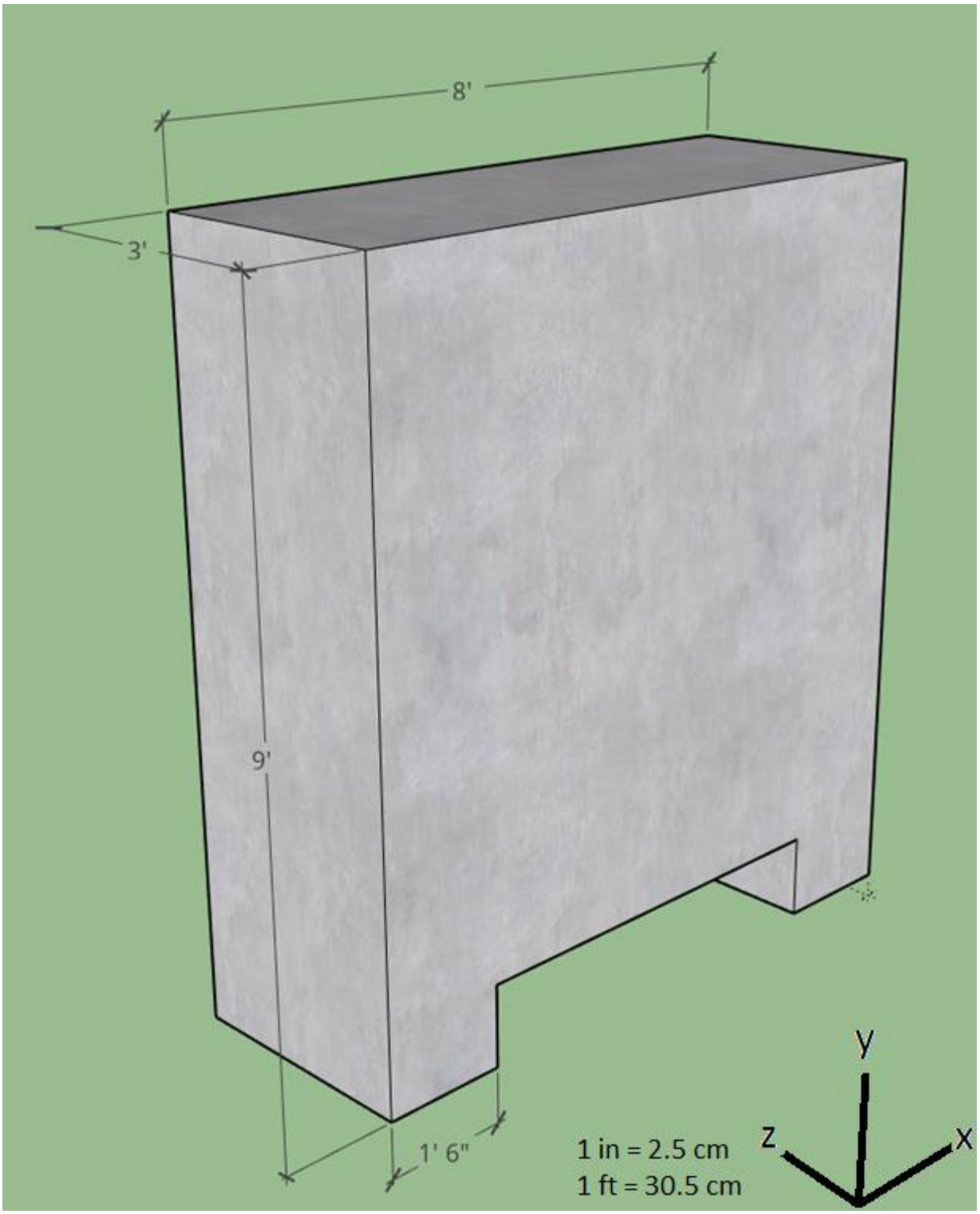

Figure 11 Specimen 2-Dimensions

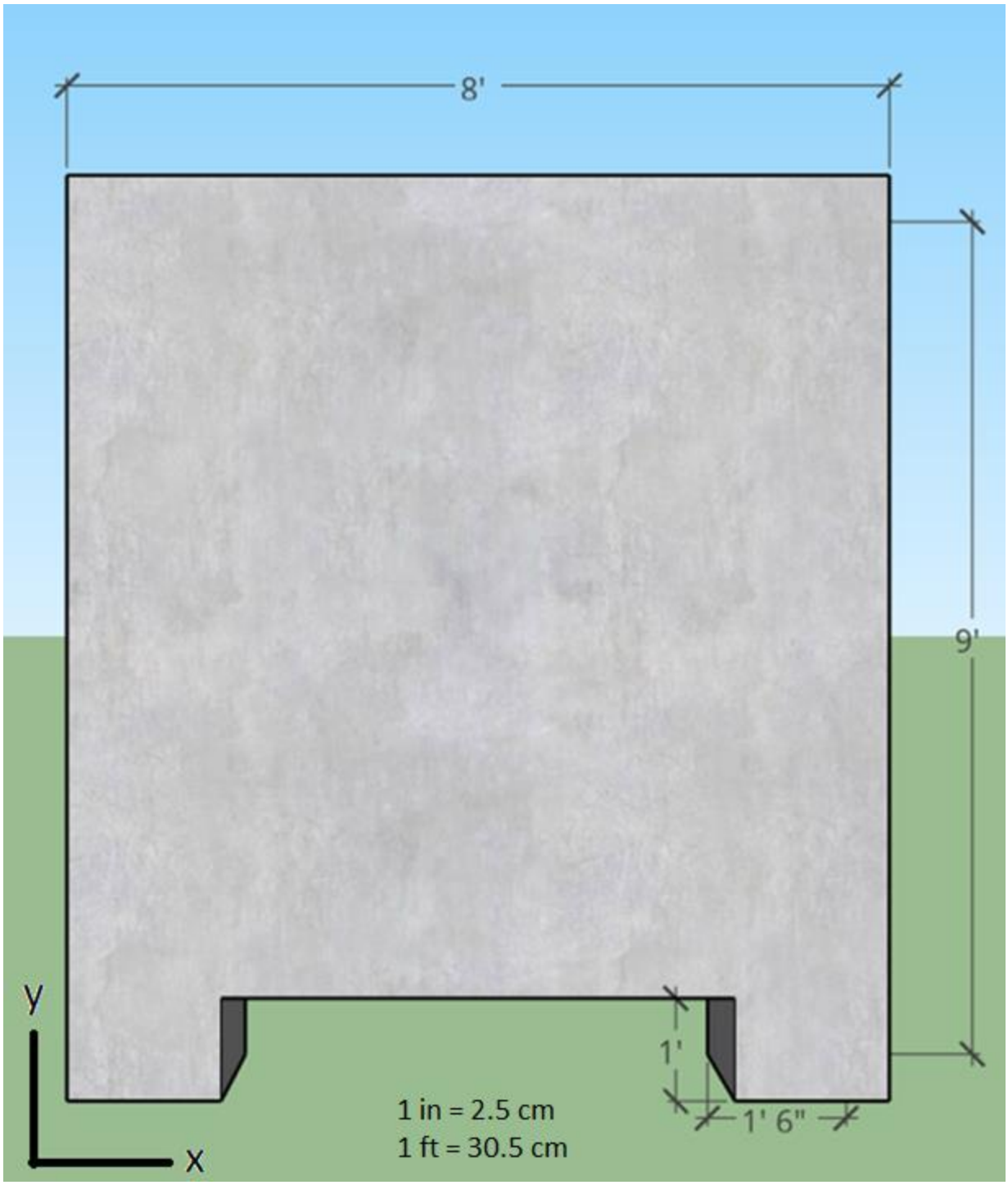

Figure 12 Specimen 2- Elevation View

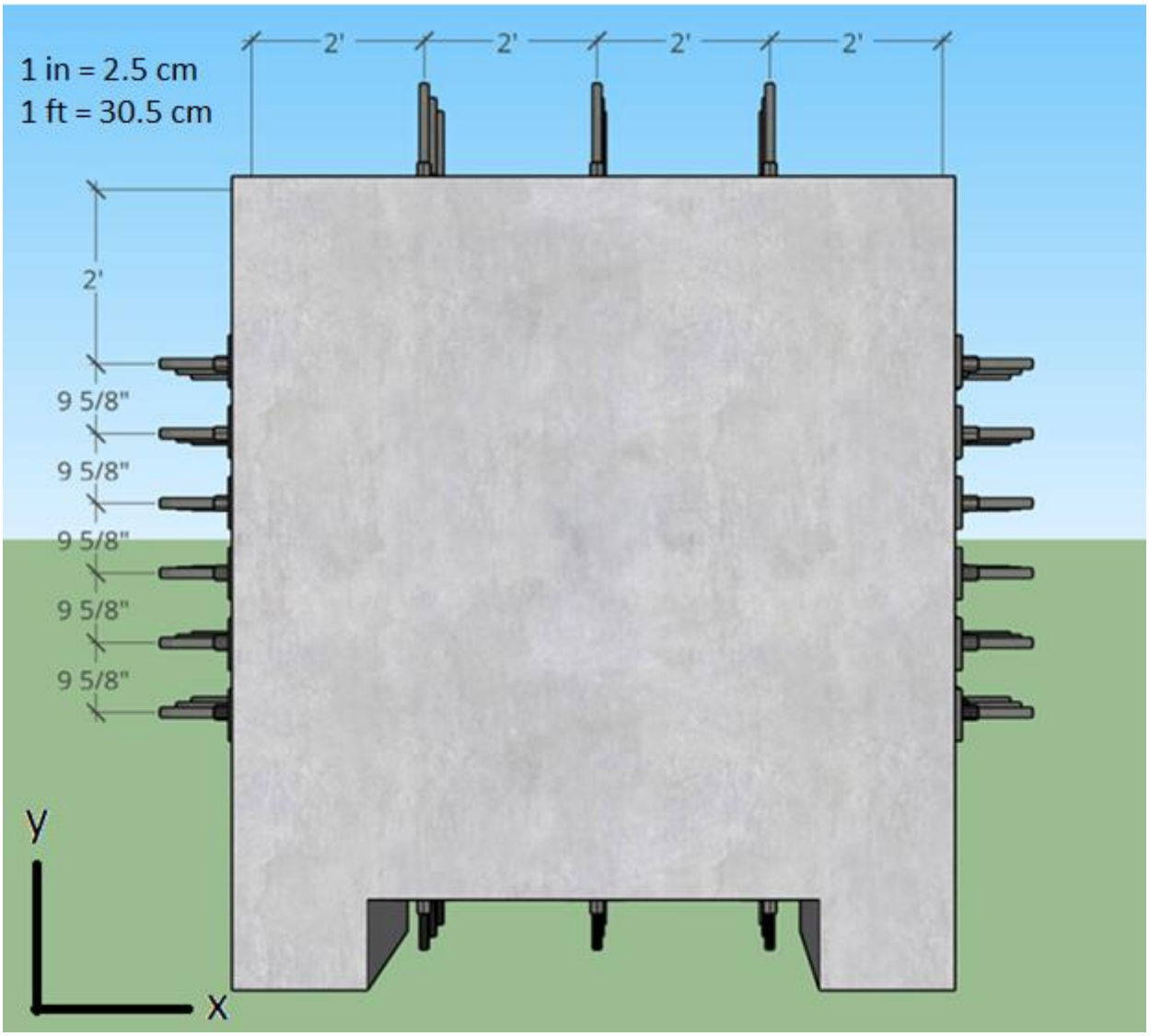

Figure 13 Specimen 2- Post-Tension Bar Layout Elevation View

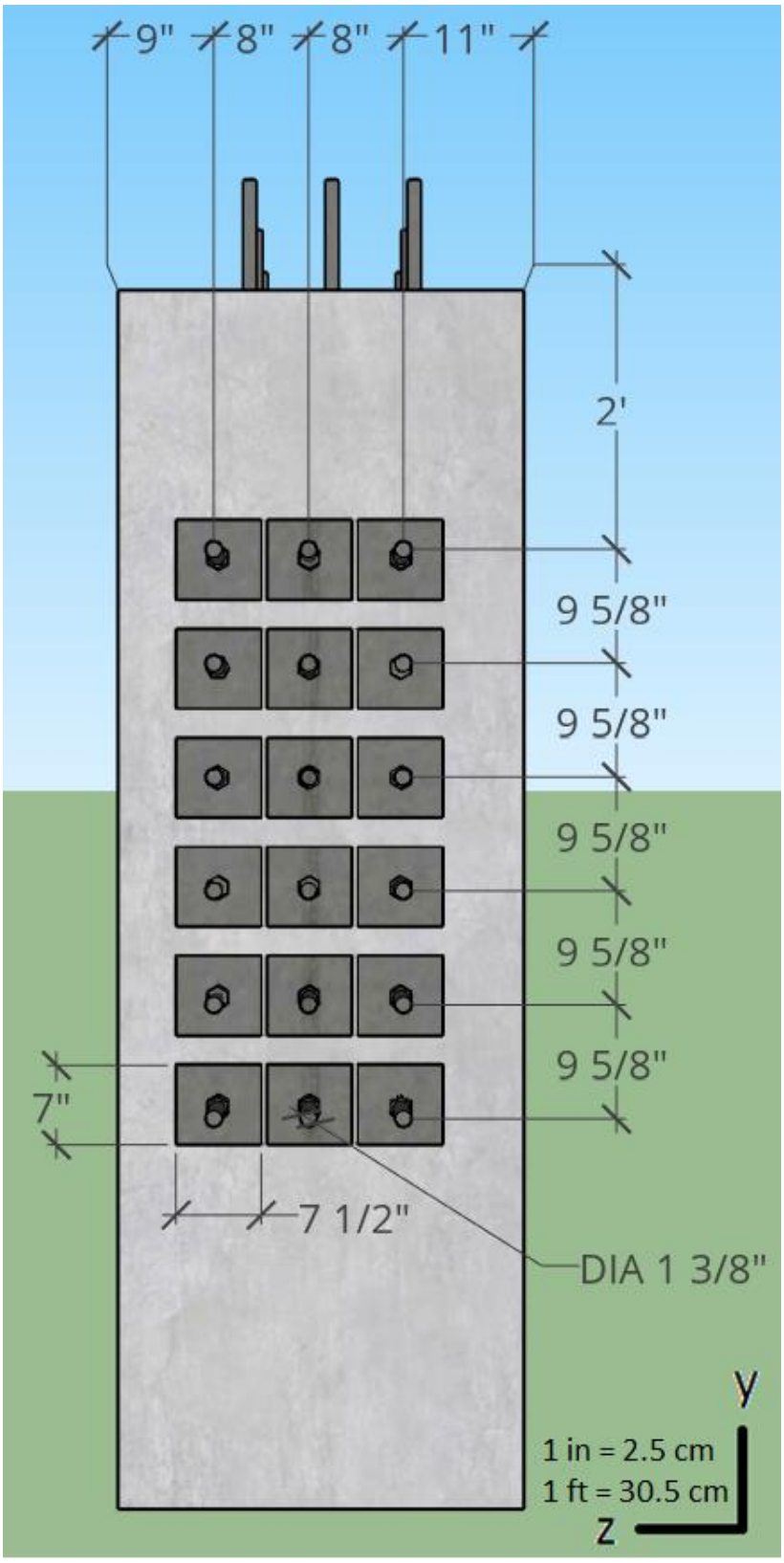

Figure 14 Specimen 2- Post-Tension Bar Layout Side View

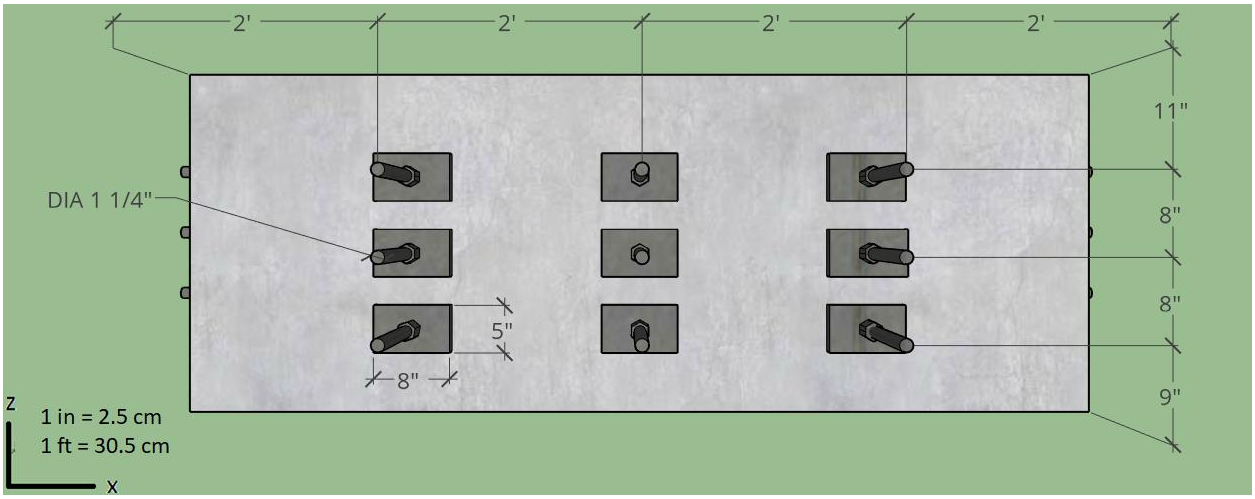

Figure 15 Specimen 2- Post-Tension Bar Layout Top View

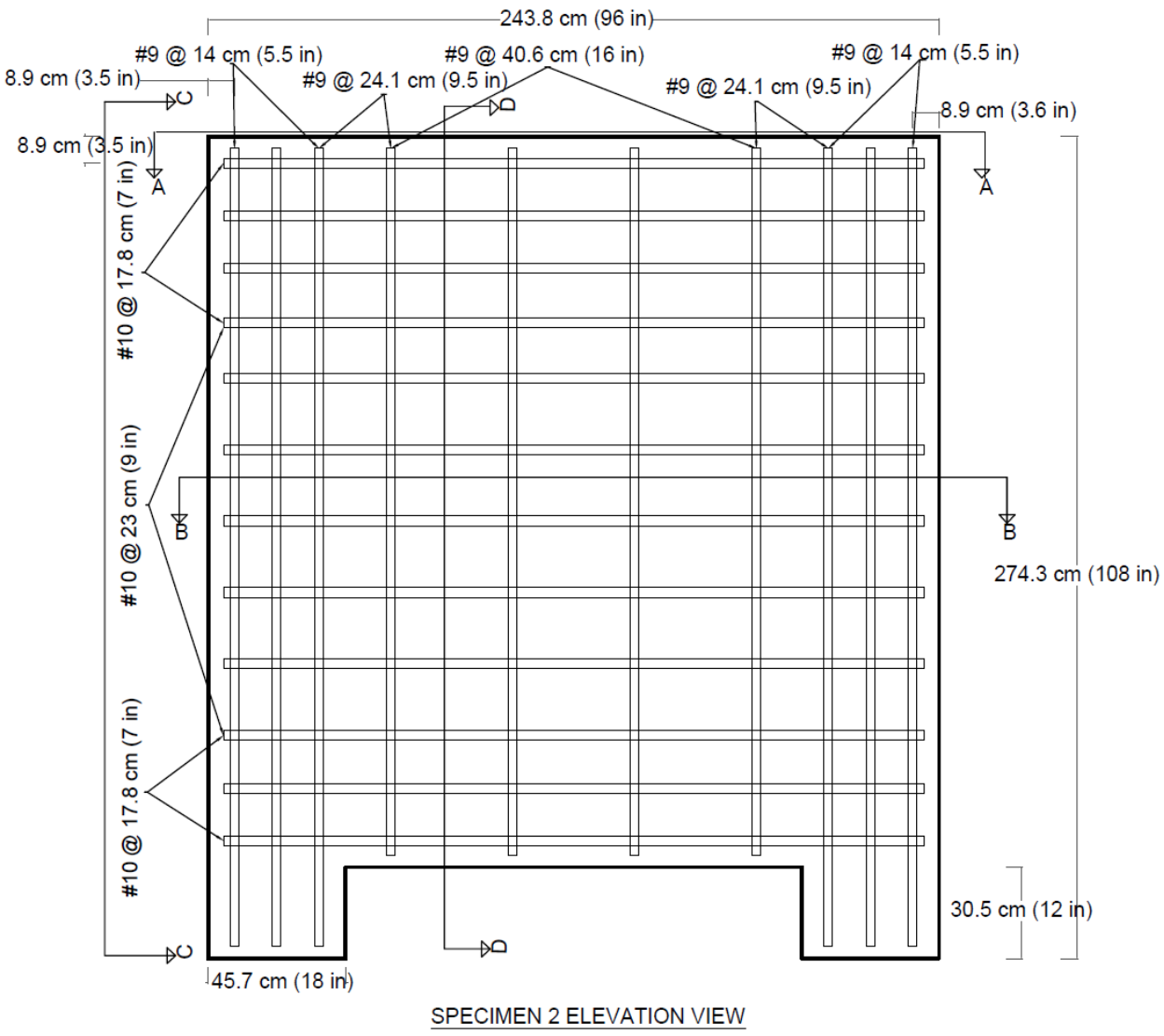

Figure 16 Specimen 2- Reinforcing Steel Layout Elevation View

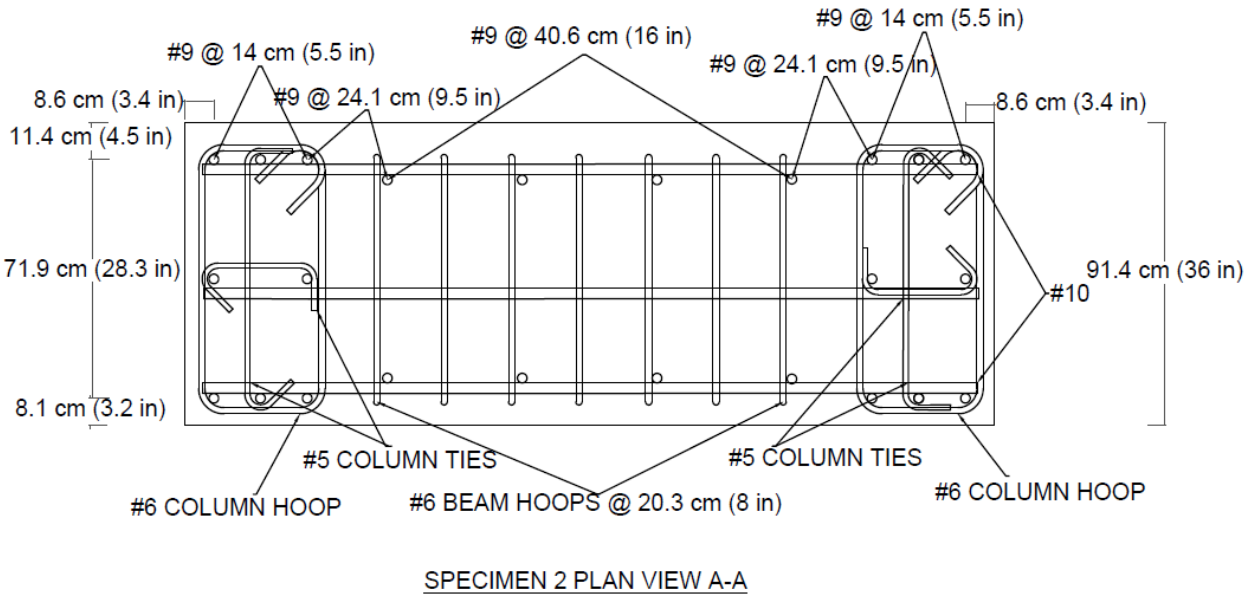

Figure 17 Specimen 2- Reinforcing Steel Layout Plan View A-A

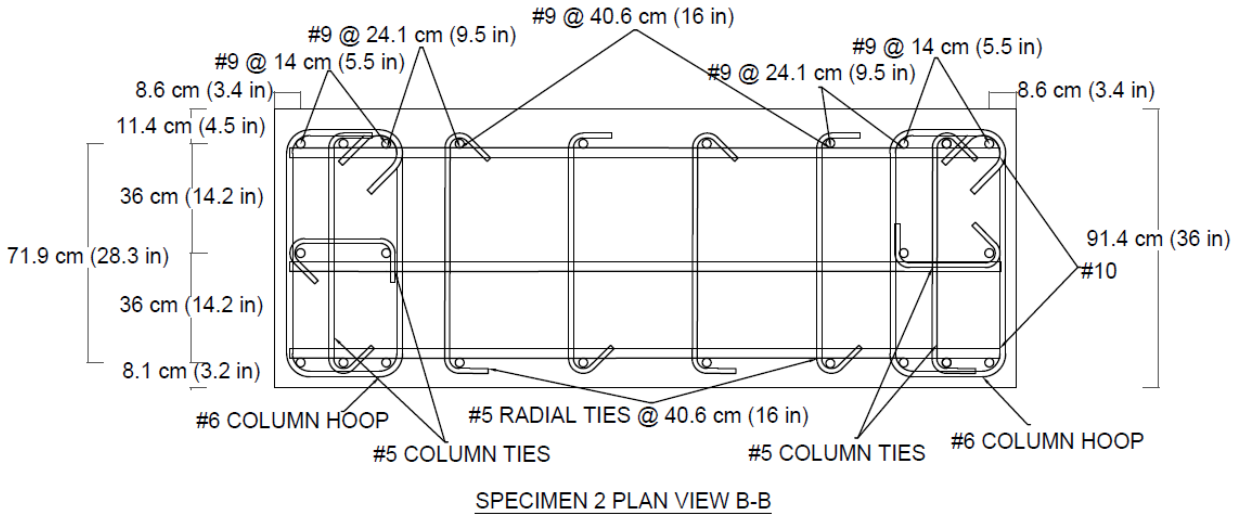

Figure 18 Specimen 2- Reinforcing Steel Layout Plan View B-B

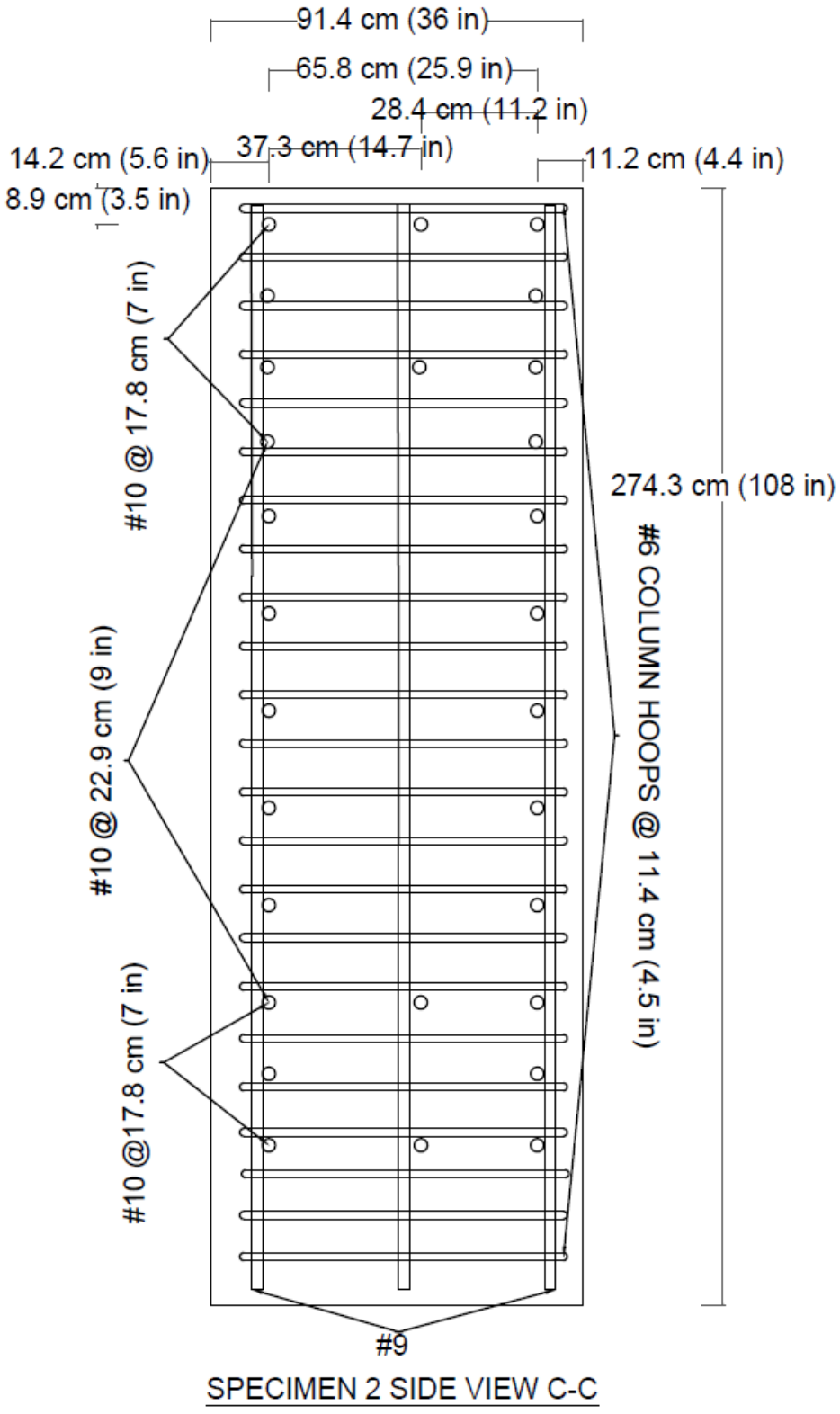

Figure 19 Specimen 2- Reinforcing Steel Layout Side View C-C

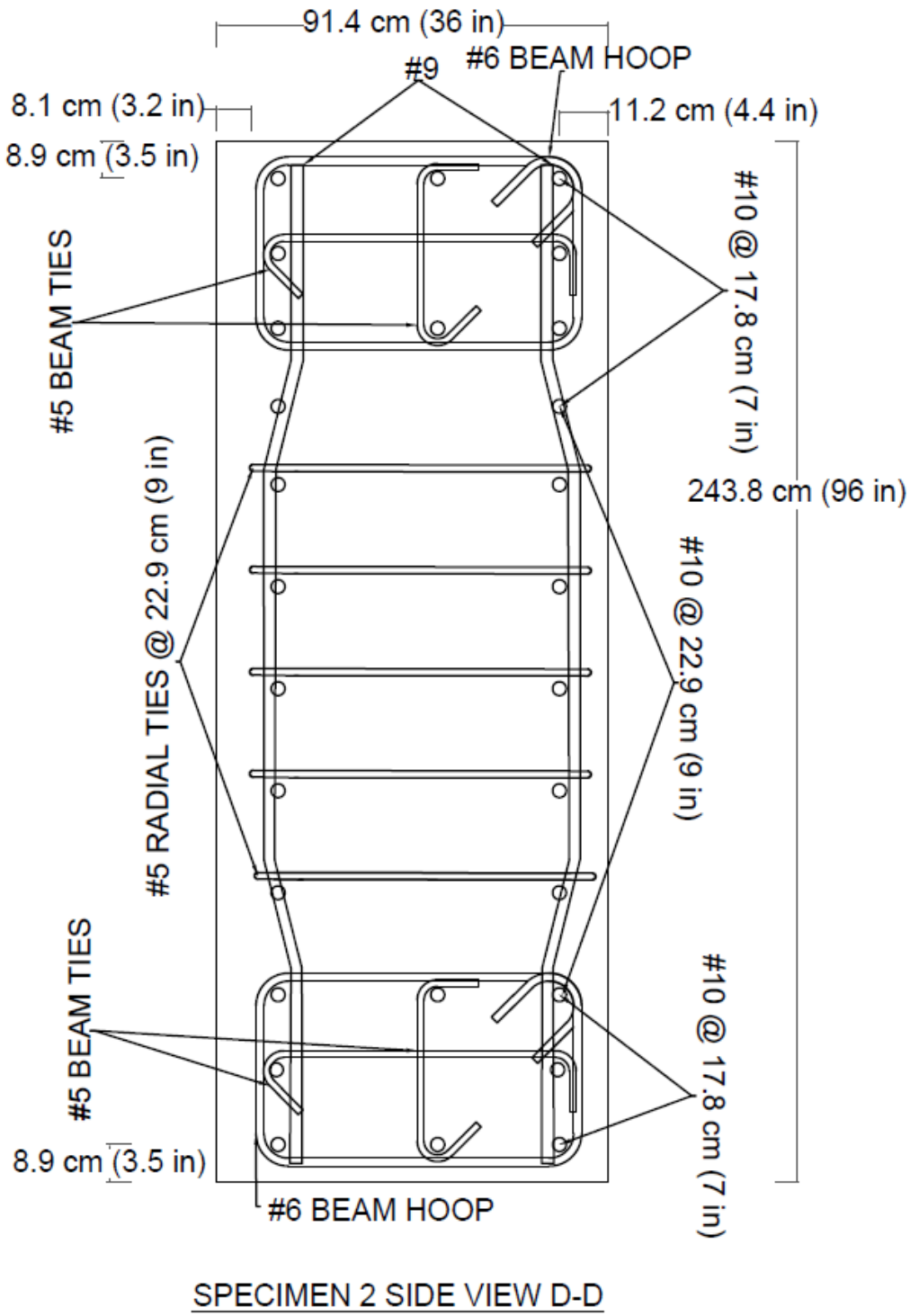

Figure 20 Specimen 2- Reinforcing Steel Layout Side View D-D

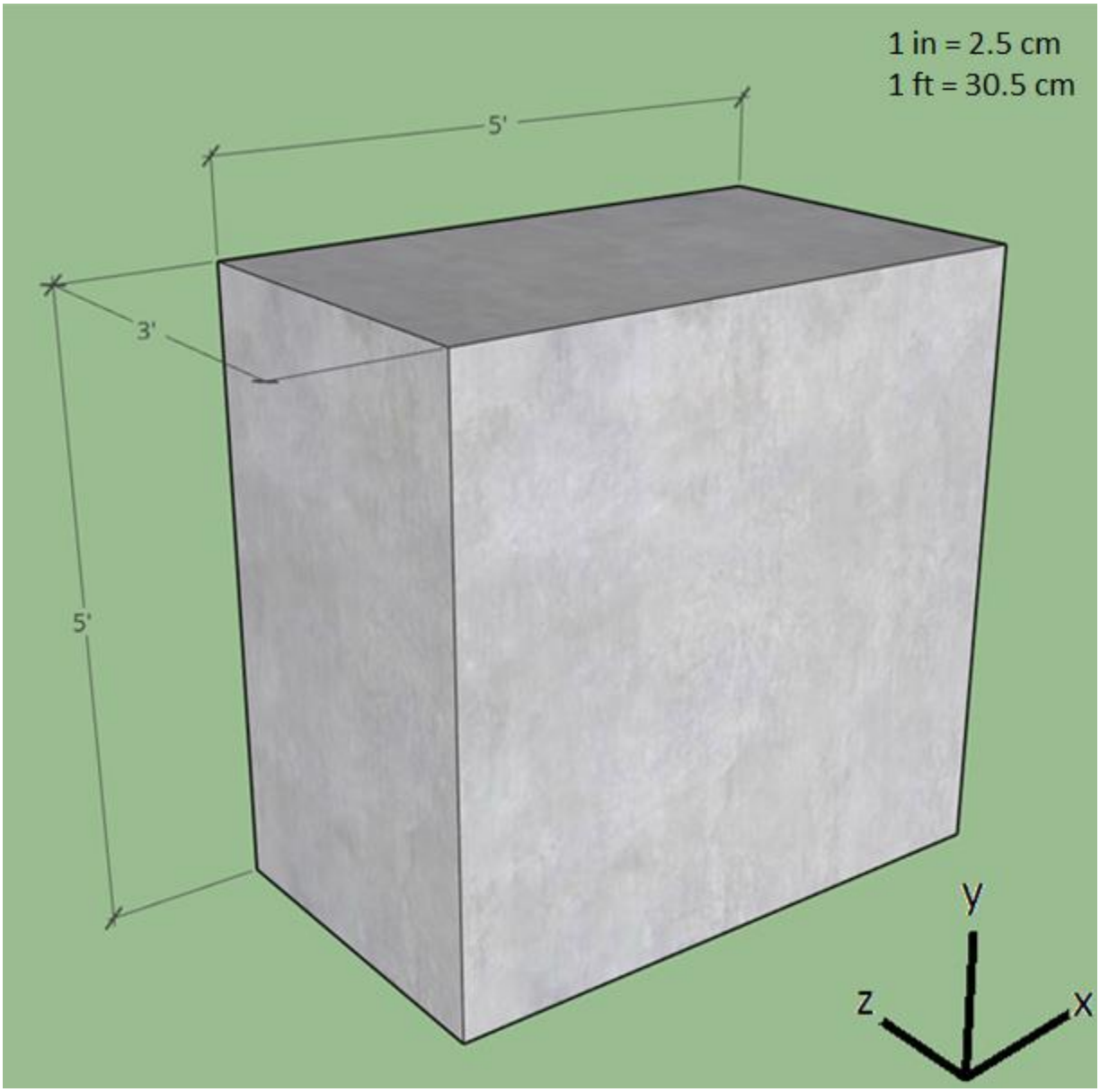

Figure 21 Specimen 3- Dimensions

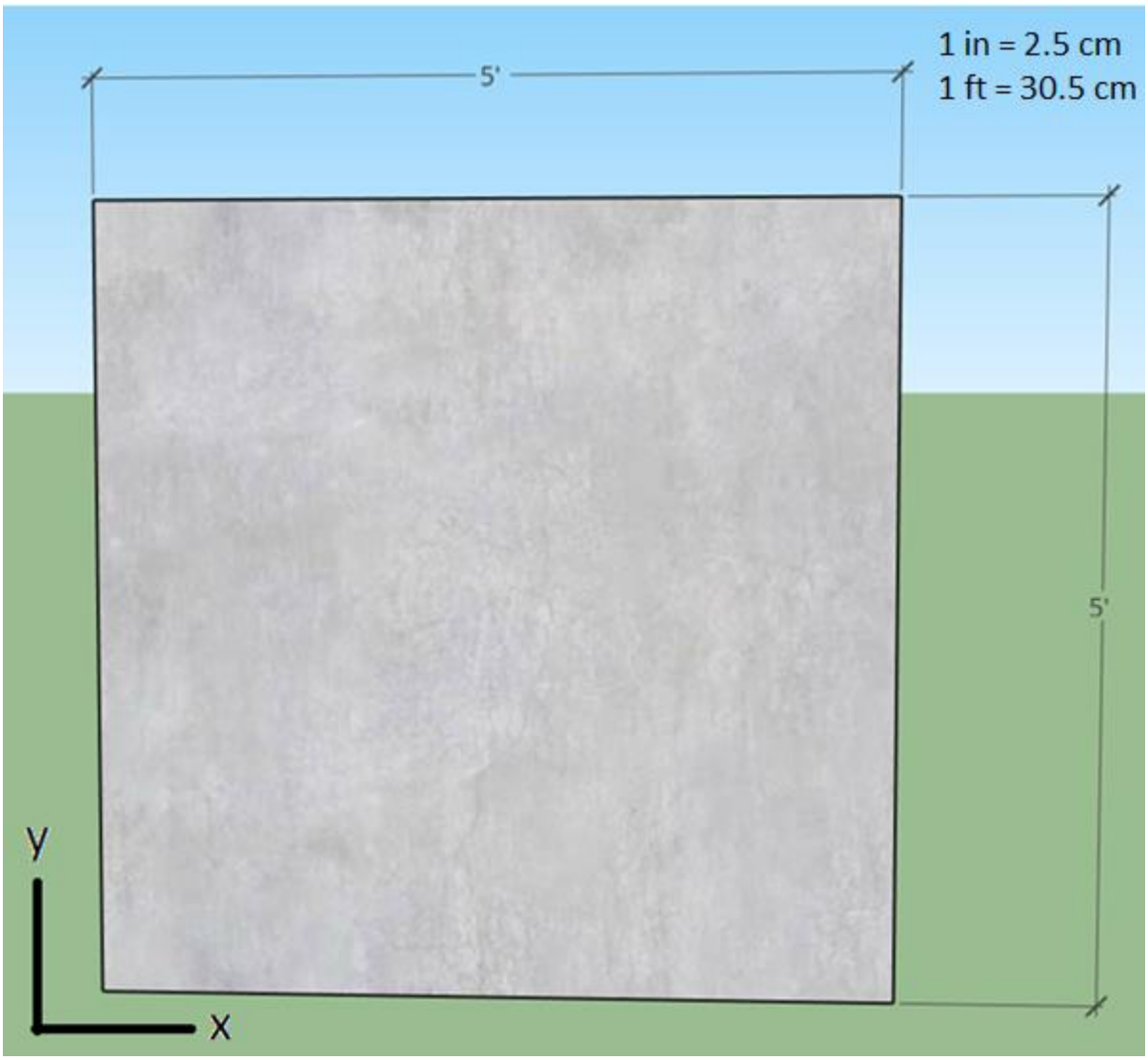

Figure 22 Specimen 3- Elevation View

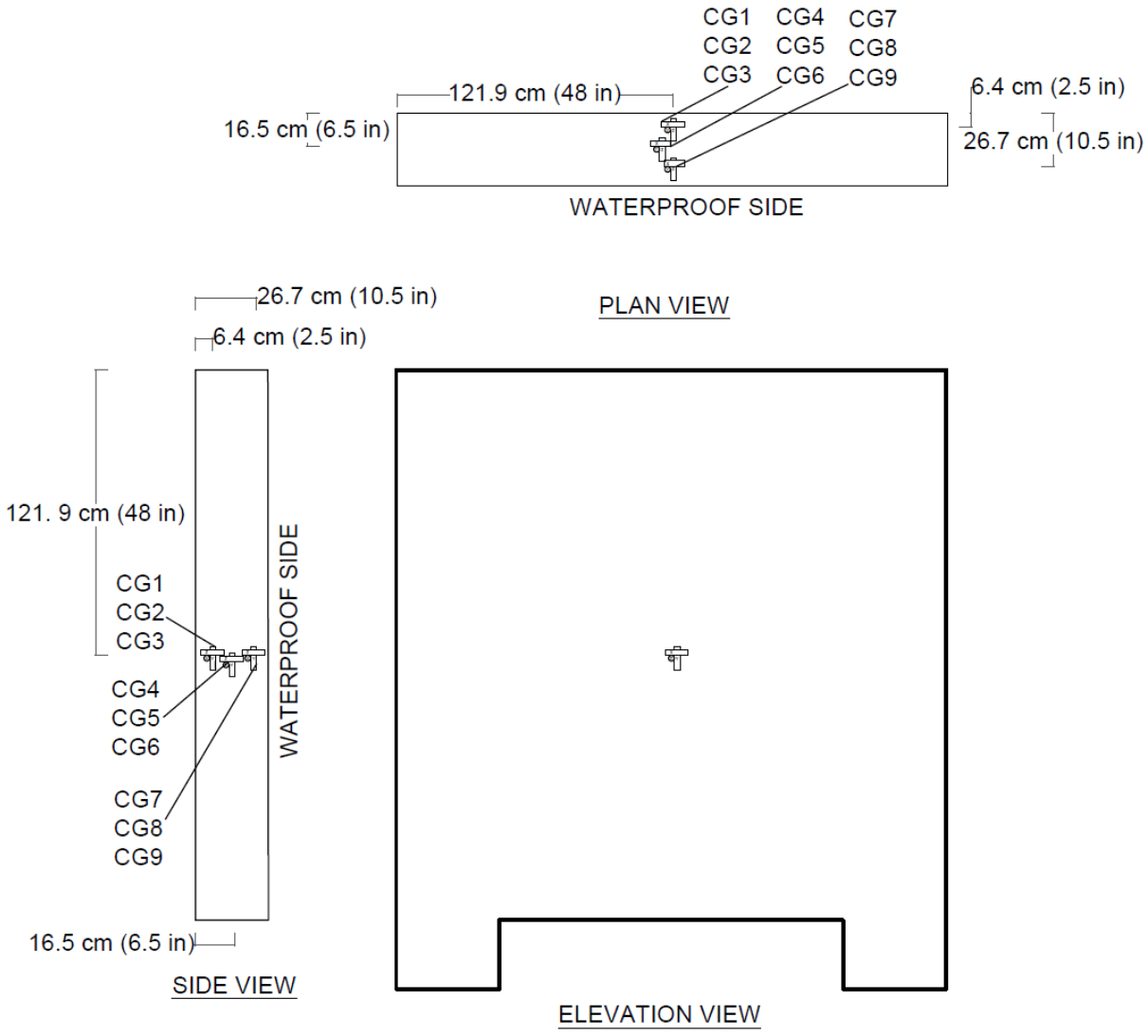

Figure 23 Specimen 1- Concrete Gage Labels and Locations

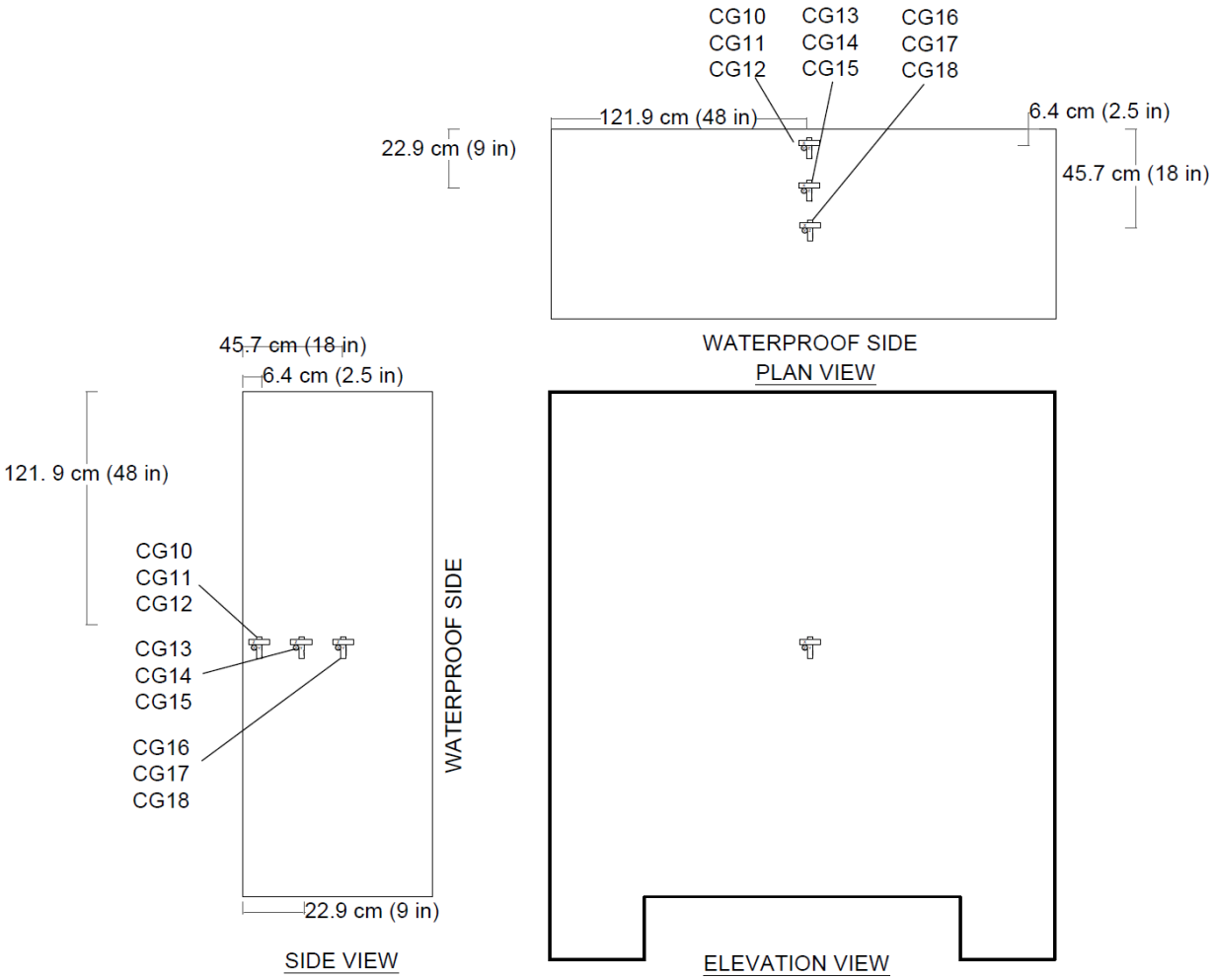

Figure 24 Specimen 2- Concrete Gage Labels and Locations

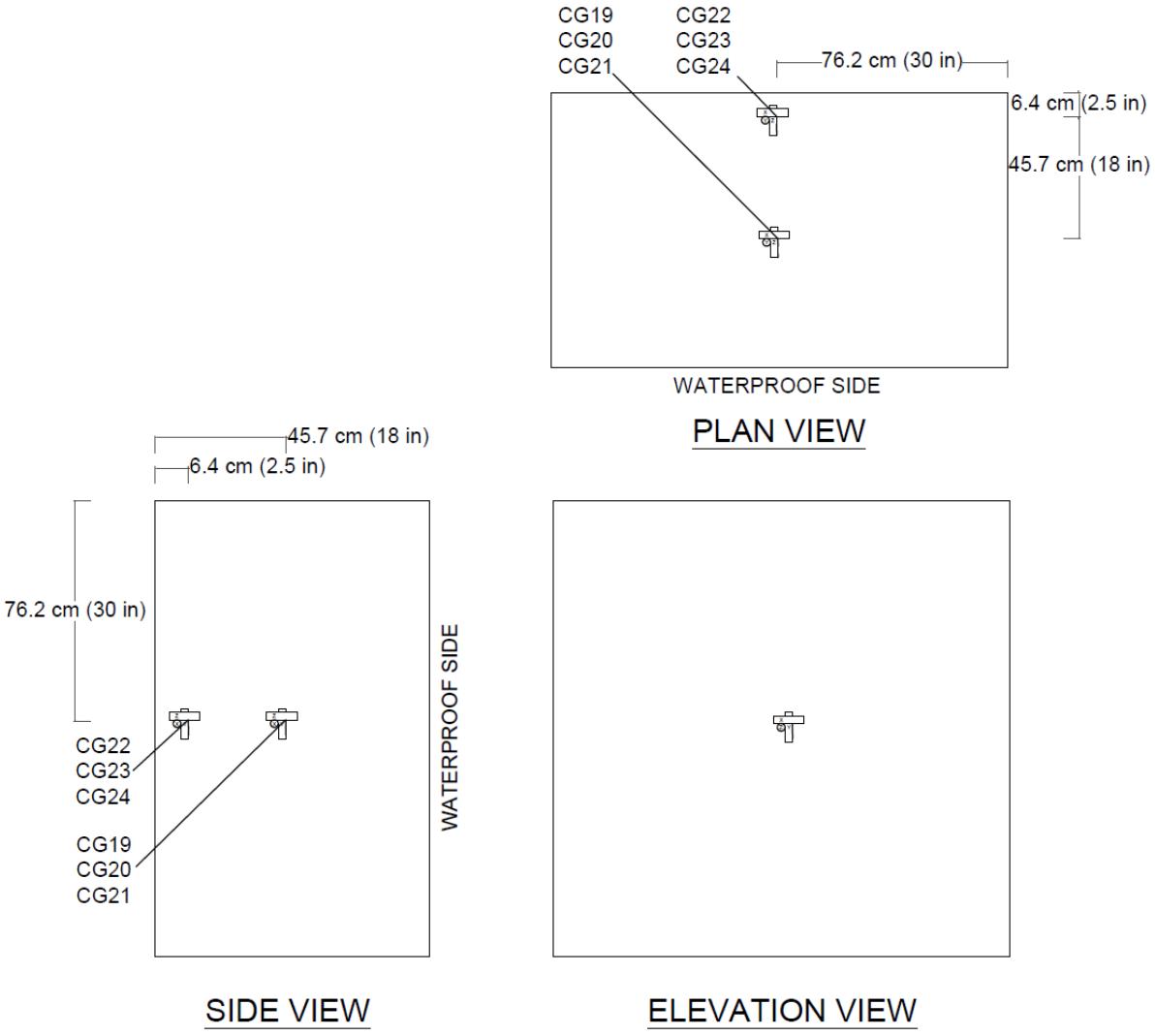

Figure 25 Specimen 3- Concrete Gage Labels and Locations

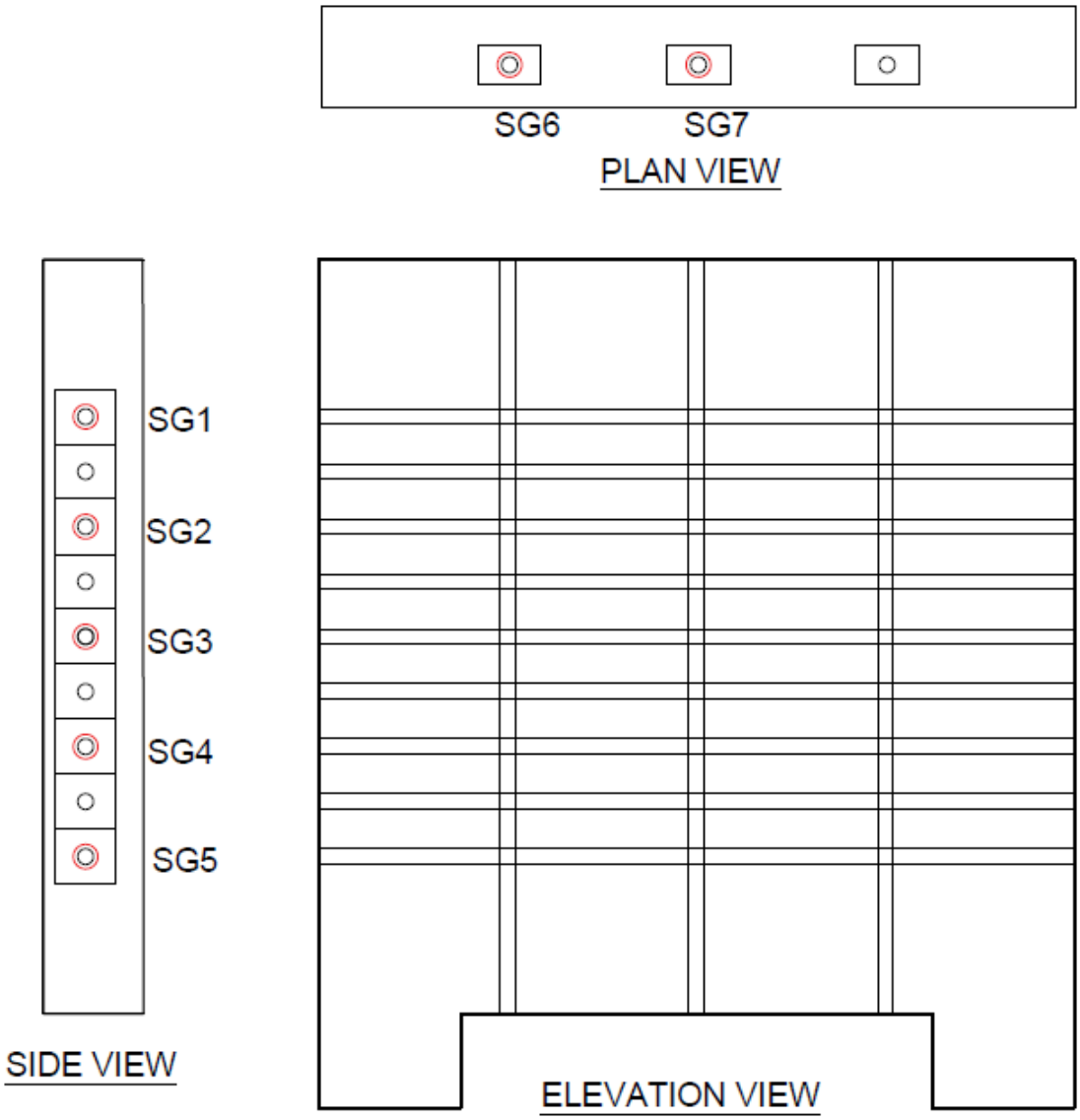

Figure 26 Specimen 1- Post-Tensioning Bar Strain Gage Labels and Locations

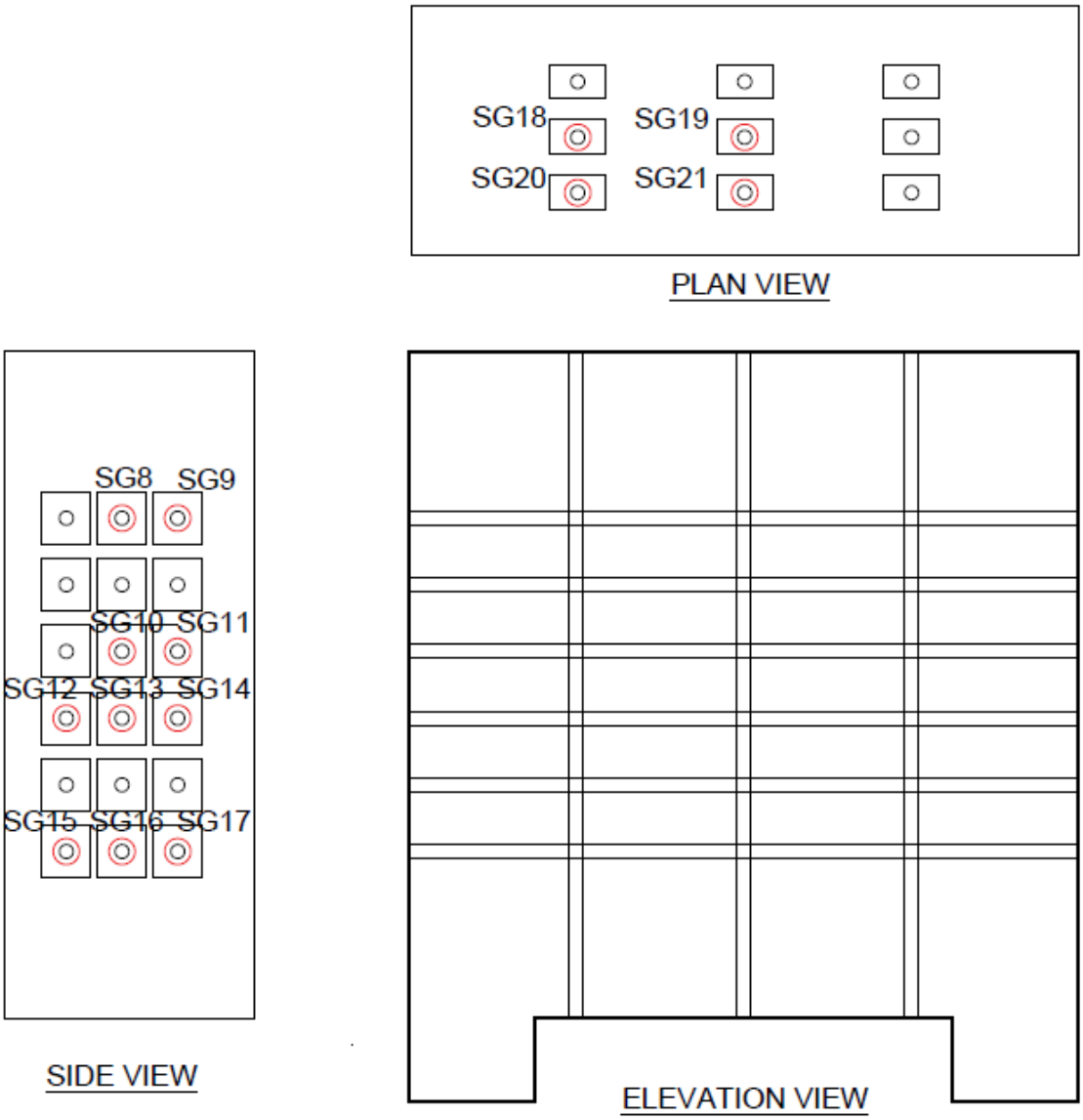

Figure 27 Specimen 2- Post-Tensioning Bar Strain Gage Labels and Locations

Figure 28 Data Logger Without Gages Connected

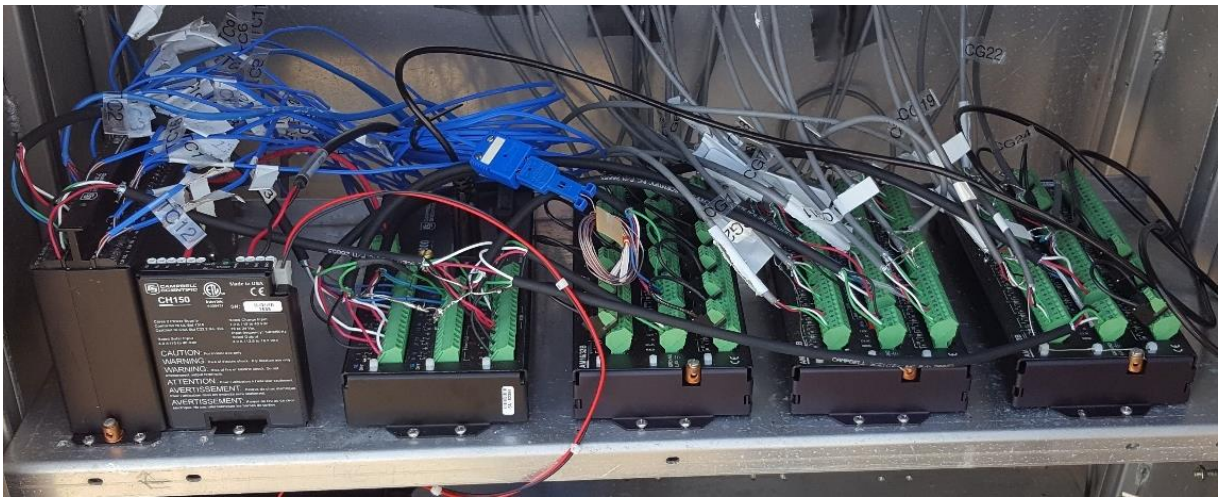

Figure 29 Data Logger Set Up with All Gages Connected

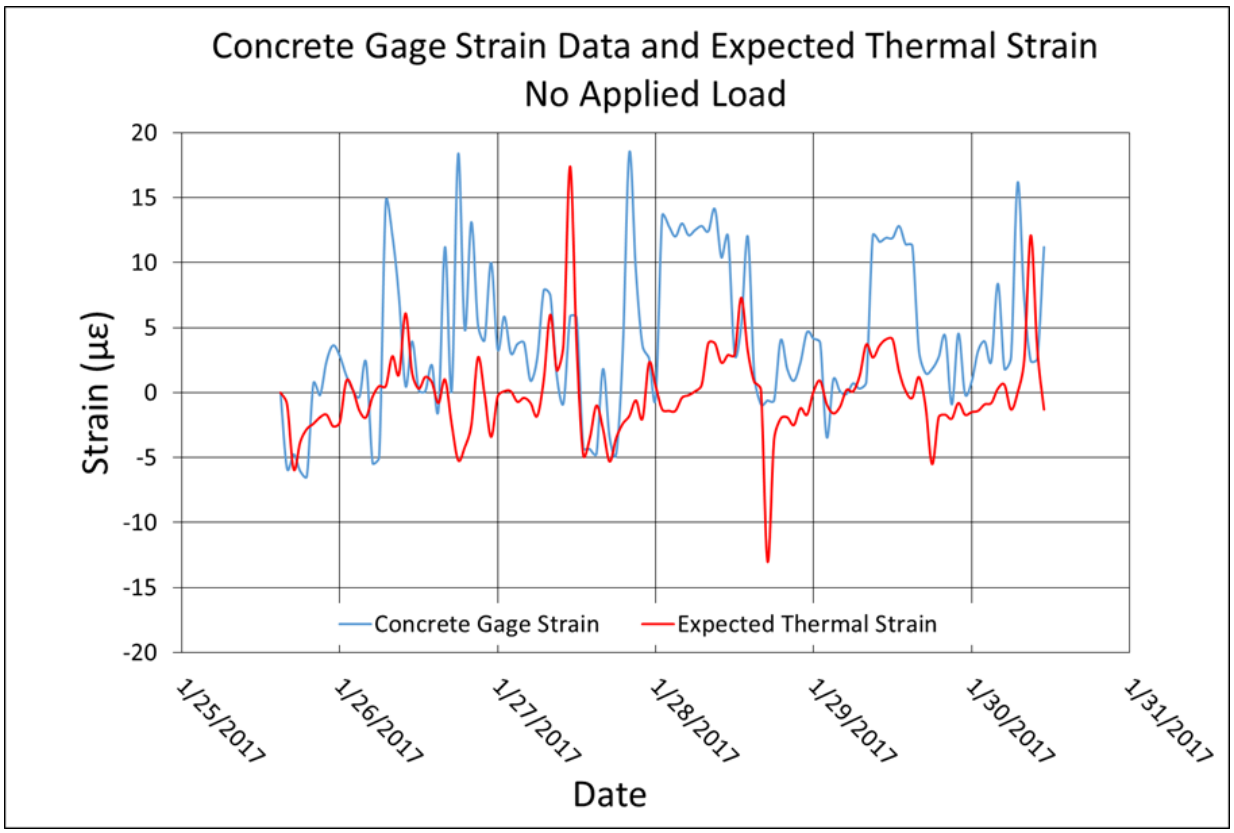

Figure 30 Concrete Gage Strain Data and Expected Thermal Strain with No Applied Load

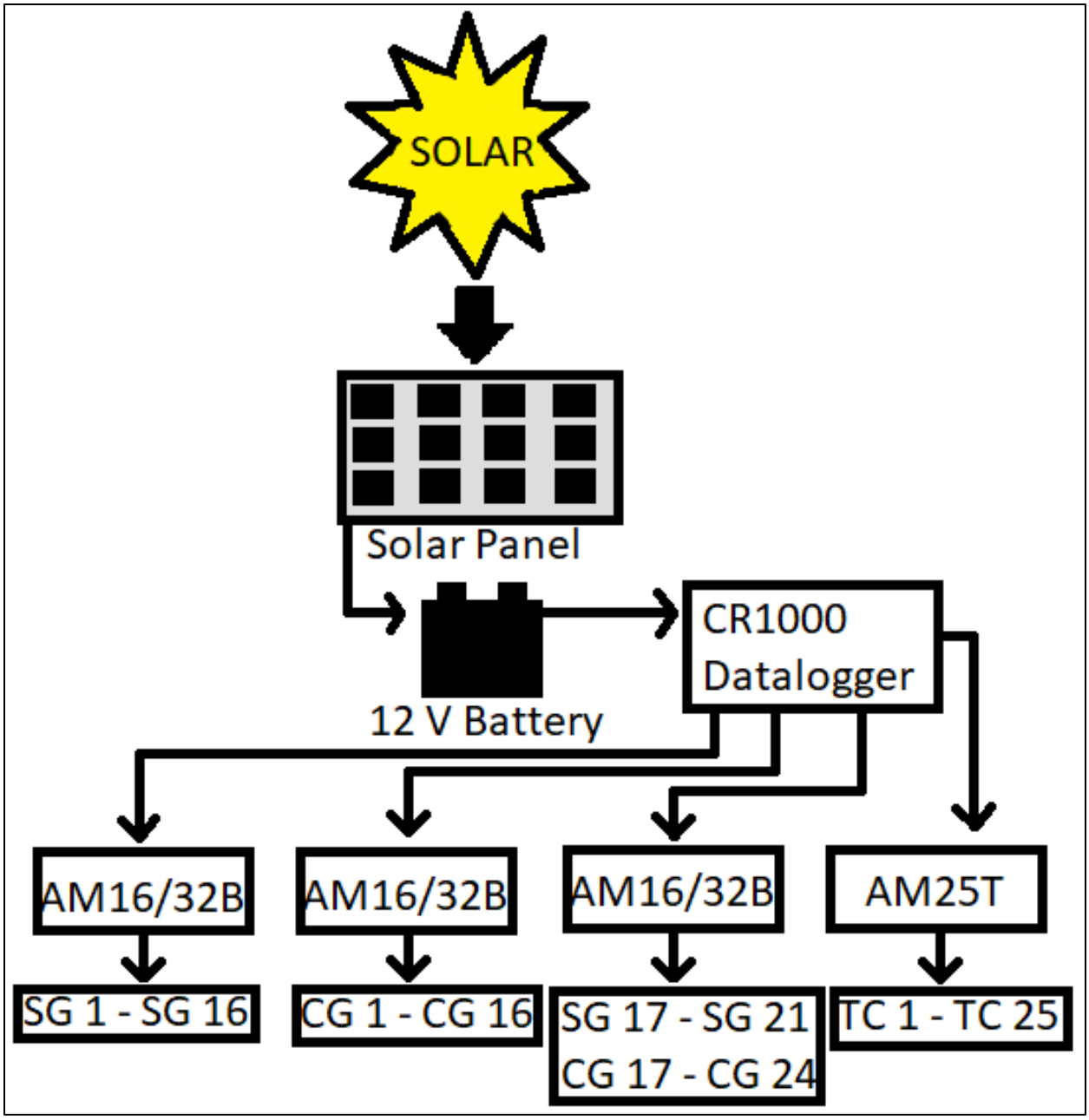

Figure 31 Representation of Data Acquisition Set Up

Figure 32 Specimen 1- Reinforcing Steel Assembled Cage

Figure 33 Specimen 1- Reinforcing Steel Assembled Cage

Figure 34 Specimen 2- Reinforcing Steel Assembled Cage

Figure 35 Specimen 2- Reinforcing Steel Assembled Cage

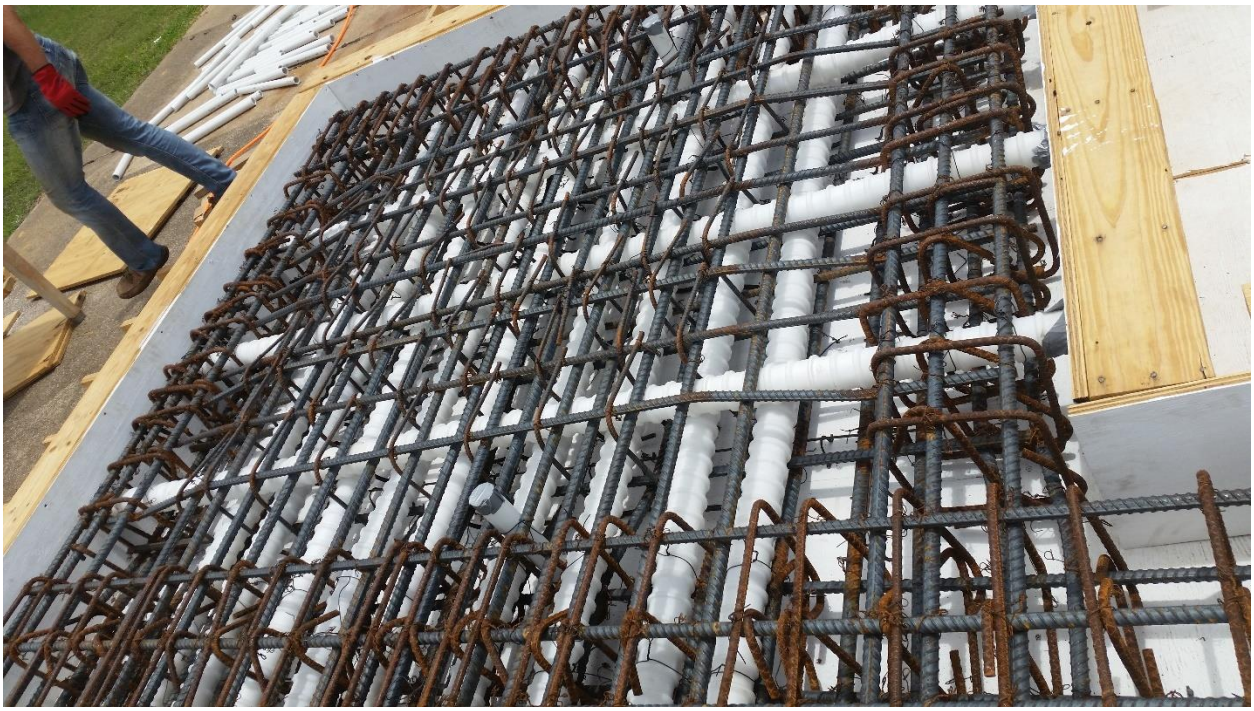

Figure 36 Specimen 1- Post-Tensioning Bar Ducts, Reinforcing Steel Cage, and Formwork View from Top

Figure 37 Specimen 1- Post-Tensioning Bar Ducts, Reinforcing Steel Cage, and Formwork View from Between Specimen 1 Feet

Figure 38 Specimen 2- Post-Tensioning Bar Ducts, Reinforcing Steel Cage, and Formwork View from Side

Figure 39 Specimen 2- Post-Tensioning Bar Ducts, Reinforcing Steel Cage, and Formwork View from Between Specimen 2 Feet

Figure 40 Specimen 2- Formwork

Figure 41 Specimen 3- Formwork

Figure 42 Typical Concrete Gage Installation

Figure 43 Specimen 1- Concrete Gage Arrangement

Figure 44 Specimen 2- Concrete Gage Arrangement

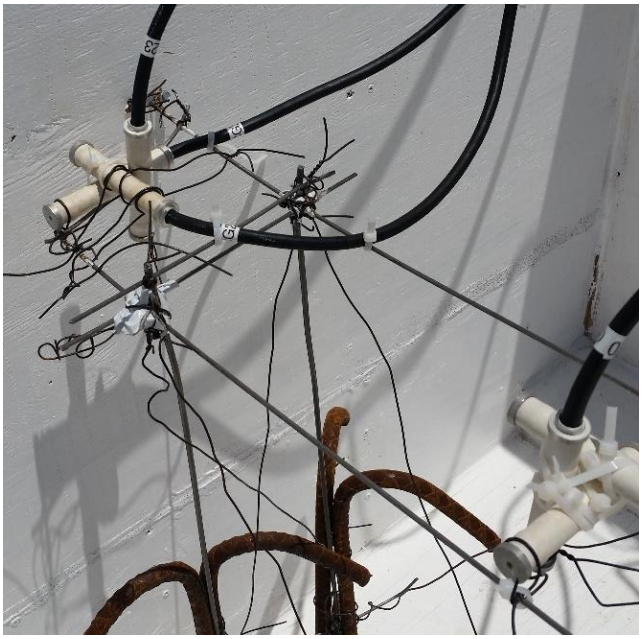

Figure 45 Specimen 3- Concrete Gage Arrangement

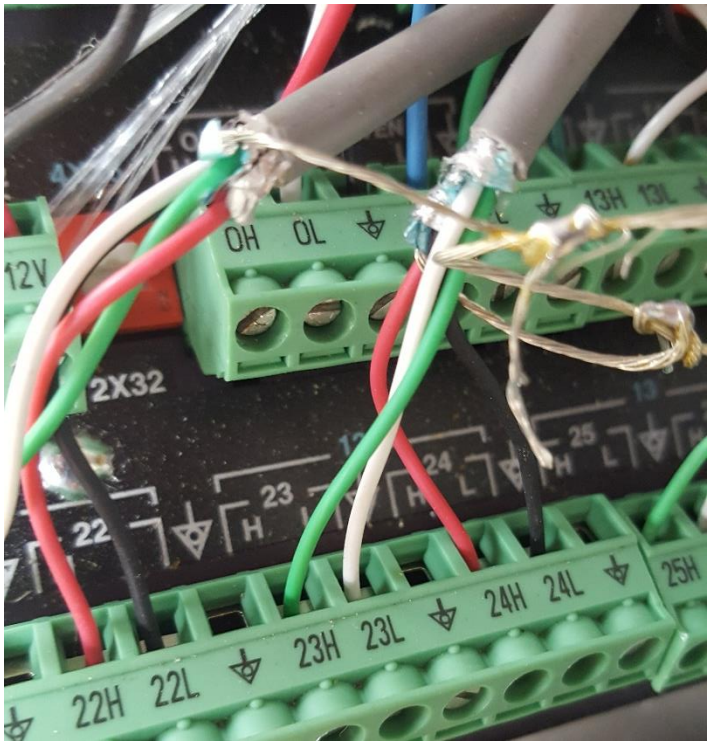

Figure 46 Concrete Gage Connection to DAQ. Odd High - Green, Odd Low - White, Even High - Red, Even Low – Black

Figure 47 Specimen 1- Pre-Pour Set Up

Figure 48 Specimen 2- Pre-Pour Set Up

Figure 49 Specimen 3- Pre-Pour Set Up

Figure 50 Specimen 1- After Concrete Pour

Figure 51 Specimen 2- Concrete Pour

Figure 52 Specimen 2- Concrete Pour Finishing

Figure 53 Specimen 2- After Concrete Pour

Figure 54 Post-Tensioning Bar After Grinding and Sanding

Figure 55 Post-Tensioning Bar with Tape Wrapped Around to Apply Uniform Pressure to Strain Gage for Strong Bond with Adhesive

Figure 56 Post-Tensioning Bar with Strain Gage and Terminal Glued On

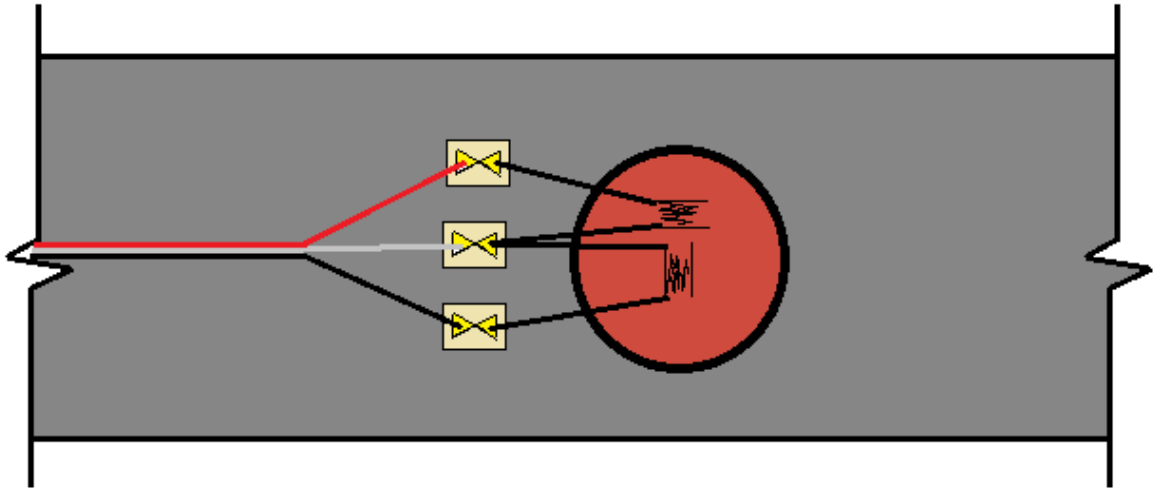

Figure 57 Illustration of Strain Gage with Extension Wire Attached

Figure 58 Specimen 1- Forms Stripped After Concrete Pour and Post-Tensioning Bars Installed

Figure 59 Specimen 2- Forms Stripped After Concrete Pour and Post-Tensioning Bars Installed

Figure 60 Specimen 1- Post-Tensioning Bars with Anchor Plates and Nuts, Side View

Figure 61 Specimen 2- Post-Tensioning Bars with Anchor Plates and Nuts, Side View

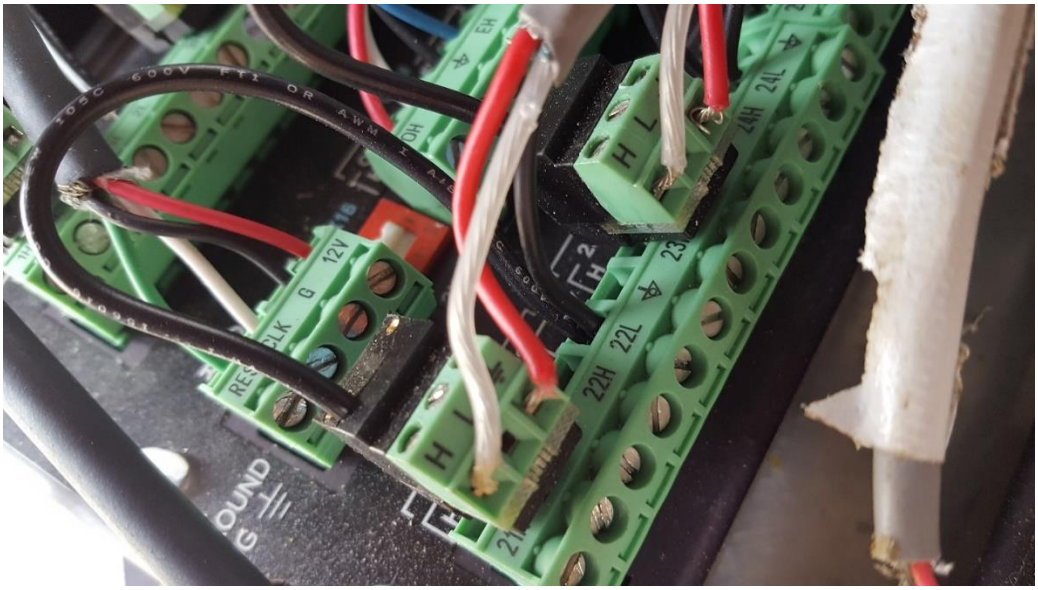

Figure 62 Strain Gage Wired to Data Acquisition. Odd High - White, Odd Ground - Red, Even Low - Black and Bridge Completion

Figure 63 Post-Tensioning Hydraulic Jack Applying Force to Vertical Bar in Specimen 2

Figure 64 Specimen 1- Lifting Off Ground into Final Position

Figure 65 Specimen 2- Lifting Off Ground into Final Position

Figure 66 Specimen 1- Final Position with Weatherproofing Applied to One Side

Figure 67 Specimen 2- Final Position (Weatherproofing Applied to Other Side)

Figure 68 Specimen 3- Final Position (Weatherproofing Applied to Other Side)

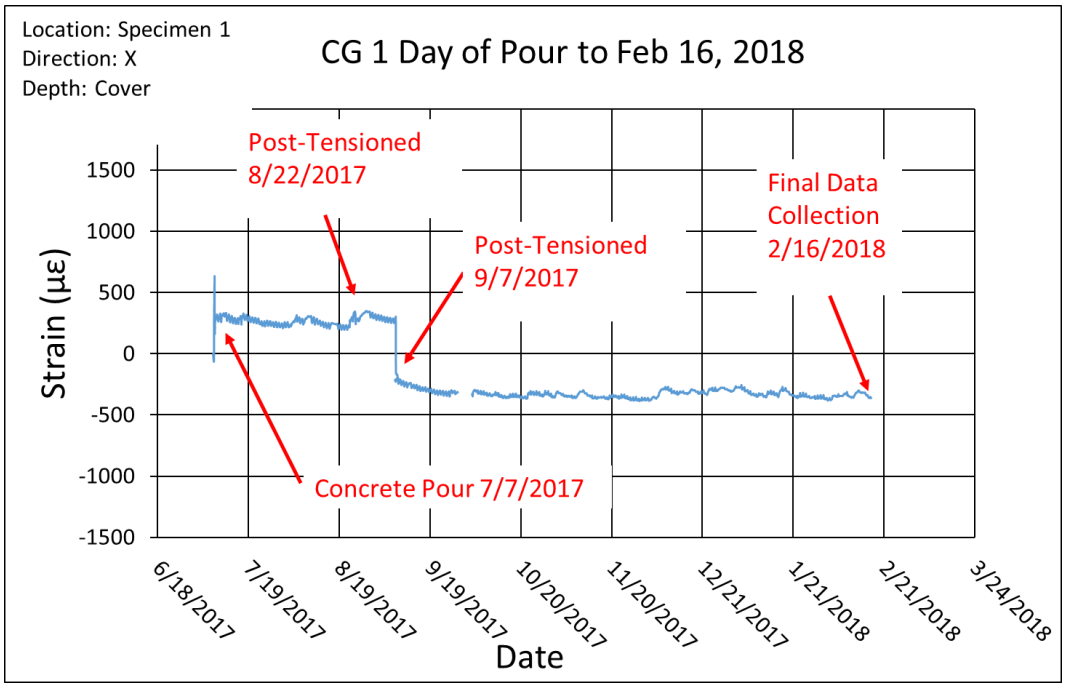

Figure 69 Concrete Gage 1 Strain Data from the Day of the Concrete Pour to February 16, 2018

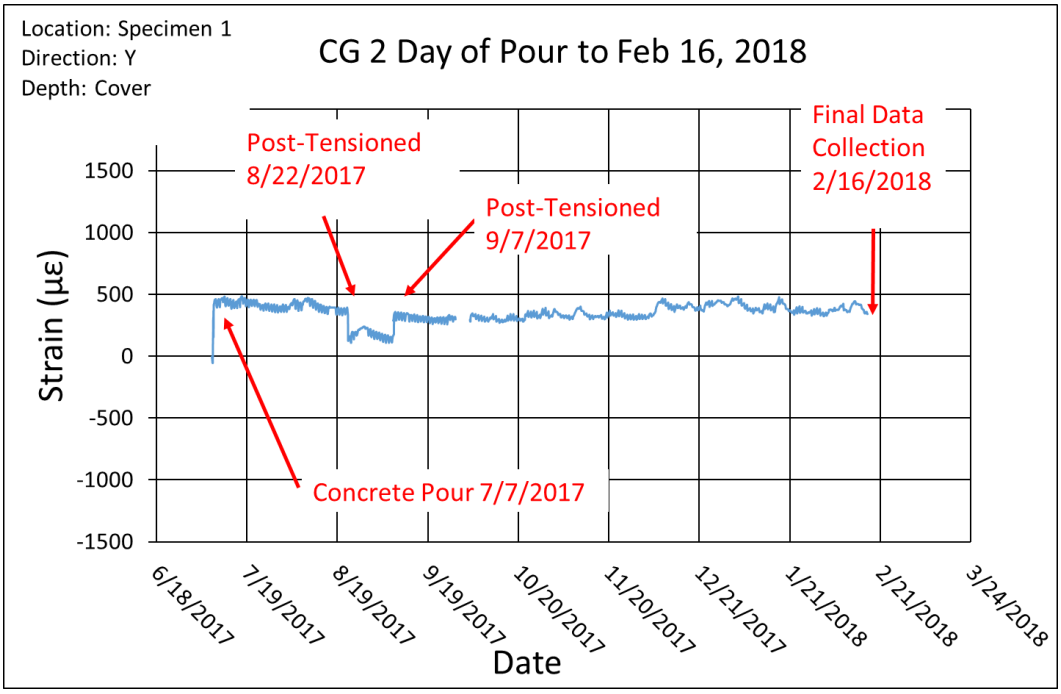

Figure 70 Concrete Gage 2 Strain Data from the Day of the Concrete Pour to February 16, 2018

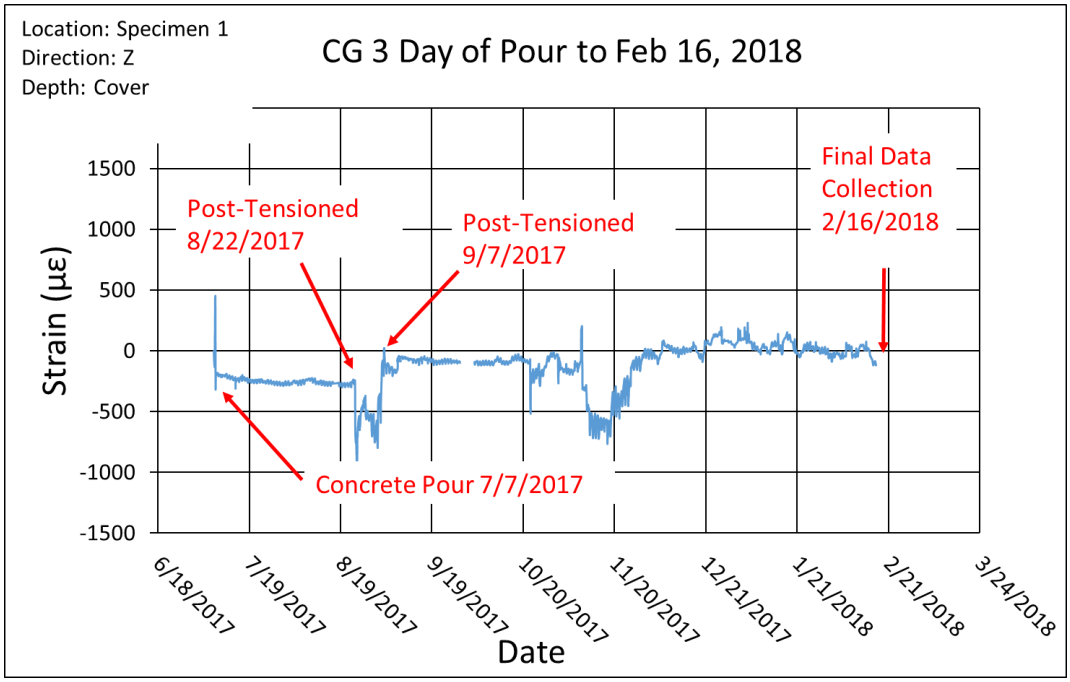

Figure 71 Concrete Gage 3 Strain Data from the Day of the Concrete Pour to February 16, 2018

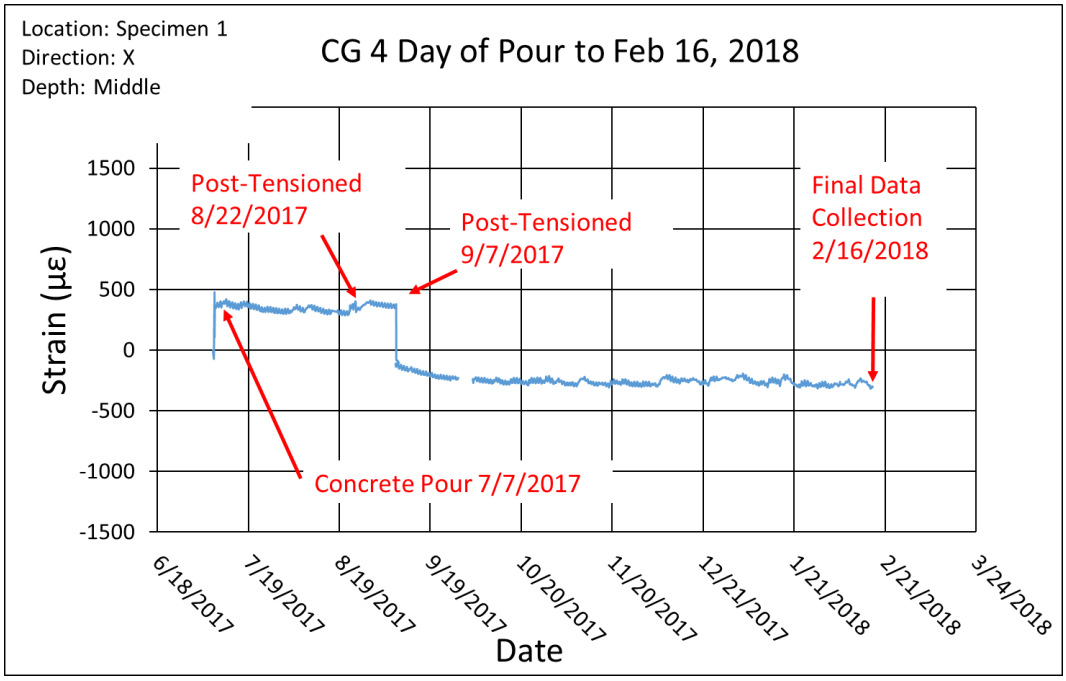

Figure 72 Concrete Gage 4 Strain Data from the Day of the Concrete Pour to February 16, 2018

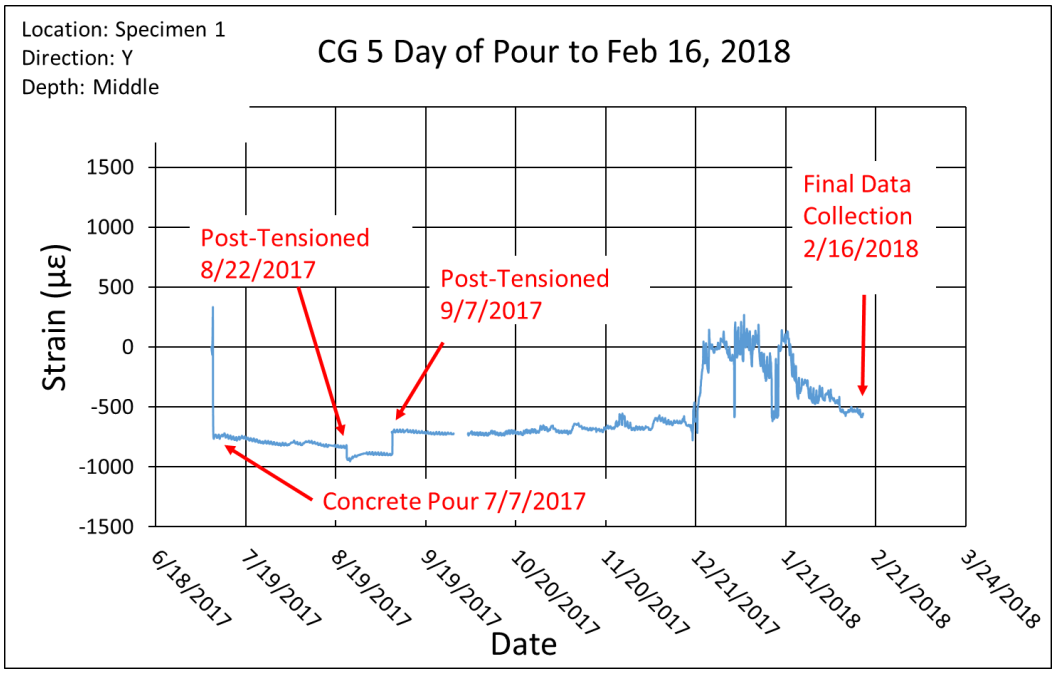

Figure 73 Concrete Gage 5 Strain Data from the Day of the Concrete Pour to February 16, 2018

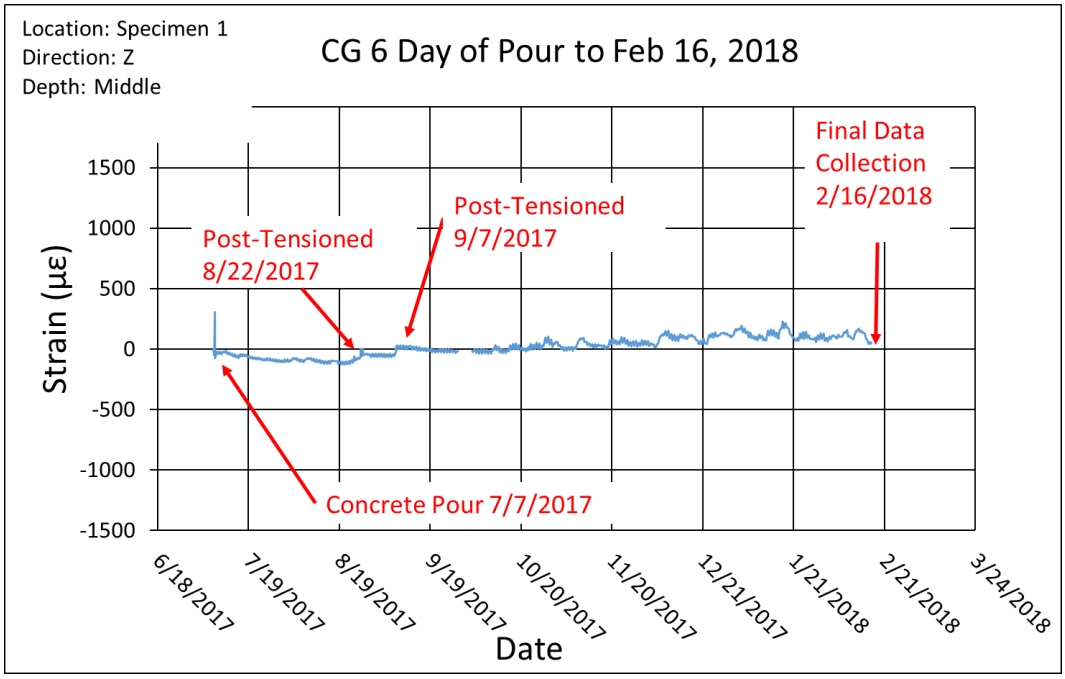

Figure 74 Concrete Gage 6 Strain Data from the Day of the Concrete Pour to February 16, 2018

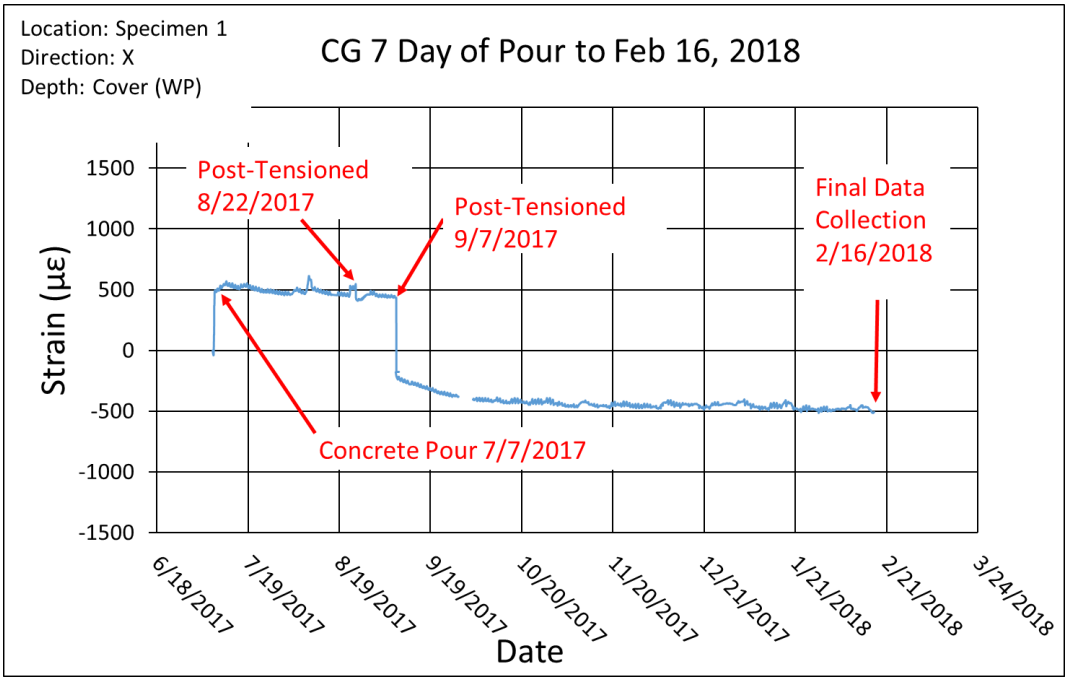

Figure 75 Concrete Gage 7 Strain Data from the Day of the Concrete Pour to February 16, 2018

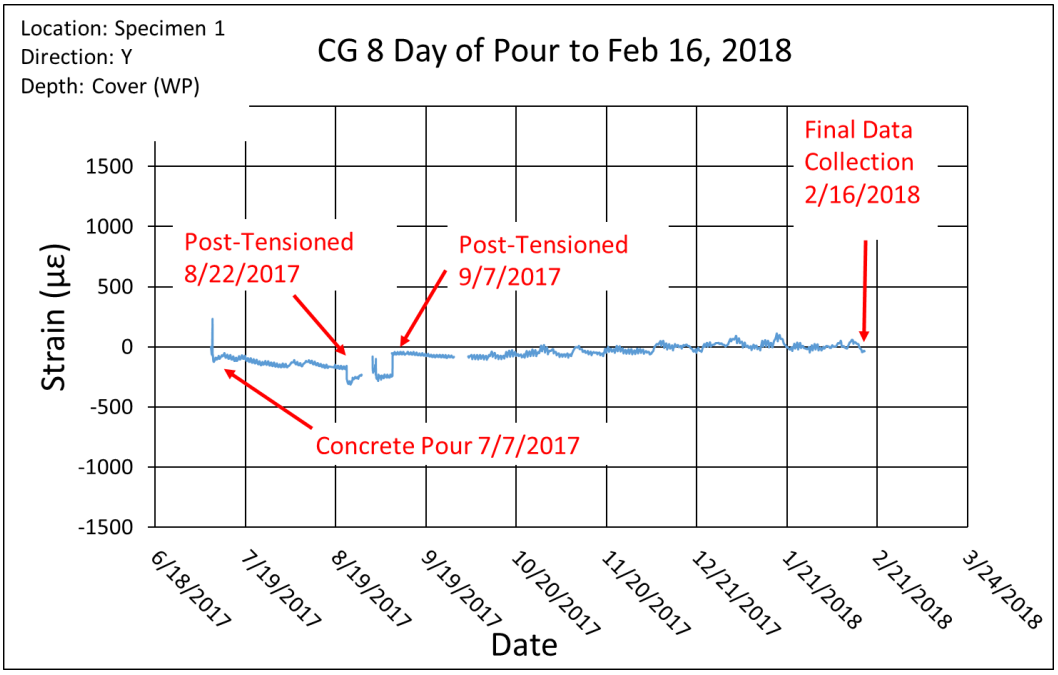

Figure 76 Concrete Gage 8 Strain Data from the Day of the Concrete Pour to February 16, 2018

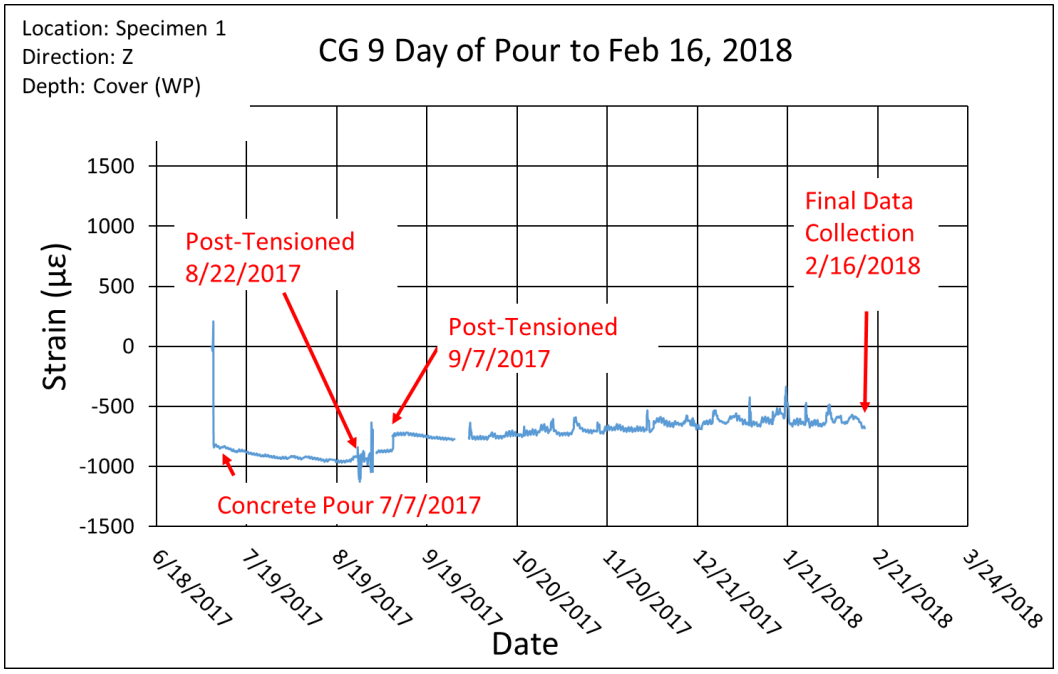

Figure 77 Concrete Gage 9 Strain Data from the Day of the Concrete Pour to February 16, 2018

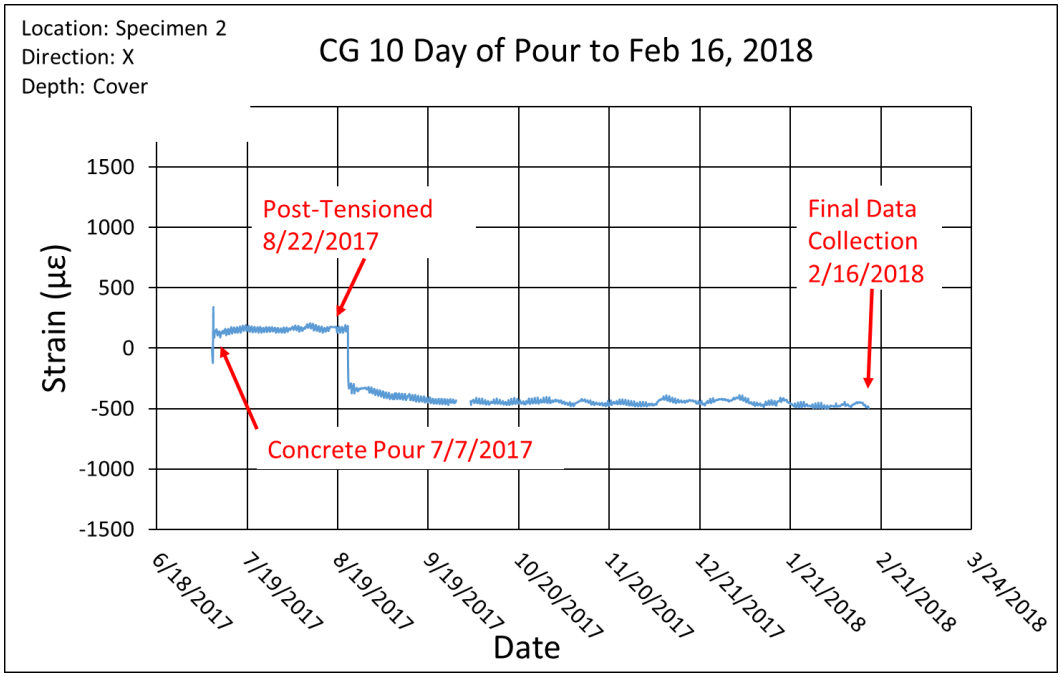

Figure 78 Concrete Gage 10 Strain Data from the Day of the Concrete Pour to February 16, 2018

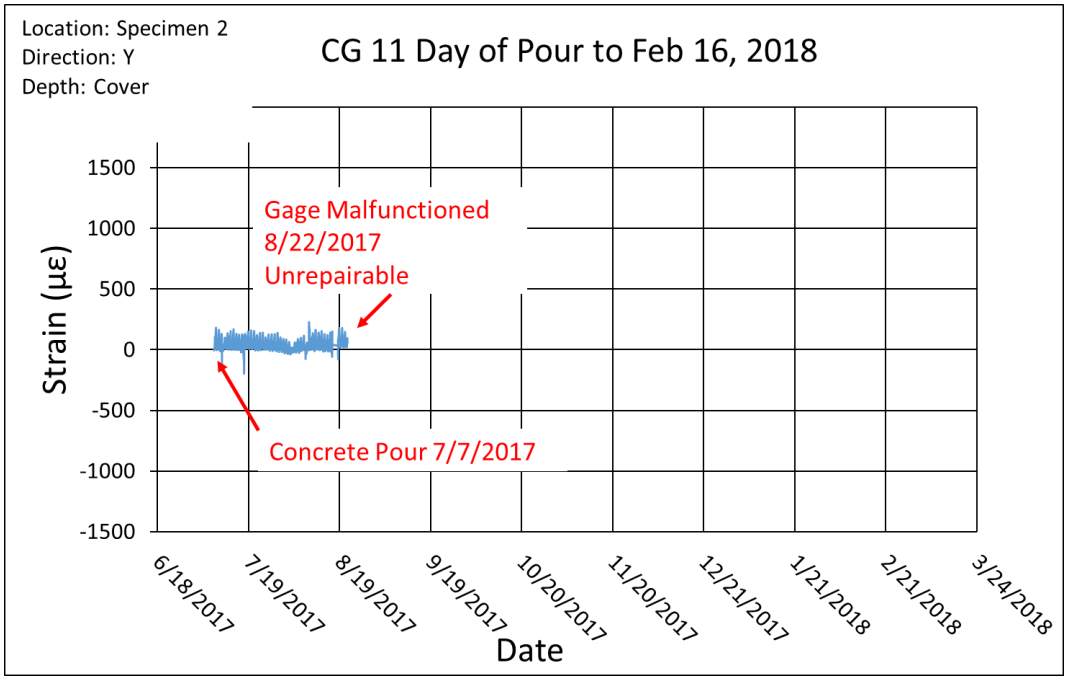

Figure 79 Concrete Gage 11 Strain Data from the Day of the Concrete Pour to February 16, 2018

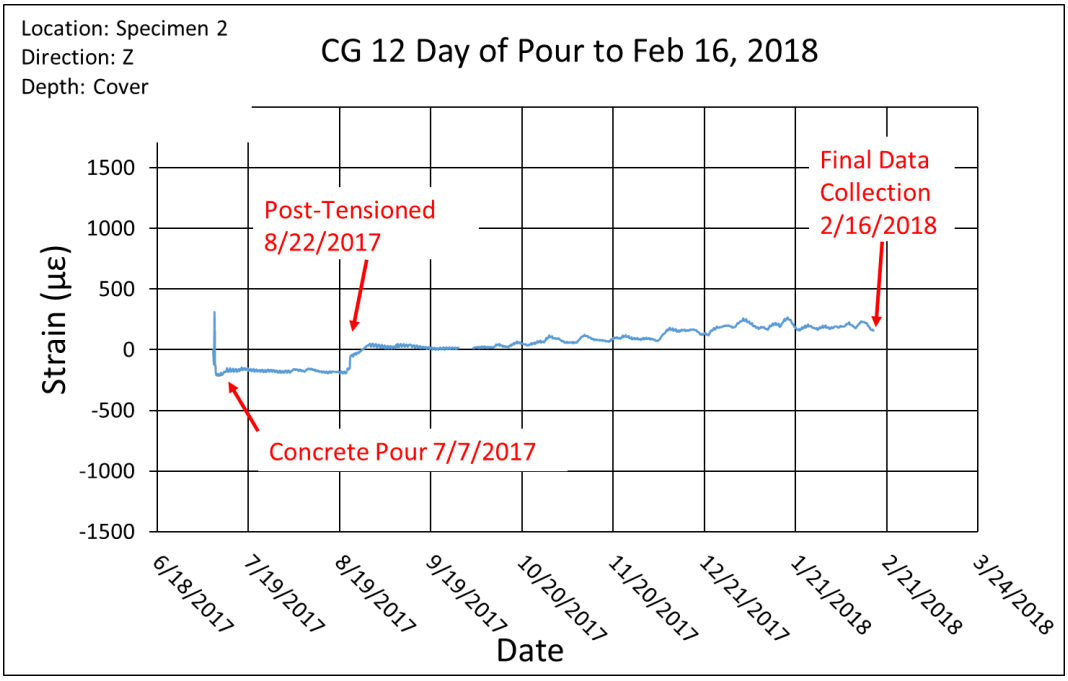

Figure 80 Concrete Gage 12 Strain Data from the Day of the Concrete Pour to February 16, 2018

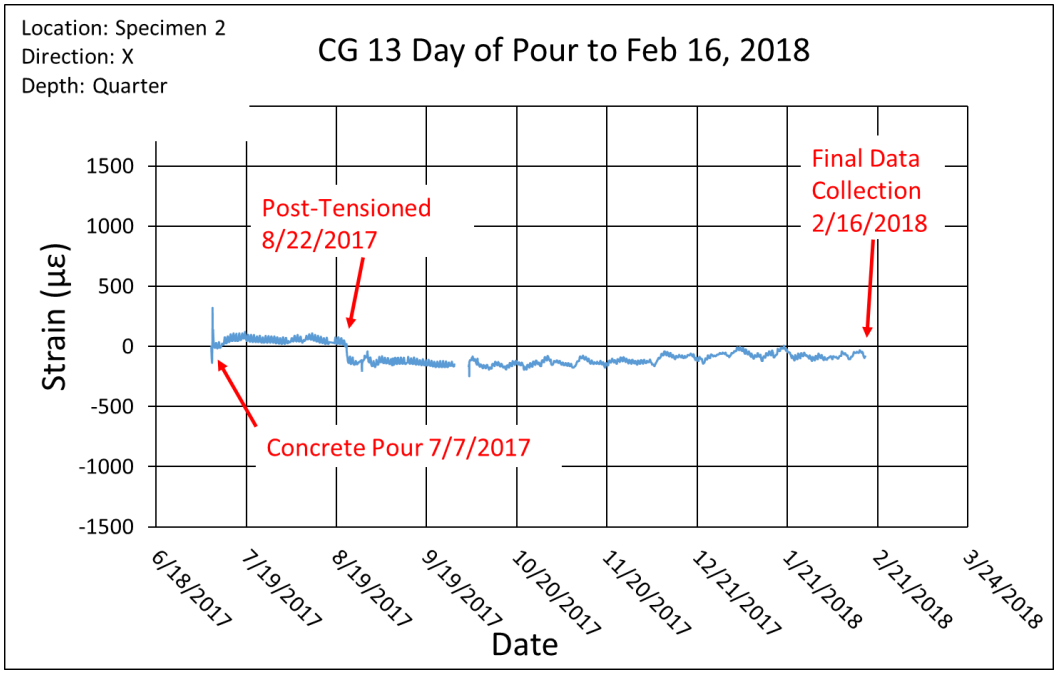

Figure 81 Concrete Gage 13 Strain Data from the Day of the Concrete Pour to February 16, 2018

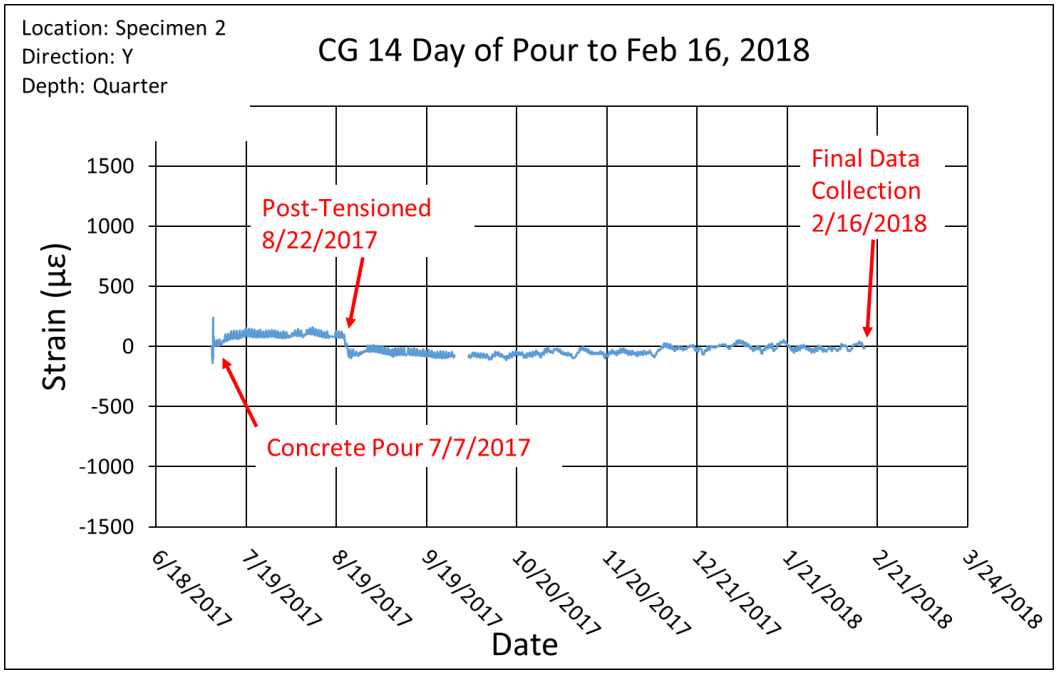

Figure 82 Concrete Gage 14 Strain Data from the Day of the Concrete Pour to February 16, 2018

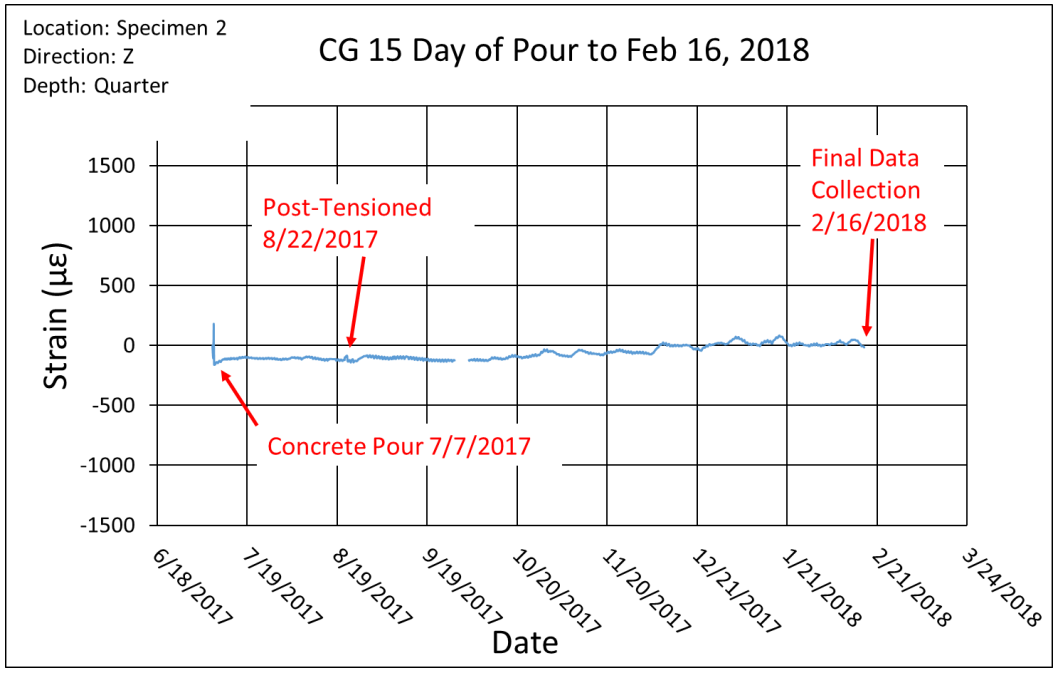

Figure 83 Concrete Gage 15 Strain Data from the Day of the Concrete Pour to February 16, 2018

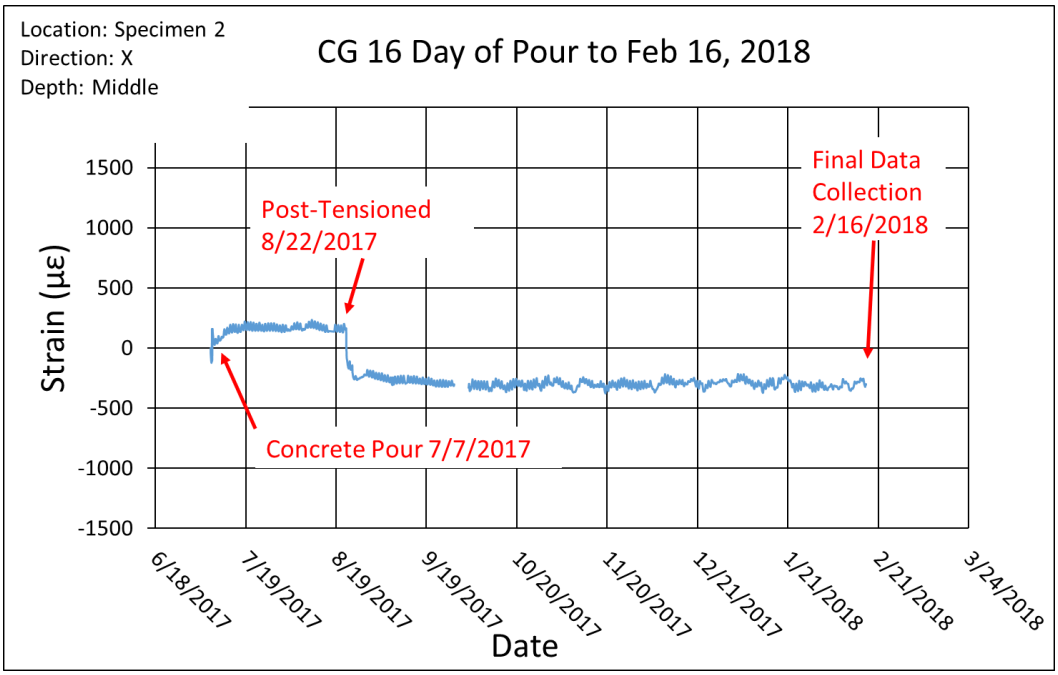

Figure 84 Concrete Gage 16 Strain Data from the Day of the Concrete Pour to February 16, 2018

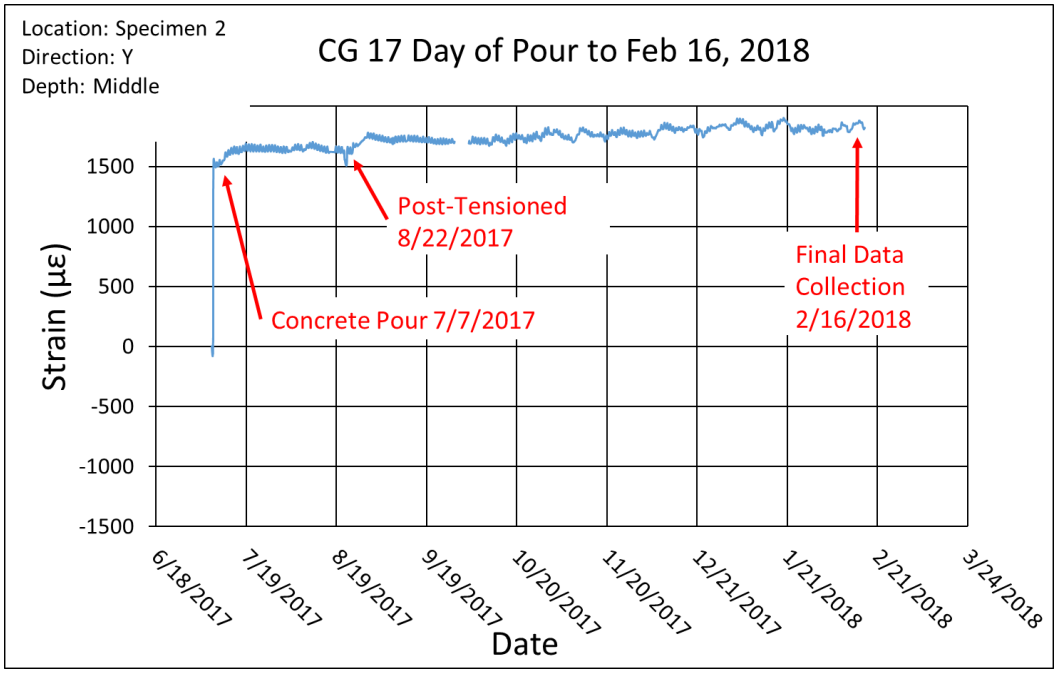

Figure 85 Concrete Gage 17 Strain Data from the Day of the Concrete Pour to February 16, 2018

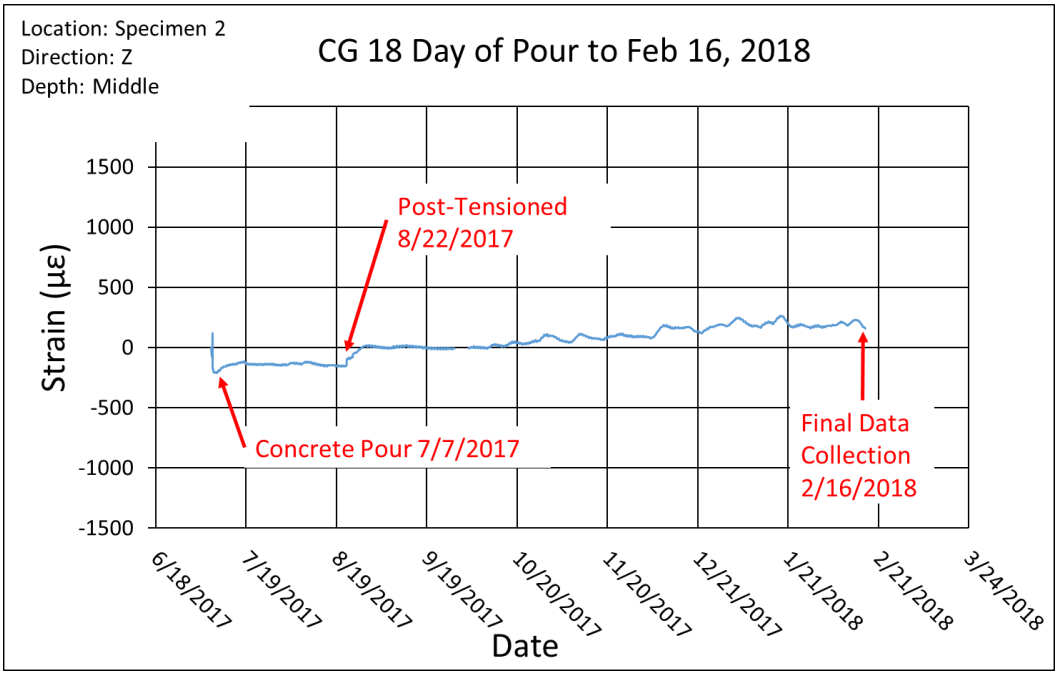

Figure 86 Concrete Gage 18 Strain Data from the Day of the Concrete Pour to February 16, 2018

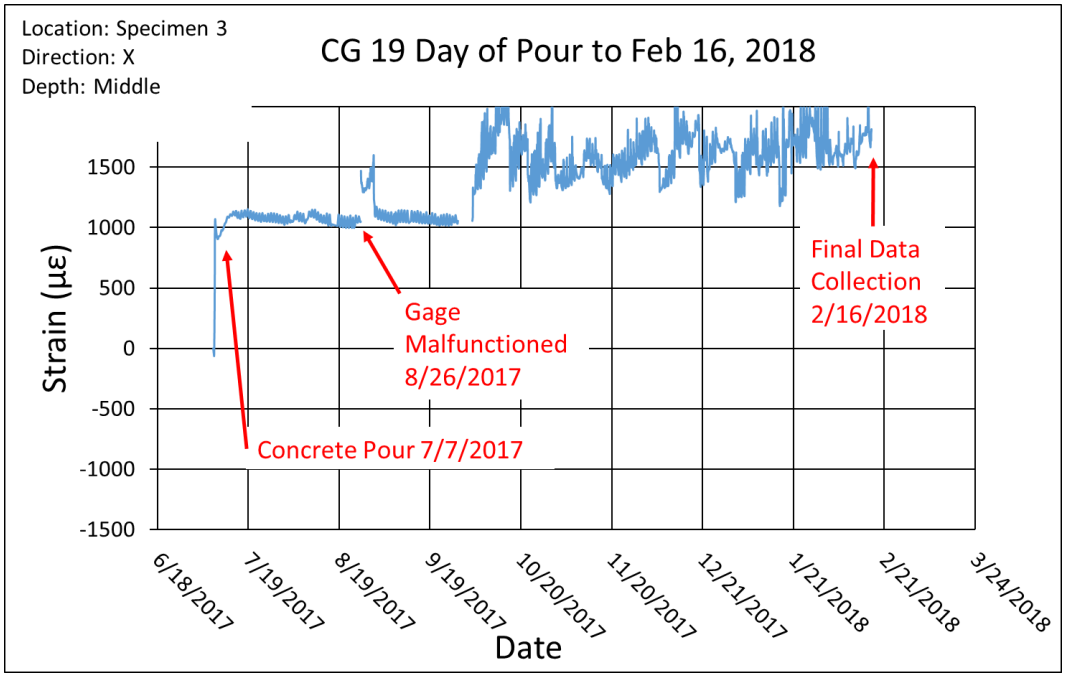

Figure 87 Concrete Gage 19 Strain Data from the Day of the Concrete Pour to February 16, 2018

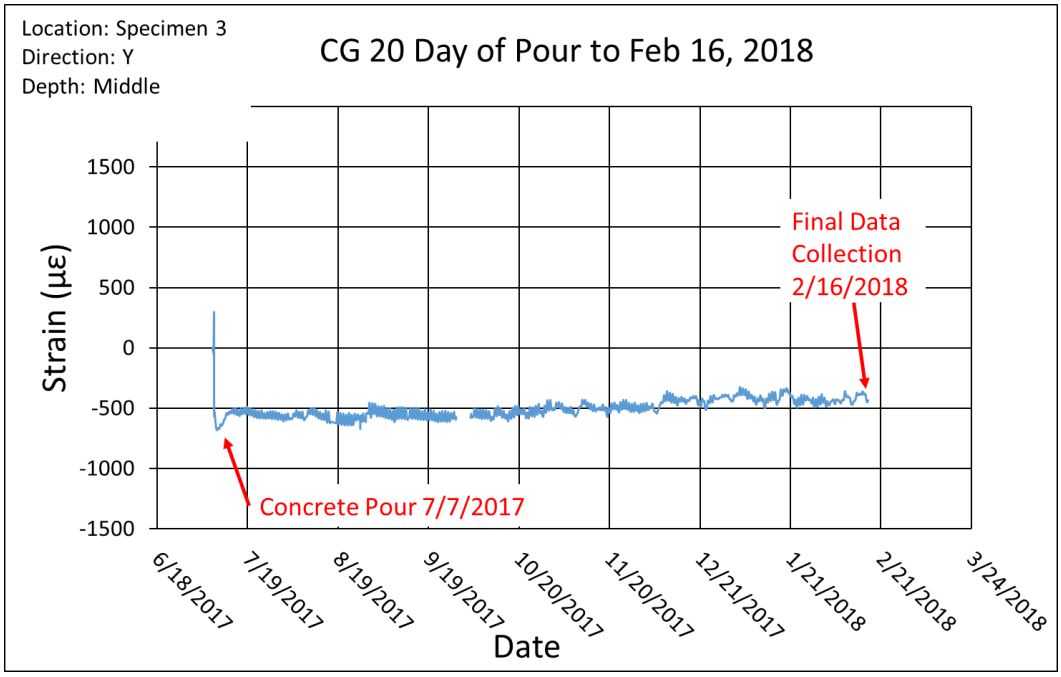

Figure 88 Concrete Gage 20 Strain Data from the Day of the Concrete Pour to February 16, 2018

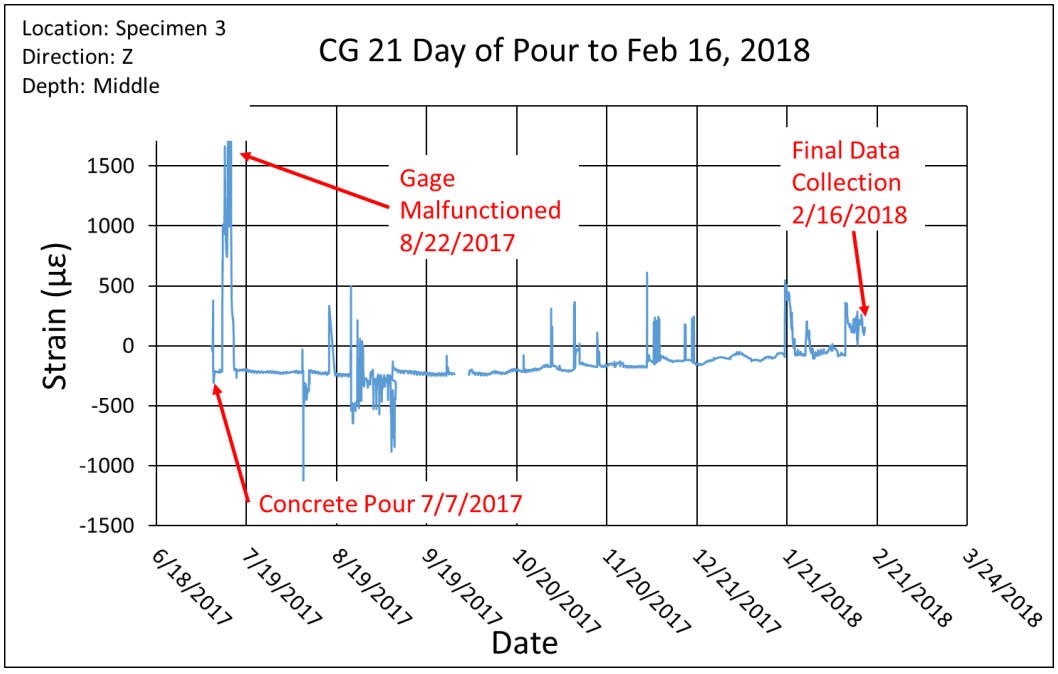

Figure 89 Concrete Gage 21 Strain Data from the Day of the Concrete Pour to February 16, 2018

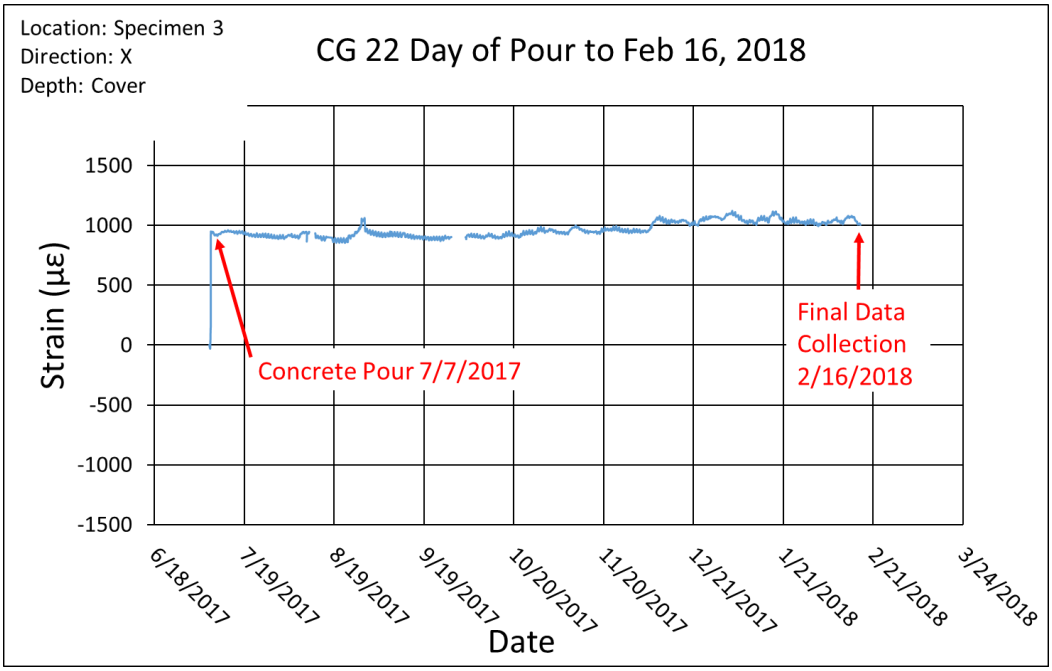

Figure 90 Concrete Gage 22 Strain Data from the Day of the Concrete Pour to February 16, 2018

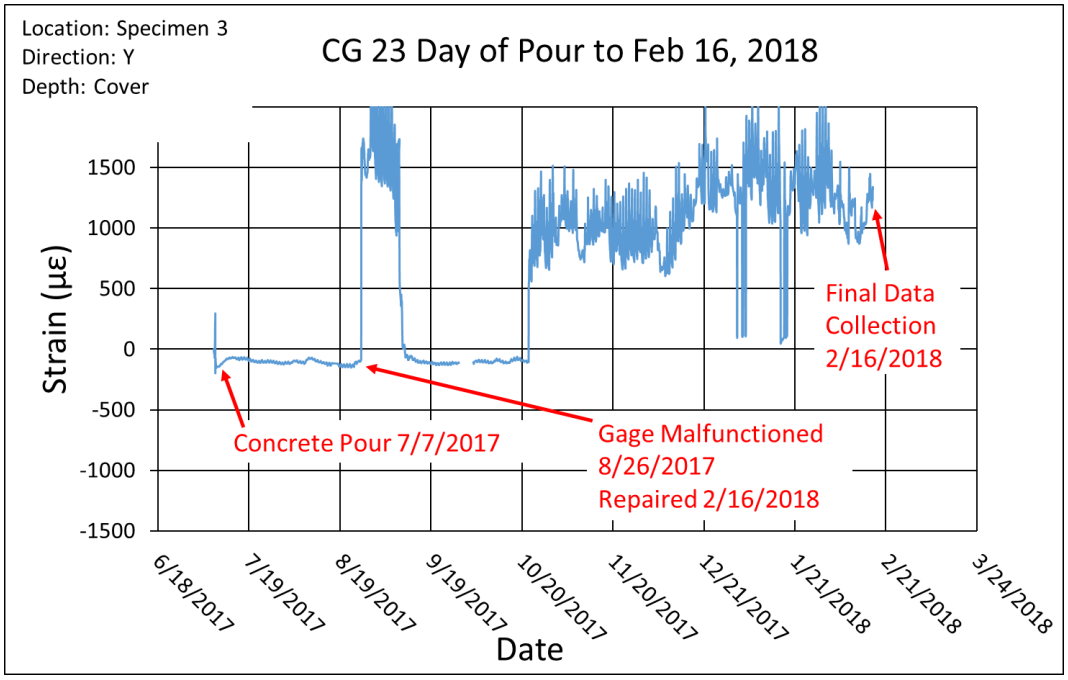

Figure 91 Concrete Gage 23 Strain Data from the Day of the Concrete Pour to February 16, 2018

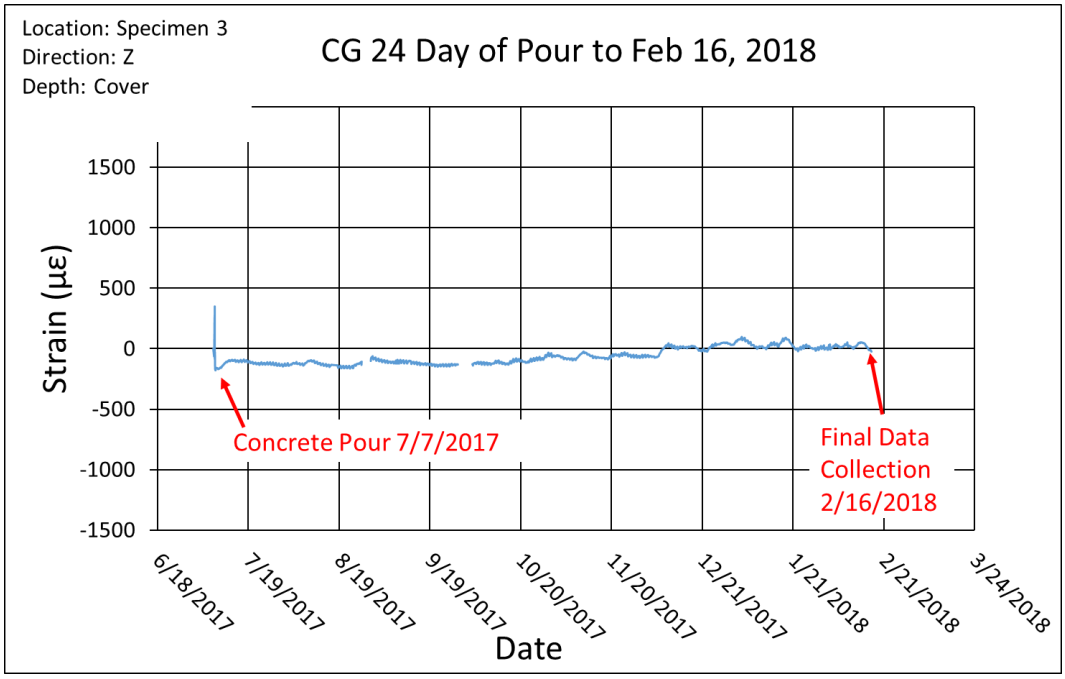

Figure 92 Concrete Gage 24 Strain Data from the Day of the Concrete Pour to February 16, 2018

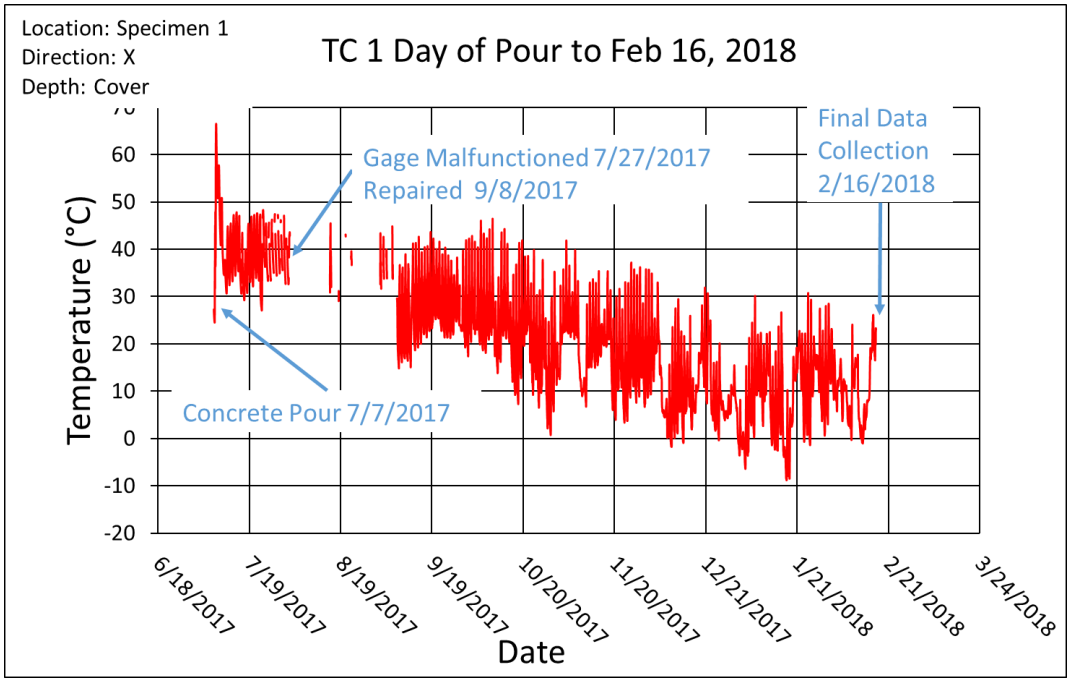

Figure 93 Thermocouple 1 Temperature Data from the Day of the Concrete Pour to February 16, 2018

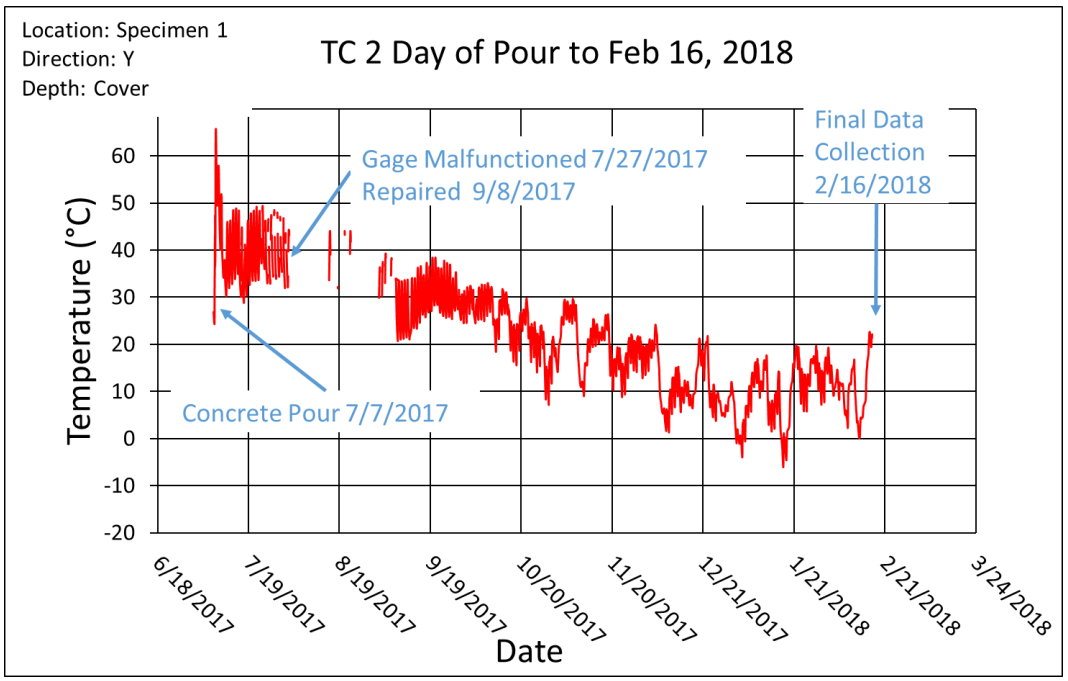

Figure 94 Thermocouple 2 Temperature Data from the Day of the Concrete Pour to February 16, 2018

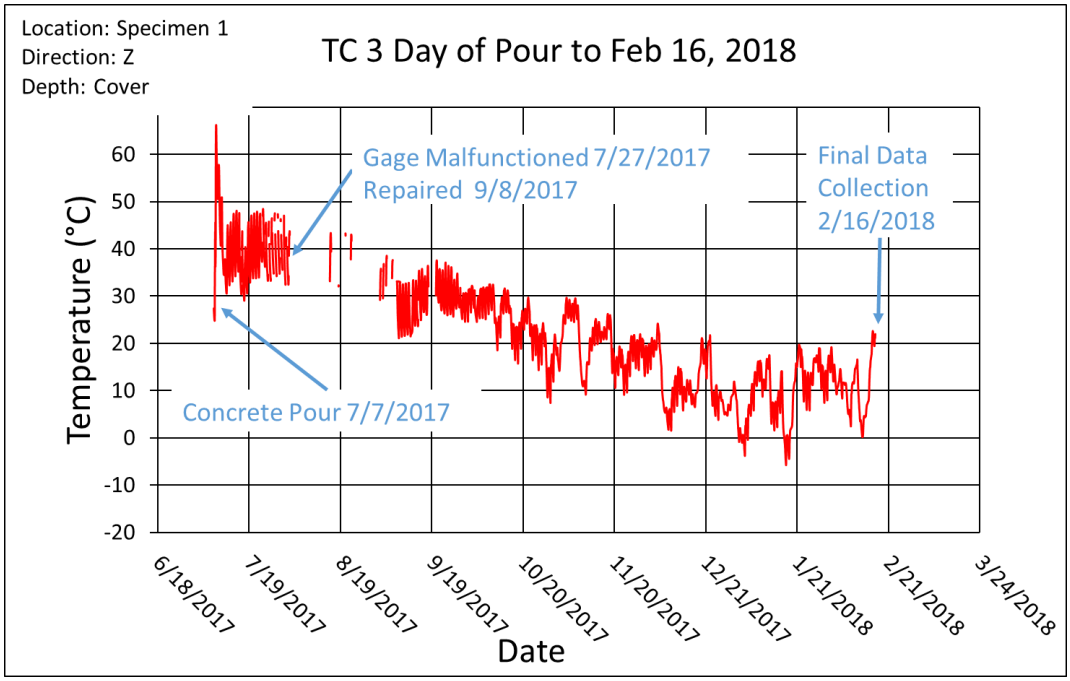

Figure 95 Thermocouple 3 Temperature Data from the Day of the Concrete Pour to February 16, 2018

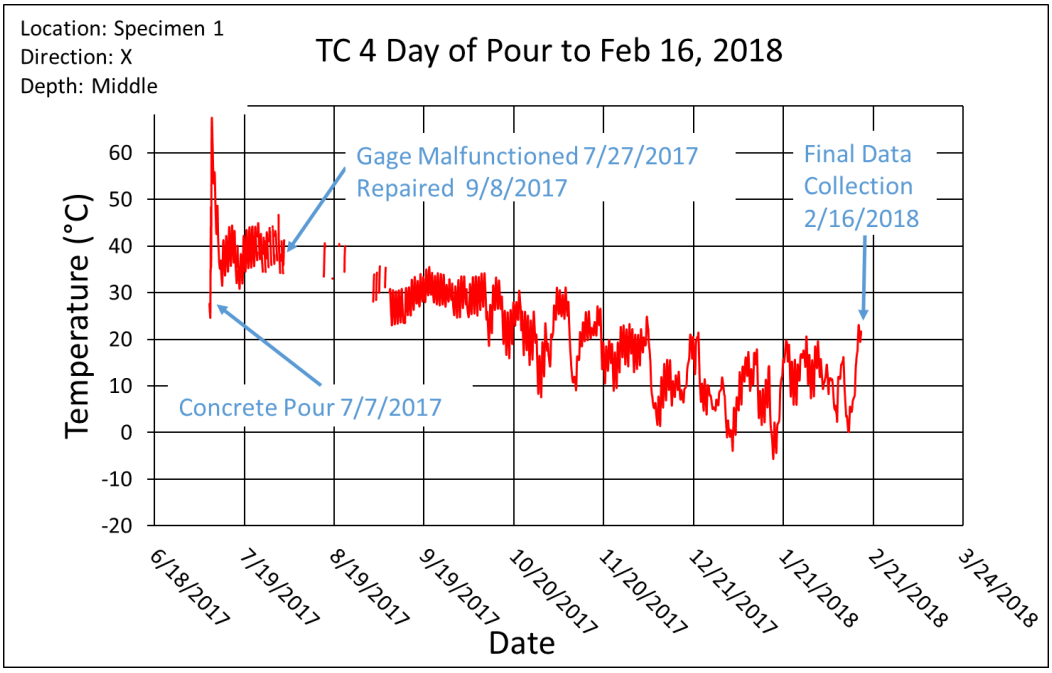

Figure 96 Thermocouple 4 Temperature Data from the Day of the Concrete Pour to February 16, 2018

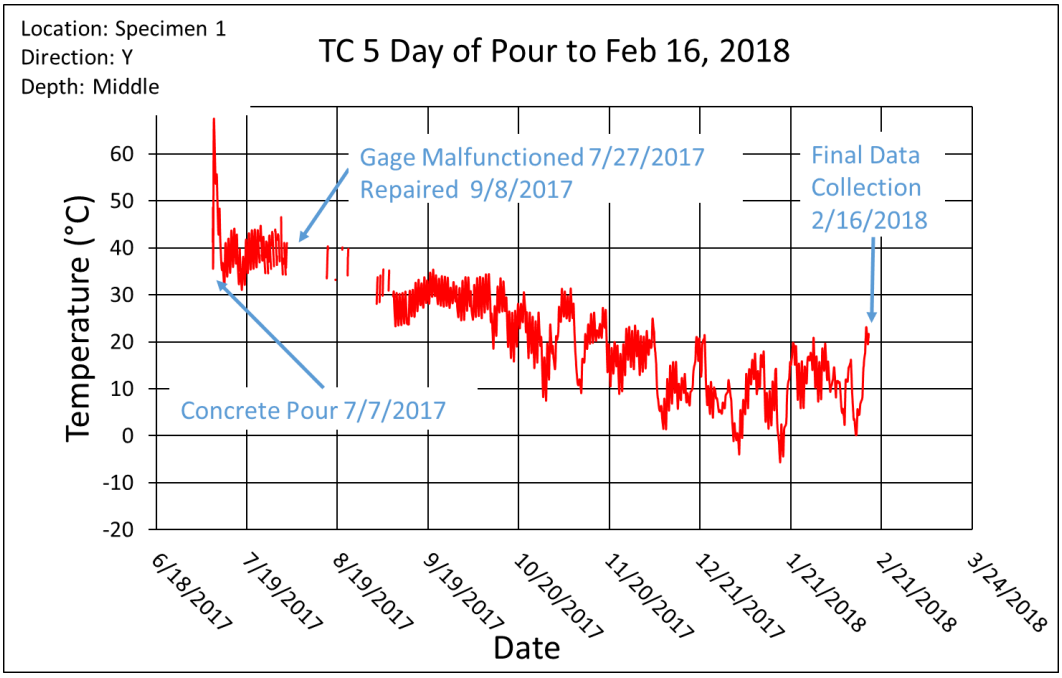

Figure 97 Thermocouple 5 Temperature Data from the Day of the Concrete Pour to February 16, 2018

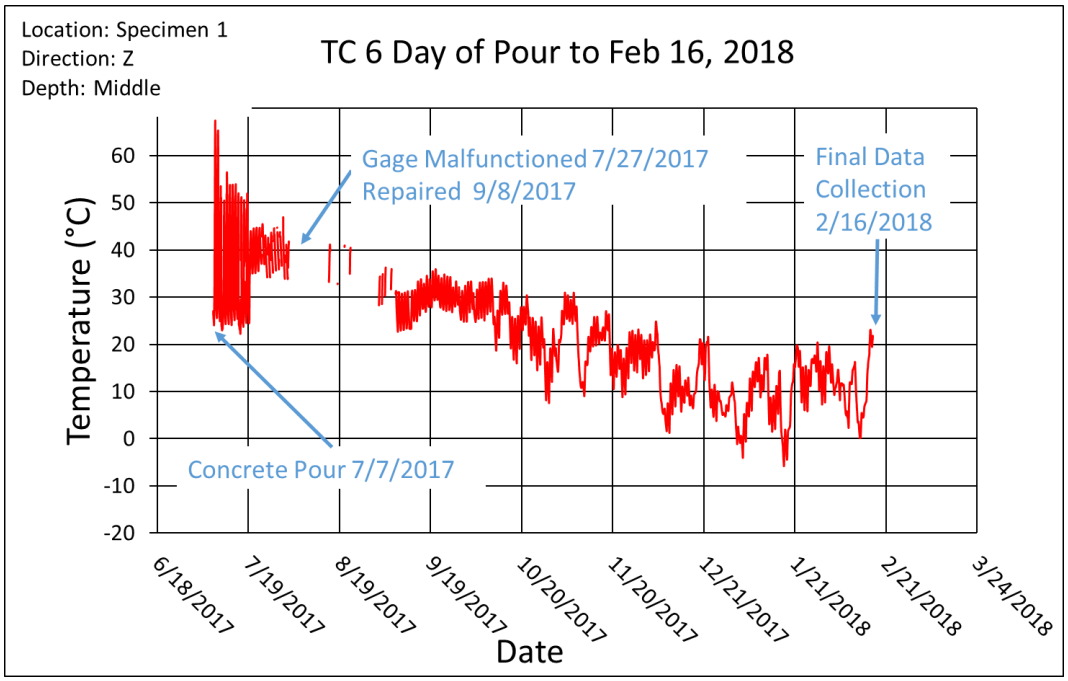

Figure 98 Thermocouple 6 Temperature Data from the Day of the Concrete Pour to February 16, 2018

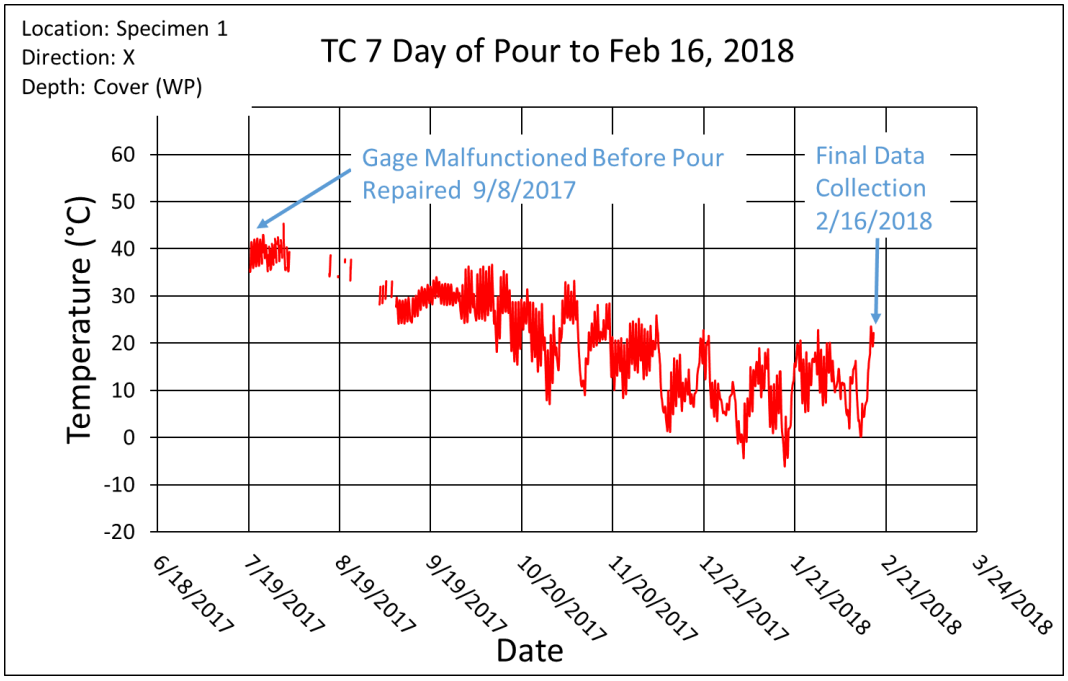

Figure 99 Thermocouple 7 Temperature Data from the Day of the Concrete Pour to February 16, 2018

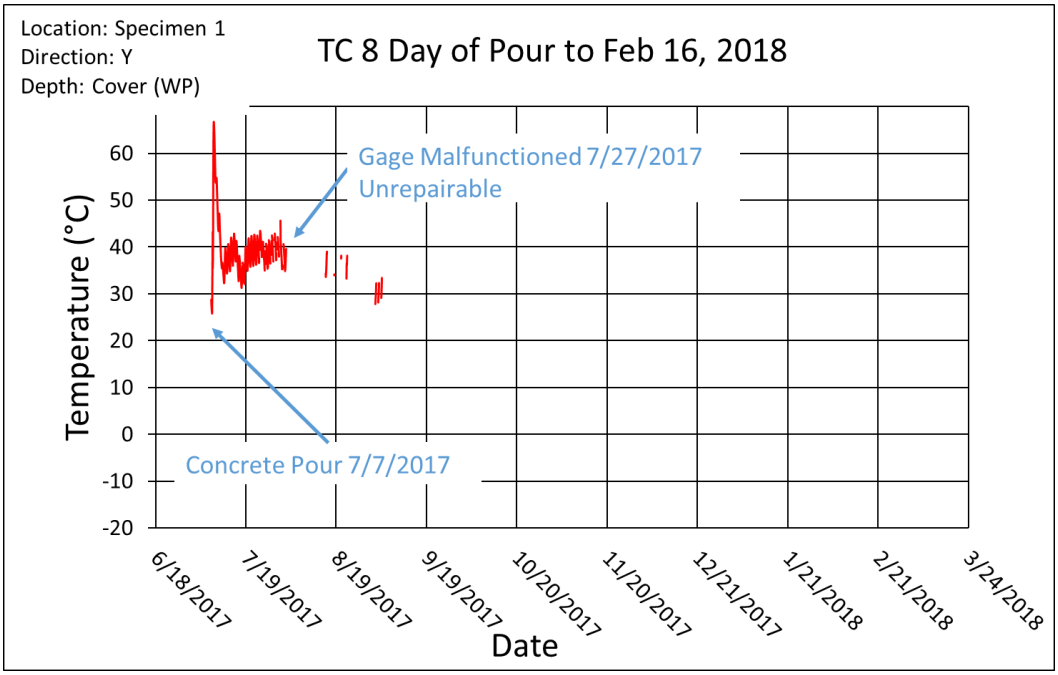

Figure 100 Thermocouple 8 Temperature Data from the Day of the Concrete Pour to February 16, 2018

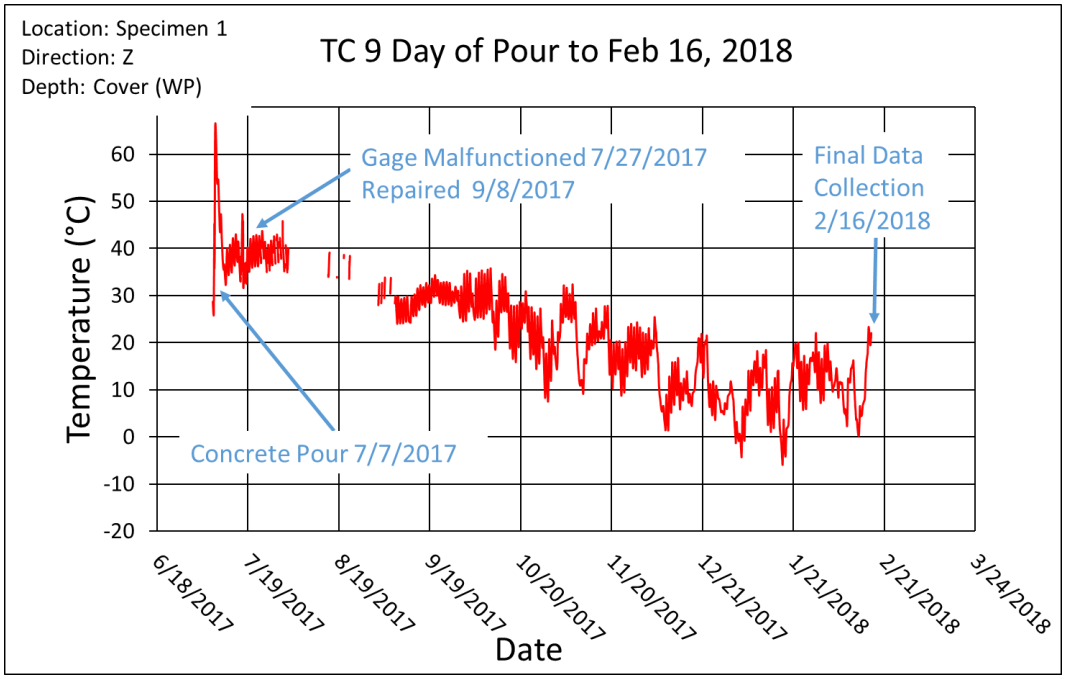

Figure 101 Thermocouple 9 Temperature Data from the Day of the Concrete Pour to February 16, 2018

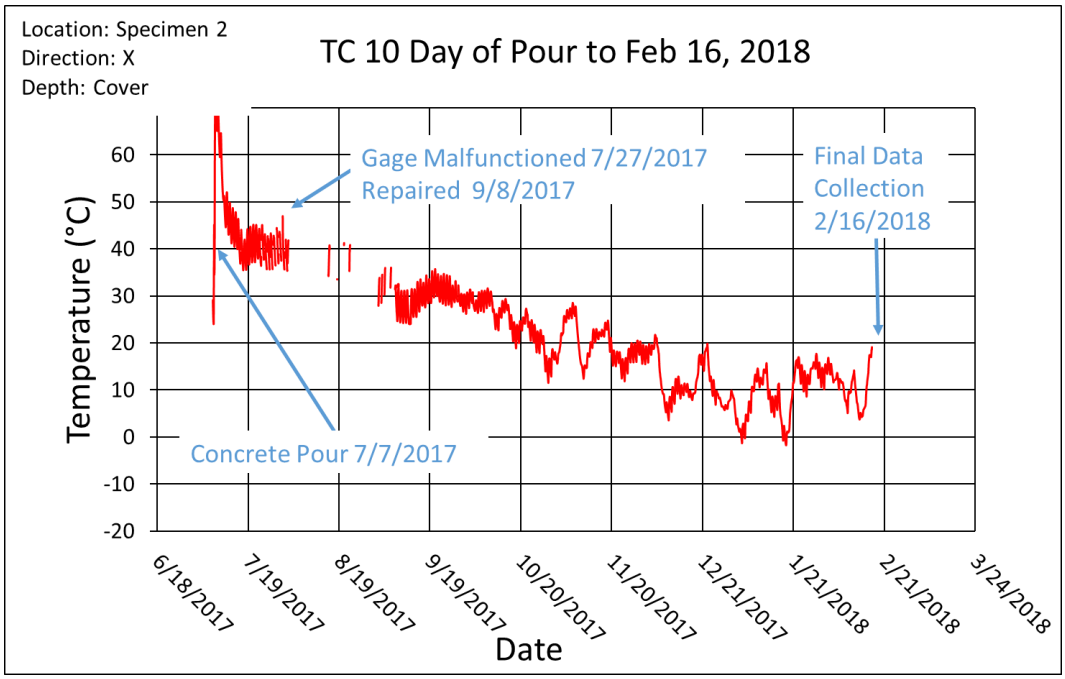

Figure 102 Thermocouple 10 Temperature Data from the Day of the Concrete Pour to February 16, 2018

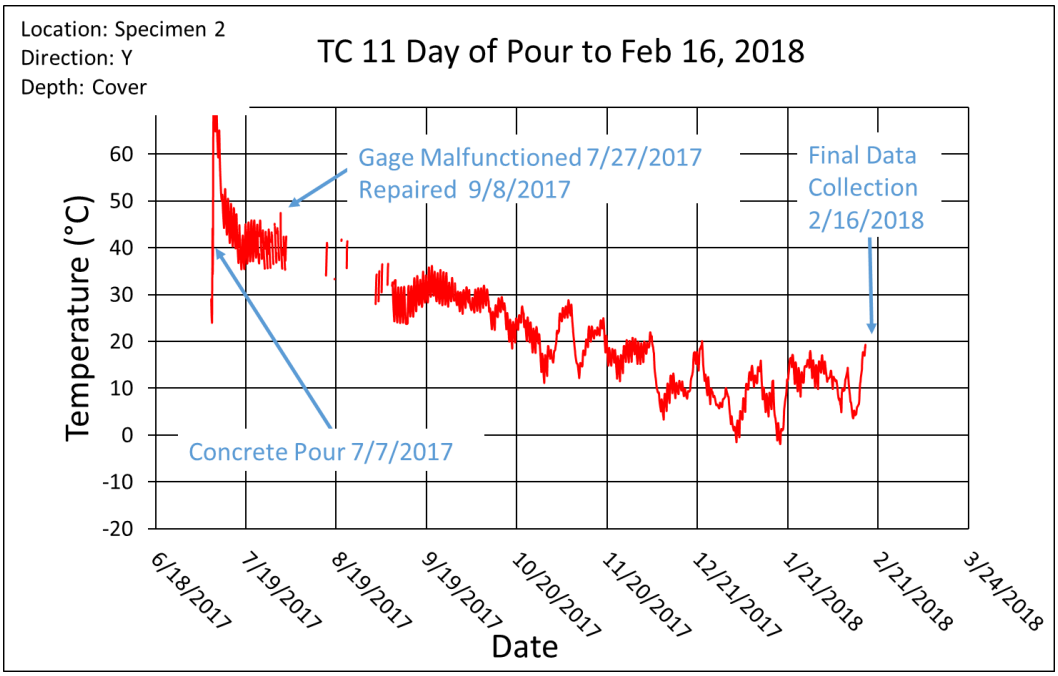

Figure 103 Thermocouple 11 Temperature Data from the Day of the Concrete Pour to February 16, 2018

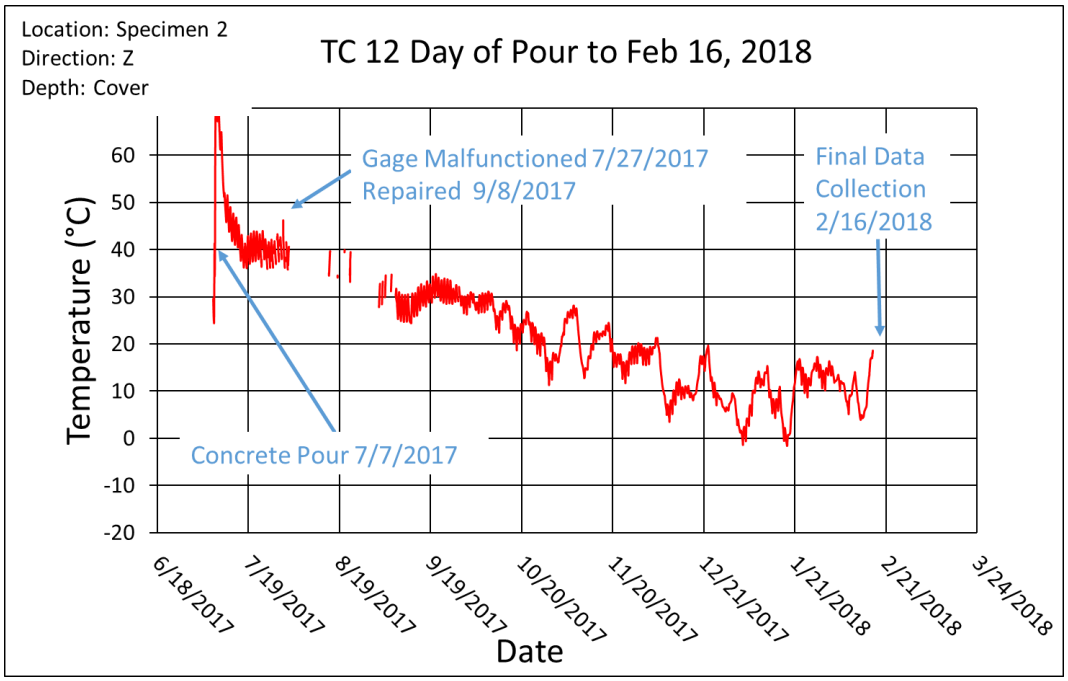

Figure 104 Thermocouple 12 Temperature Data from the Day of the Concrete Pour to February 16, 2018

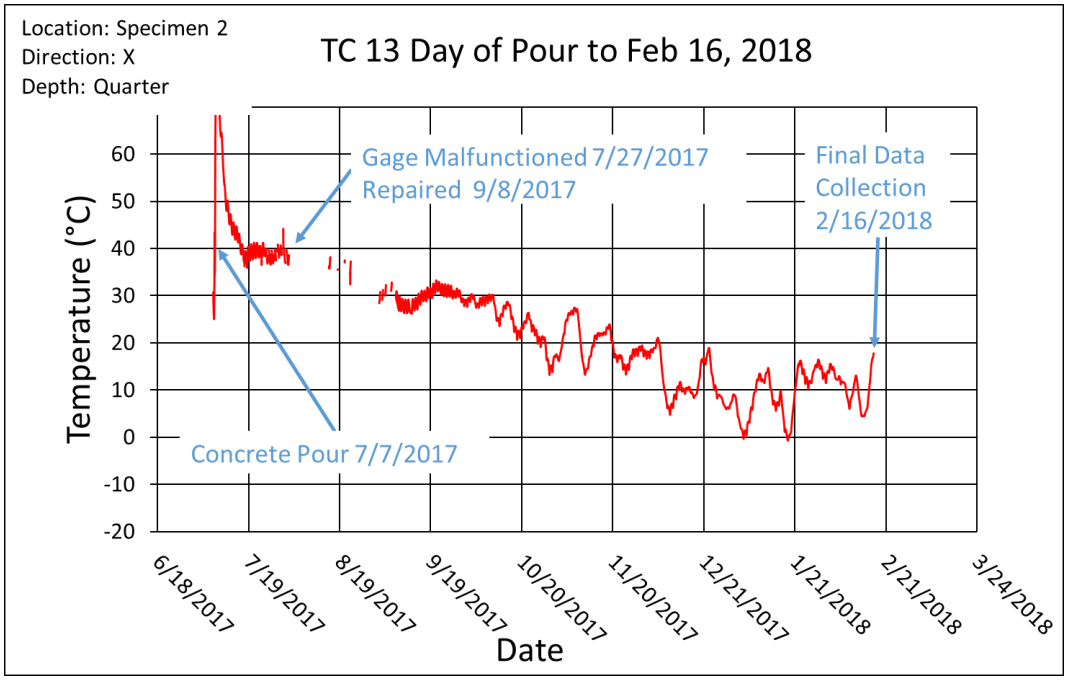

Figure 105 Thermocouple 13 Temperature Data from the Day of the Concrete Pour to February 16, 2018

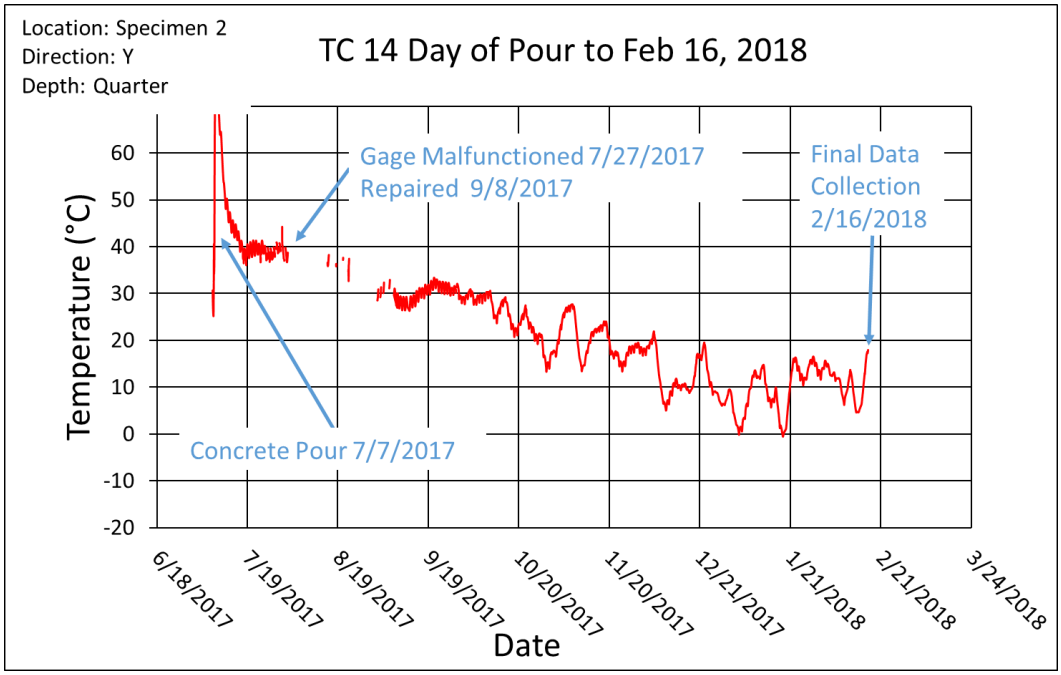

Figure 106 Thermocouple 14 Temperature Data from the Day of the Concrete Pour to February 16, 2018

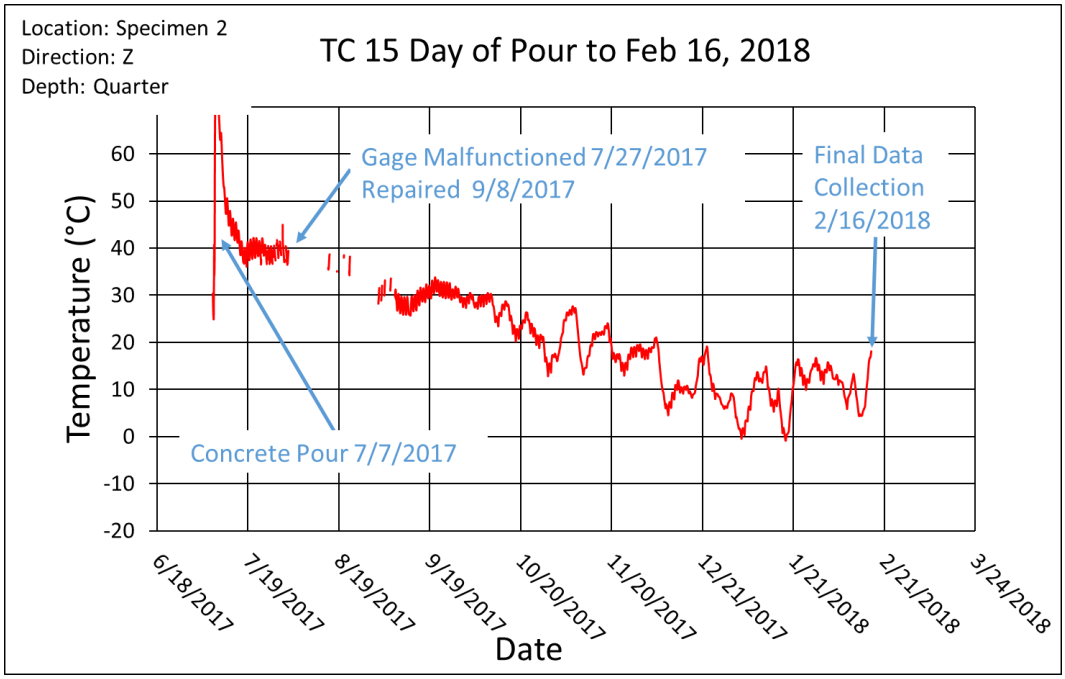

Figure 107 Thermocouple 15 Temperature Data from the Day of the Concrete Pour to February 16, 2018

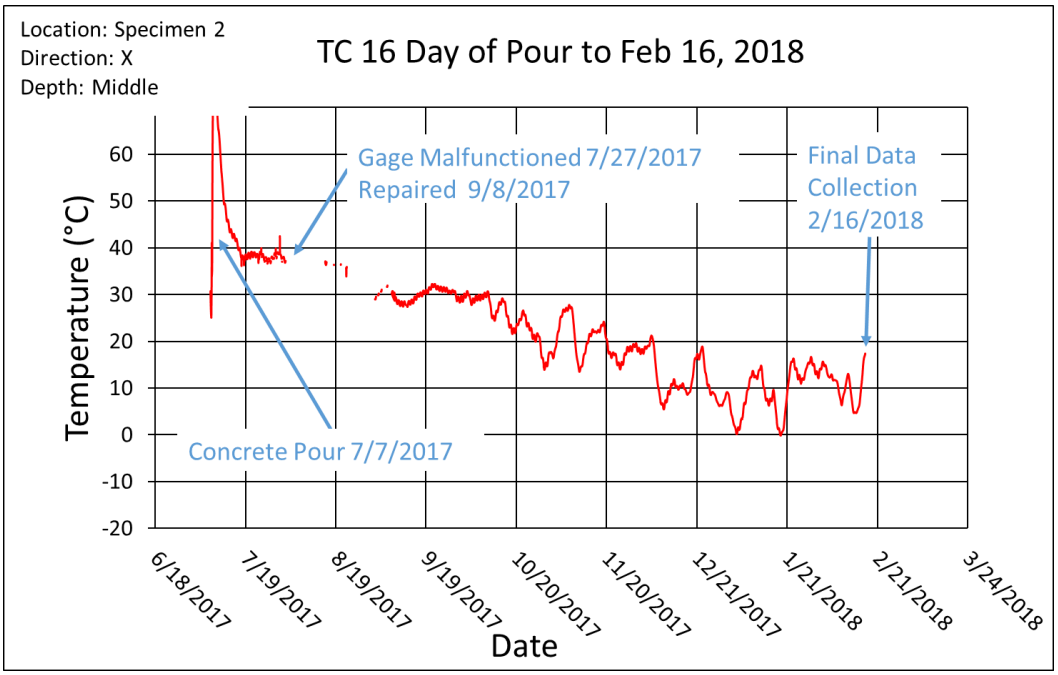

Figure 108 Thermocouple 16 Temperature Data from the Day of the Concrete Pour to February 16, 2018

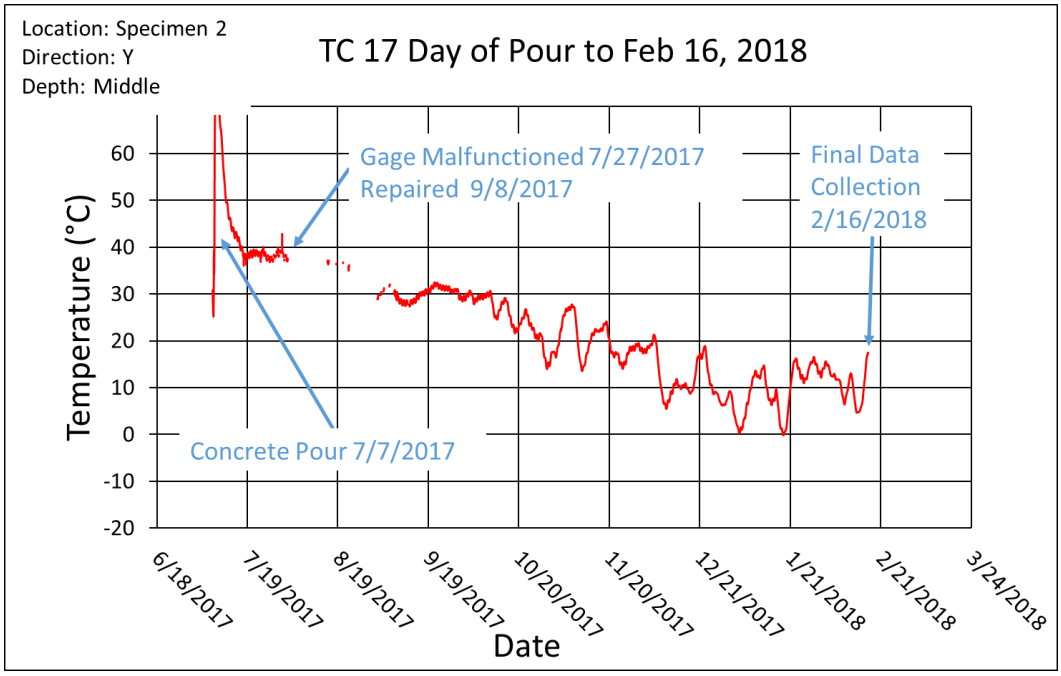

Figure 109 Thermocouple 17 Temperature Data from the Day of the Concrete Pour to February 16, 2018

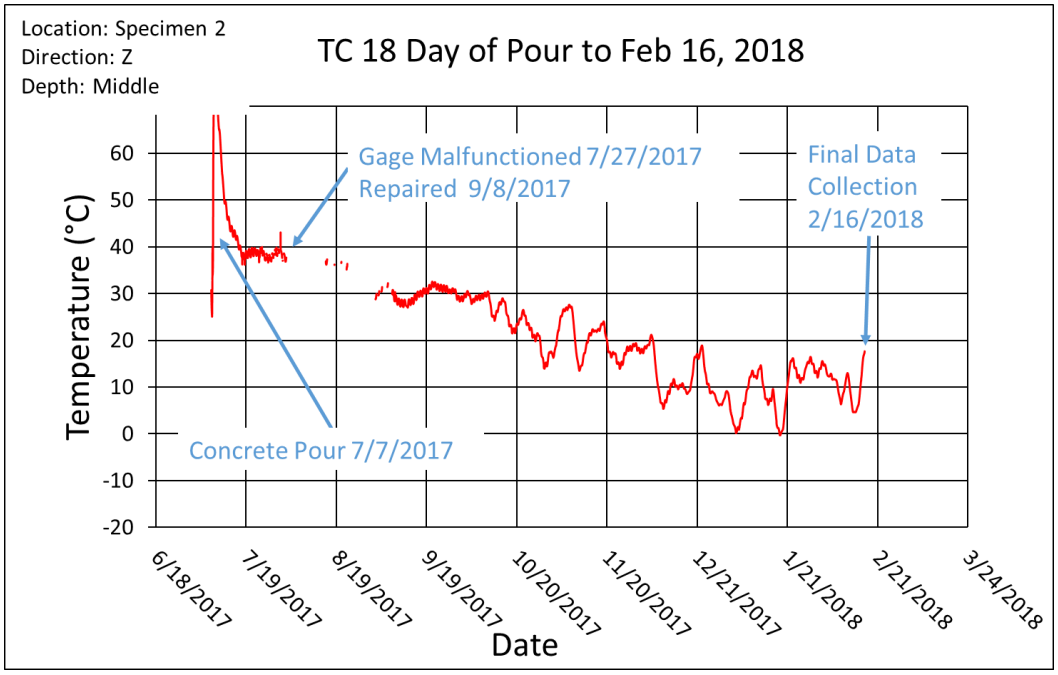

Figure 110 Thermocouple 18 Temperature Data from the Day of the Concrete Pour to February 16, 2018

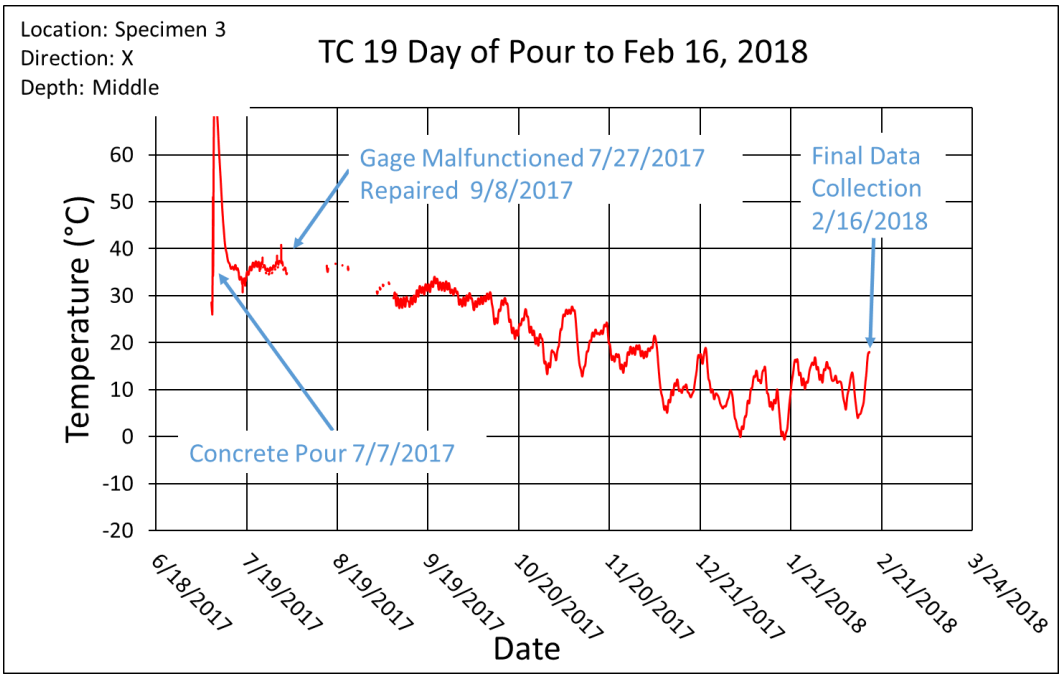

Figure 111 Thermocouple 19 Temperature Data from the Day of the Concrete Pour to February 16, 2018

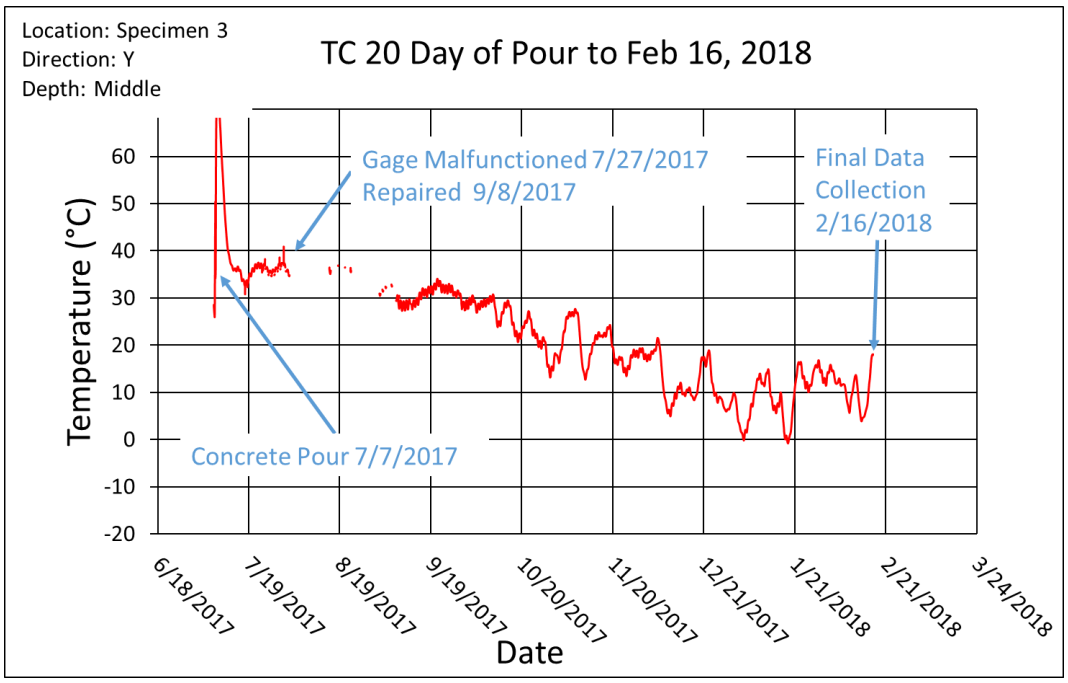

Figure 112 Thermocouple 20 Temperature Data from the Day of the Concrete Pour to February 16, 2018

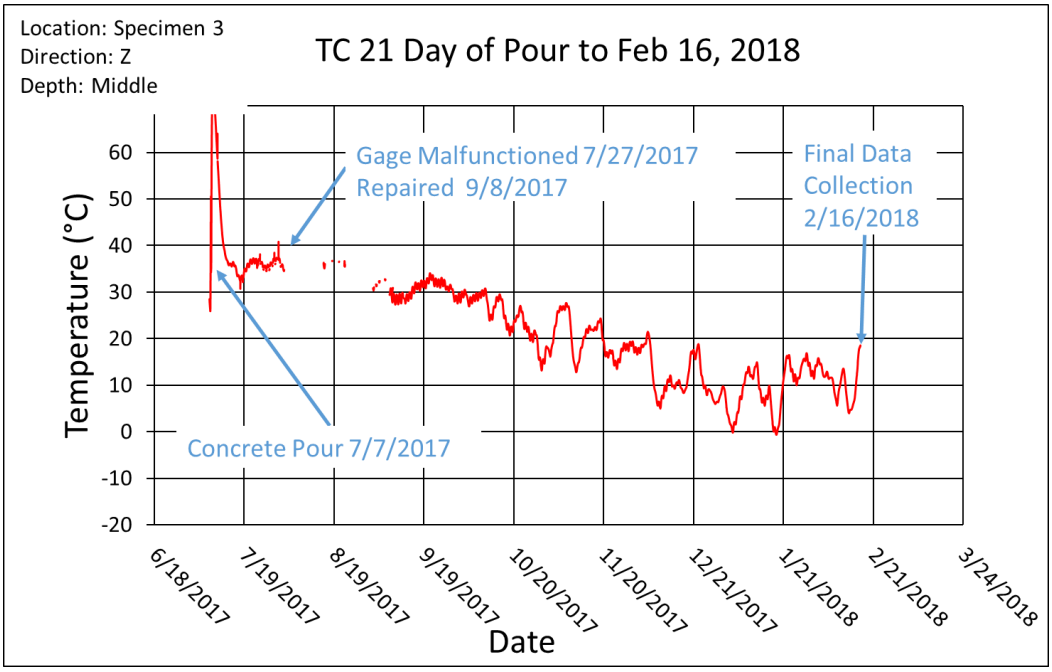

Figure 113 Thermocouple 21 Temperature Data from the Day of the Concrete Pour to February 16, 2018

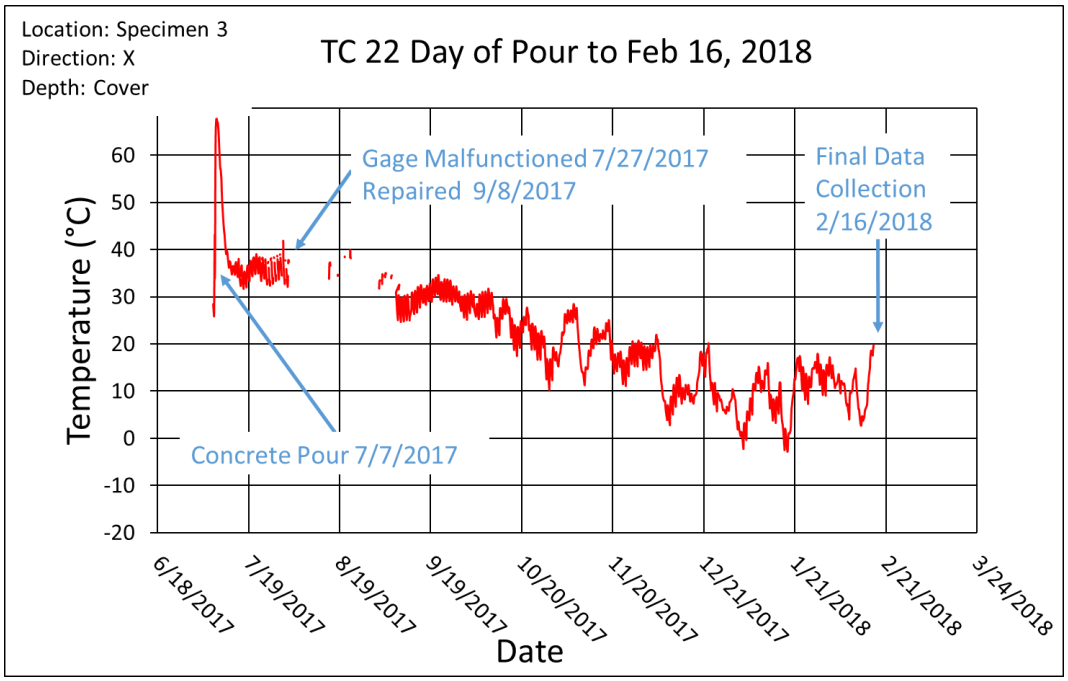

Figure 114 Thermocouple 22 Temperature Data from the Day of the Concrete Pour to February 16, 2018

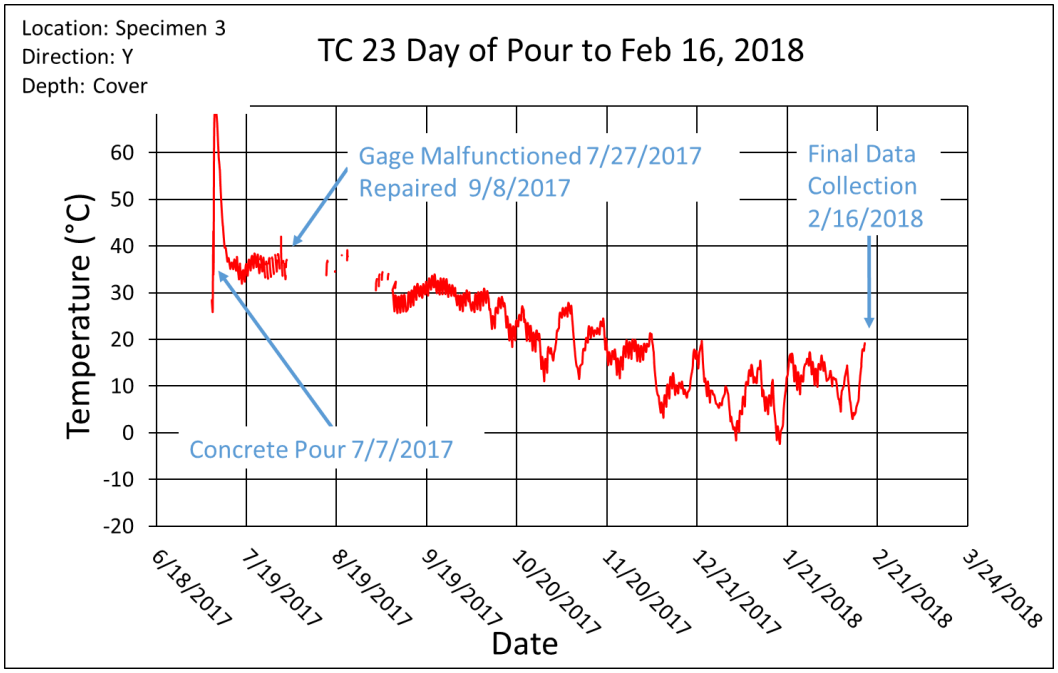

Figure 115 Thermocouple 23 Temperature Data from the Day of the Concrete Pour to February 16, 2018

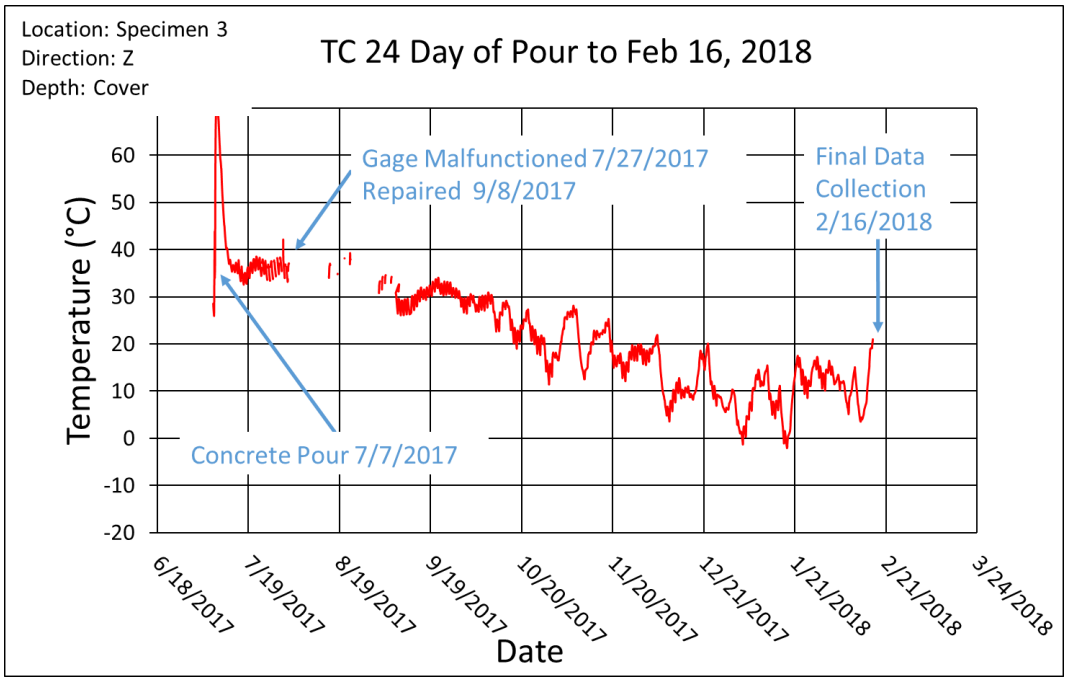

Figure 116 Thermocouple 24 Temperature Data from the Day of the Concrete Pour to February 16, 2018

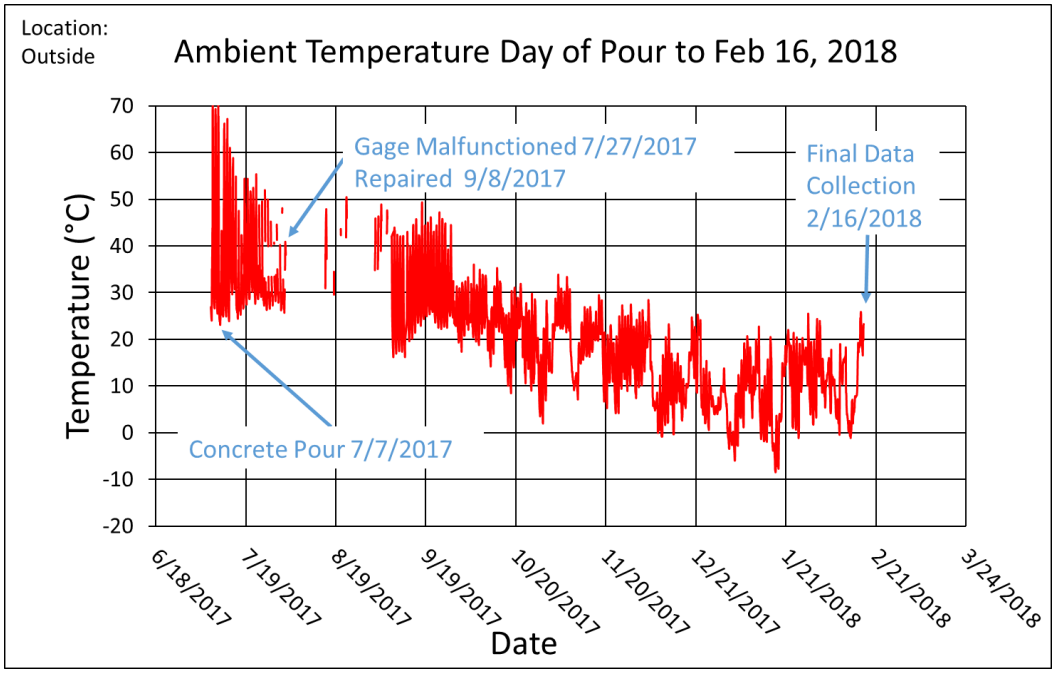

Figure 117 Ambient Temperature Data from the Day of the Concrete Pour to February 16, 2018

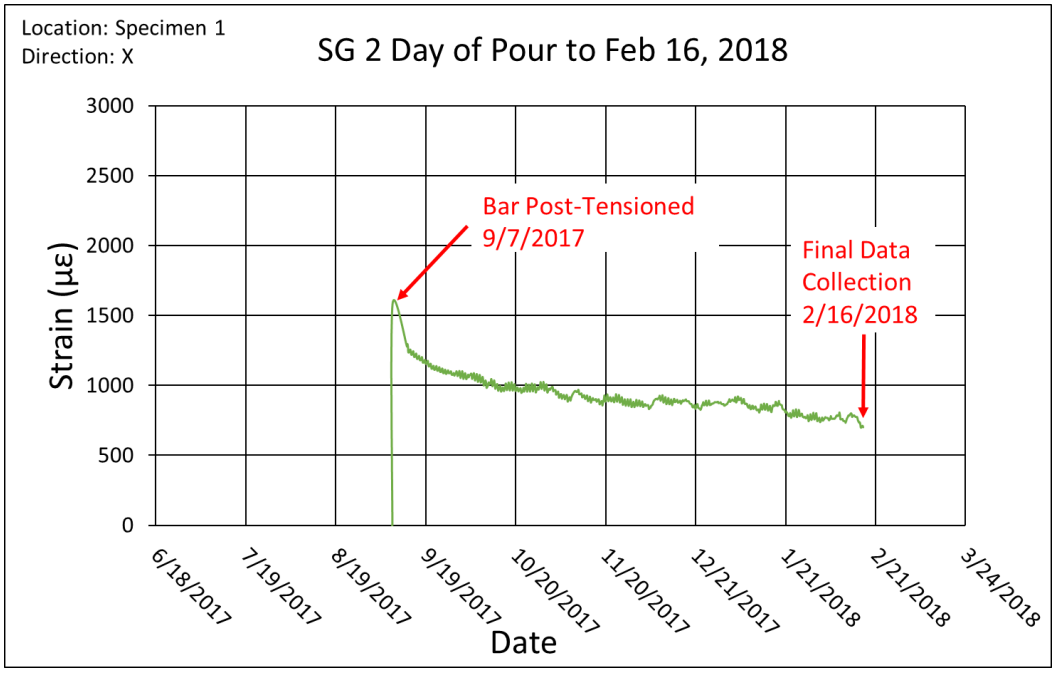

Figure 118 Post-Tensioning Bar Strain Gage 2 Strain Data from the Day of the Concrete Pour to February 16, 2018

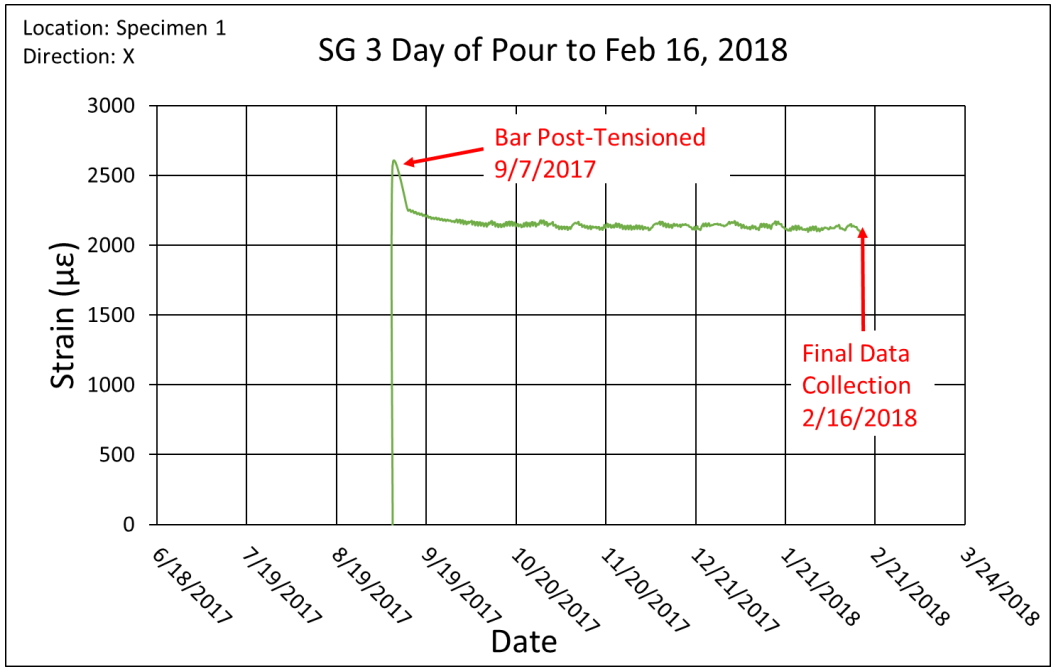

Figure 119 Post-Tensioning Bar Strain Gage 3 Strain Data from the Day of the Concrete Pour to February 16, 2018

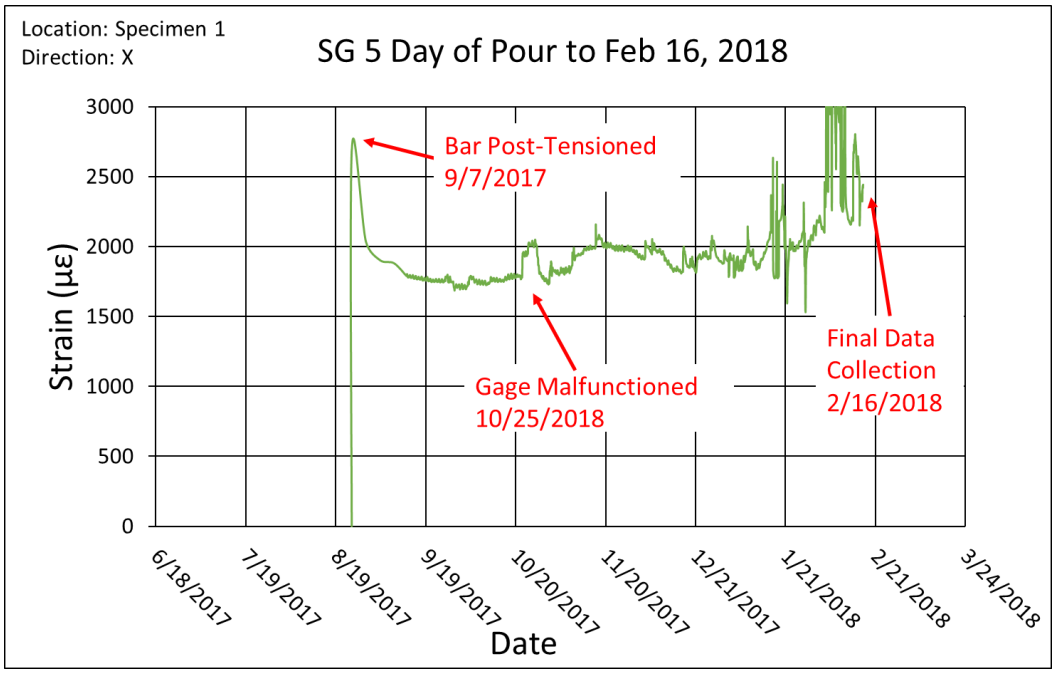

Figure 120 Post-Tensioning Bar Strain Gage 5 Strain Data from the Day of the Concrete Pour to February 16, 2018

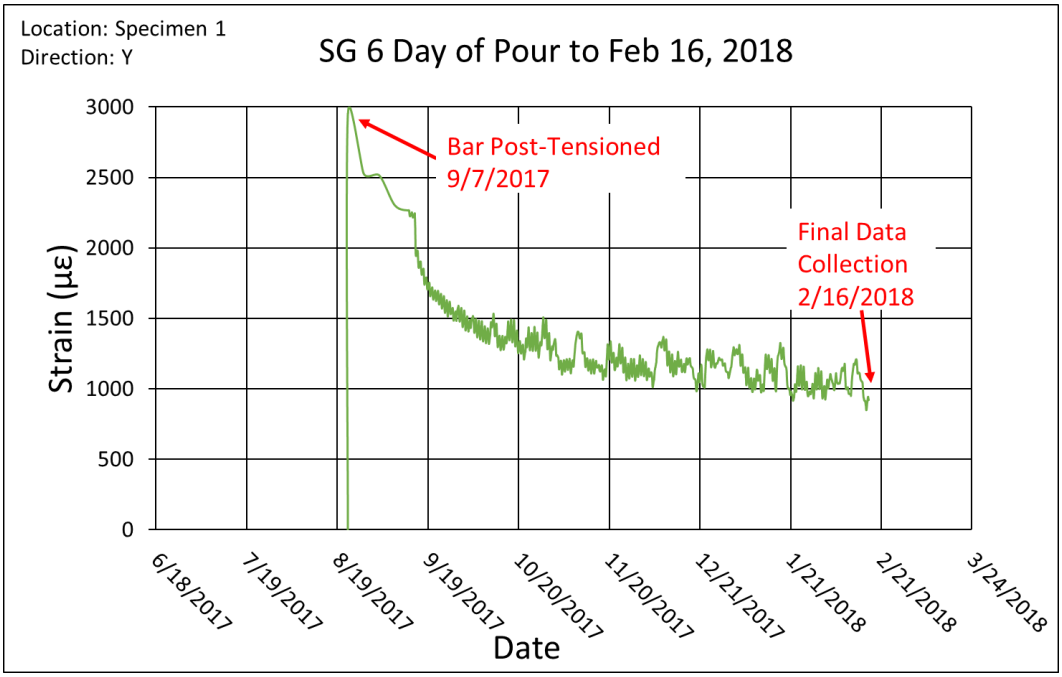

Figure 121 Post-Tensioning Bar Strain Gage 6 Strain Data from the Day of the Concrete Pour to February 16, 2018

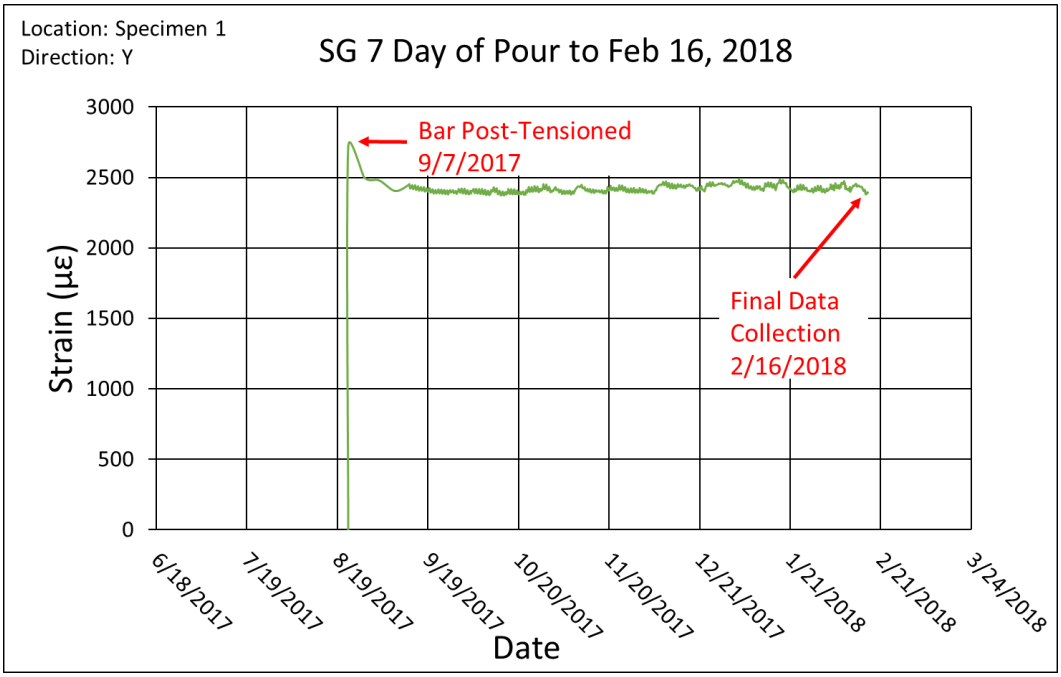

Figure 122 Post-Tensioning Bar Strain Gage 7 Strain Data from the Day of the Concrete Pour to February 16, 2018

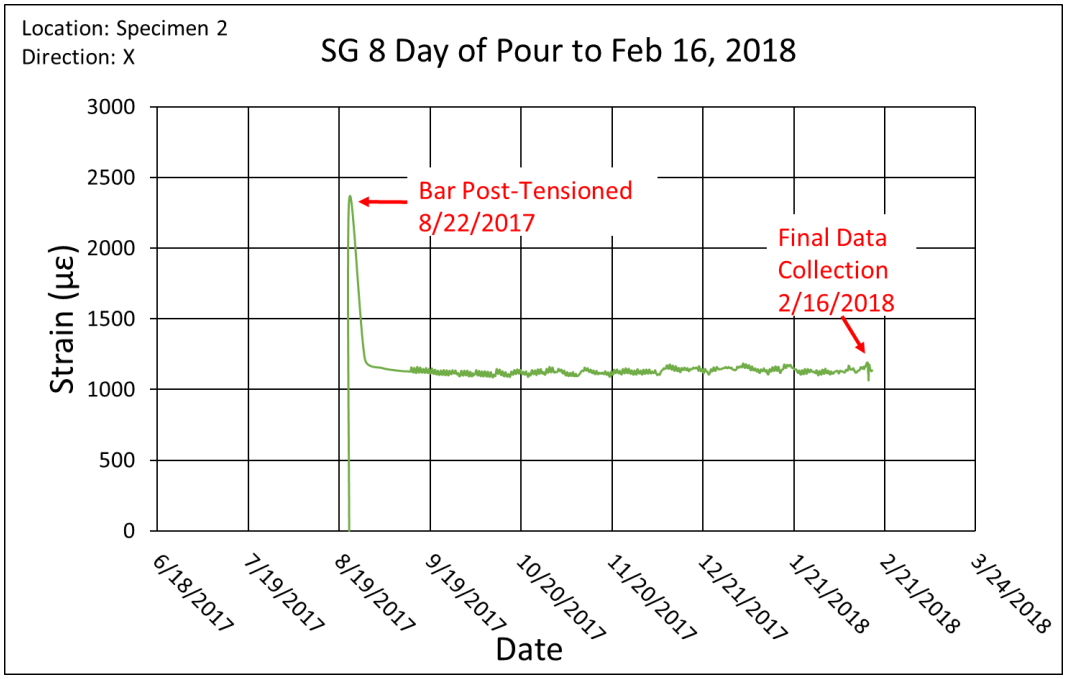

Figure 123 Post-Tensioning Bar Strain Gage 8 Strain Data from the Day of the Concrete Pour to February 16, 2018

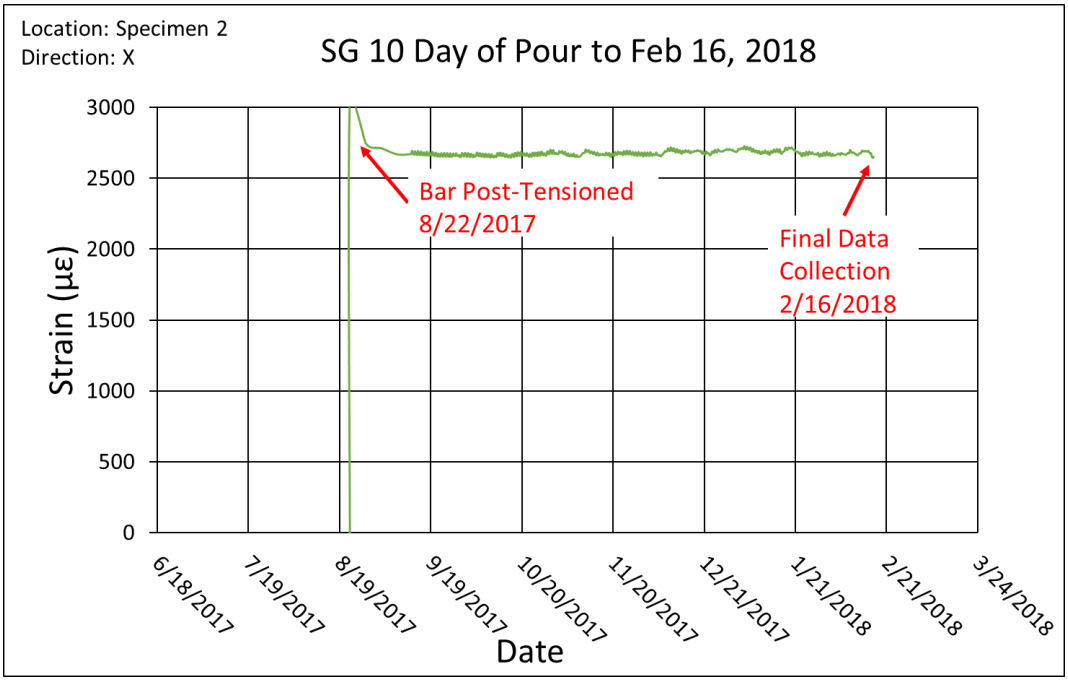

Figure 124 Post-Tensioning Bar Strain Gage 10 Strain Data from the Day of the Concrete Pour to February 16, 2018

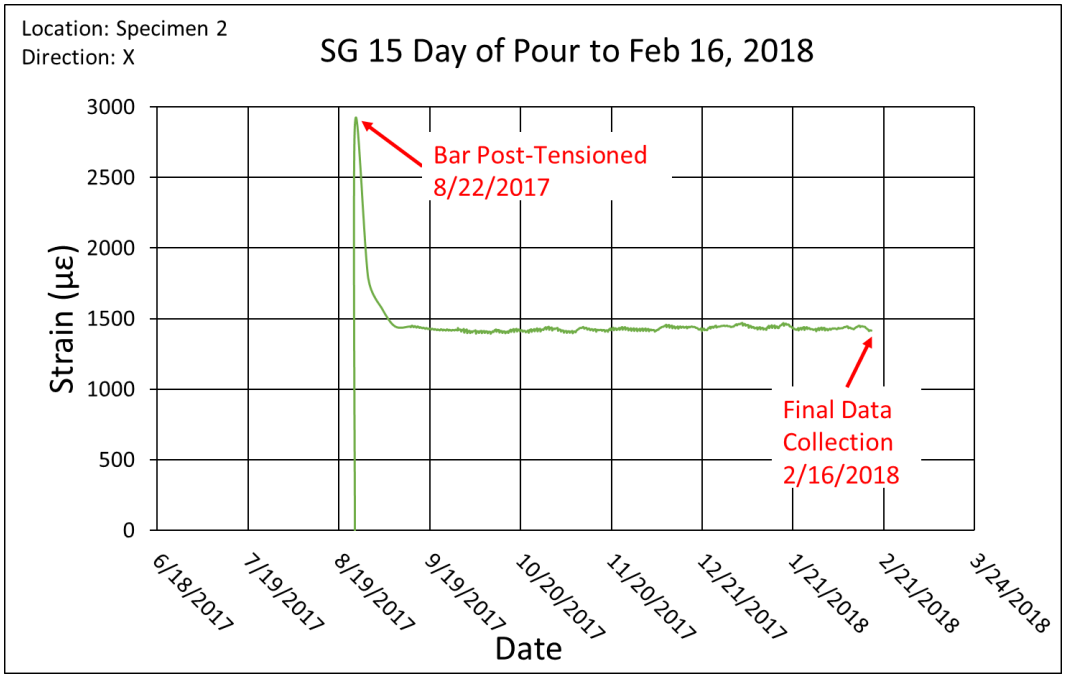

Figure 125 Post-Tensioning Bar Strain Gage 15 Strain Data from the Day of the Concrete Pour to February 16, 2018

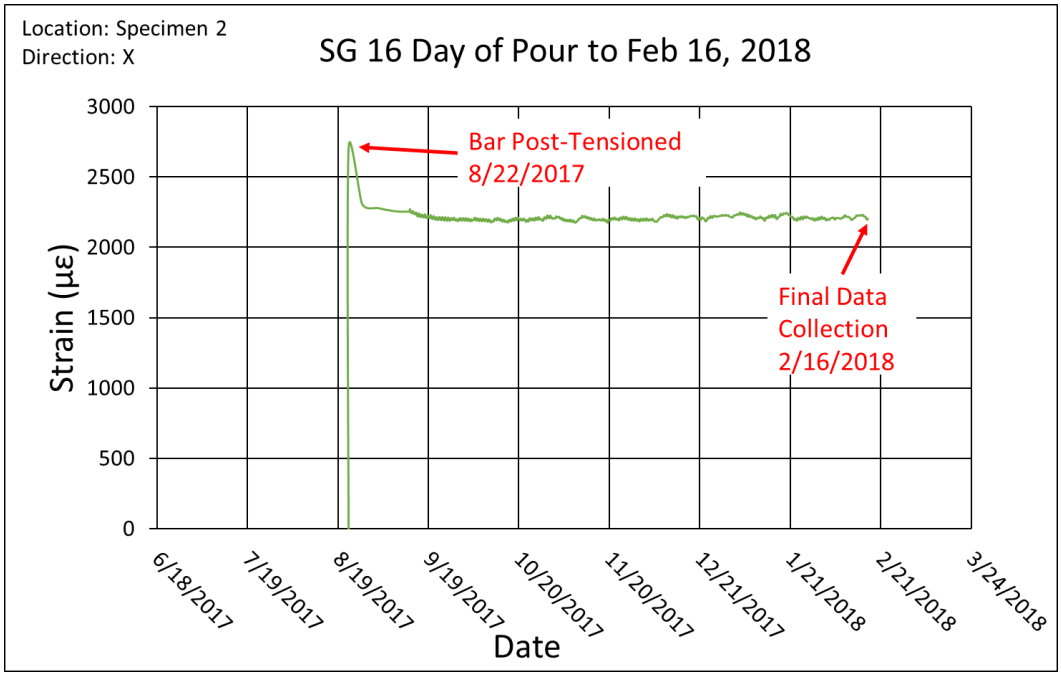

Figure 126 Post-Tensioning Bar Strain Gage 16 Strain Data from the Day of the Concrete Pour to February 16, 2018

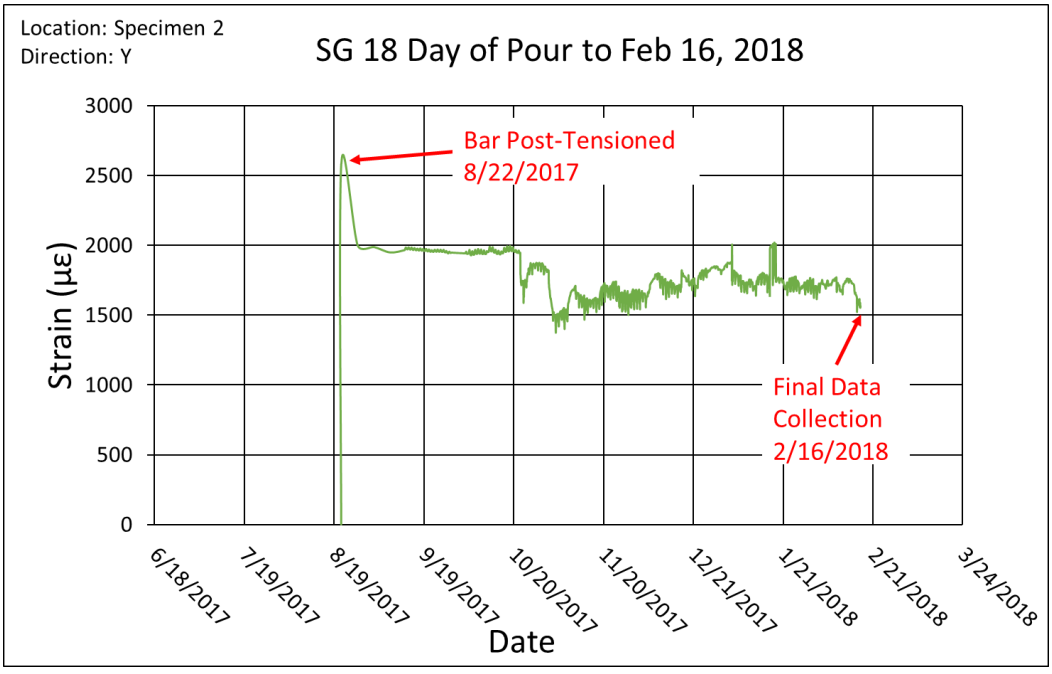

Figure 127 Post-Tensioning Bar Strain Gage 18 Strain Data from the Day of the Concrete Pour to February 16, 2018

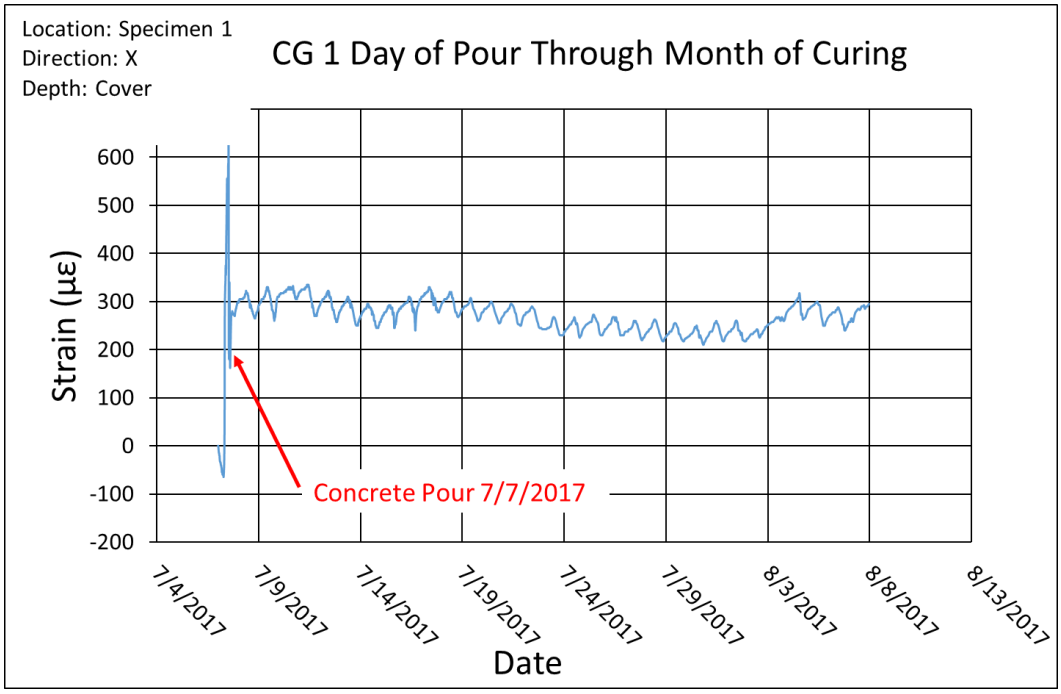

Figure 128 Concrete Gage 1 Strain Data from the Day Concrete was Poured Through One Month of Curing

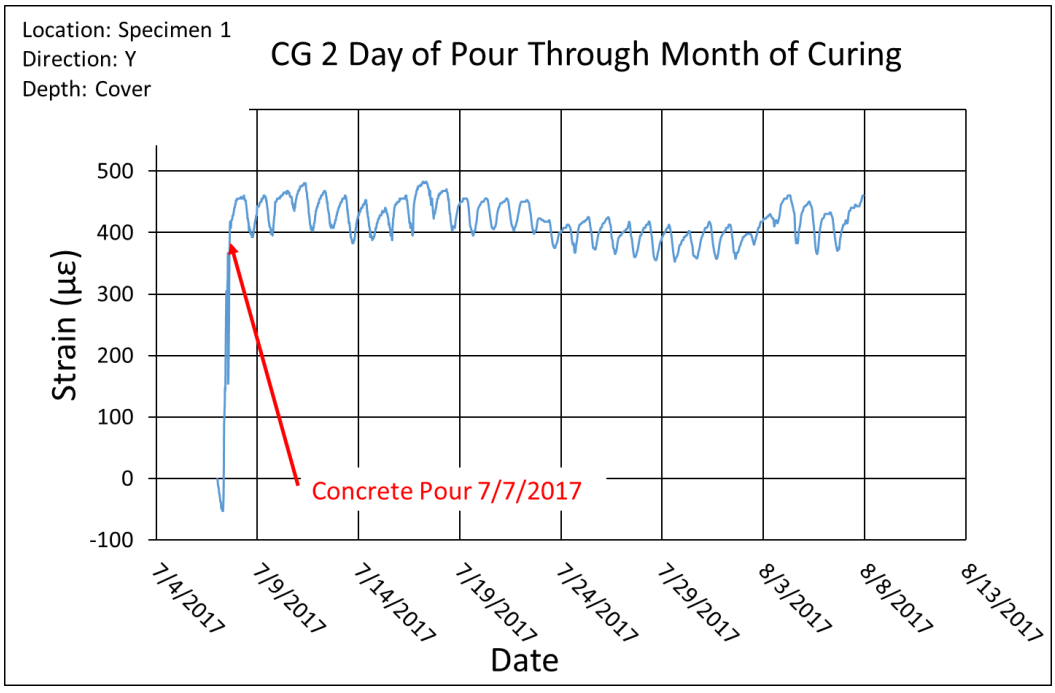

Figure 129 Concrete Gage 2 Strain Data from the Day Concrete was Poured Through One Month of Curing

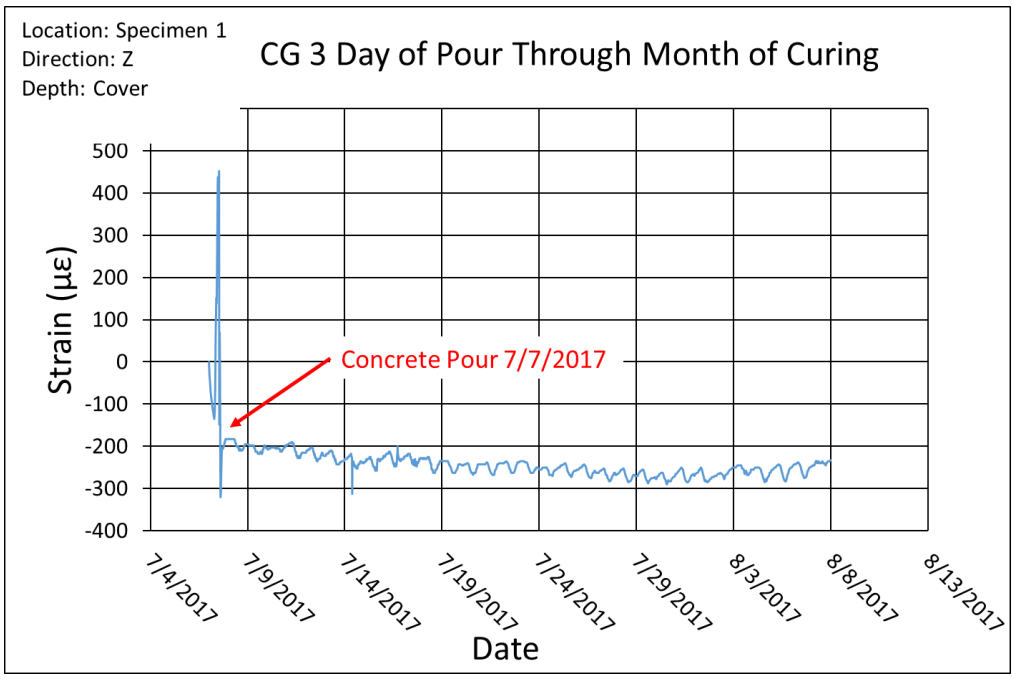

Figure 130 Concrete Gage 3 Strain Data from the Day Concrete was Poured Through One Month of Curing

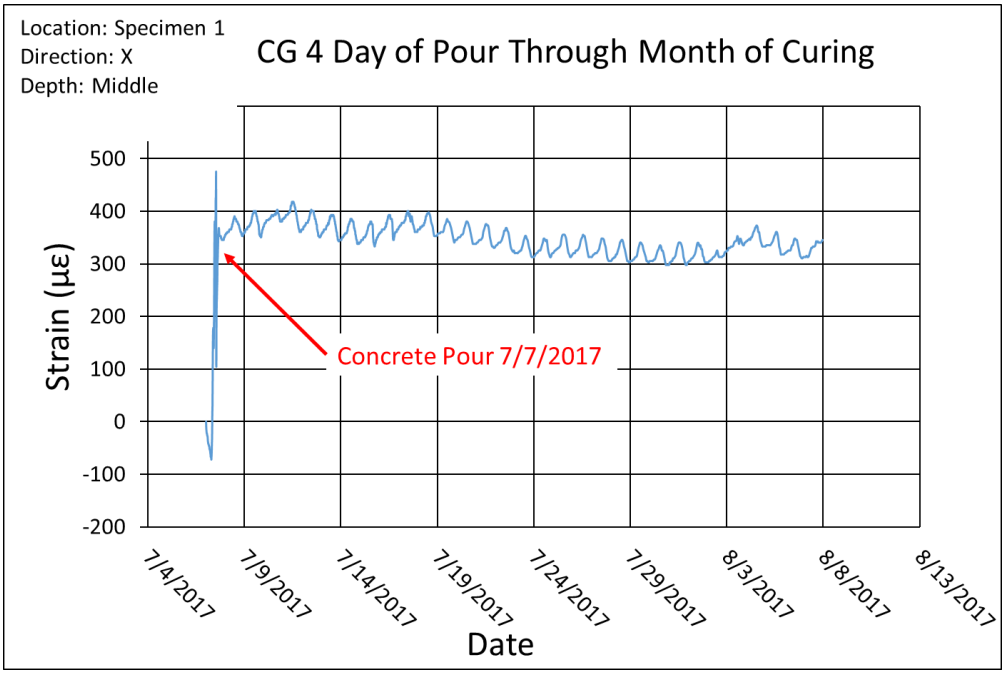

Figure 131 Concrete Gage 4 Strain Data from the Day Concrete was Poured Through One Month of Curing

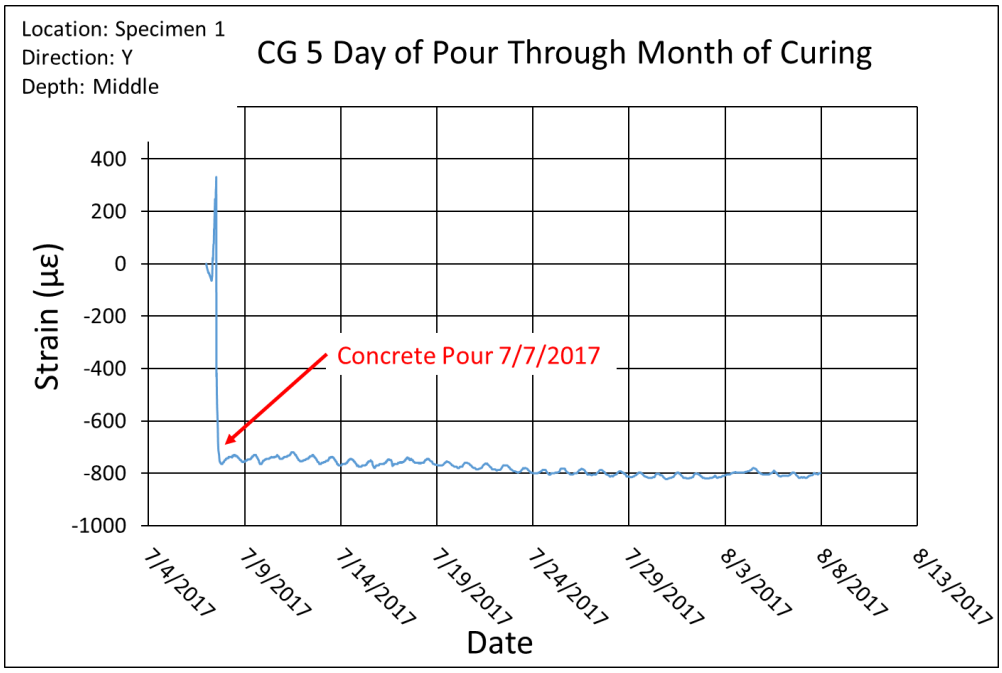

Figure 132 Concrete Gage 5 Strain Data from the Day Concrete was Poured Through One Month of Curing

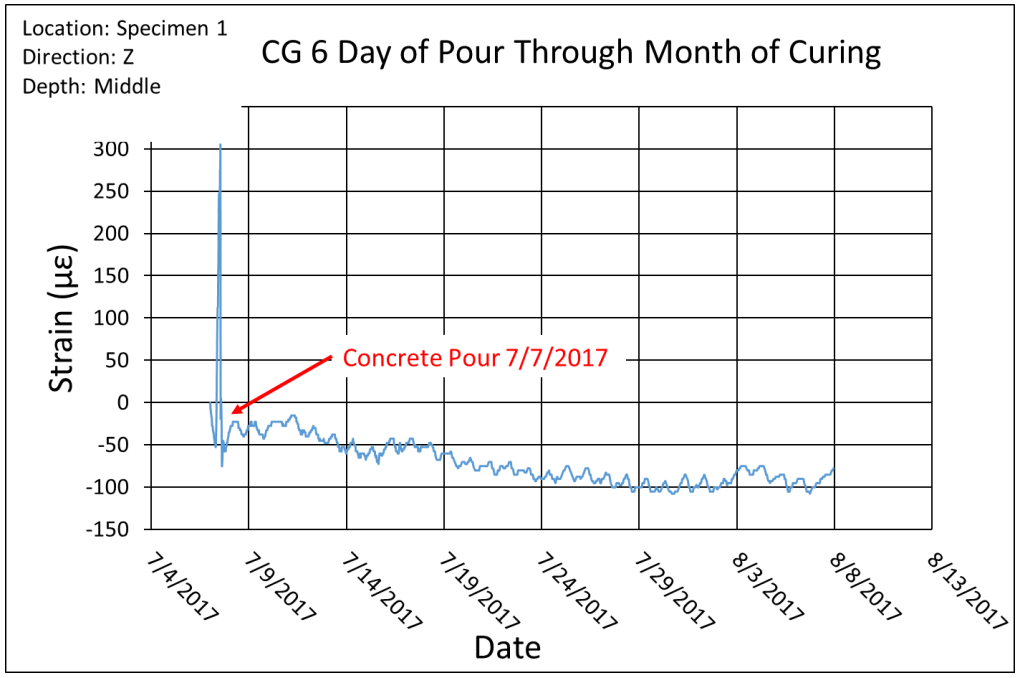

Figure 133 Concrete Gage 6 Strain Data from the Day Concrete was Poured Through One Month of Curing

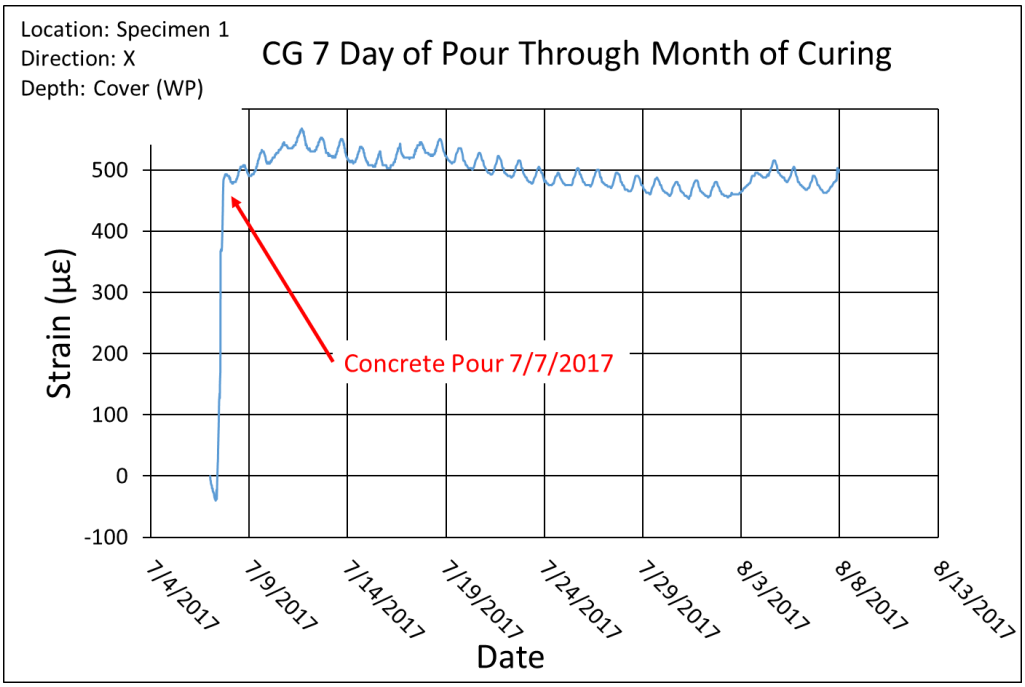

Figure 134 Concrete Gage 7 Strain Data from the Day Concrete was Poured Through One Month of Curing

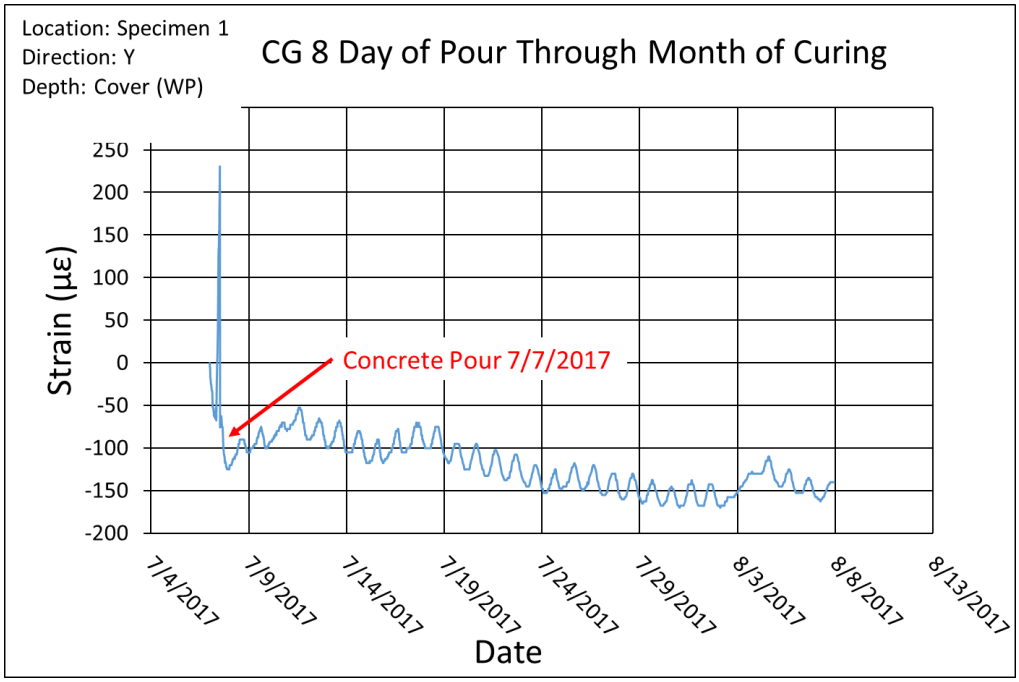

Figure 135 Concrete Gage 8 Strain Data from the Day Concrete was Poured Through One Month of Curing

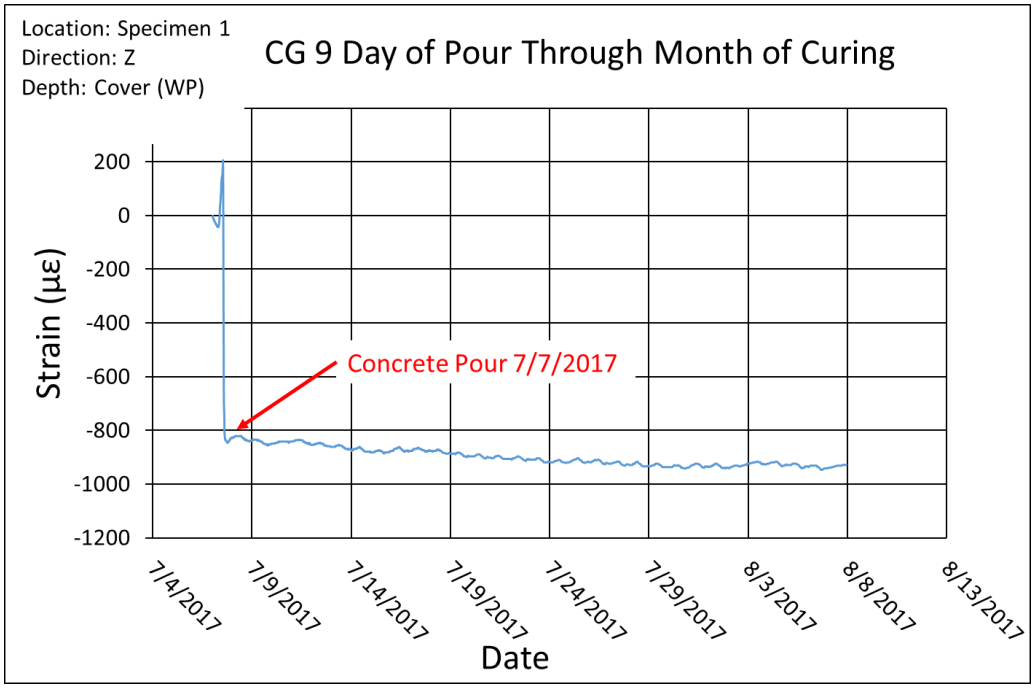

Figure 136 Concrete Gage 9 Strain Data from the Day Concrete was Poured Through One Month of Curing

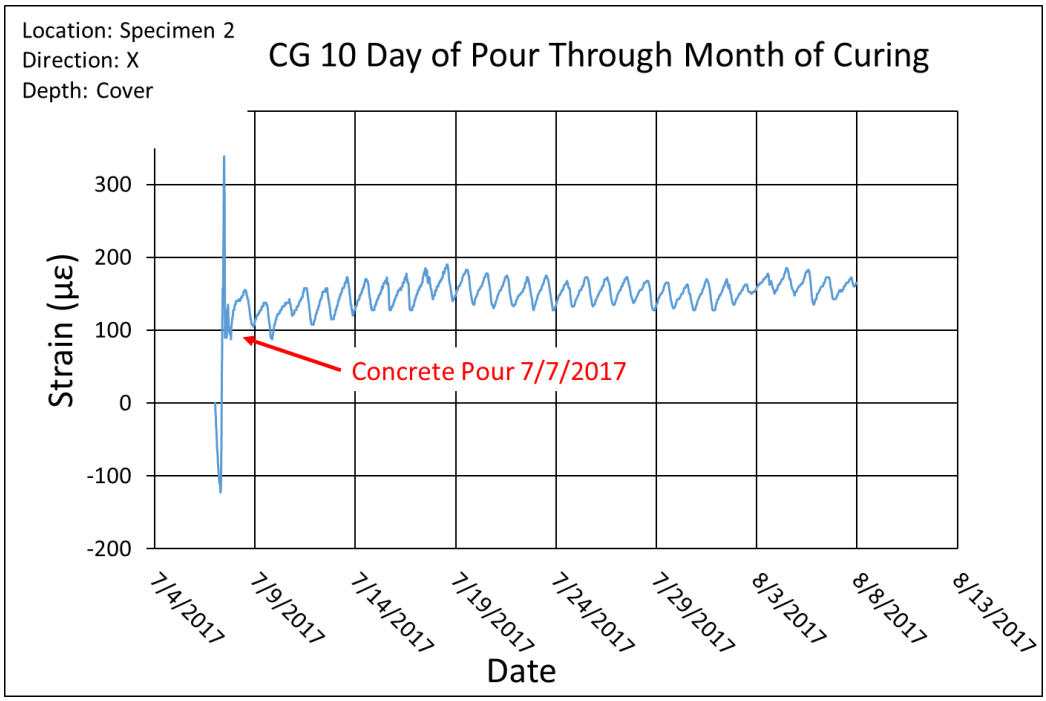

Figure 137 Concrete Gage 10 Strain Data from the Day Concrete was Poured Through One Month of Curing

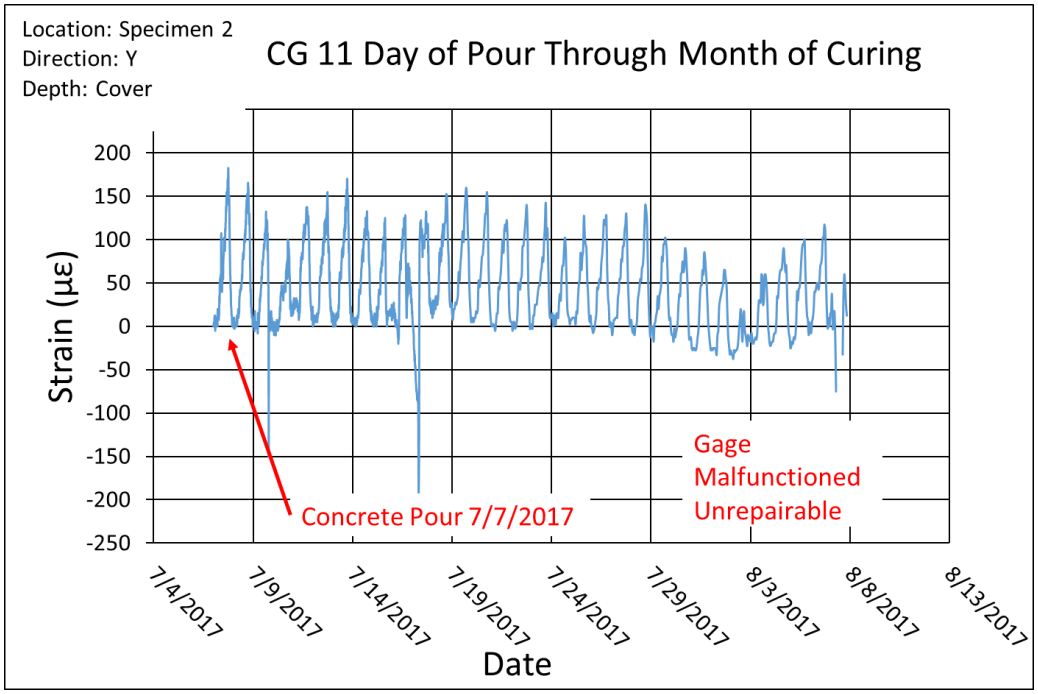

Figure 138 Concrete Gage 11 Strain Data from the Day Concrete was Poured Through One Month of Curing

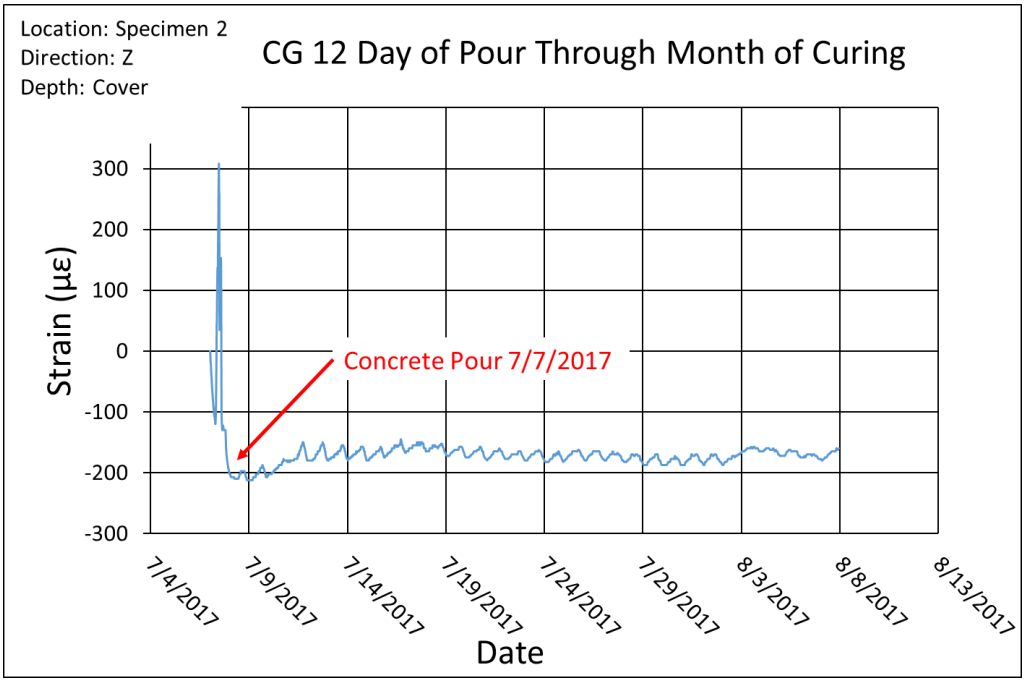

Figure 139 Concrete Gage 12 Strain Data from the Day Concrete was Poured Through One Month of Curing

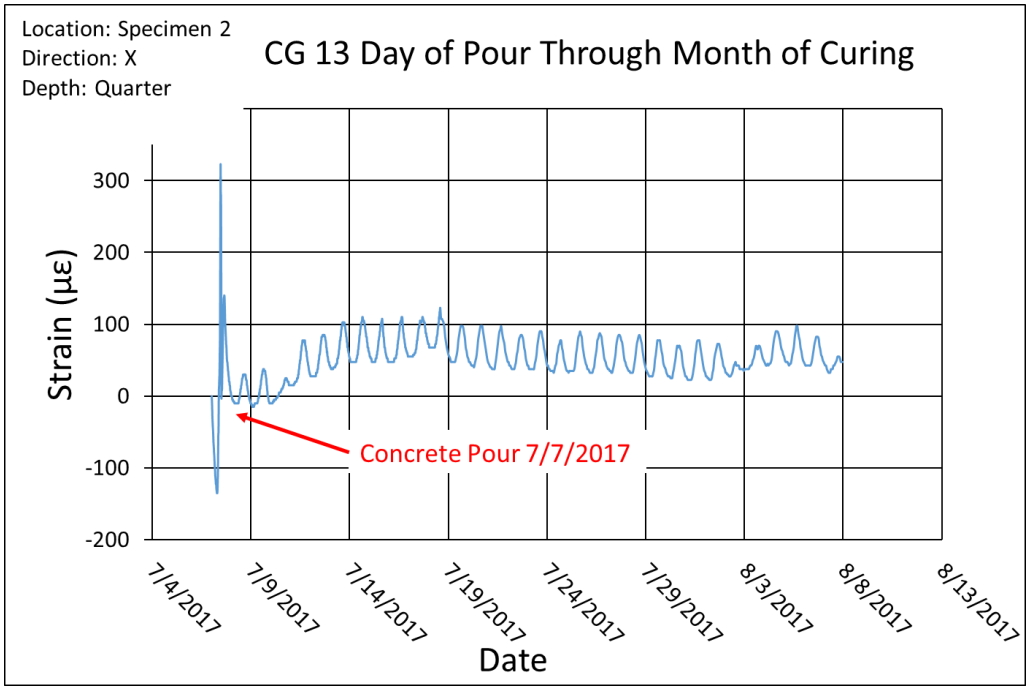

Figure 140 Concrete Gage 13 Strain Data from the Day Concrete was Poured Through One Month of Curing

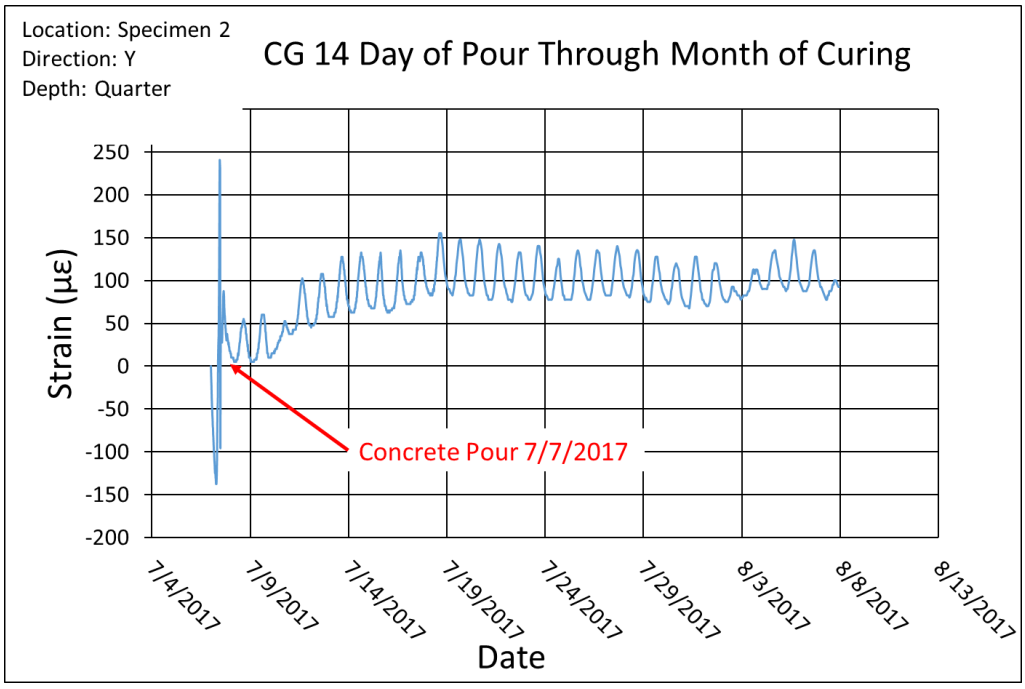

Figure 141 Concrete Gage 14 Strain Data from the Day Concrete was Poured Through One Month of Curing

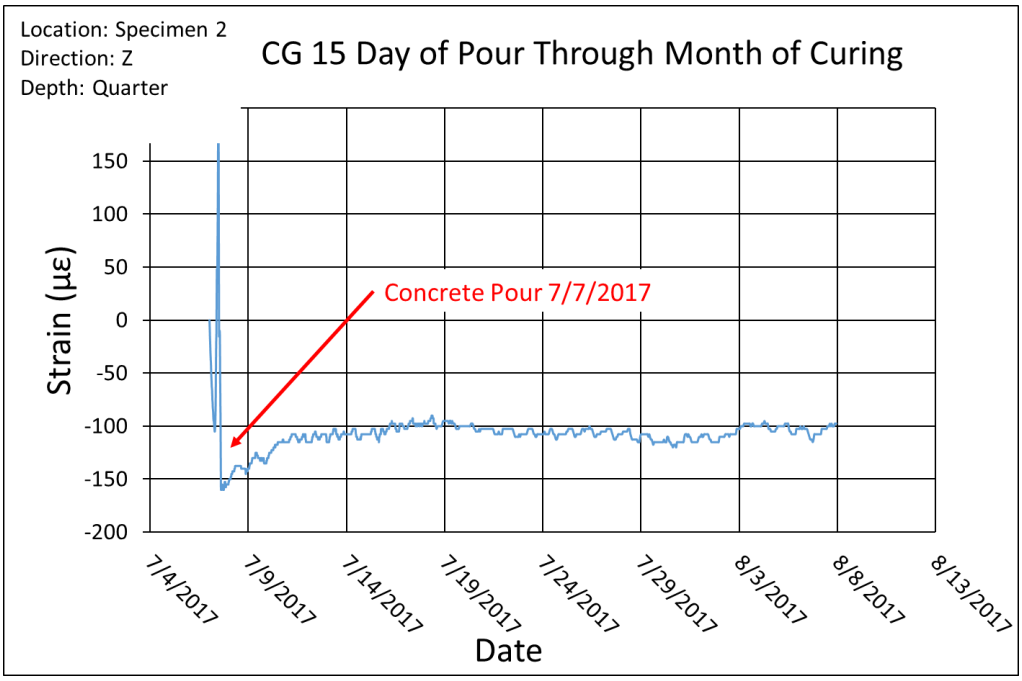

Figure 142 Concrete Gage 15 Strain Data from the Day Concrete was Poured Through One Month of Curing

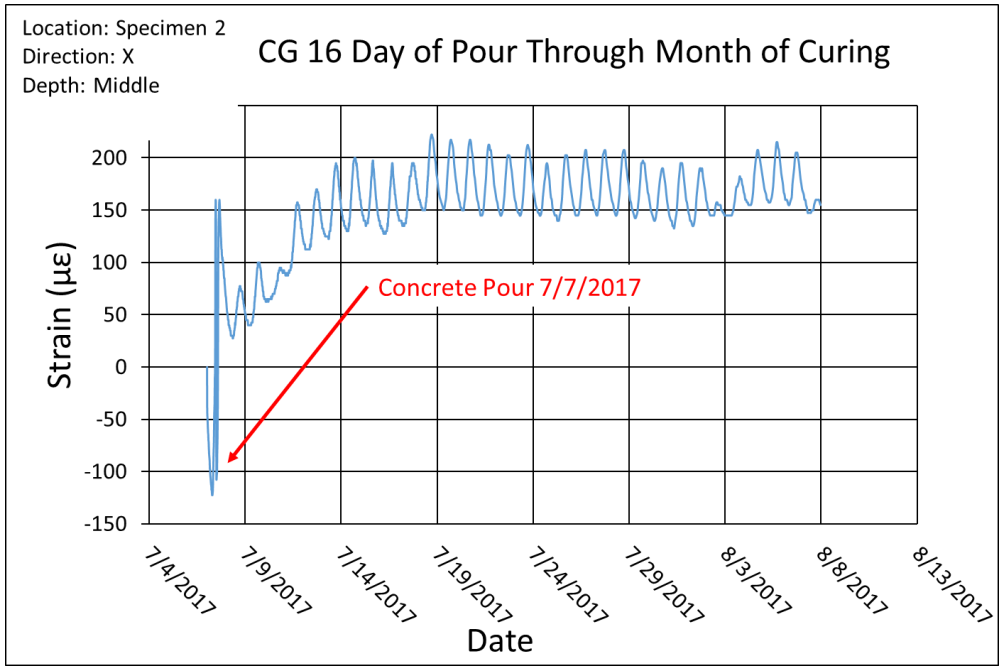

Figure 143 Concrete Gage 16 Strain Data from the Day Concrete was Poured Through One Month of Curing

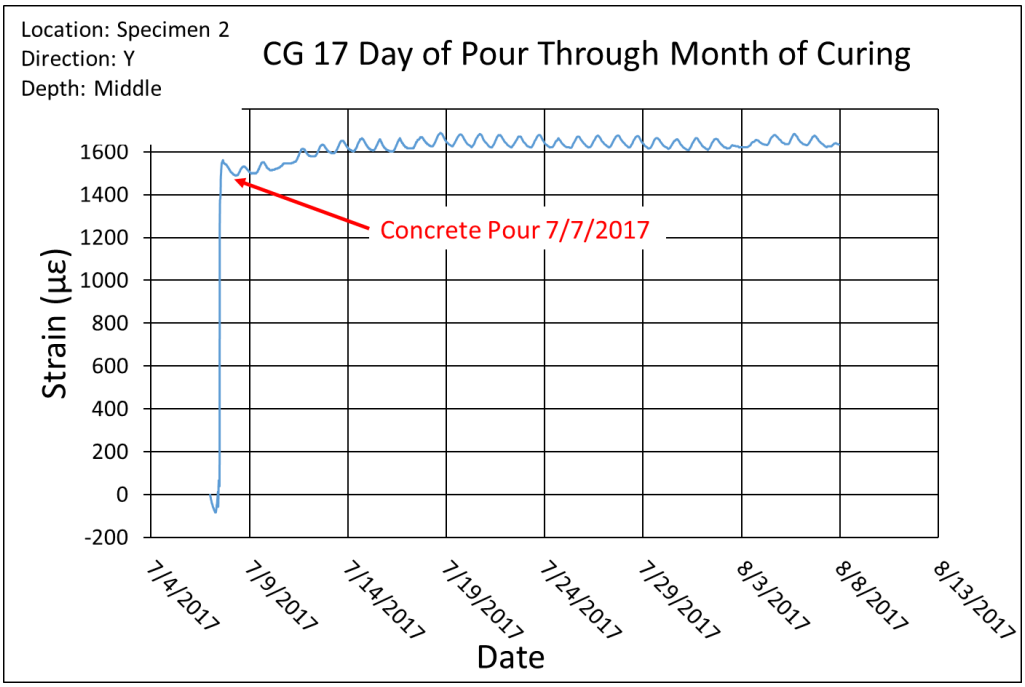

Figure 144 Concrete Gage 17 Strain Data from the Day Concrete was Poured Through One Month of Curing

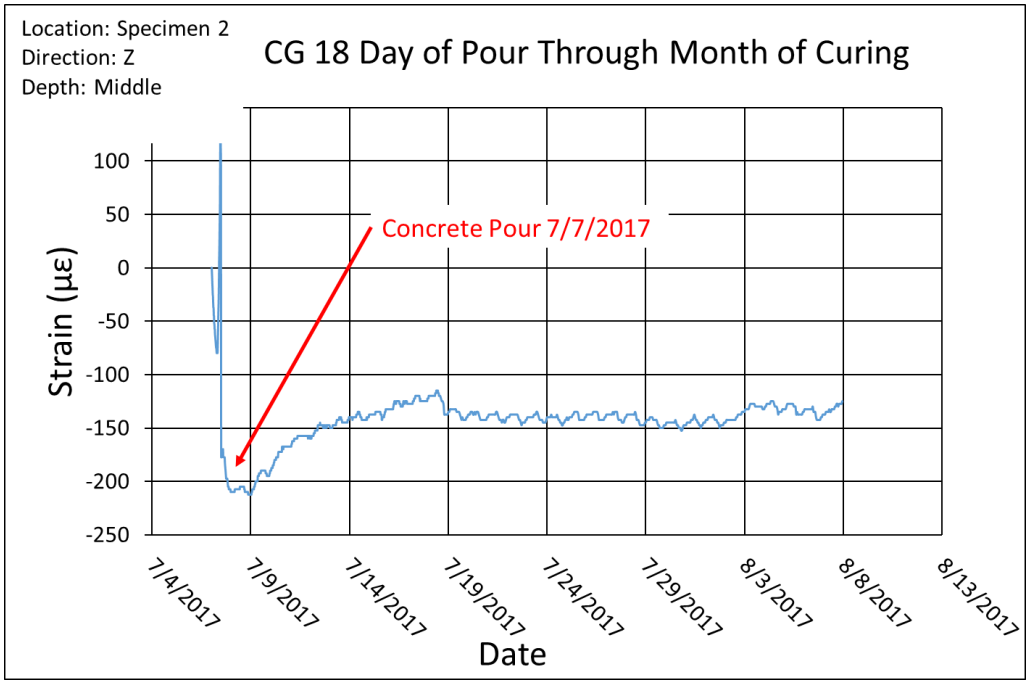

Figure 145 Concrete Gage 18 Strain Data from the Day Concrete was Poured Through One Month of Curing

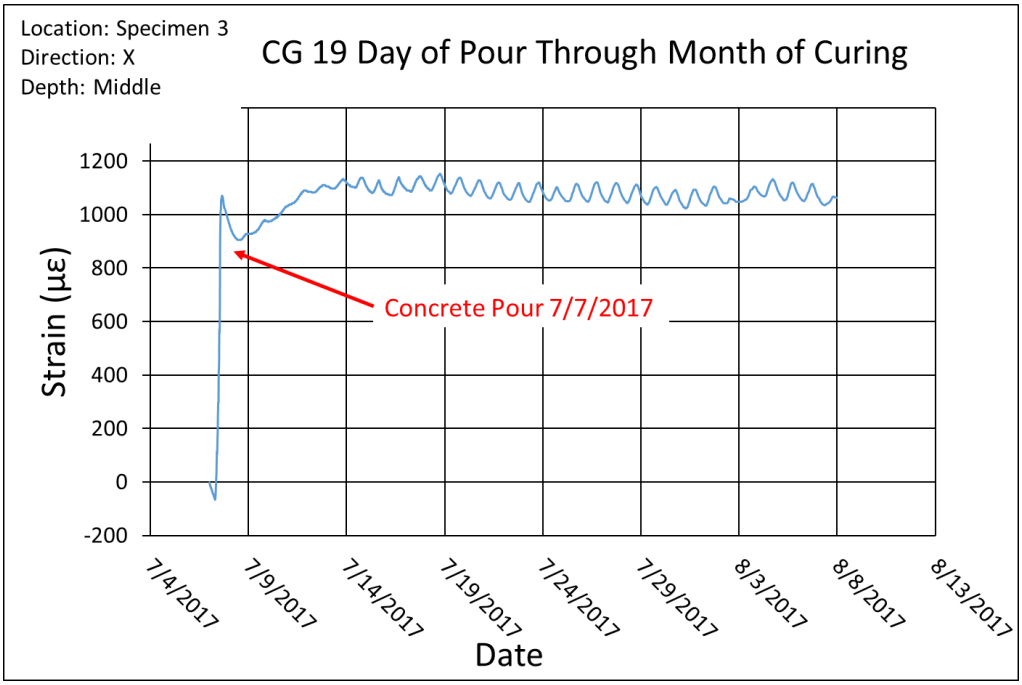

Figure 146 Concrete Gage 19 Strain Data from the Day Concrete was Poured Through One Month of Curing

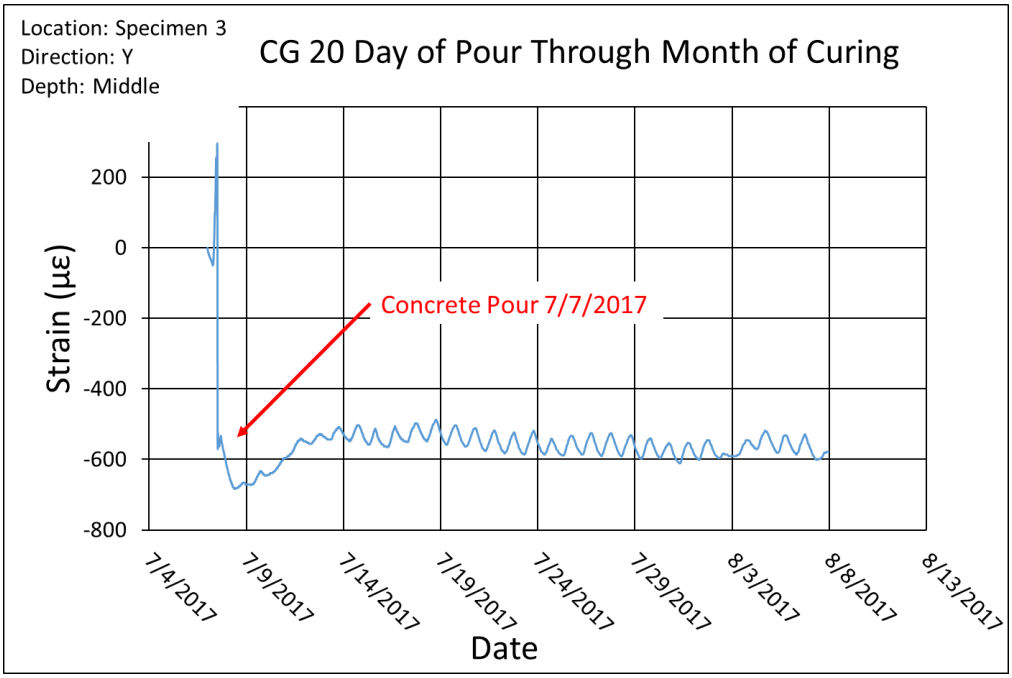

Figure 147 Concrete Gage 20 Strain Data from the Day Concrete was Poured Through One Month of Curing

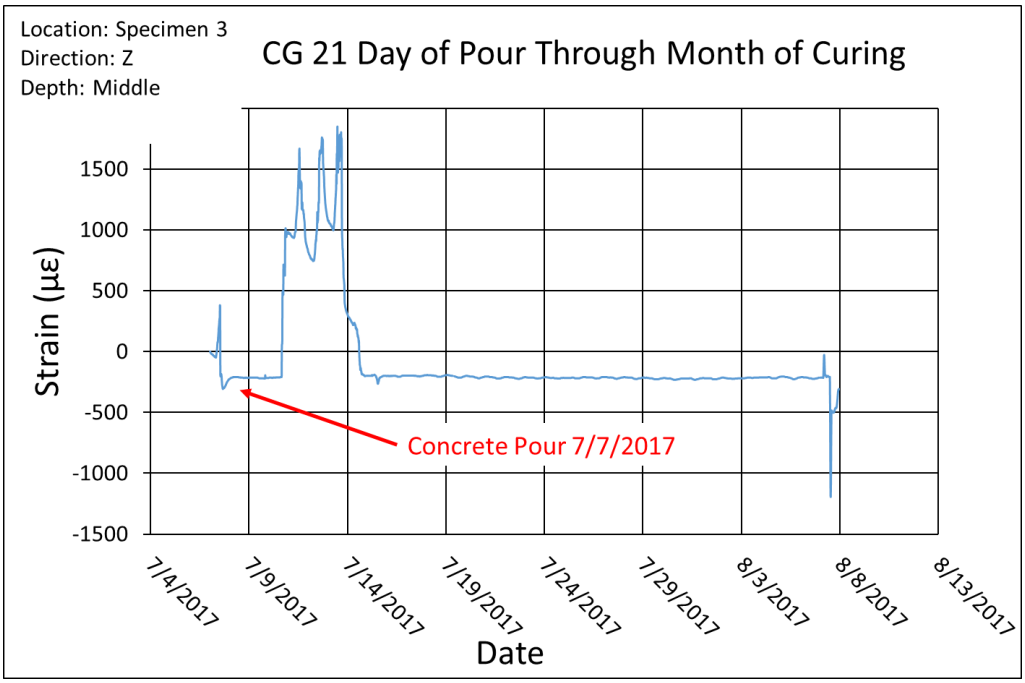

Figure 148 Concrete Gage 21 Strain Data from the Day Concrete was Poured Through One Month of Curing

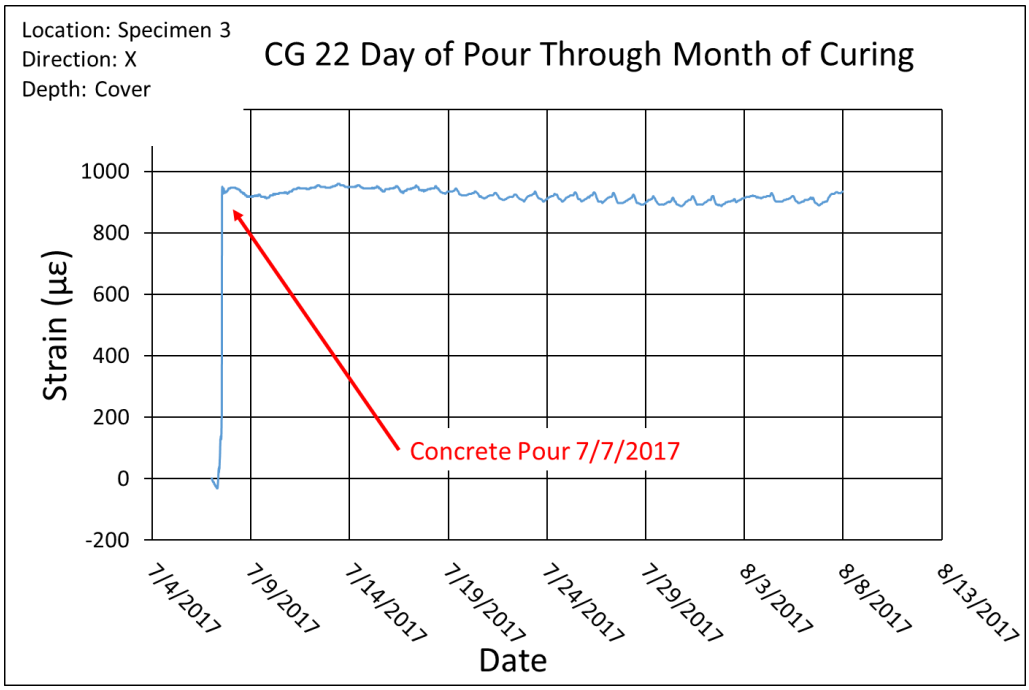

Figure 149 Concrete Gage 22 Strain Data from the Day Concrete was Poured Through One Month of Curing

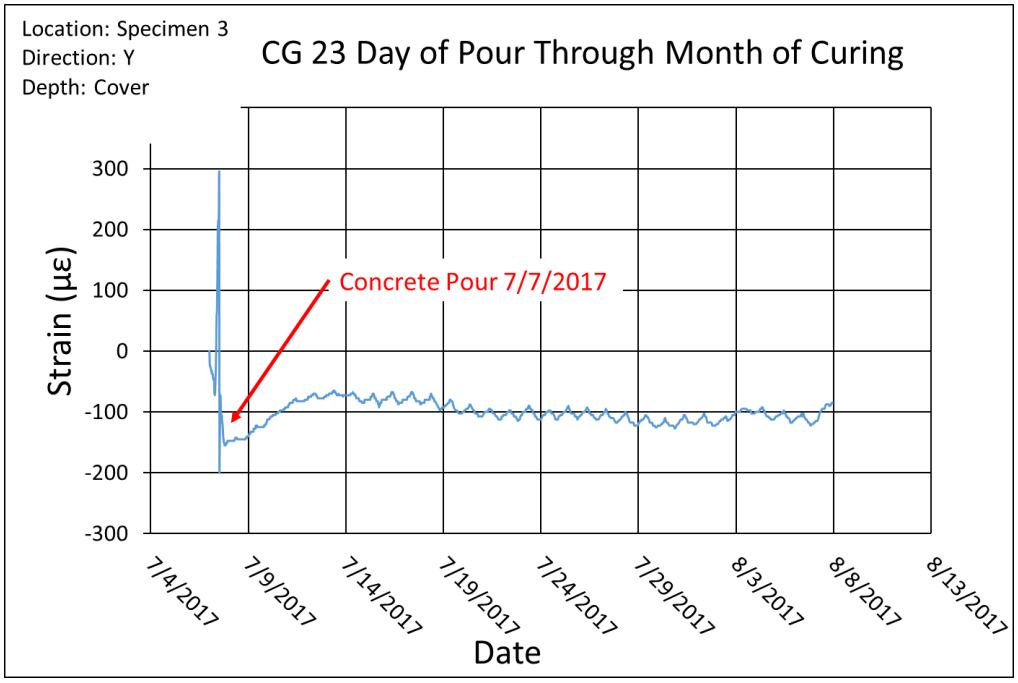

Figure 150 Concrete Gage 23 Strain Data from the Day Concrete was Poured Through One Month of Curing

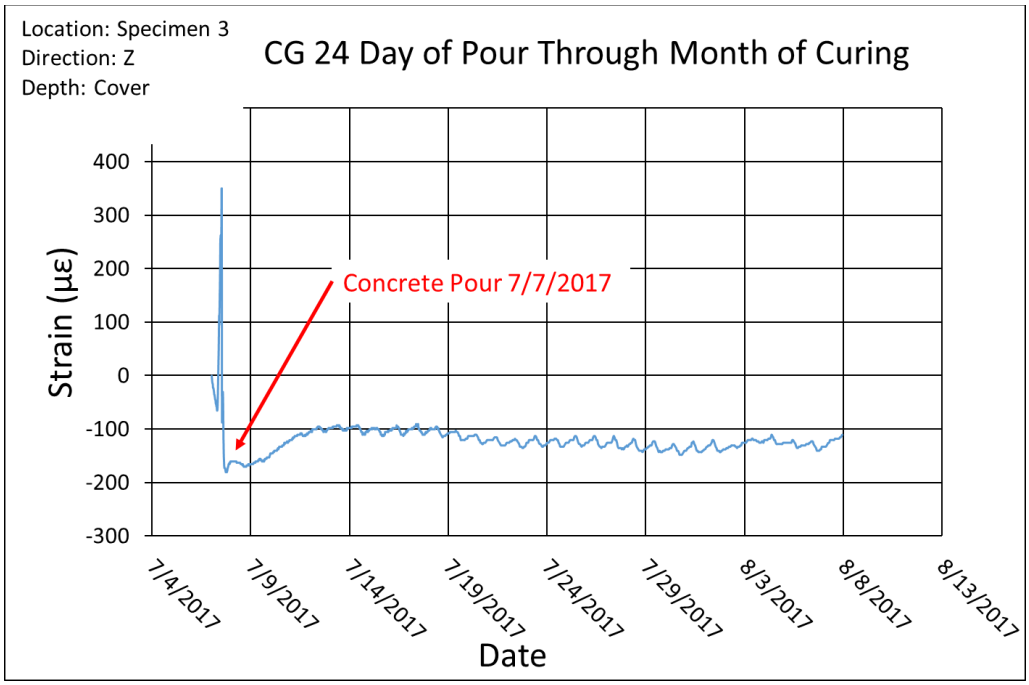

Figure 151 Concrete Gage 24 Strain Data from the Day Concrete was Poured Through One Month of Curing

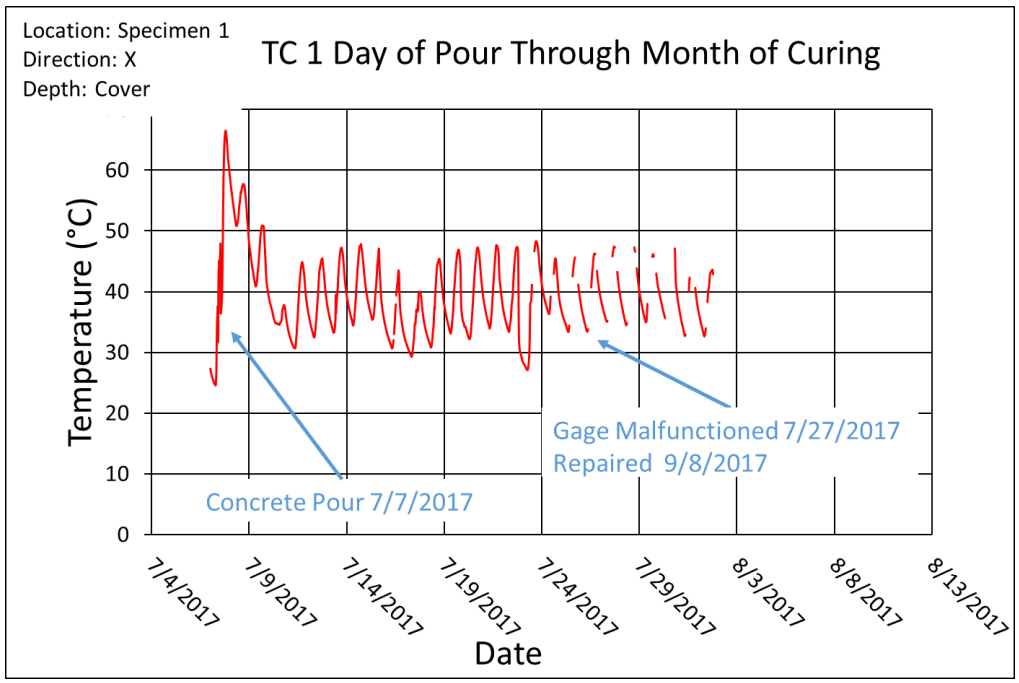

Figure 152 Thermocouple 1 Temperature Data from the Day Concrete Was Poured Through One Month of Curing

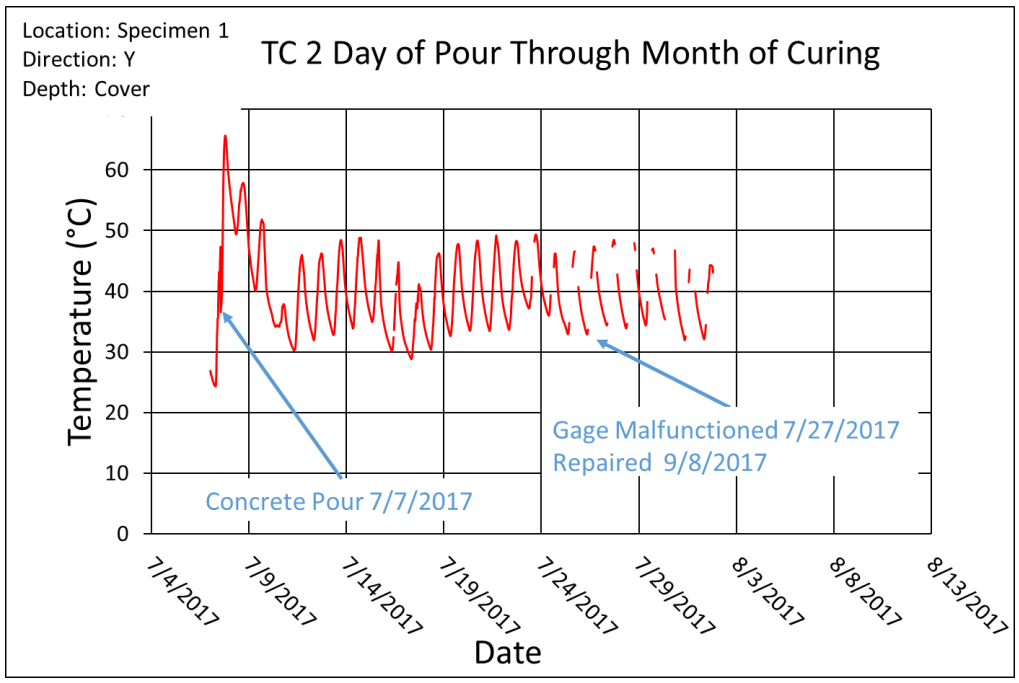

Figure 153 Thermocouple 2 Temperature Data from the Day Concrete Was Poured Through One Month of Curing

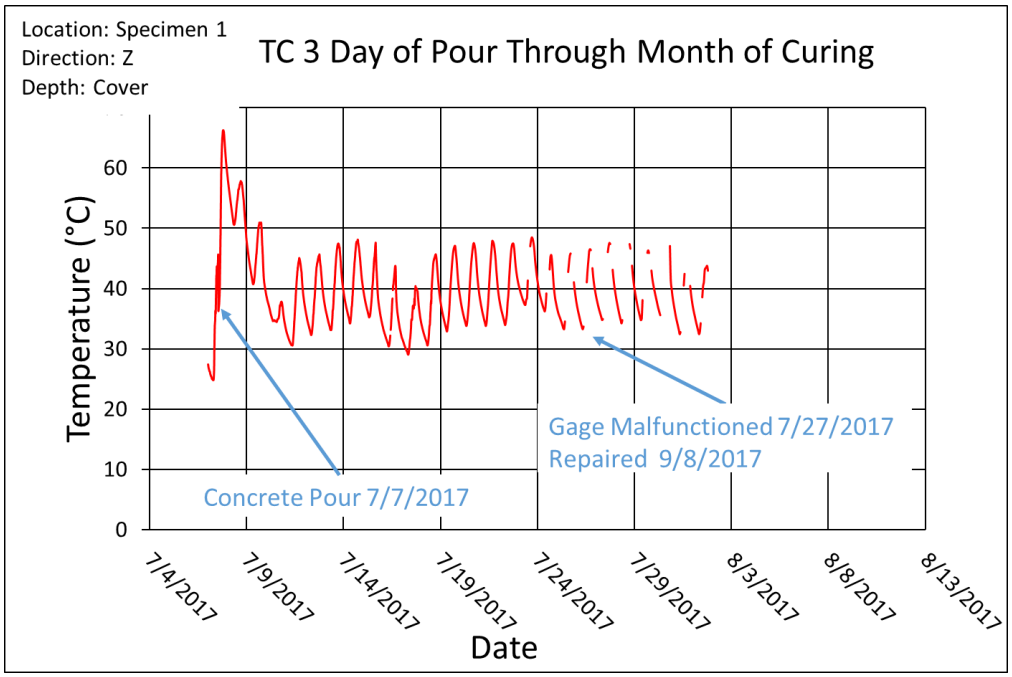

Figure 154 Thermocouple 3 Temperature Data from the Day Concrete Was Poured Through One Month of Curing

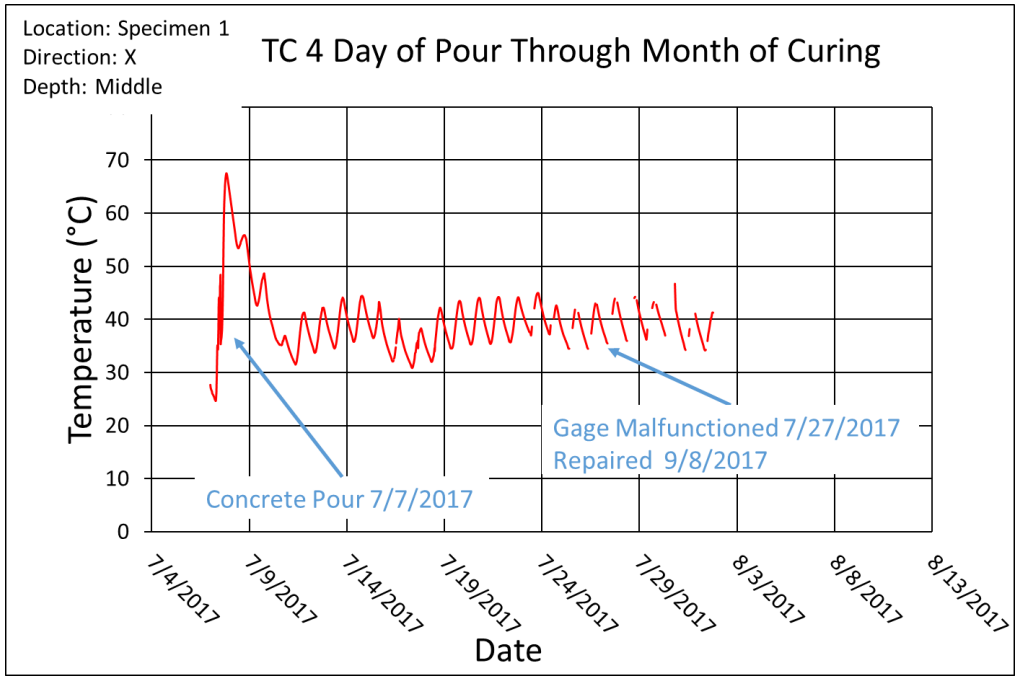

Figure 155 Thermocouple 4 Temperature Data from the Day Concrete Was Poured Through One Month of Curing

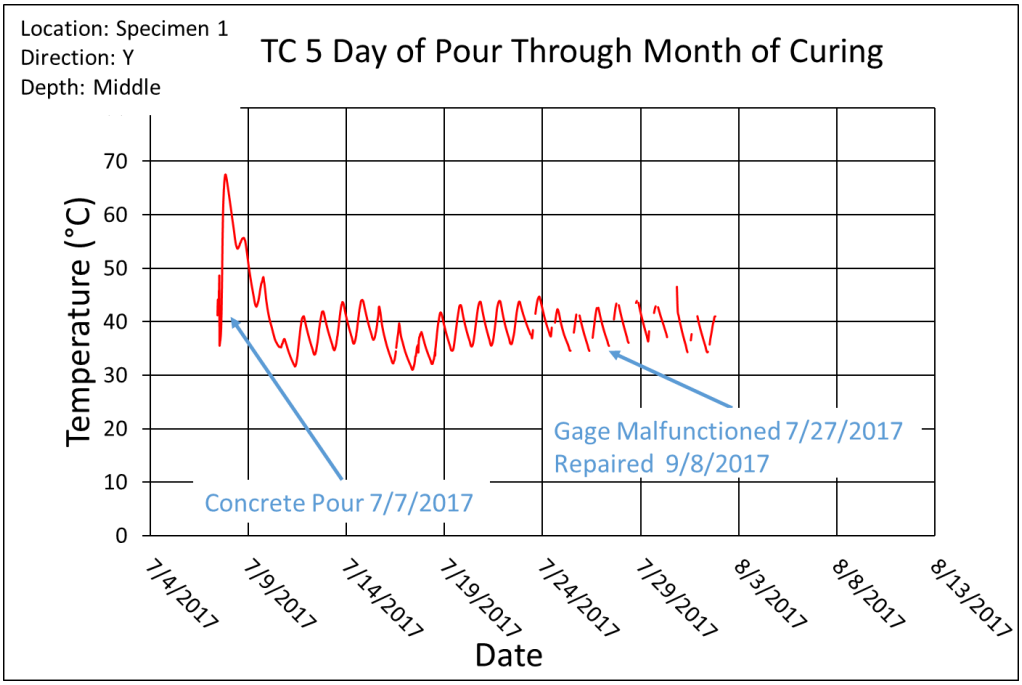

Figure 156 Thermocouple 5 Temperature Data from the Day Concrete Was Poured Through One Month of Curing

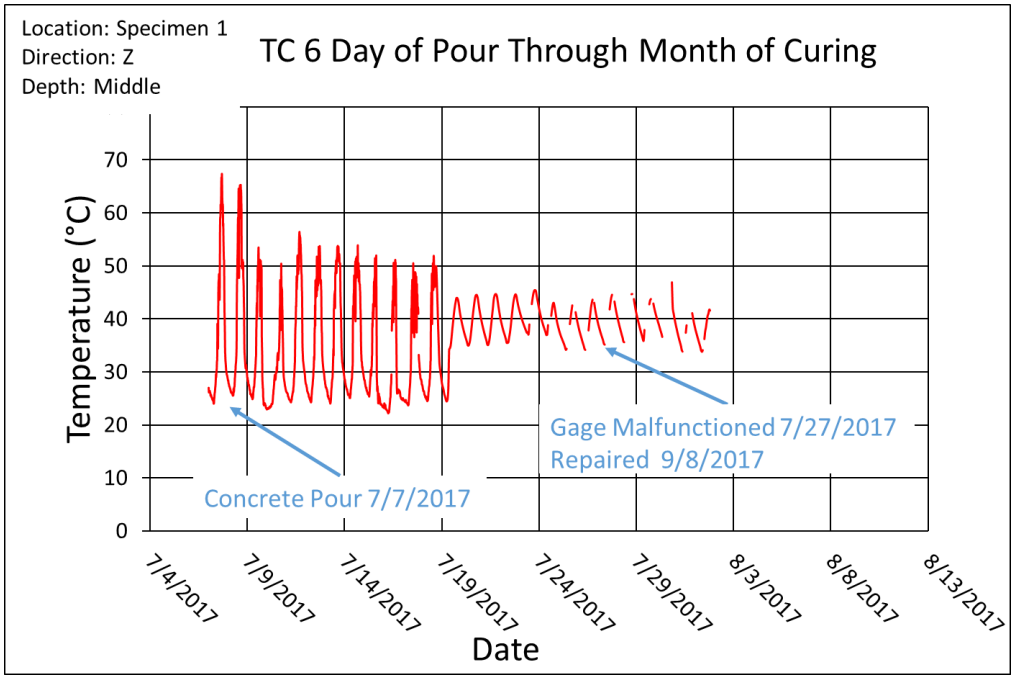

Figure 157 Thermocouple 6 Temperature Data from the Day Concrete Was Poured Through One Month of Curing

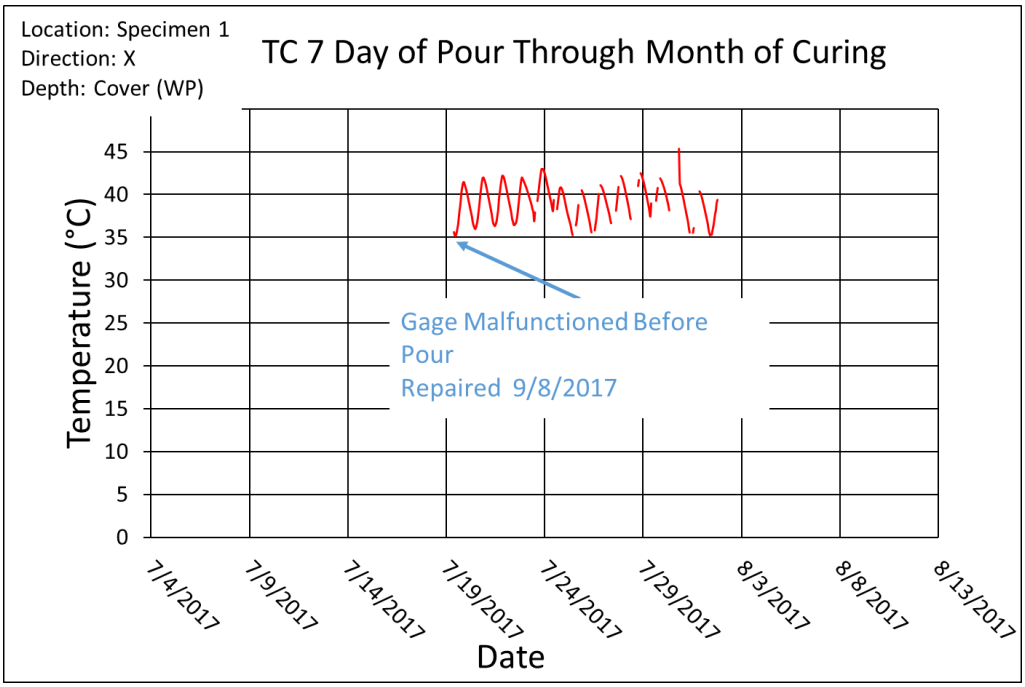

Figure 158 Thermocouple 7 Temperature Data from the Day Concrete Was Poured Through One Month of Curing

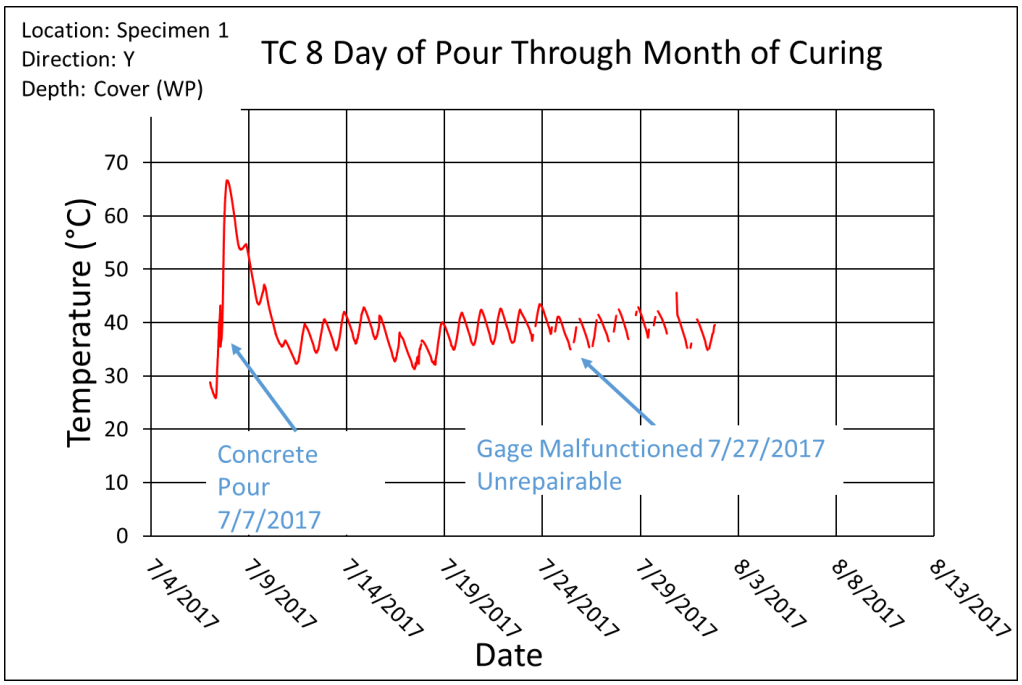

Figure 159 Thermocouple 8 Temperature Data from the Day Concrete Was Poured Through One Month of Curing

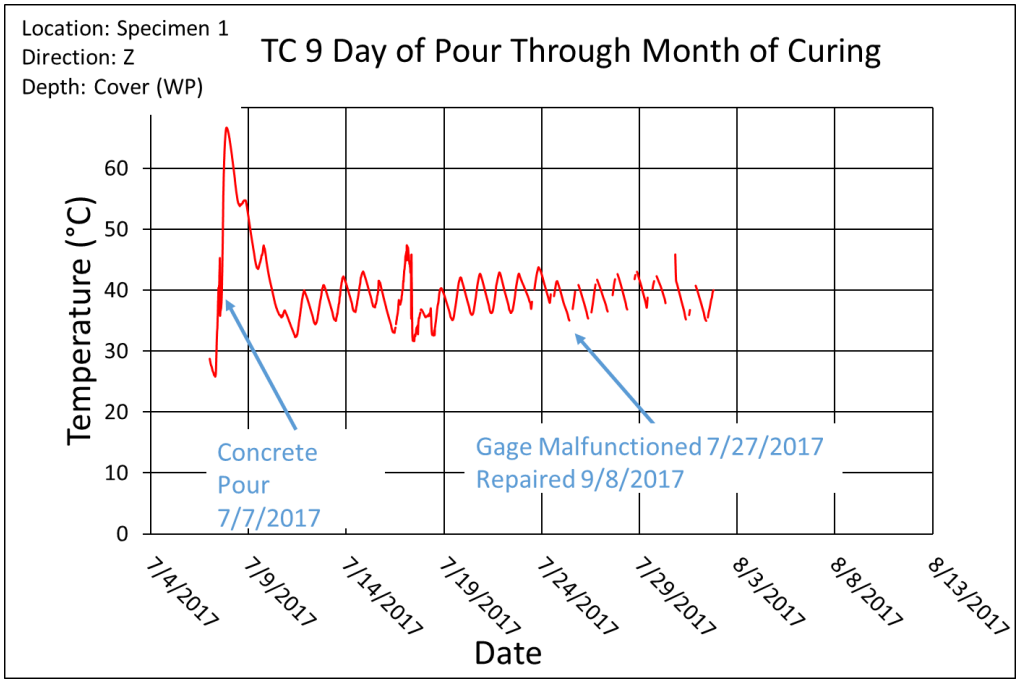

Figure 160 Thermocouple 9 Temperature Data from the Day Concrete Was Poured Through One Month of Curing

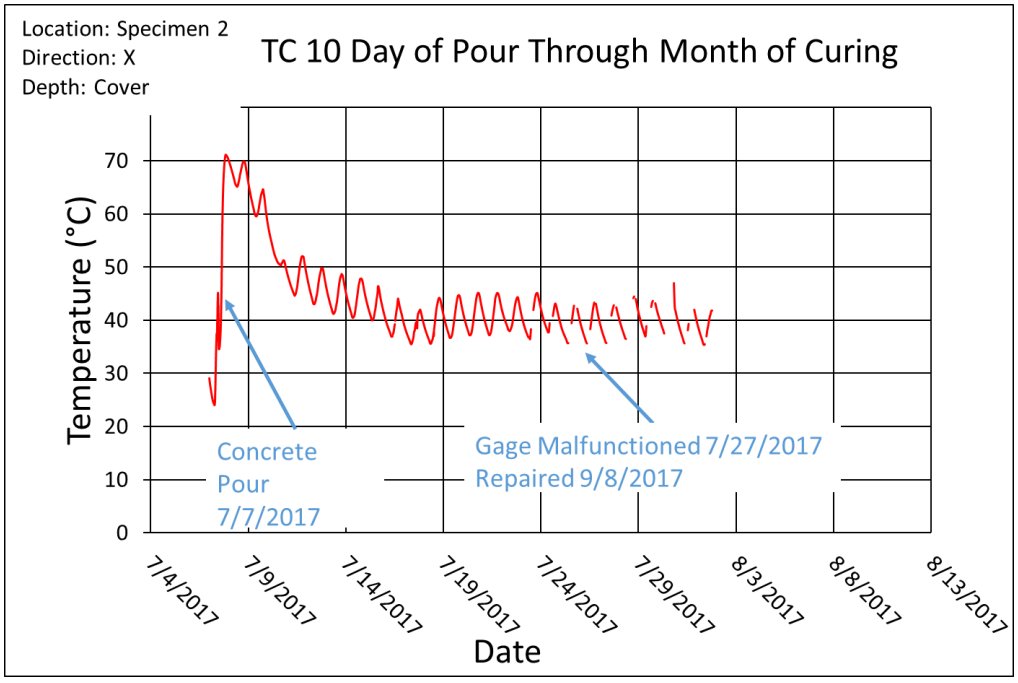

Figure 161 Thermocouple 10 Temperature Data from the Day Concrete Was Poured Through One Month of Curing

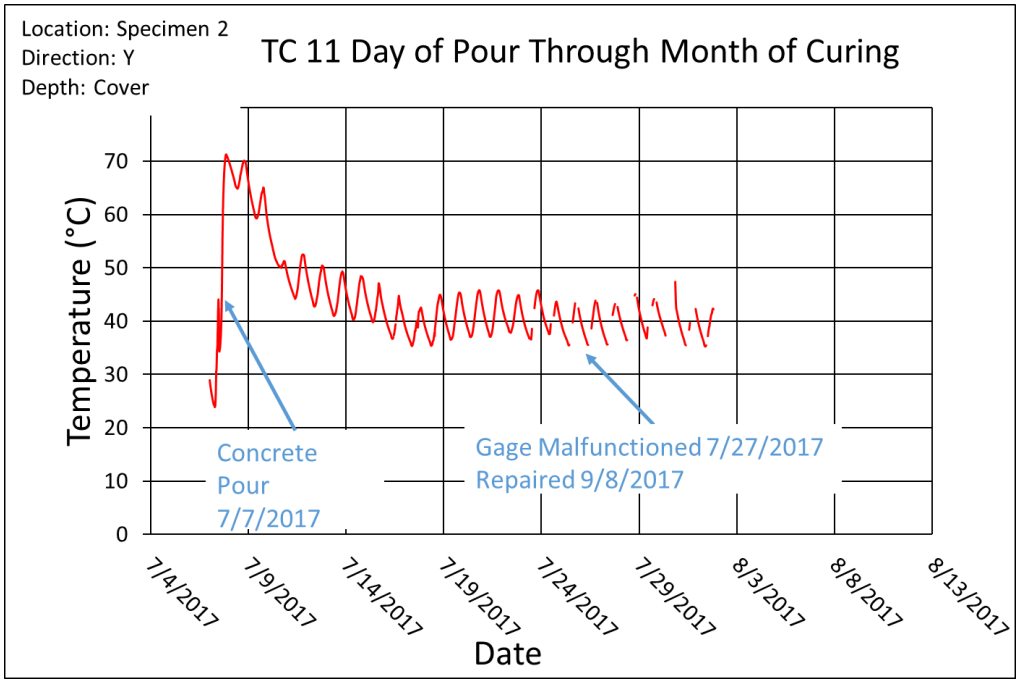

Figure 162 Thermocouple 11 Temperature Data from the Day Concrete Was Poured Through One Month of Curing

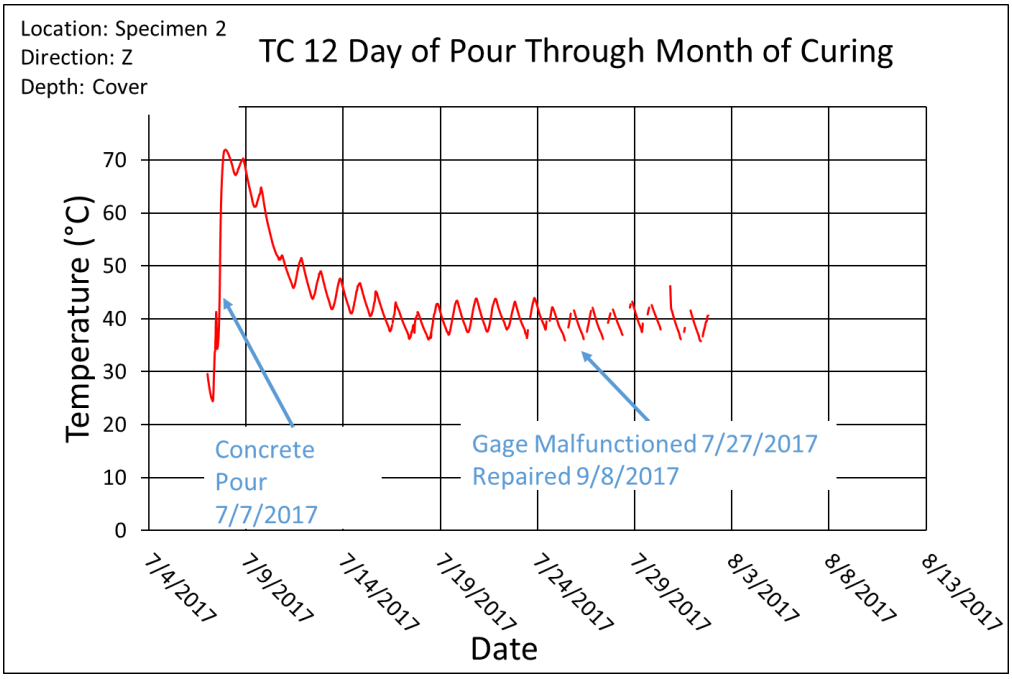

Figure 163 Thermocouple 12 Temperature Data from the Day Concrete Was Poured Through One Month of Curing

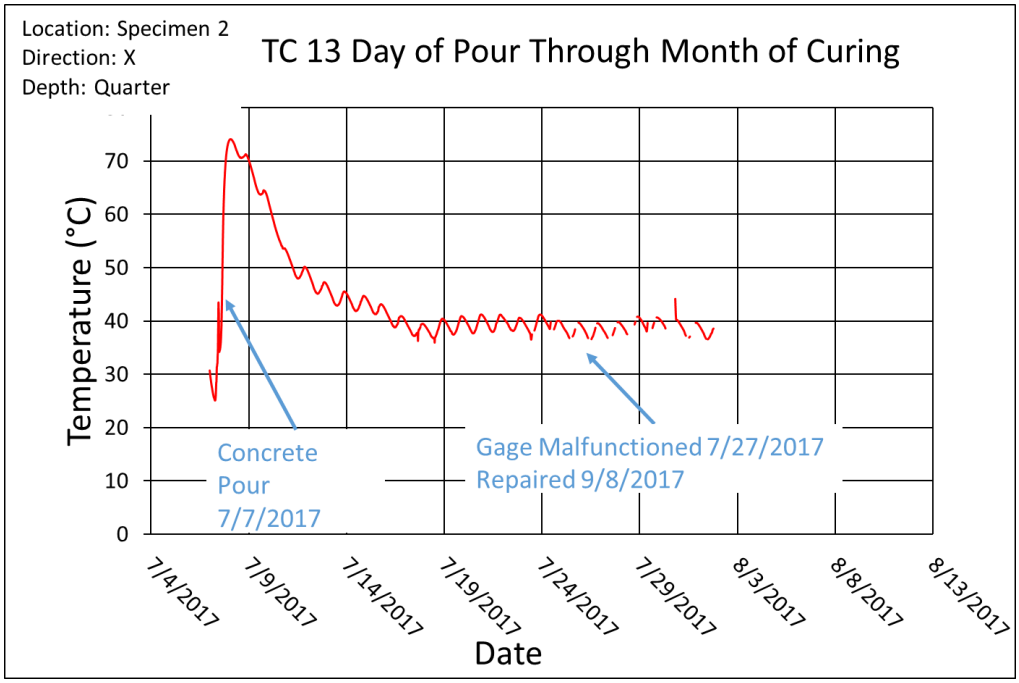

Figure 164 Thermocouple 13 Temperature Data from the Day Concrete Was Poured Through One Month of Curing

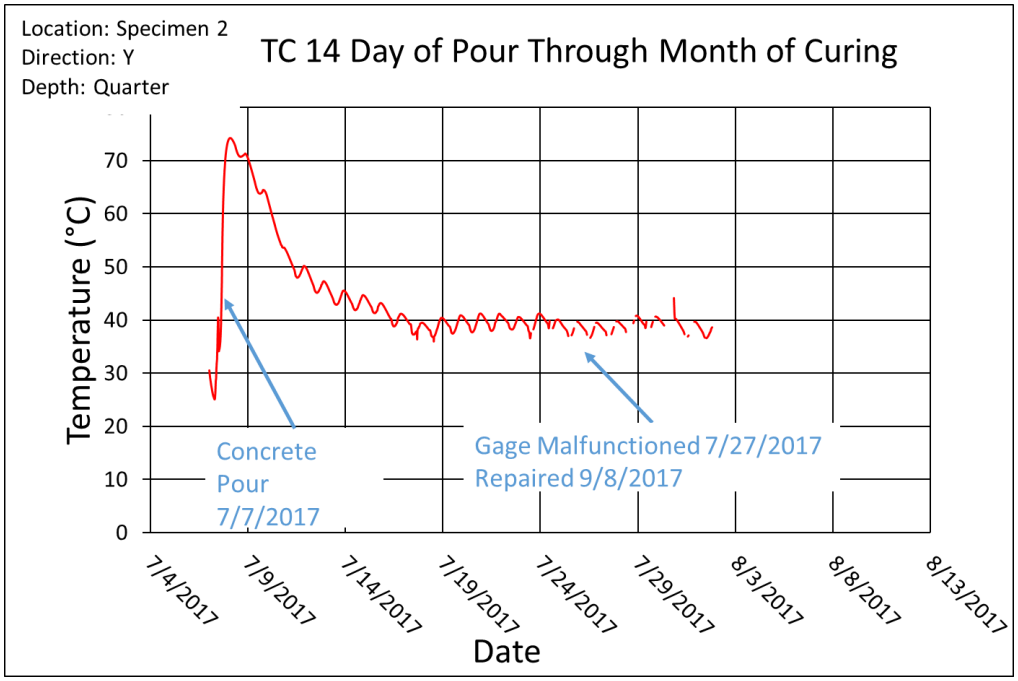

Figure 165 Thermocouple 14 Temperature Data from the Day Concrete Was Poured Through One Month of Curing

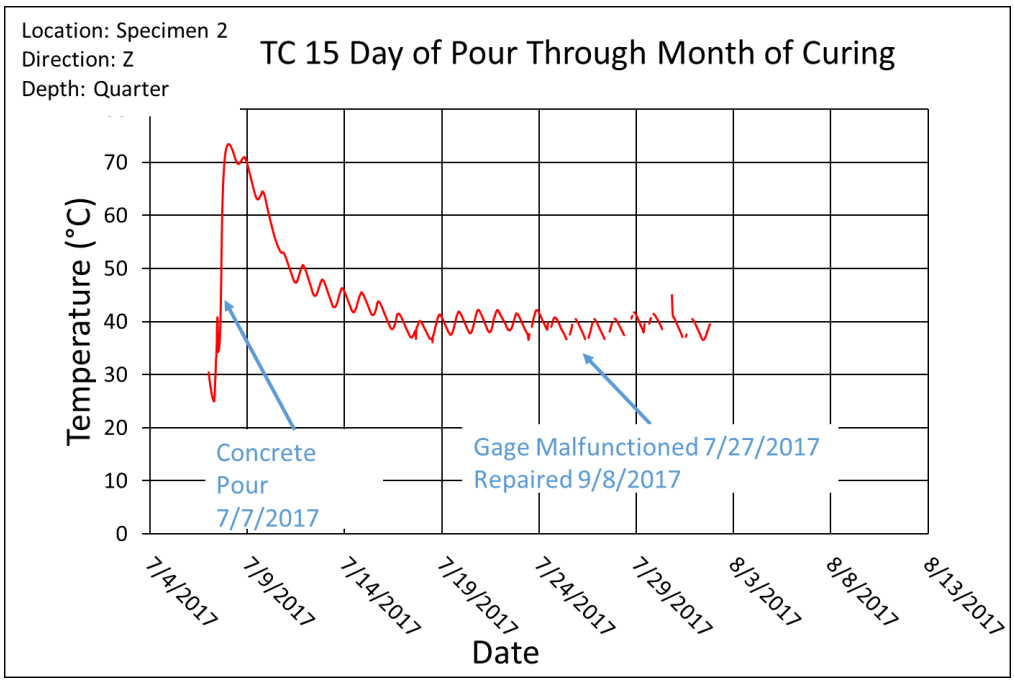

Figure 166 Thermocouple 15 Temperature Data from the Day Concrete Was Poured Through One Month of Curing

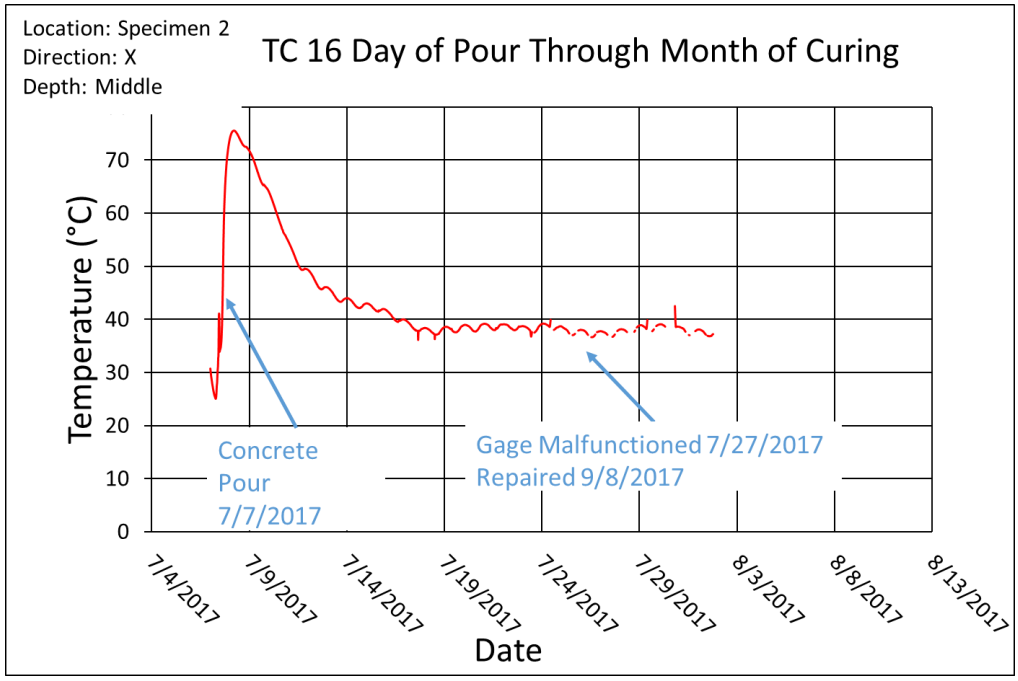

Figure 167 Thermocouple 16 Temperature Data from the Day Concrete Was Poured Through One Month of Curing

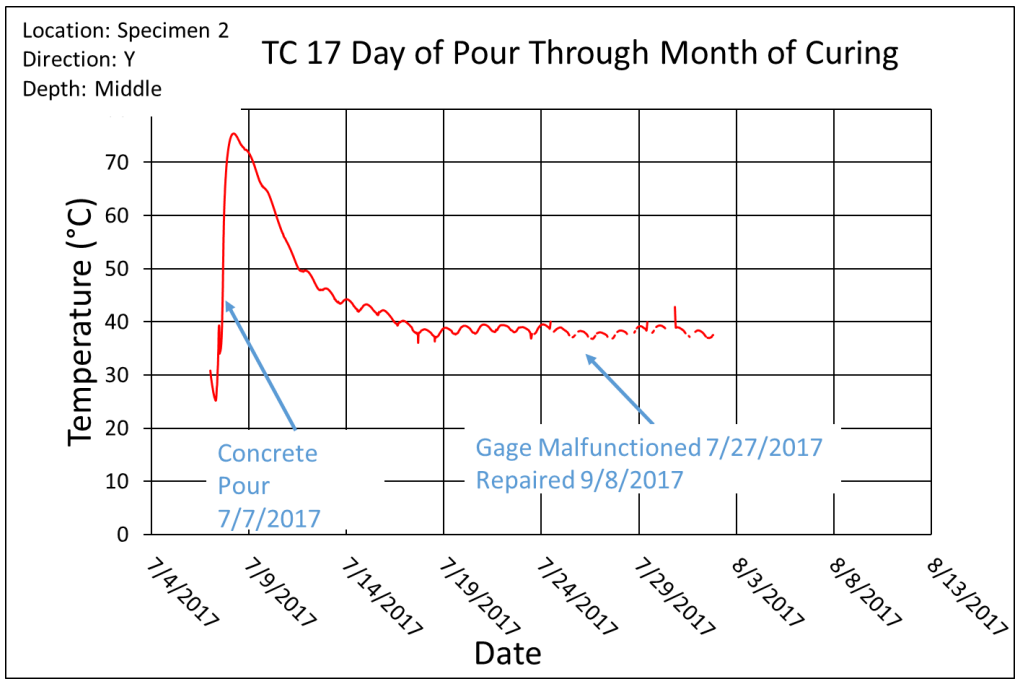

Figure 168 Thermocouple 17 Temperature Data from the Day Concrete Was Poured Through One Month of Curing

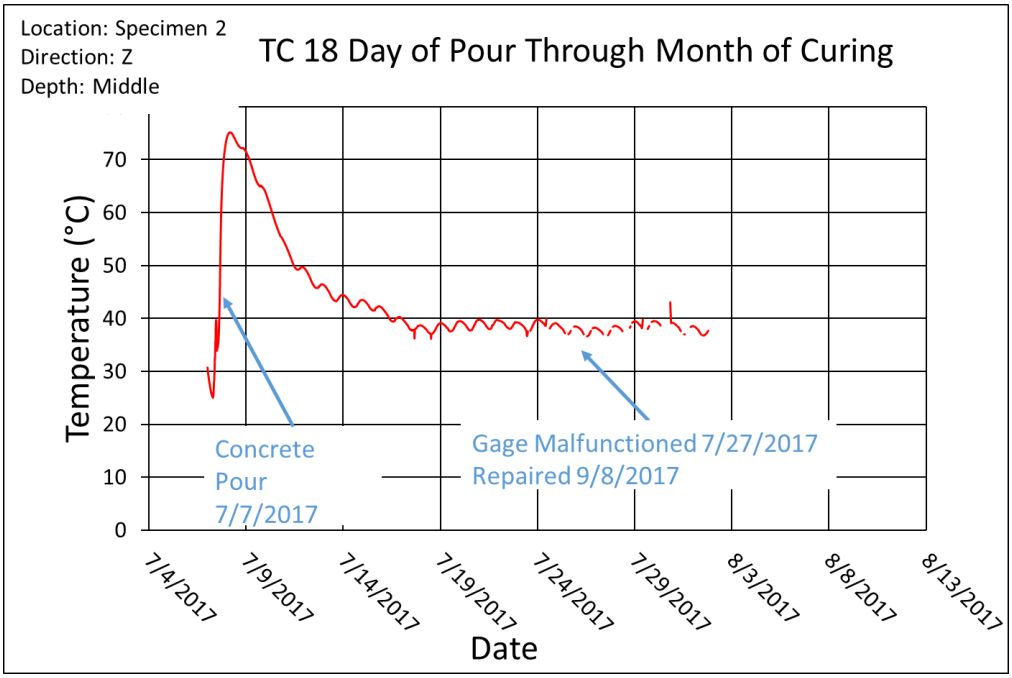

Figure 169 Thermocouple 18 Temperature Data from the Day Concrete Was Poured Through One Month of Curing

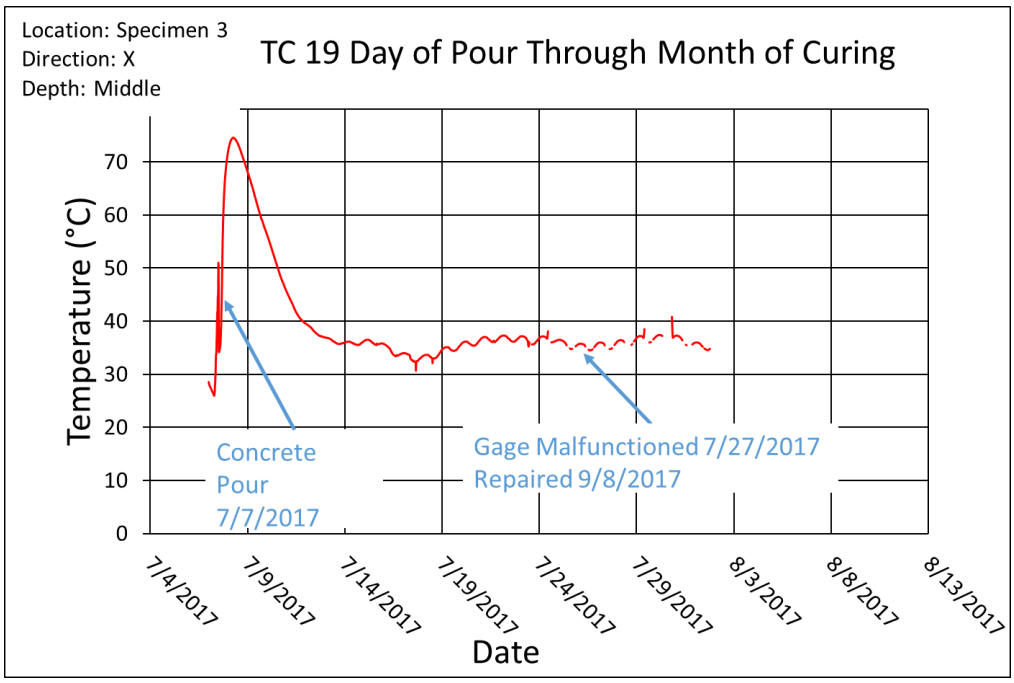

Figure 170 Thermocouple 19 Temperature Data from the Day Concrete Was Poured Through One Month of Curing

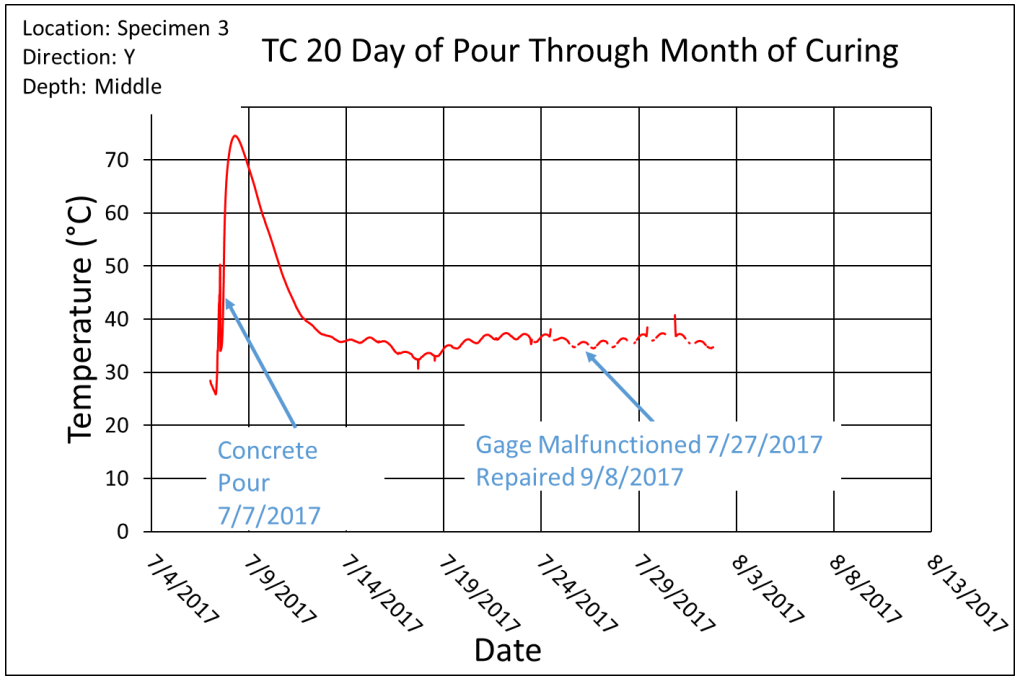

Figure 171 Thermocouple 20 Temperature Data from the Day Concrete Was Poured Through One Month of Curing

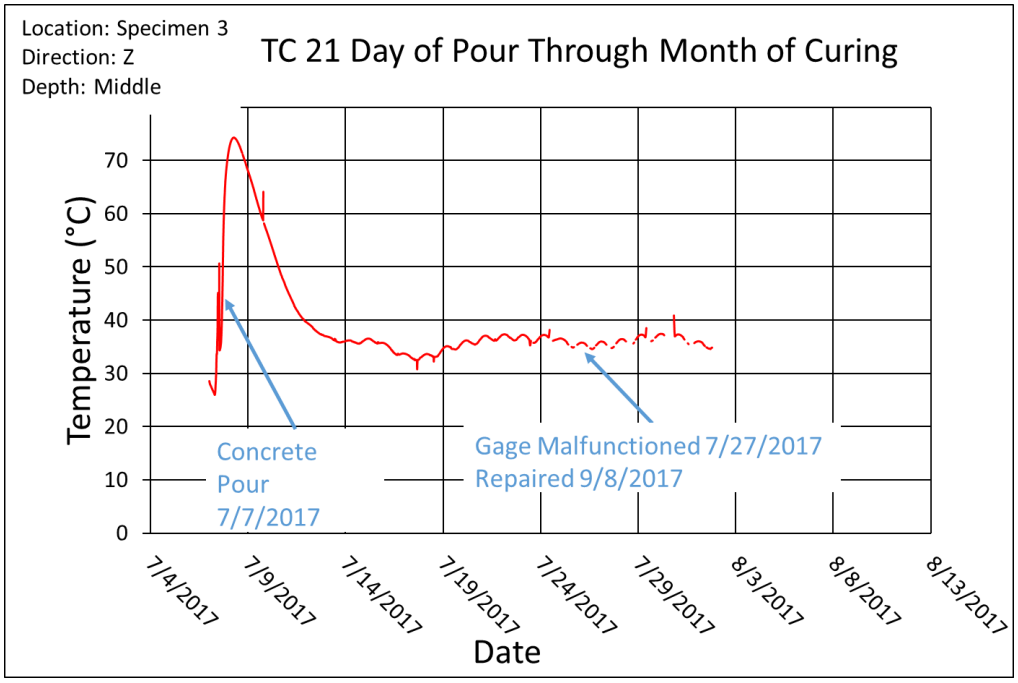

Figure 172 Thermocouple 21 Temperature Data from the Day Concrete Was Poured Through One Month of Curing

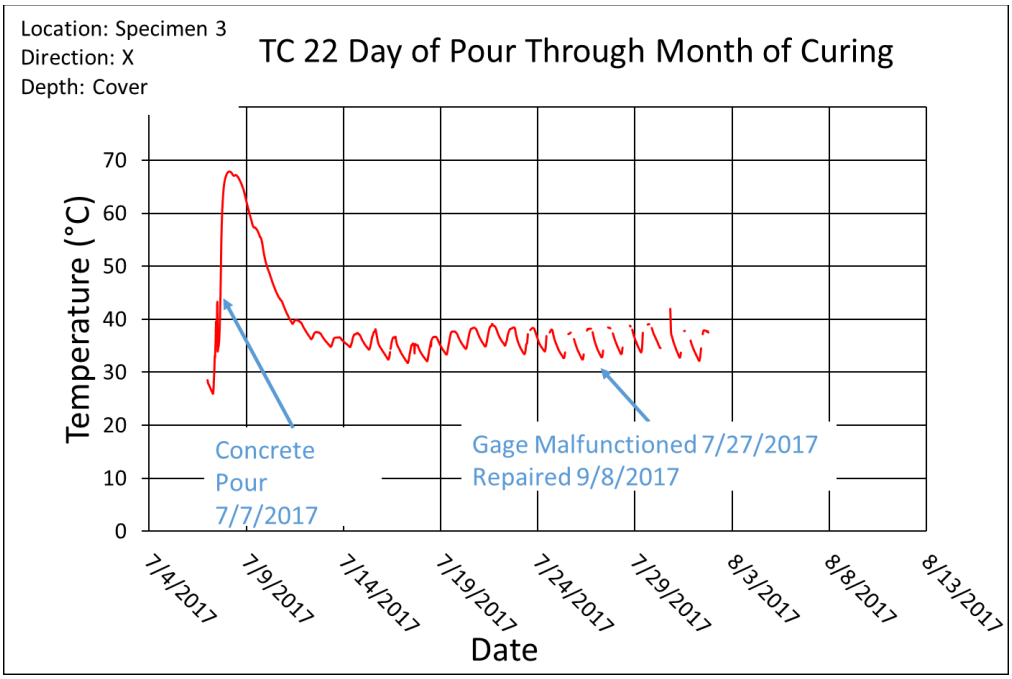

Figure 173 Thermocouple 22 Temperature Data from the Day Concrete Was Poured Through One Month of Curing

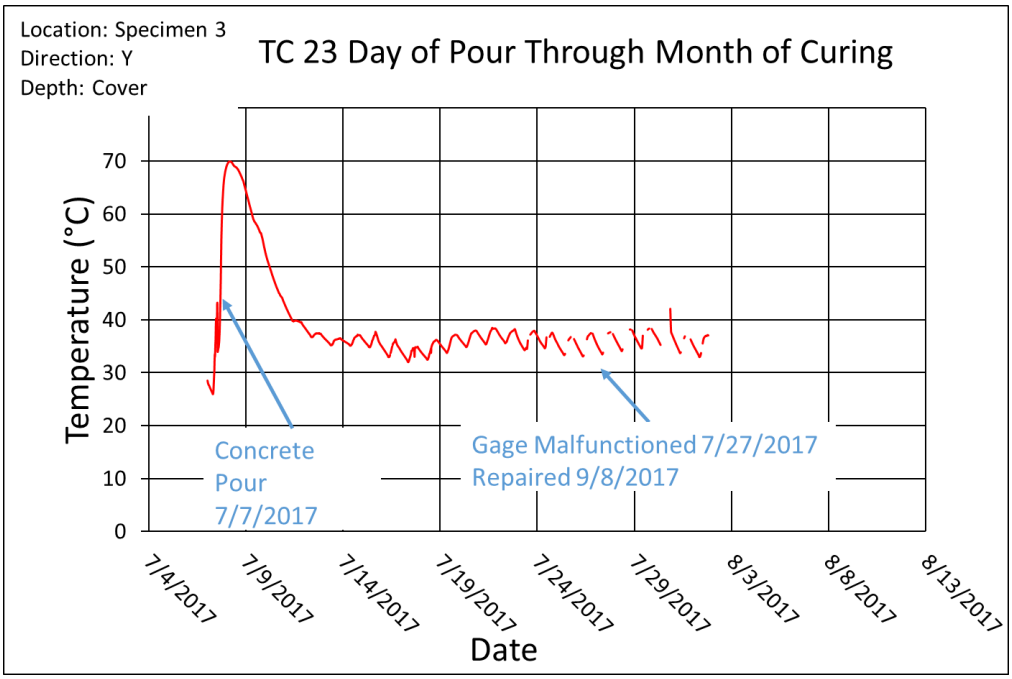

Figure 174 Thermocouple 23 Temperature Data from the Day Concrete Was Poured Through One Month of Curing

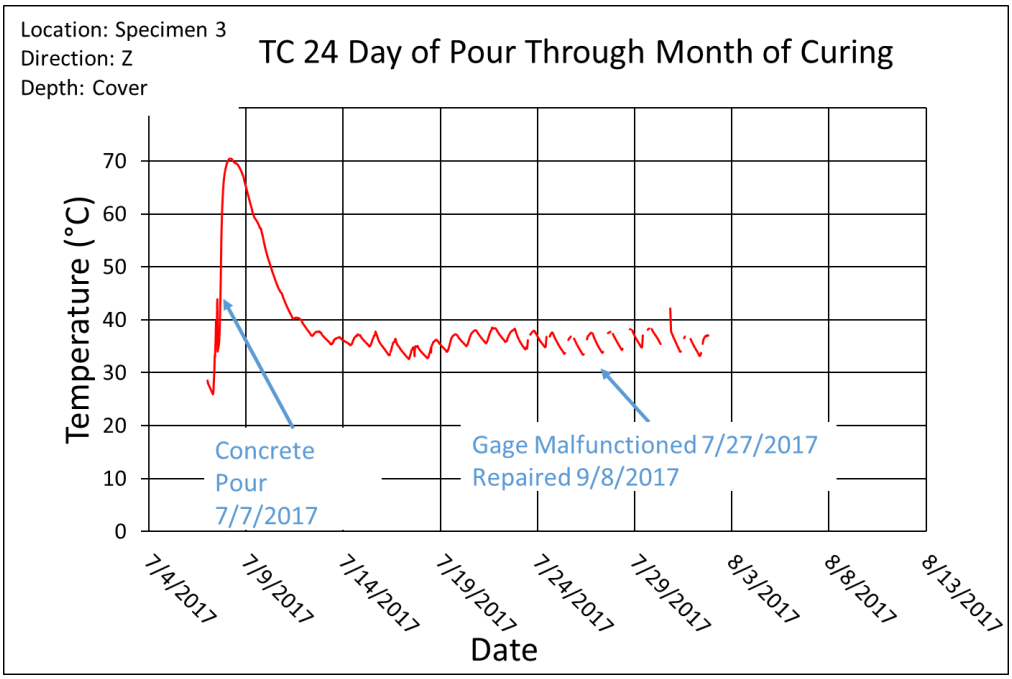

Figure 175 Thermocouple 24 Temperature Data from the Day Concrete Was Poured Through One Month of Curing

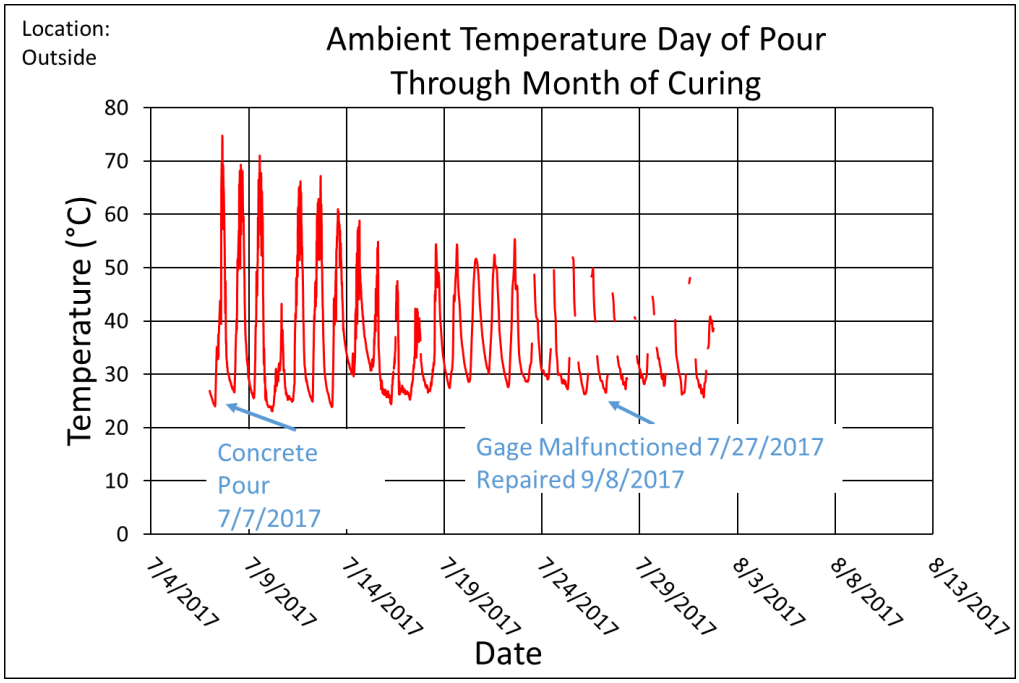

Figure 176 Ambient Temperature Data from the Day Concrete Was Poured Through One Month of Curing

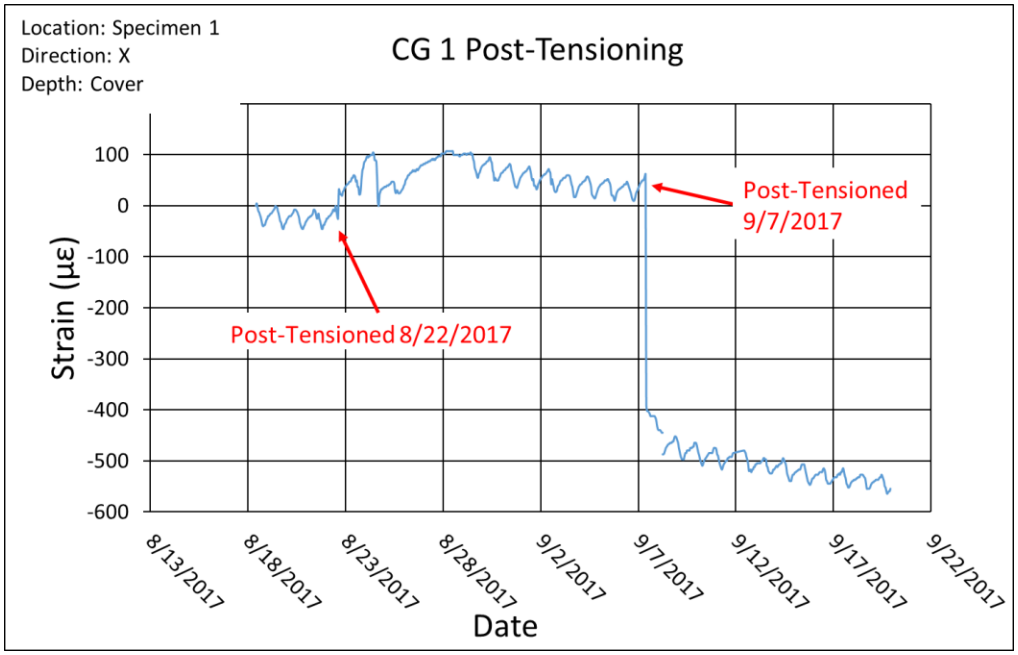

Figure 177 Concrete Gage 1 Strain Data During Post-Tensioning

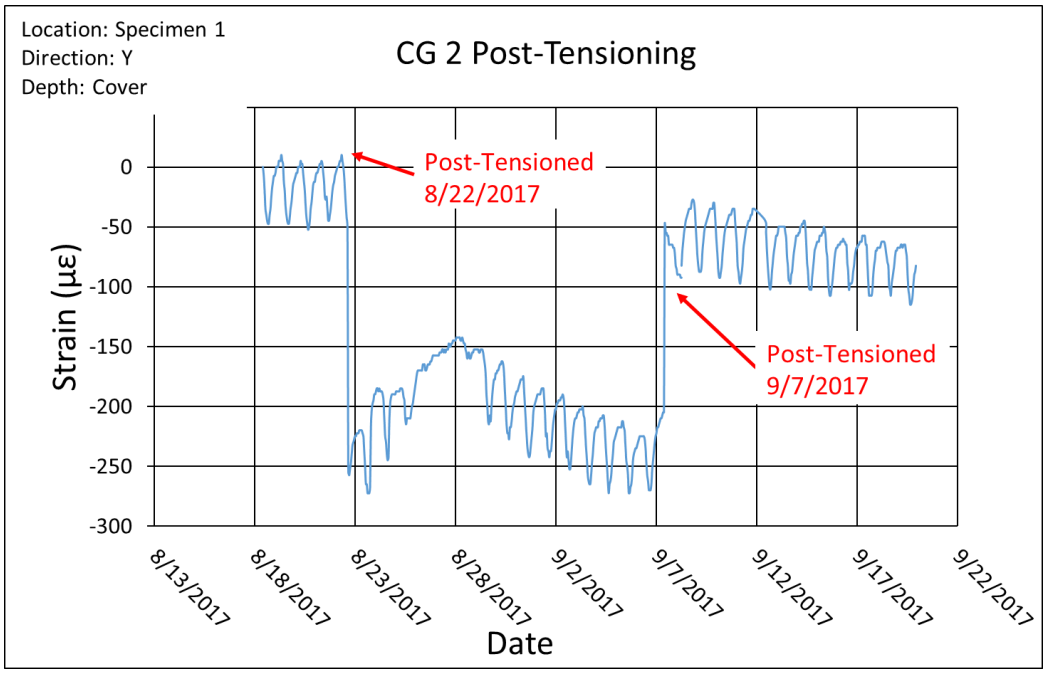

Figure 178 Concrete Gage 2 Strain Data During Post-Tensioning

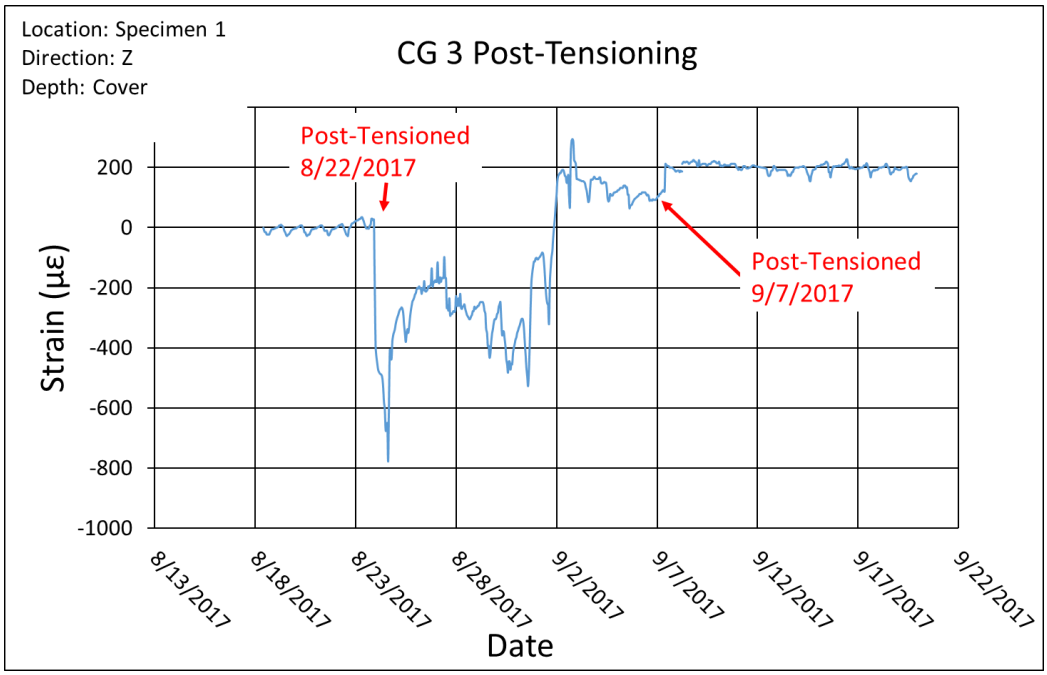

Figure 179 Concrete Gage 3 Strain Data During Post-Tensioning

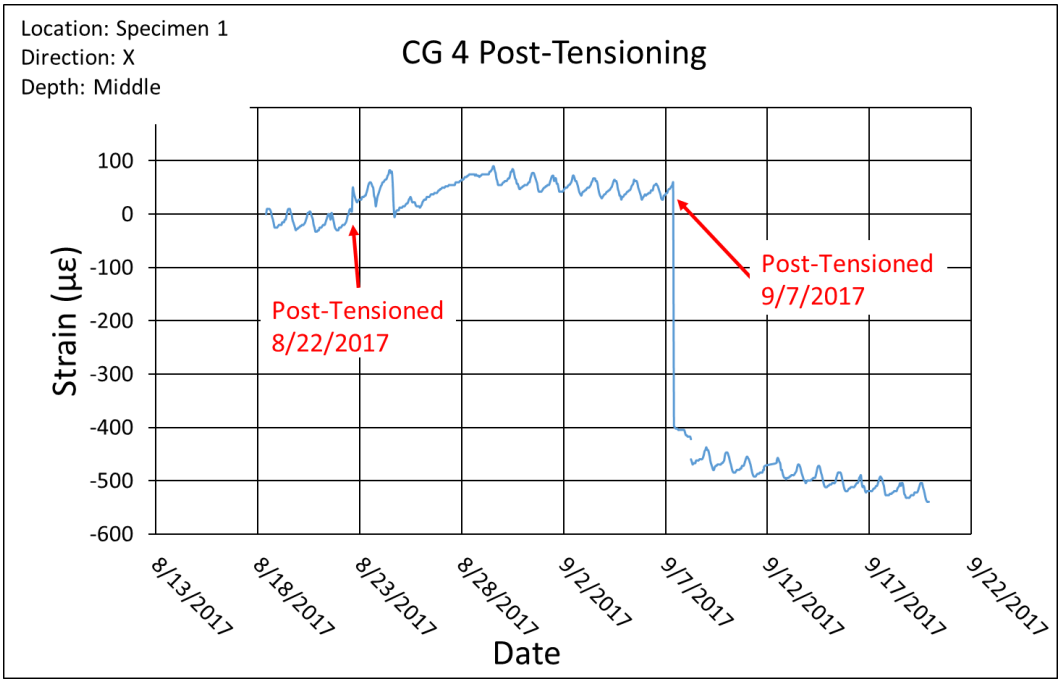

Figure 180 Concrete Gage 4 Strain Data During Post-Tensioning

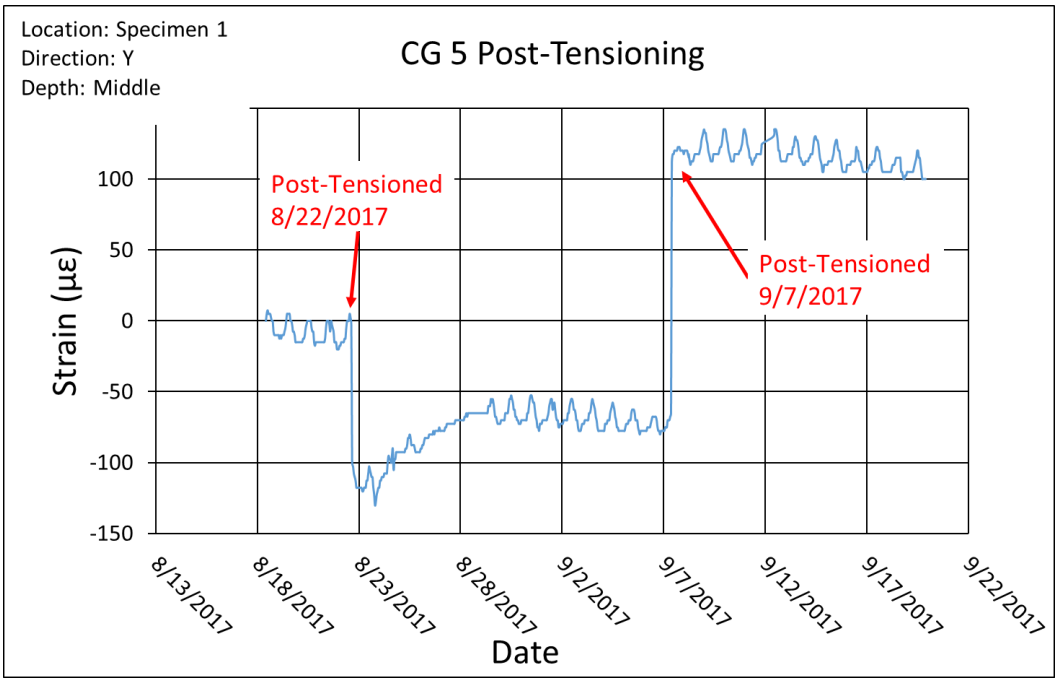

Figure 181 Concrete Gage 5 Strain Data During Post-Tensioning

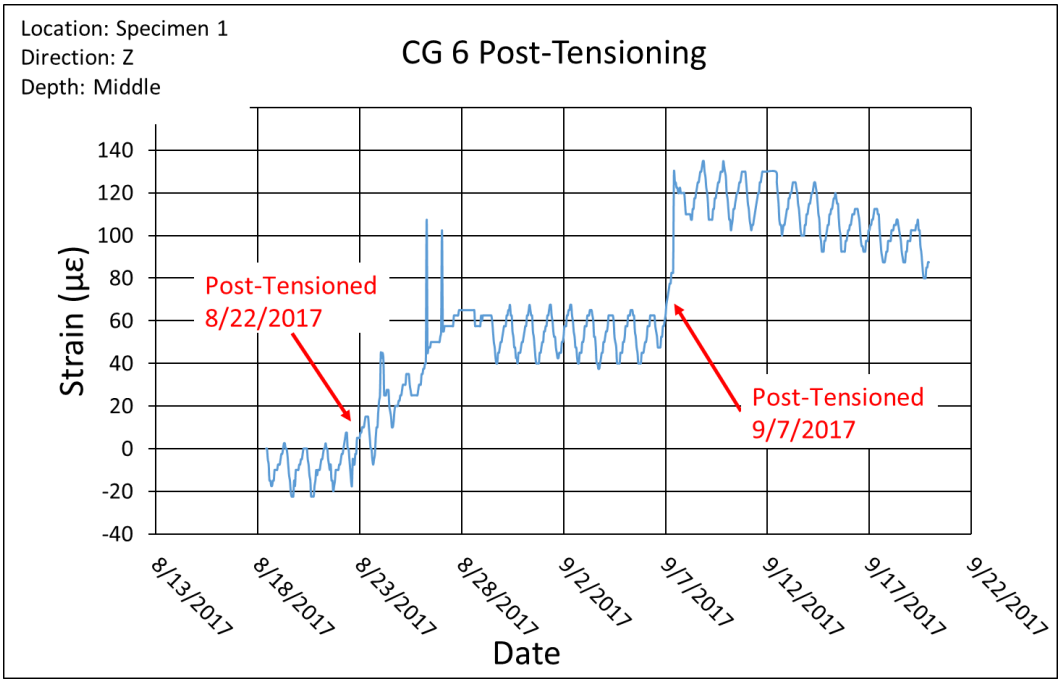

Figure 182 Concrete Gage 6 Strain Data During Post-Tensioning

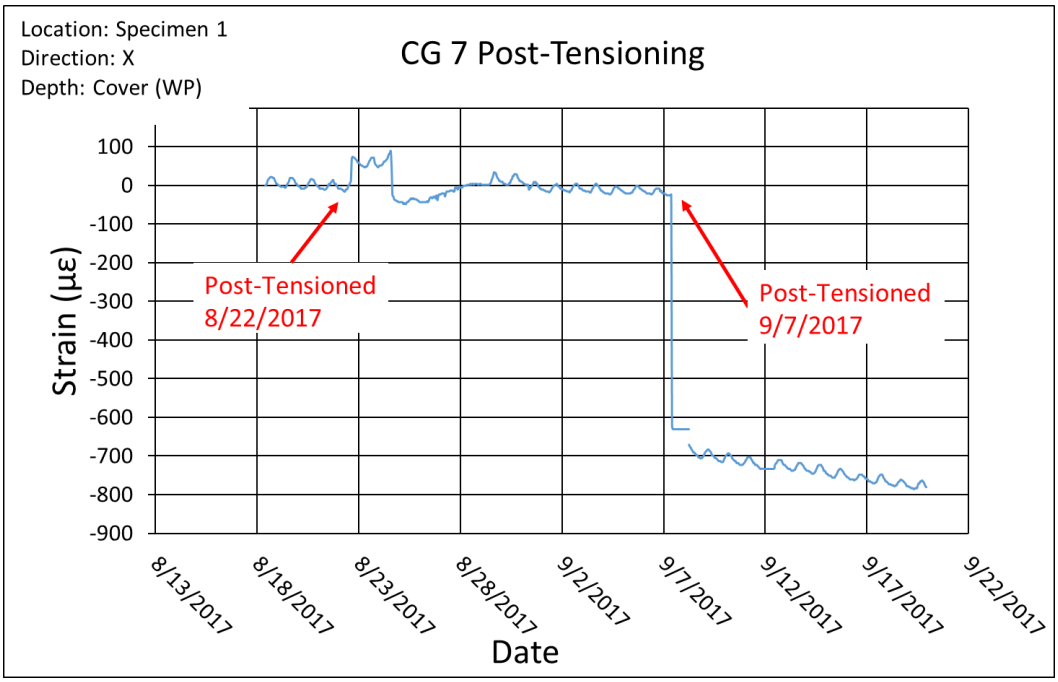

Figure 183 Concrete Gage 7 Strain Data During Post-Tensioning

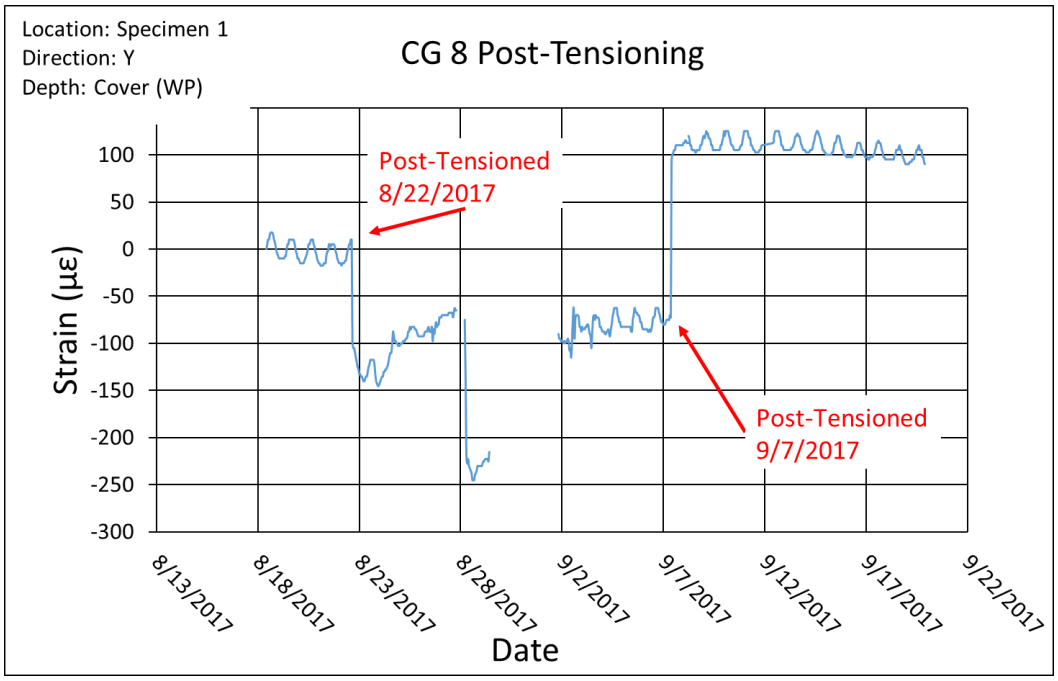

Figure 184 Concrete Gage 8 Strain Data During Post-Tensioning

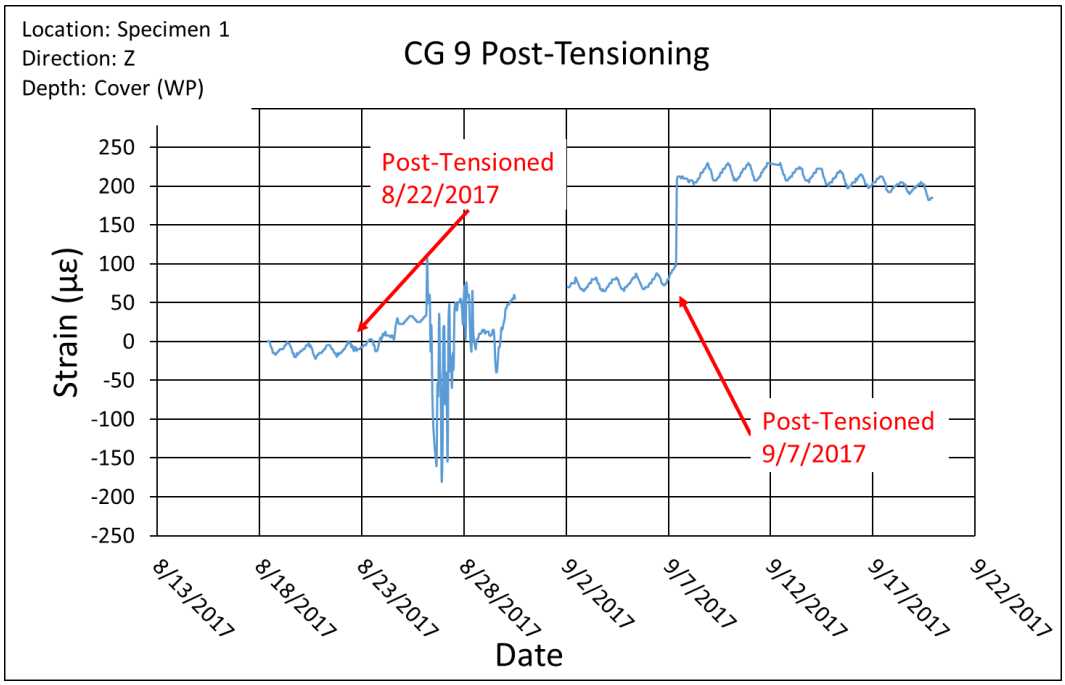

Figure 185 Concrete Gage 9 Strain Data During Post-Tensioning

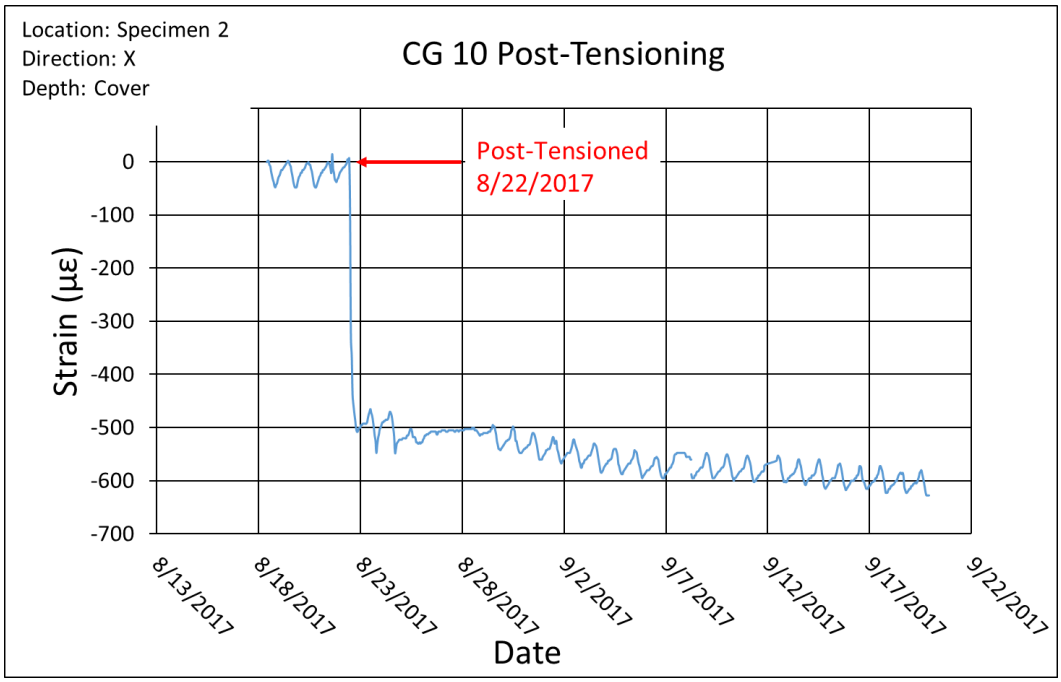

Figure 186 Concrete Gage 10 Strain Data During Post-Tensioning

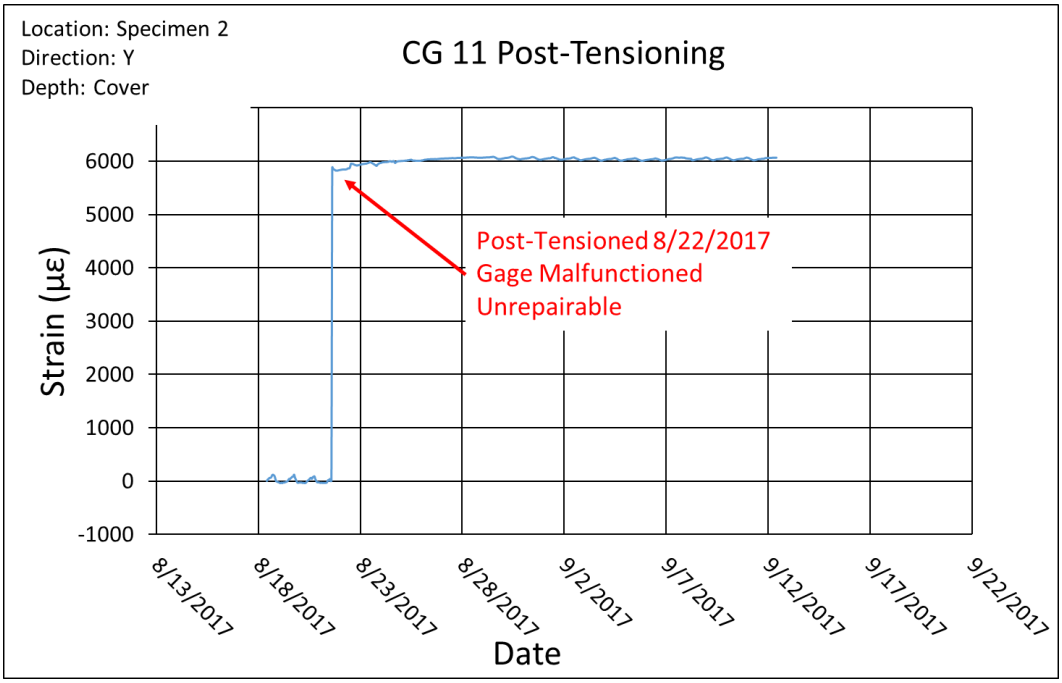

Figure 187 Concrete Gage 11 Strain Data During Post-Tensioning

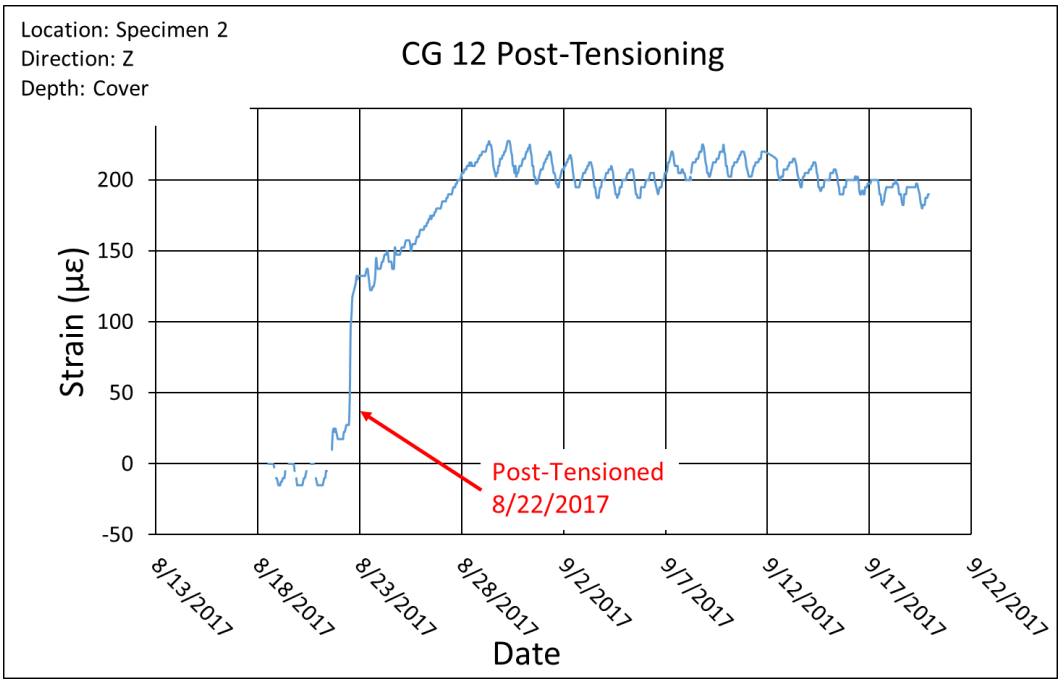

Figure 188 Concrete Gage 12 Strain Data During Post-Tensioning

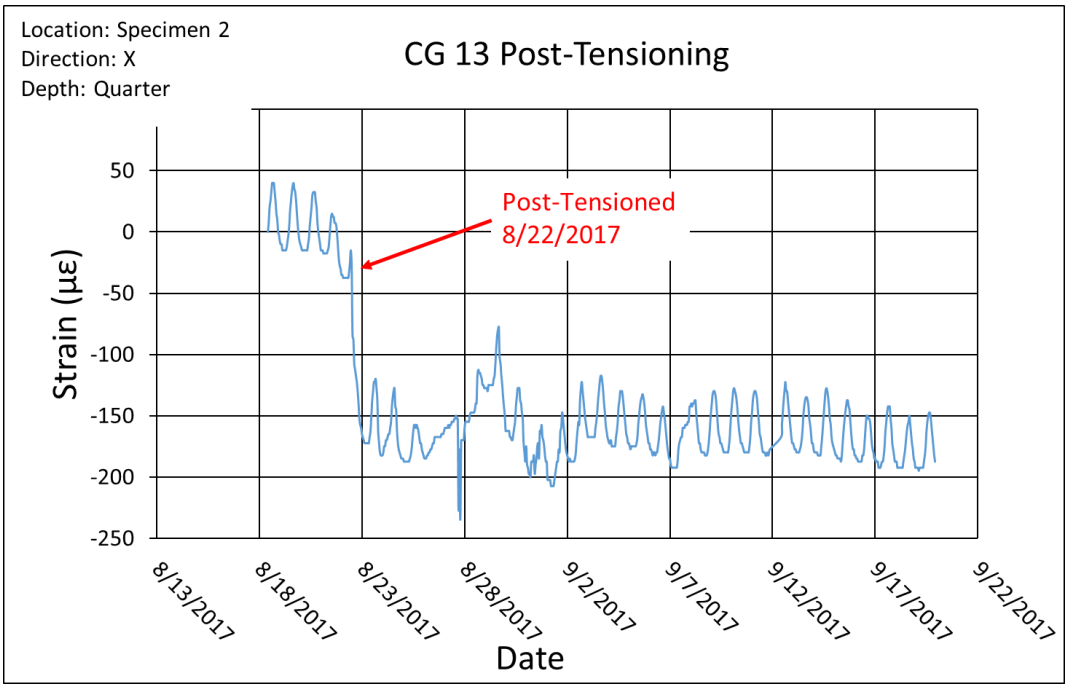

Figure 189 Concrete Gage 13 Strain Data During Post-Tensioning

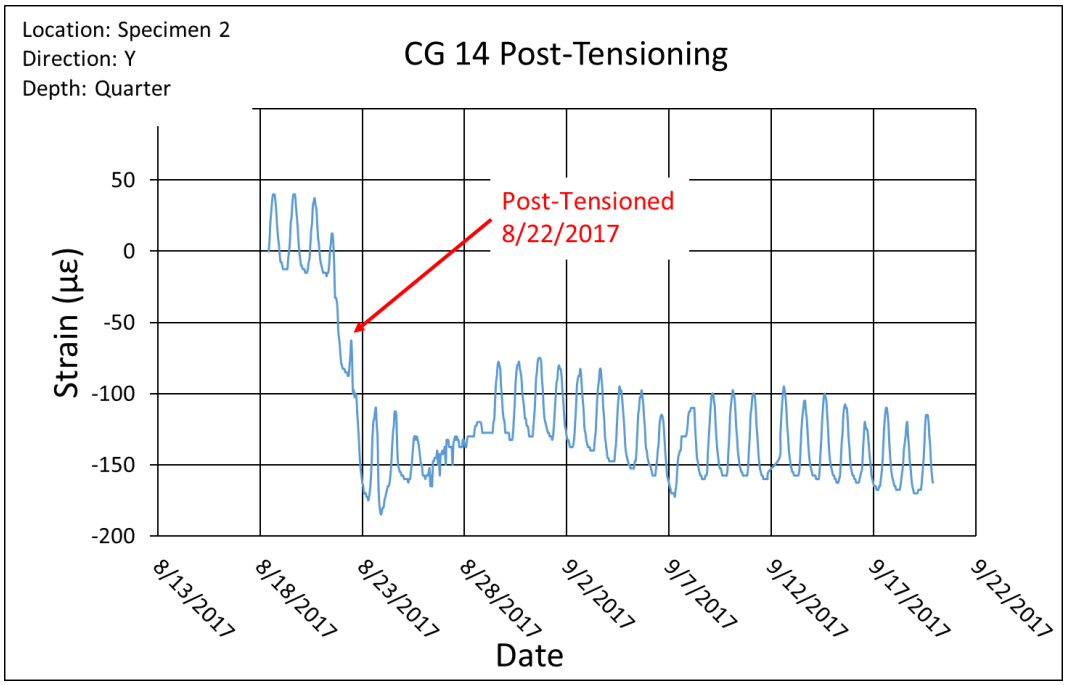

Figure 190 Concrete Gage 14 Strain Data During Post-Tensioning

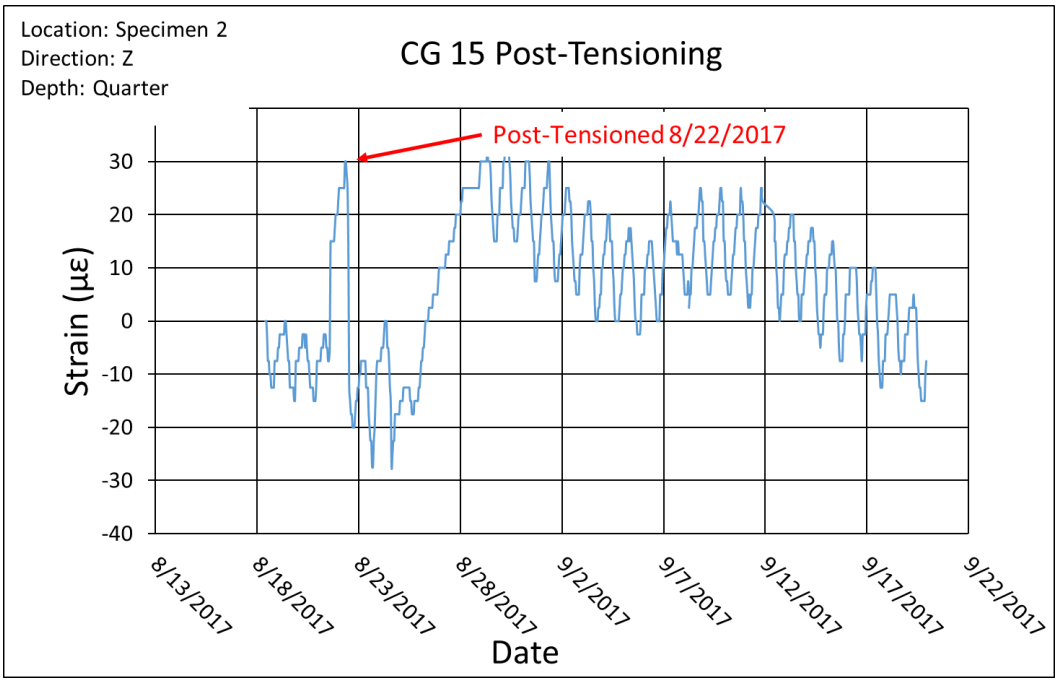

Figure 191 Concrete Gage 15 Strain Data During Post-Tensioning

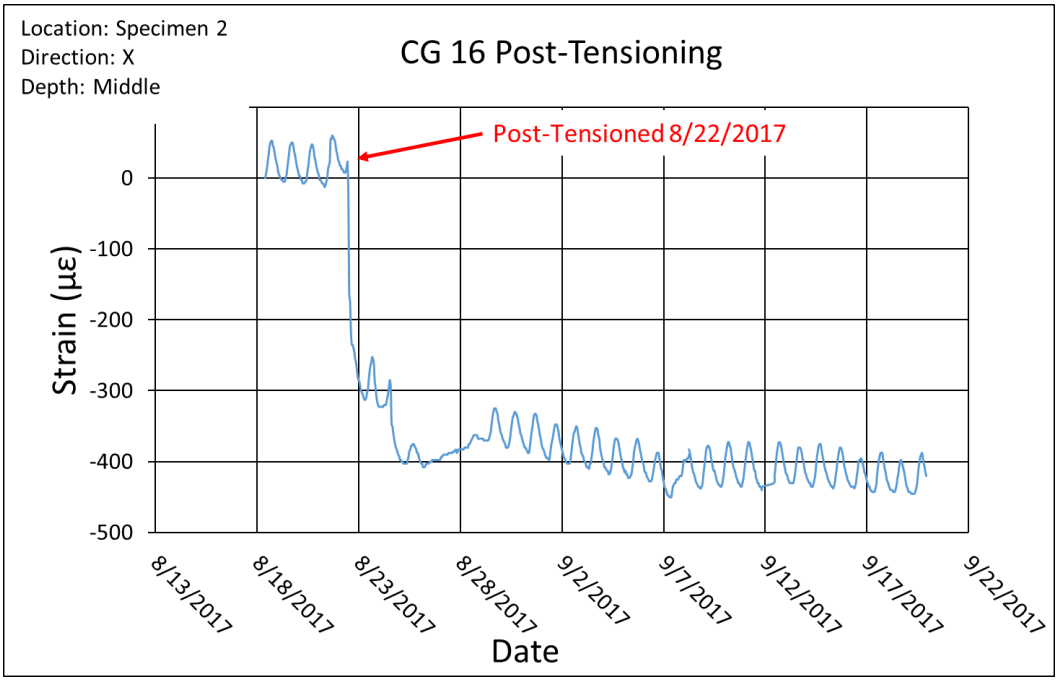

Figure 192 Concrete Gage 16 Strain Data During Post-Tensioning

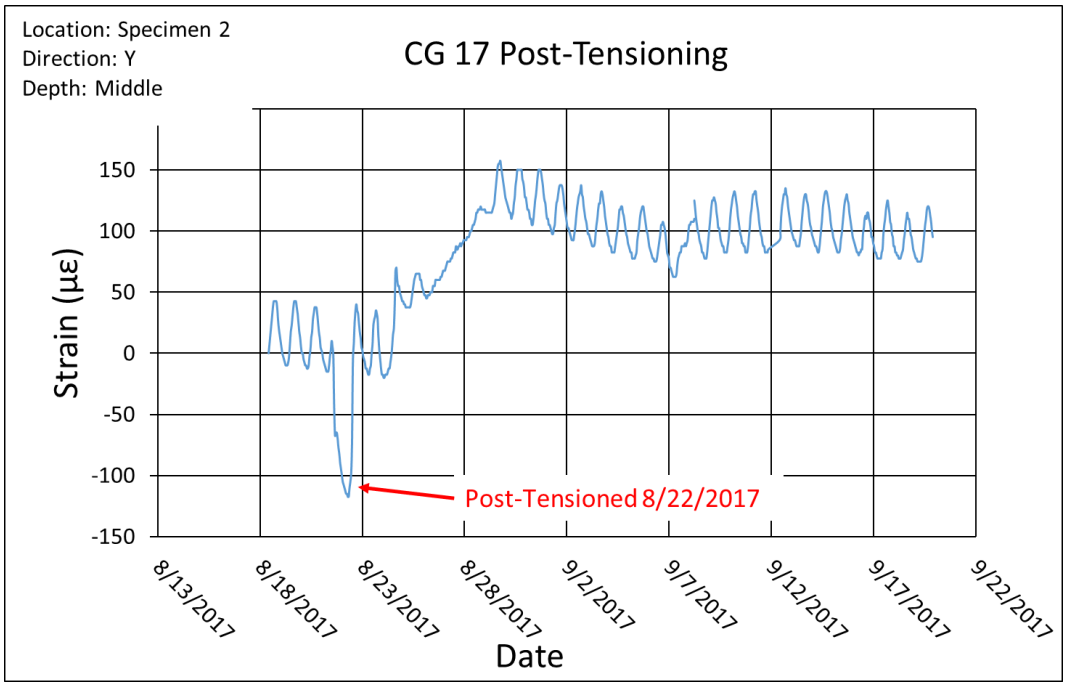

Figure 193 Concrete Gage 17 Strain Data During Post-Tensioning

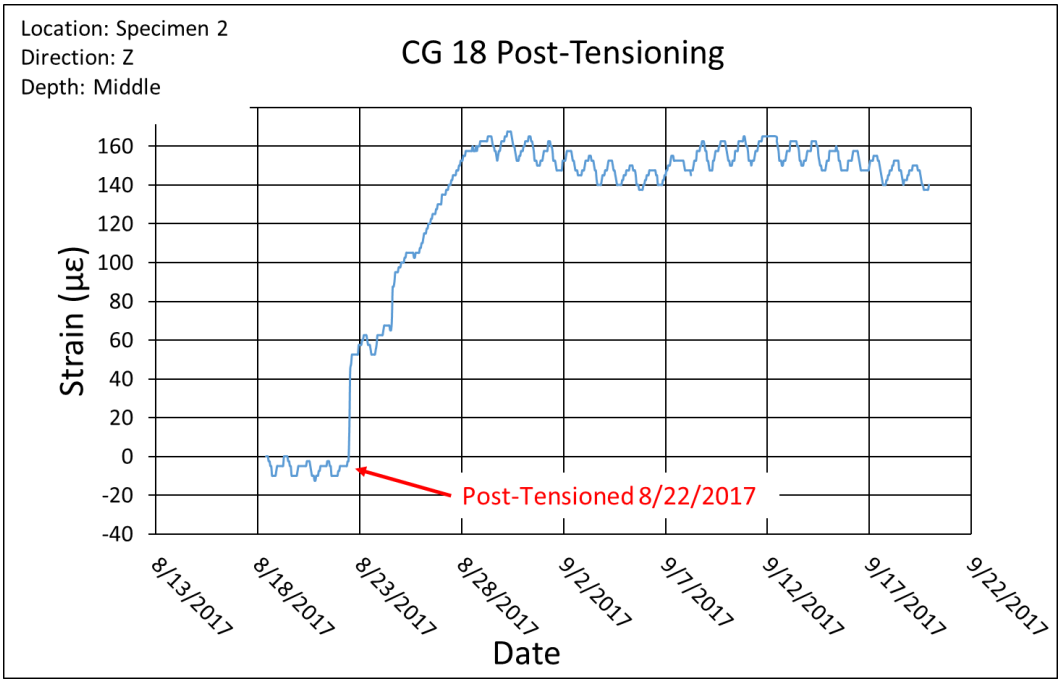

Figure 194 Concrete Gage 18 Strain Data During Post-Tensioning

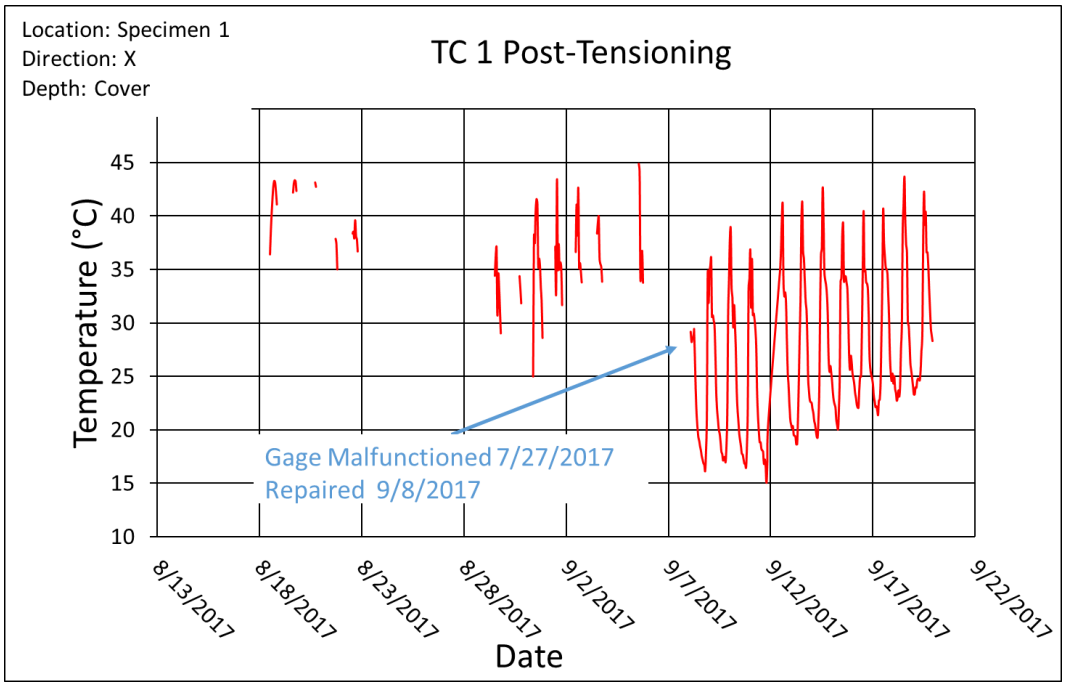

Figure 195 Thermocouple 1 Temperature Data During Post-Tensioning

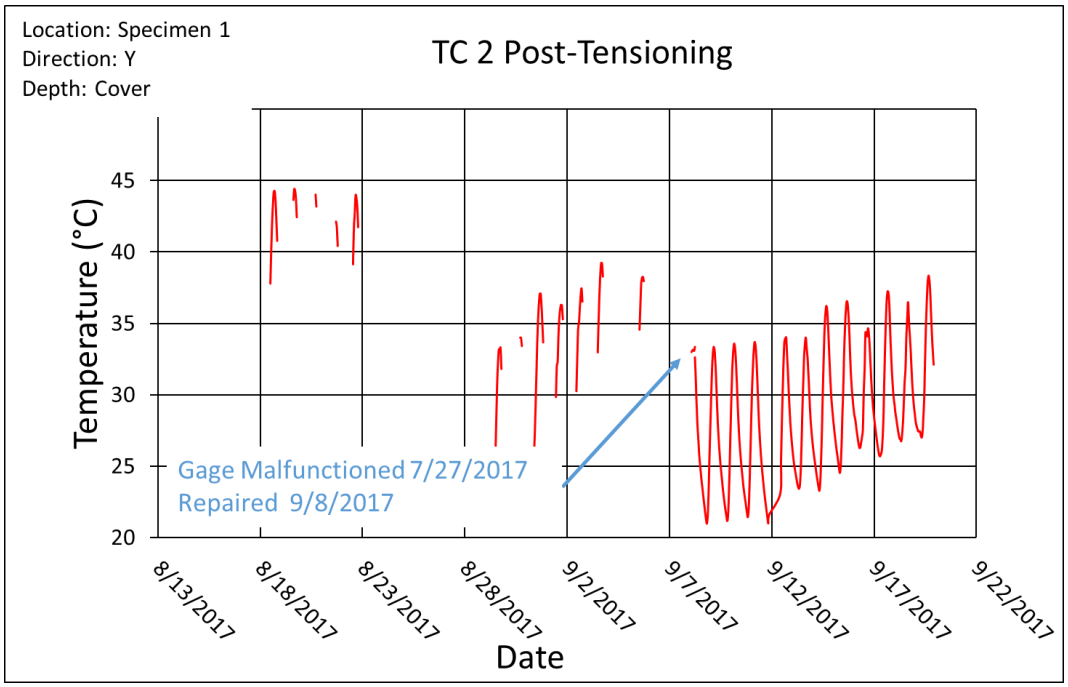

Figure 196 Thermocouple 2 Temperature Data During Post-Tensioning

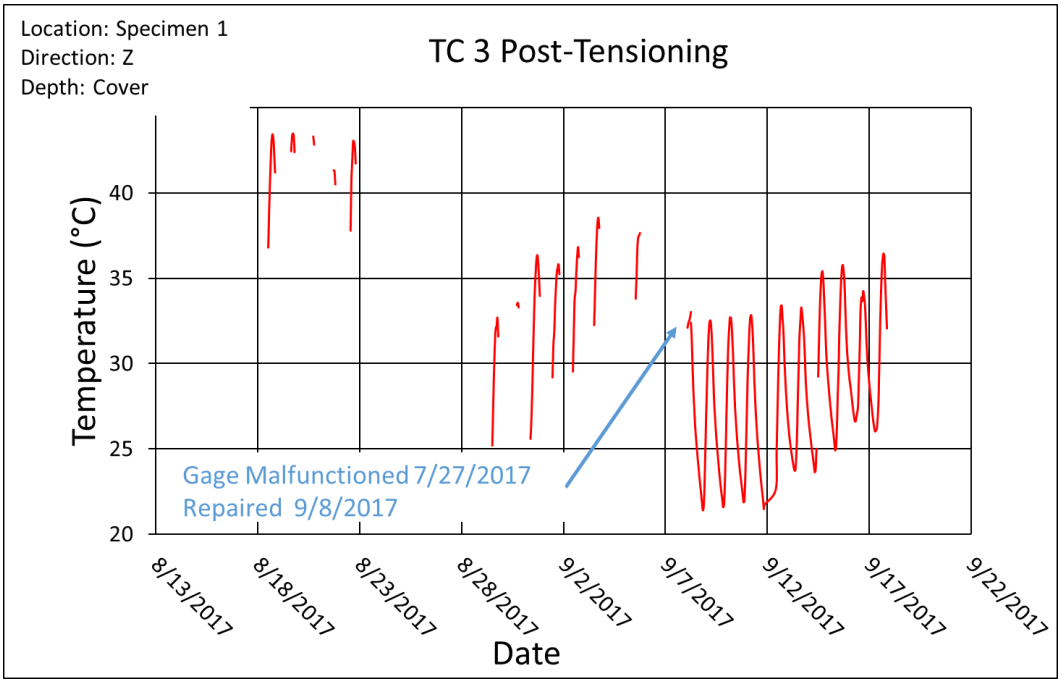

Figure 197 Thermocouple 3 Temperature Data During Post-Tensioning

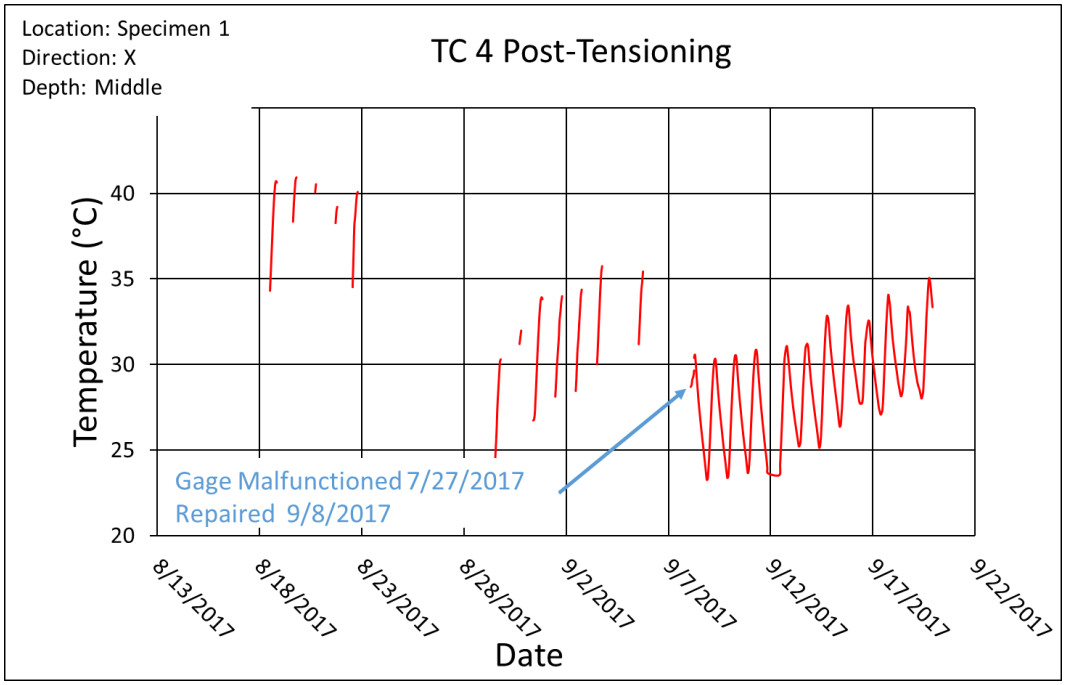

Figure 198 Thermocouple 4 Temperature Data During Post-Tensioning

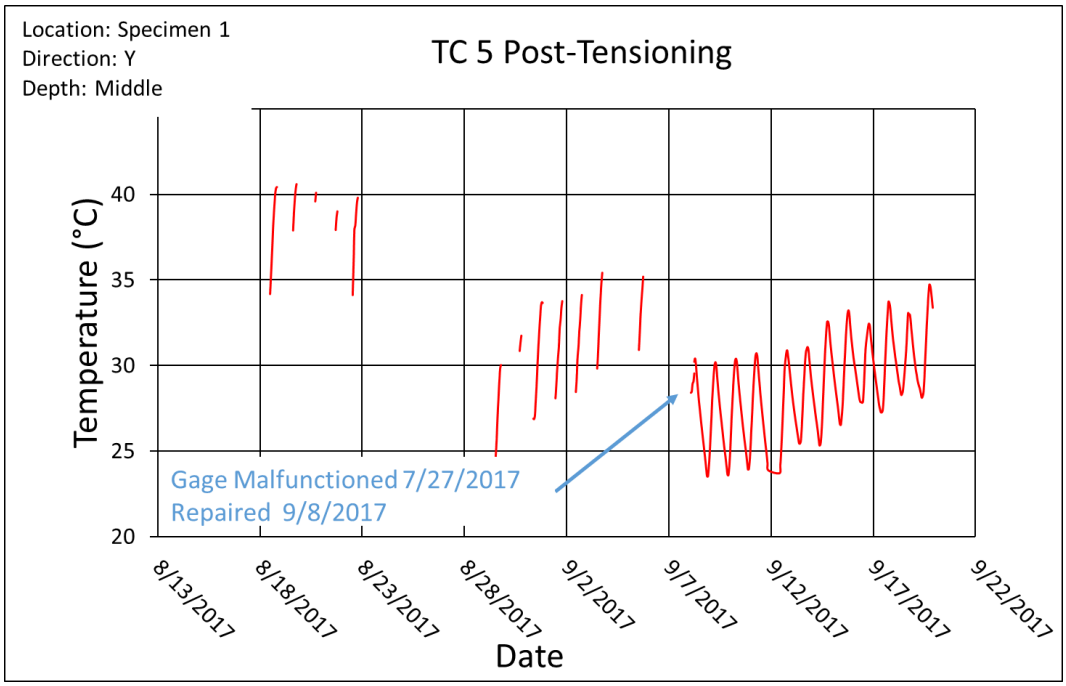

Figure 199 Thermocouple 5 Temperature Data During Post-Tensioning

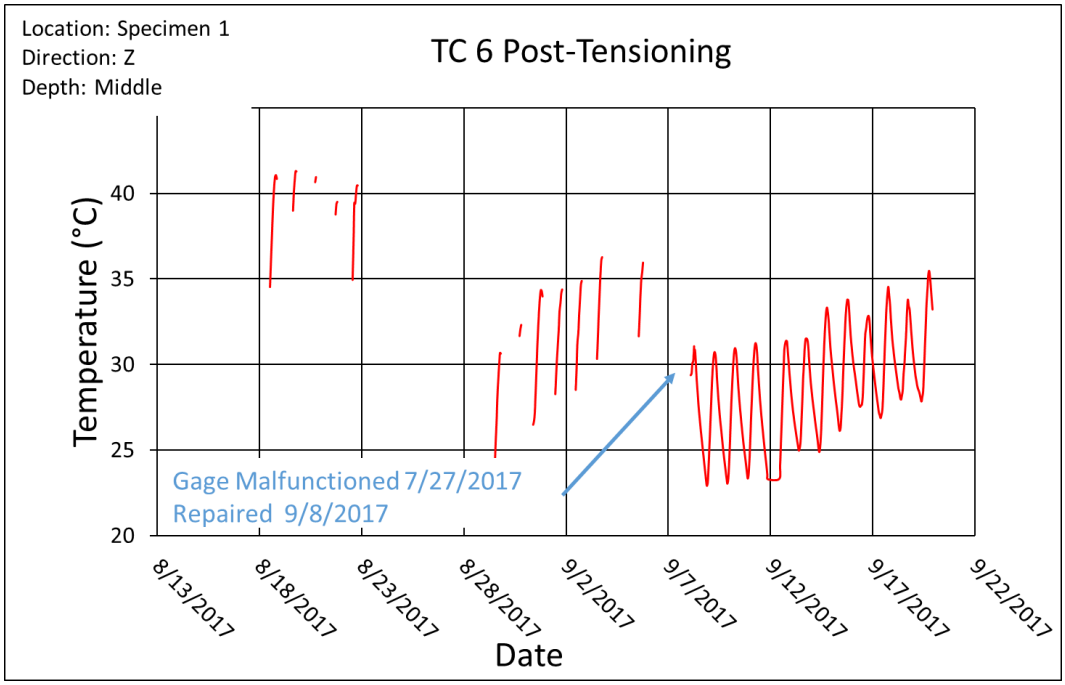

Figure 200 Thermocouple 6 Temperature Data During Post-Tensioning

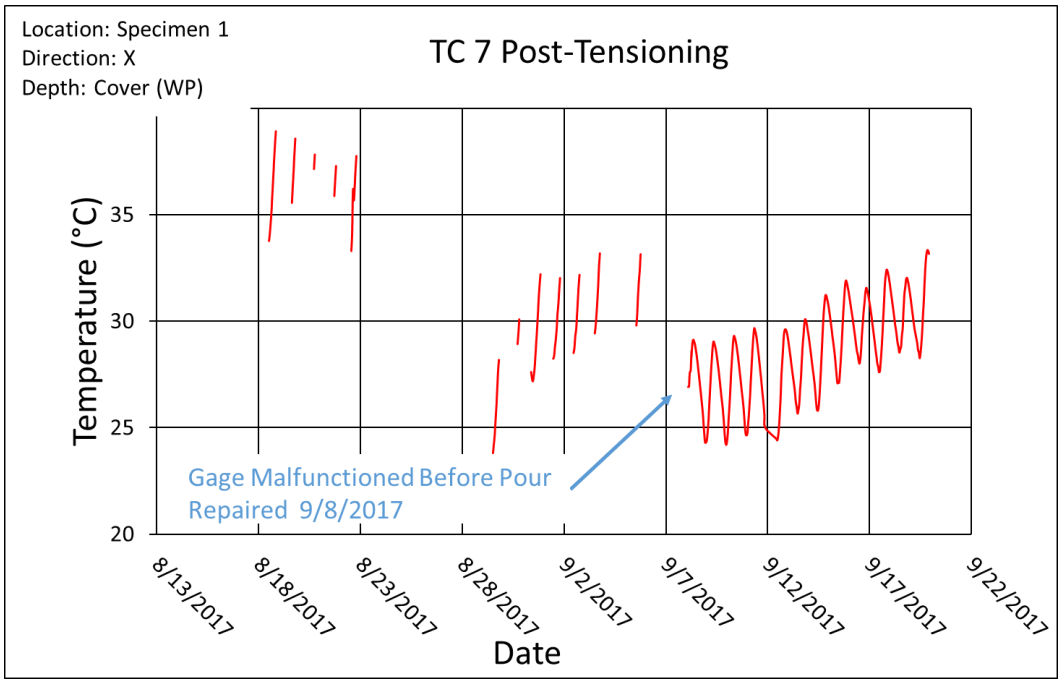

Figure 201 Thermocouple 7 Temperature Data During Post-Tensioning

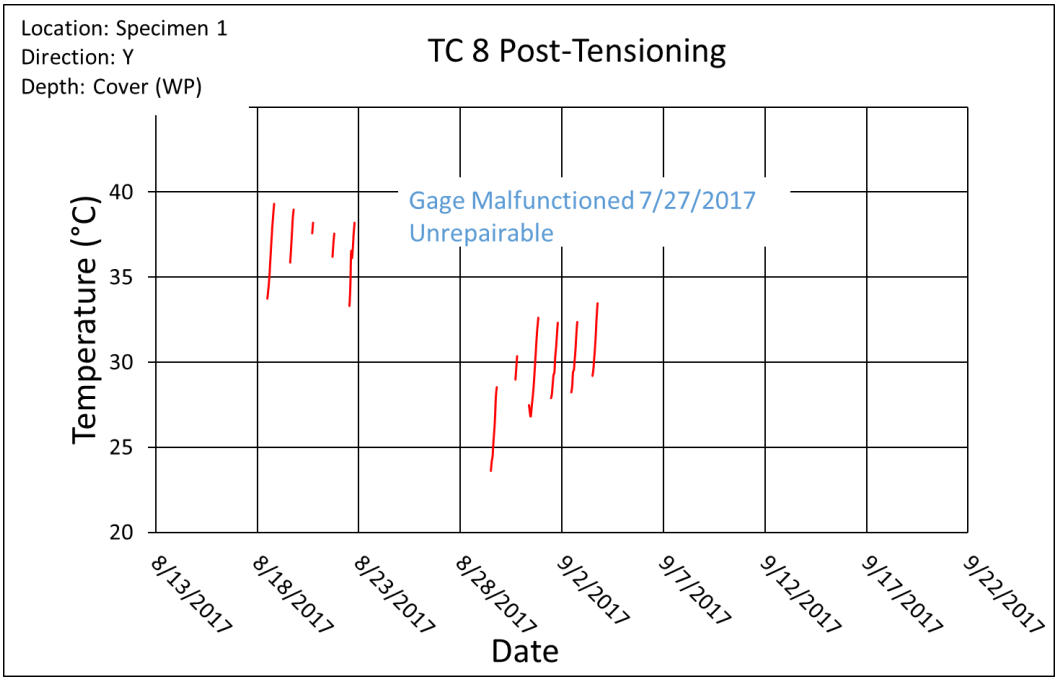

Figure 202 Thermocouple 8 Temperature Data During Post-Tensioning

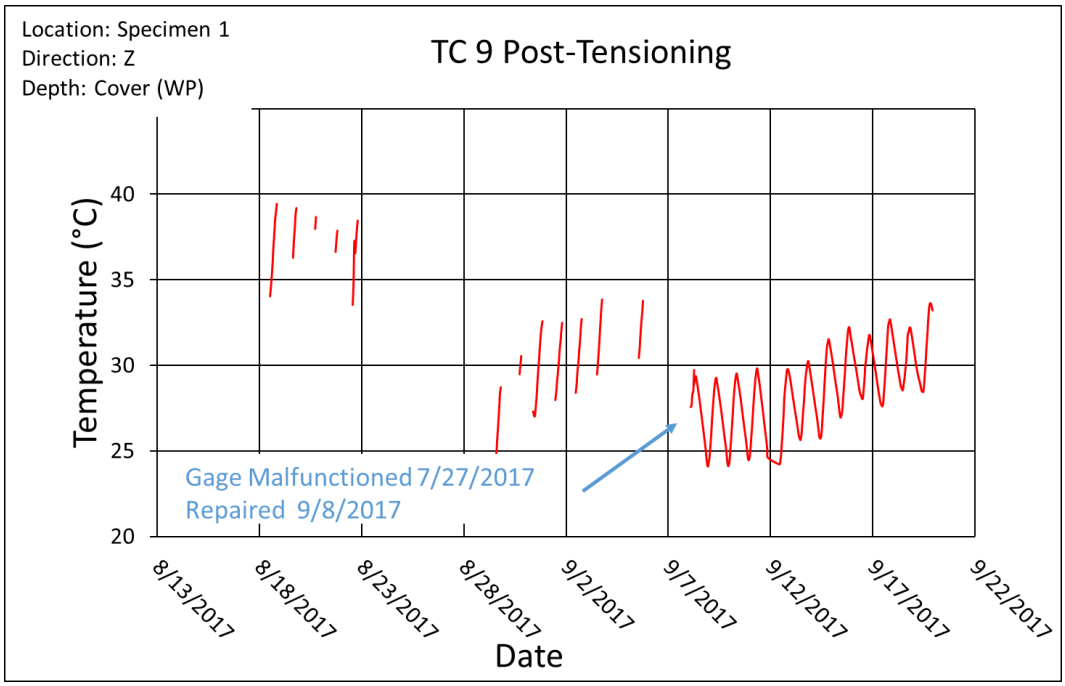

Figure 203 Thermocouple 9 Temperature Data During Post-Tensioning

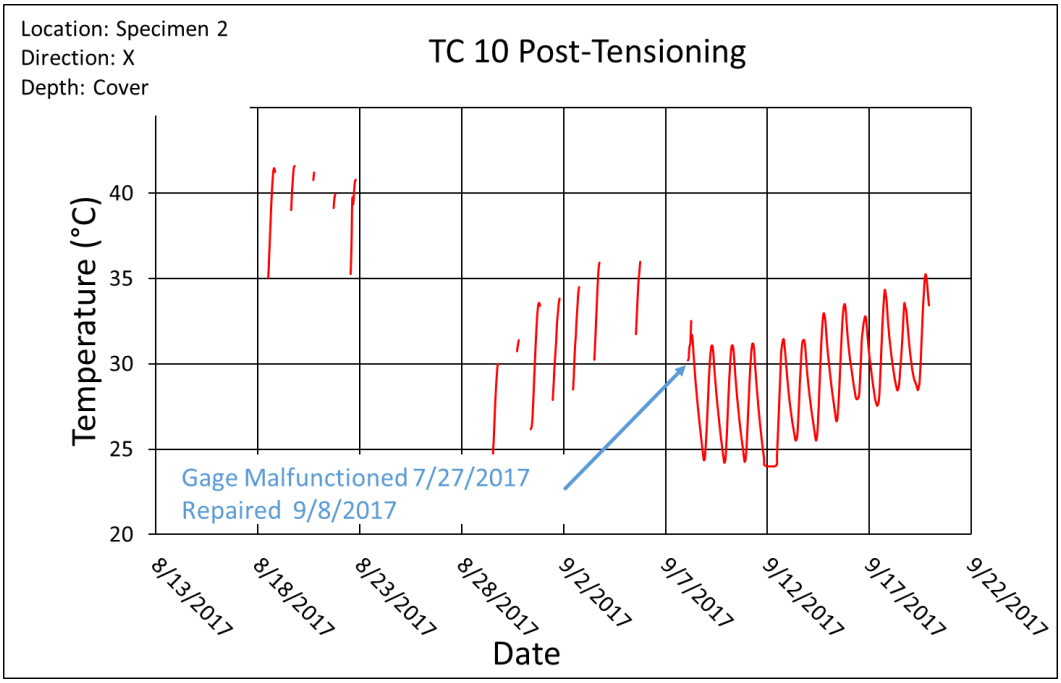

Figure 204 Thermocouple 10 Temperature Data During Post-Tensioning

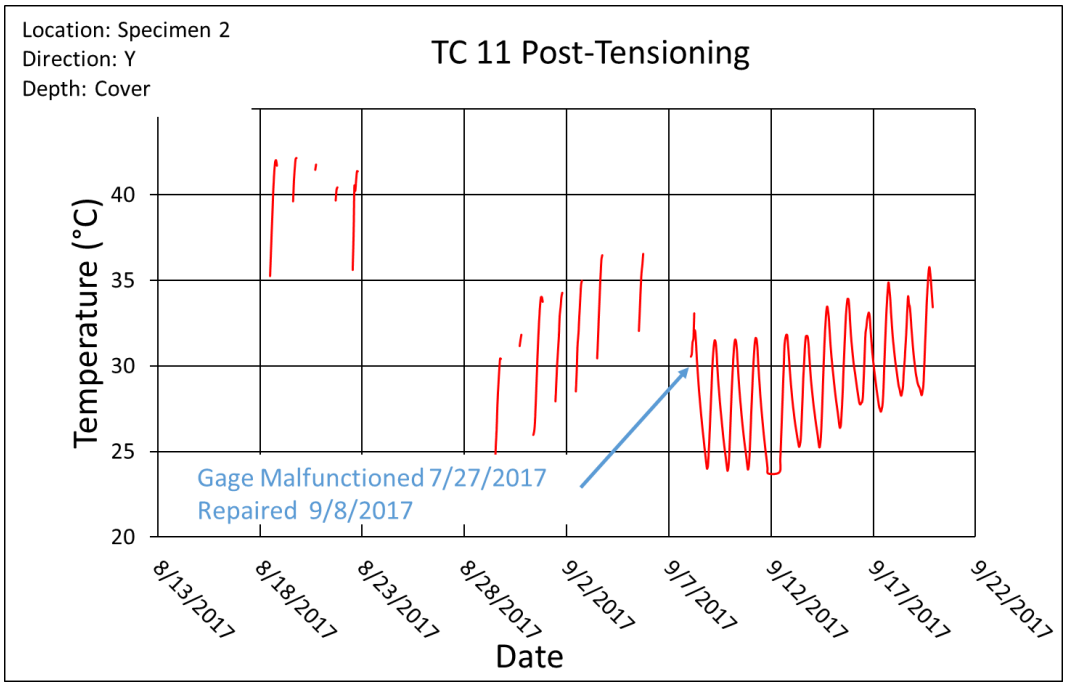

Figure 205 Thermocouple 11 Temperature Data During Post-Tensioning

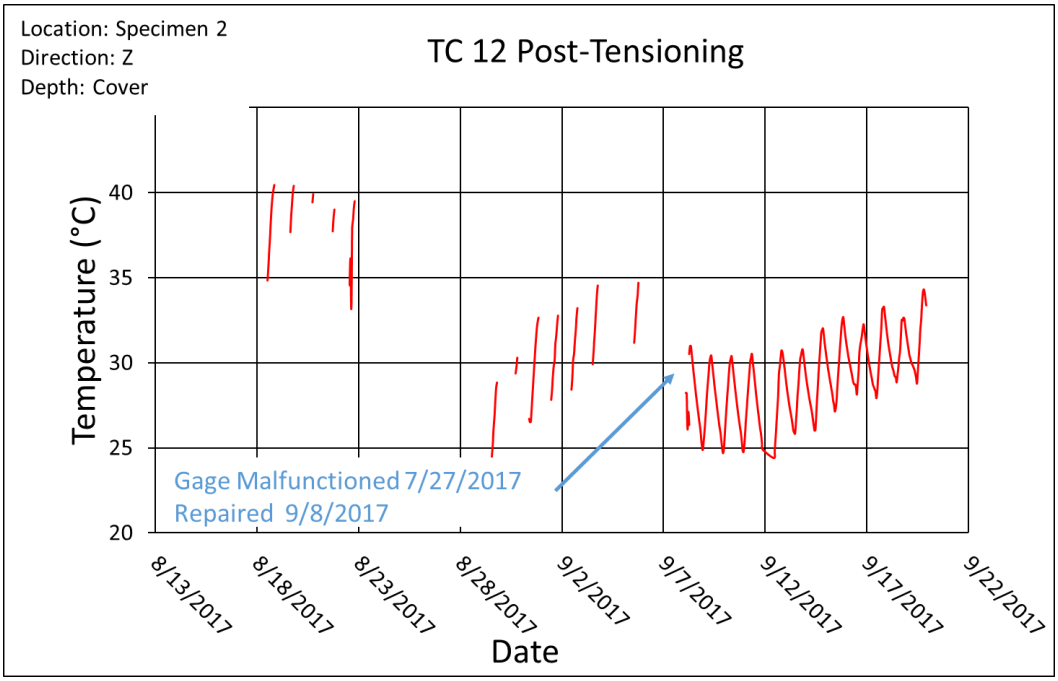

Figure 206 Thermocouple 12 Temperature Data During Post-Tensioning

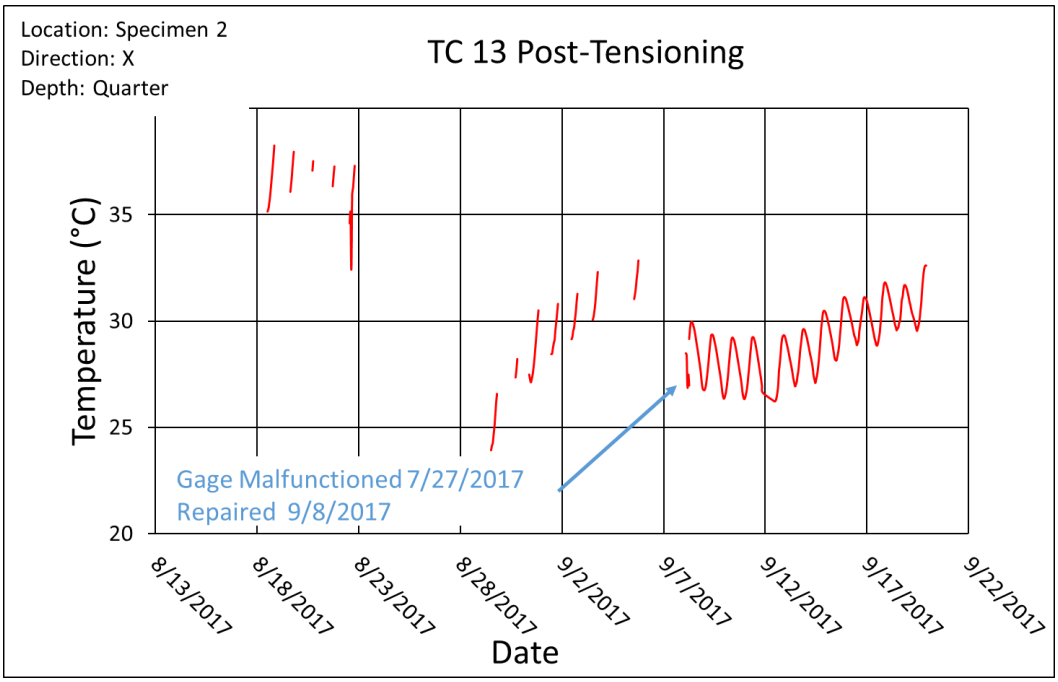

Figure 207 Thermocouple 13 Temperature Data During Post-Tensioning

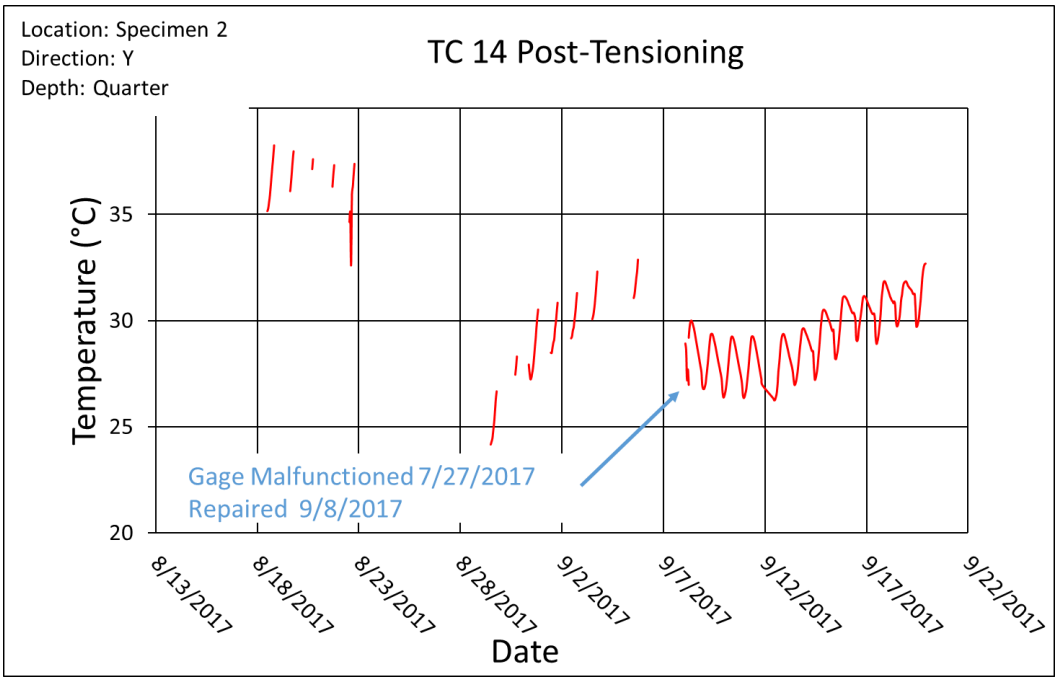

Figure 208 Thermocouple 14 Temperature Data During Post-Tensioning

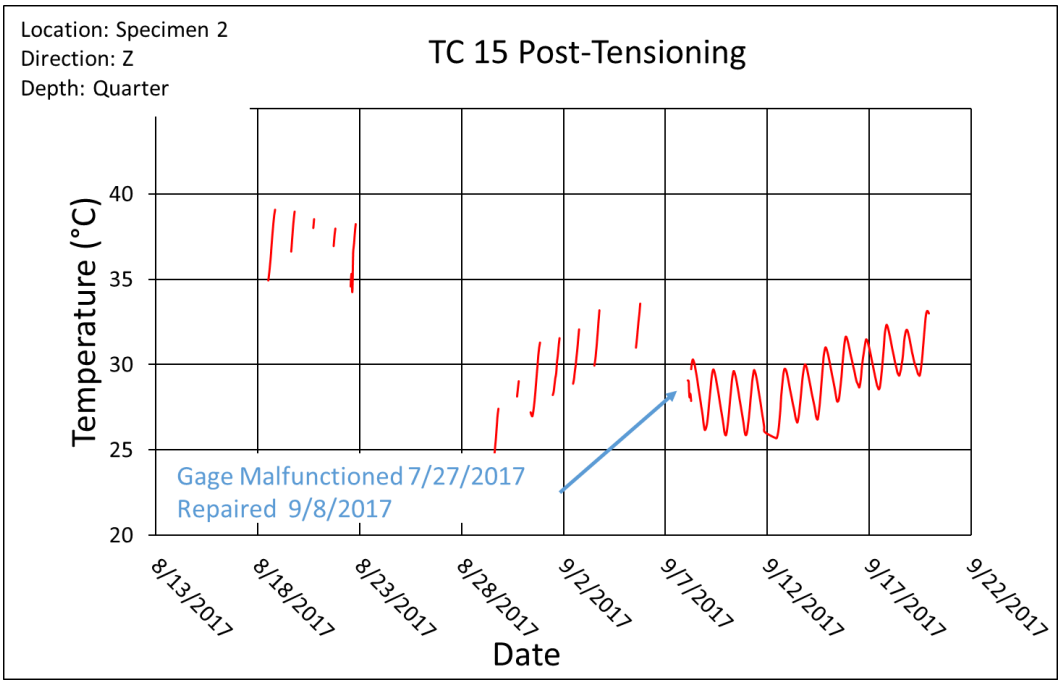

Figure 209 Thermocouple 15 Temperature Data During Post-Tensioning

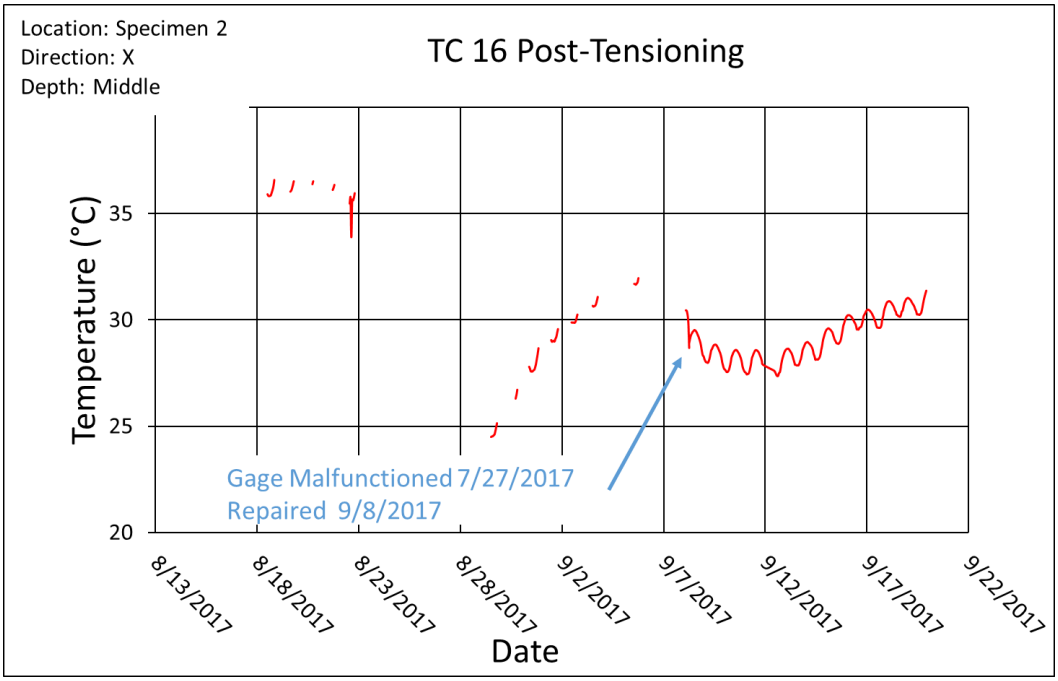

Figure 210 Thermocouple 16 Temperature Data During Post-Tensioning

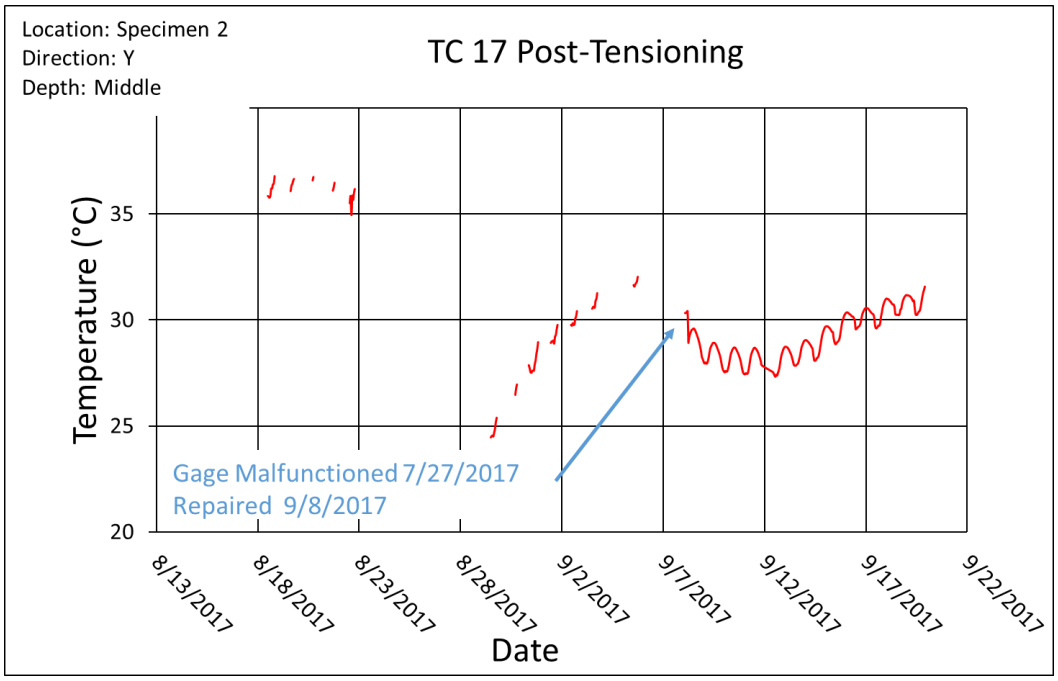

Figure 211 Thermocouple 17 Temperature Data During Post-Tensioning

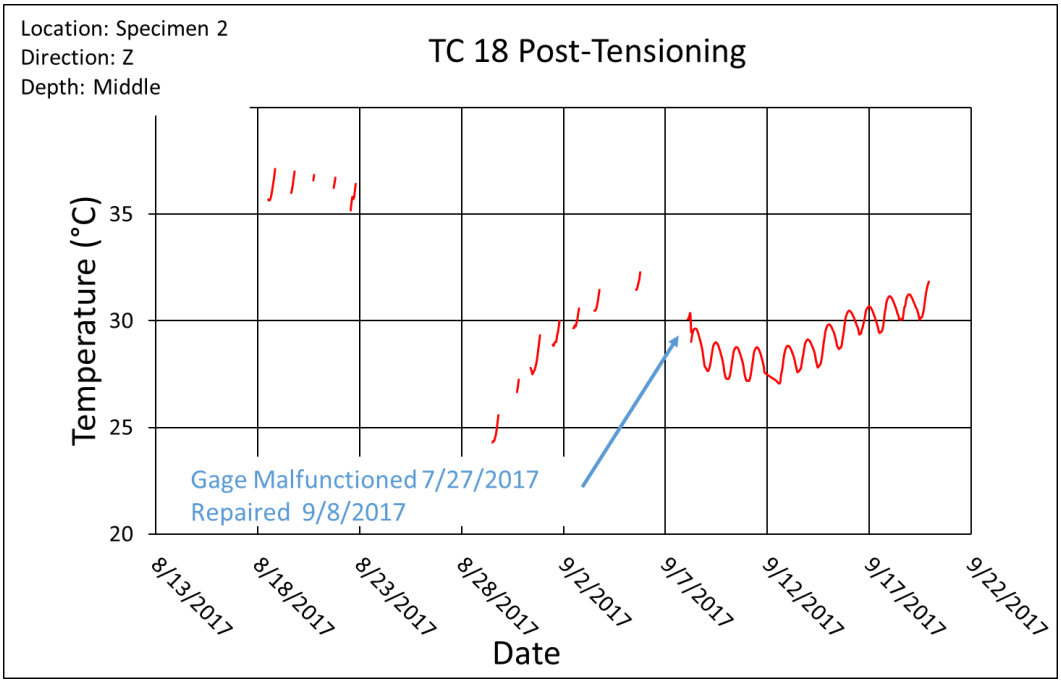

Figure 212 Thermocouple 18 Temperature Data During Post-Tensioning

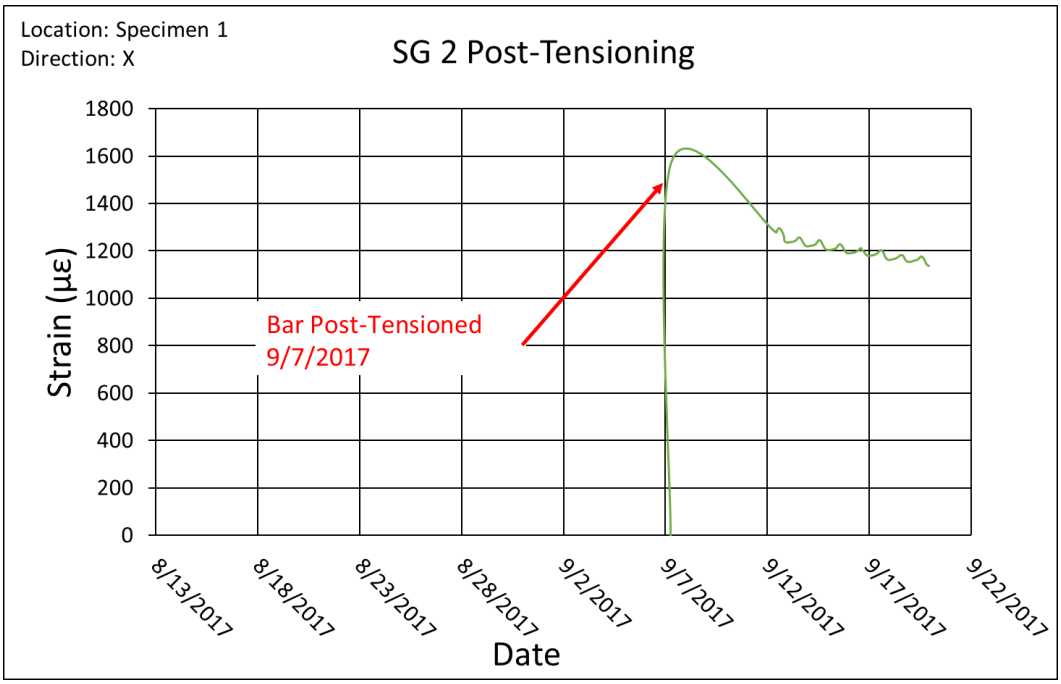

Figure 213 Post-Tensioning Bar Strain Gage 2 Strain Data During Post-Tensioning

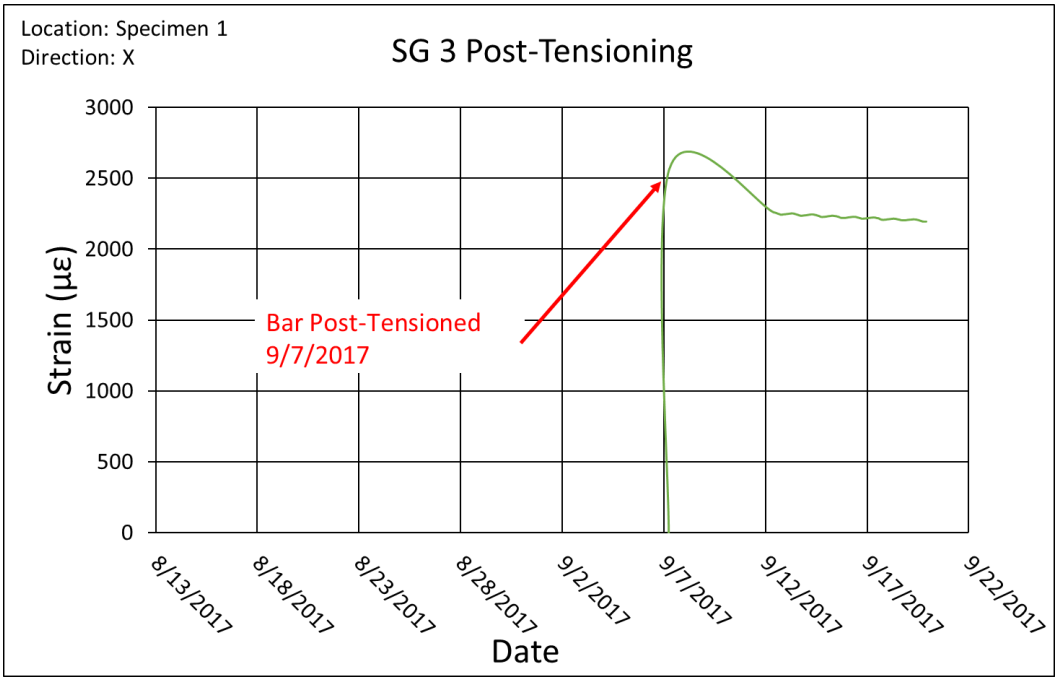

Figure 214 Post-Tensioning Bar Strain Gage 3 Strain Data During Post-Tensioning

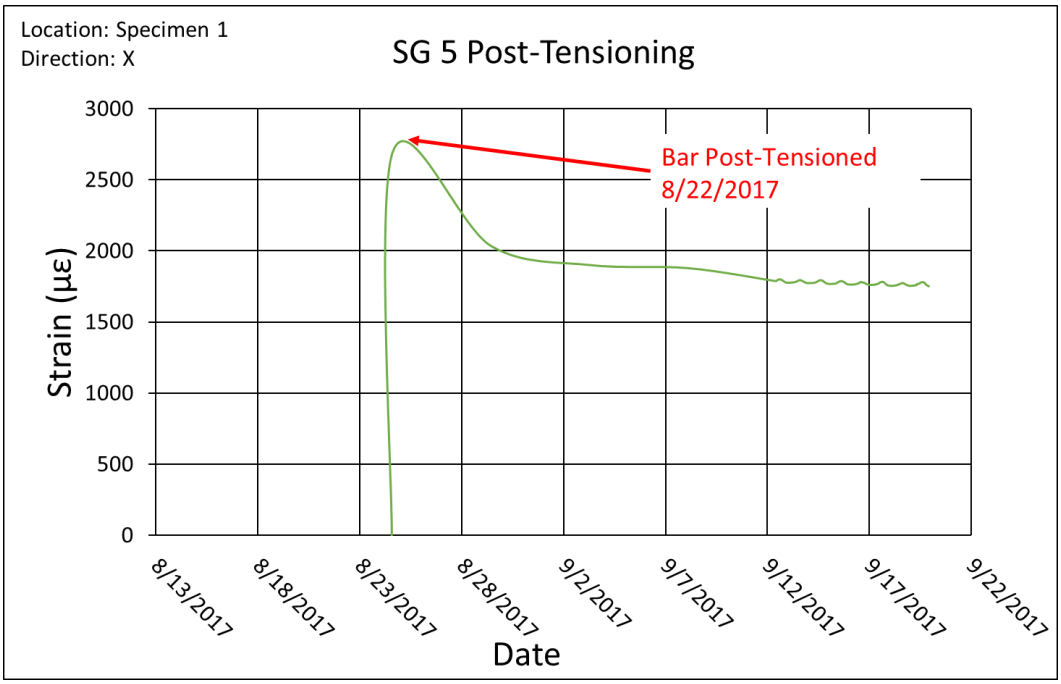

Figure 215 Post-Tensioning Bar Strain Gage 5 Strain Data During Post-Tensioning

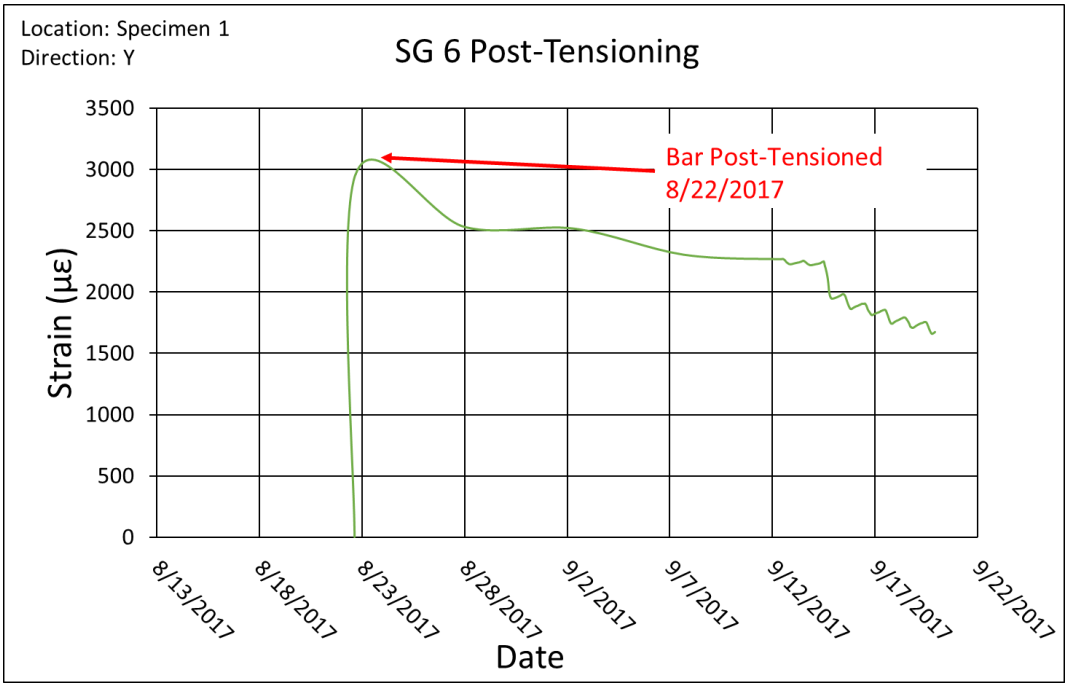

Figure 216 Post-Tensioning Bar Strain Gage 6 Strain Data During Post-Tensioning

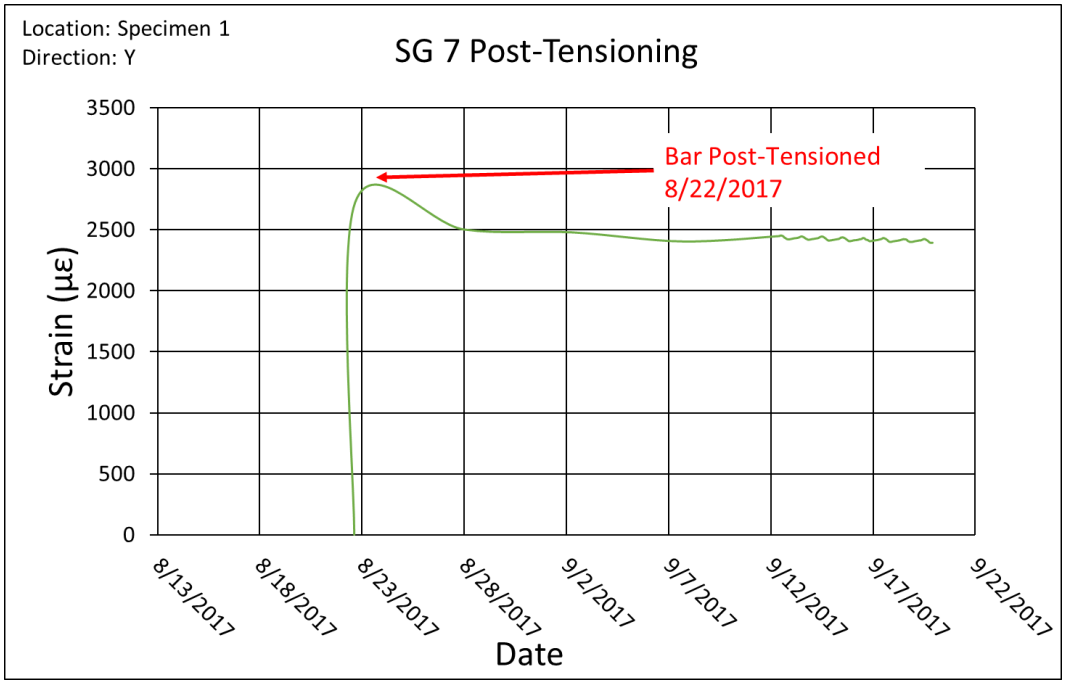

Figure 217 Post-Tensioning Bar Strain Gage 7 Strain Data During Post-Tensioning

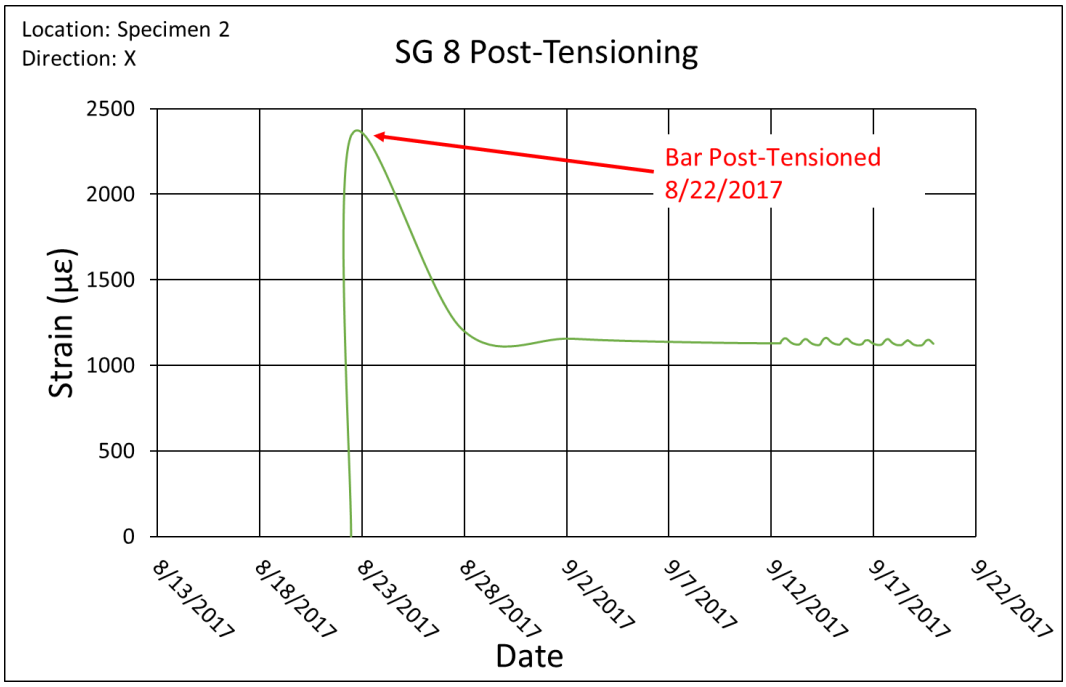

Figure 218 Post-Tensioning Bar Strain Gage 8 Strain Data During Post-Tensioning

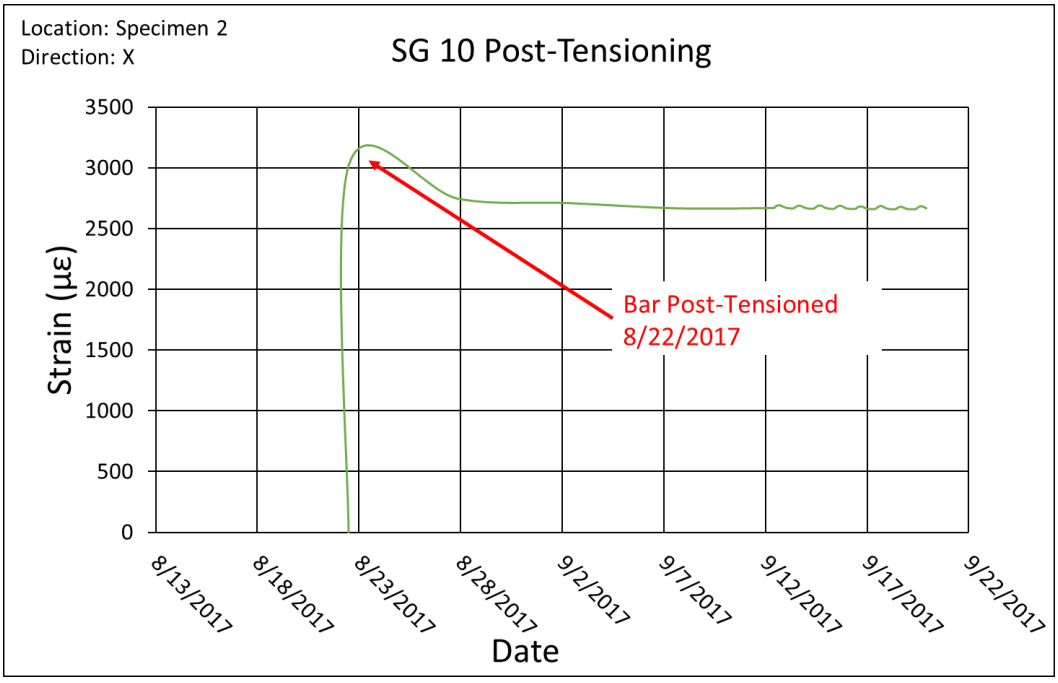

Figure 219 Post-Tensioning Bar Strain Gage 10 Strain Data During Post-Tensioning

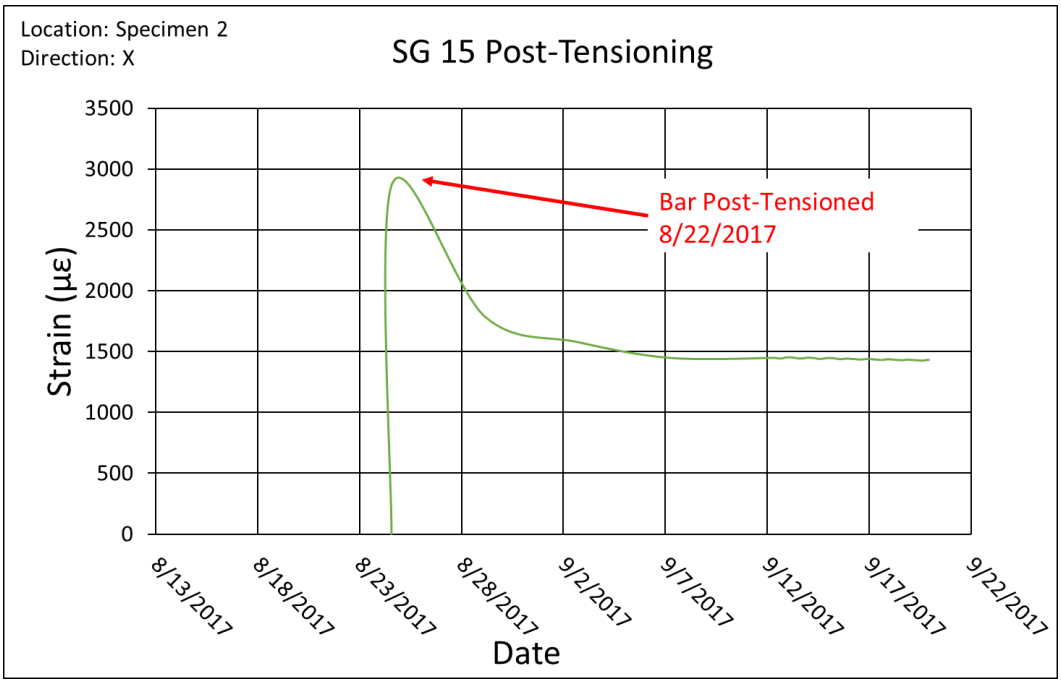

Figure 220 Post-Tensioning Bar Strain Gage 15 Strain Data During Post-Tensioning

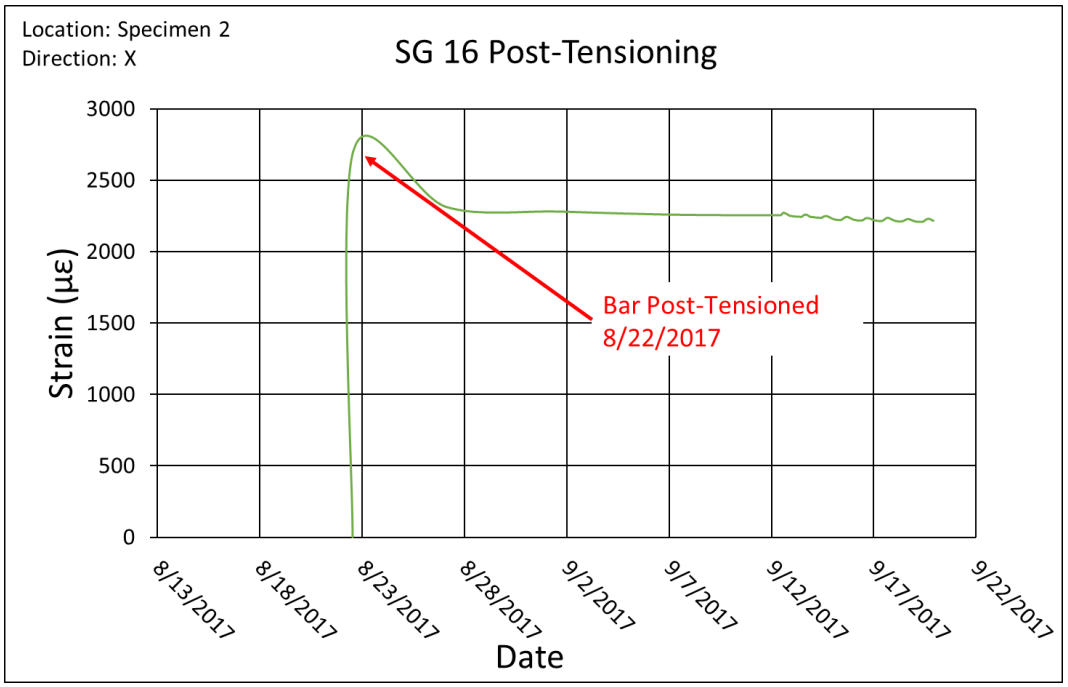

Figure 221 Post-Tensioning Bar Strain Gage 16 Strain Data During Post-Tensioning

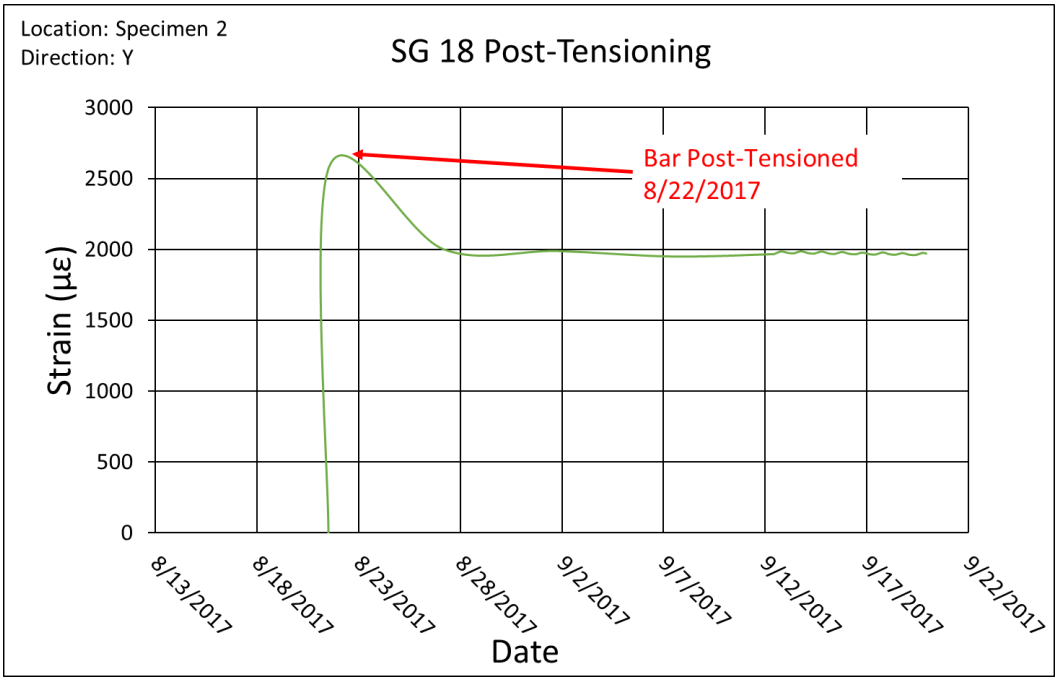

Figure 222 Post-Tensioning Bar Strain Gage 18 Strain Data During Post-Tensioning

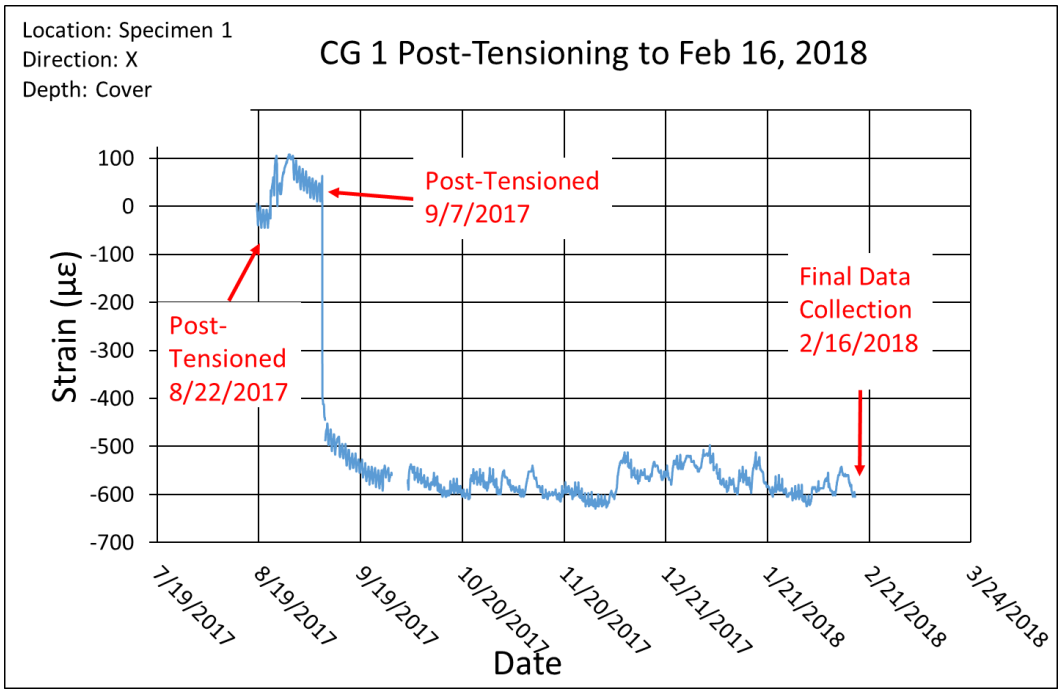

Figure 223 Concrete Gage 1 Strain Data from Post-Tensioning to February 16, 2018

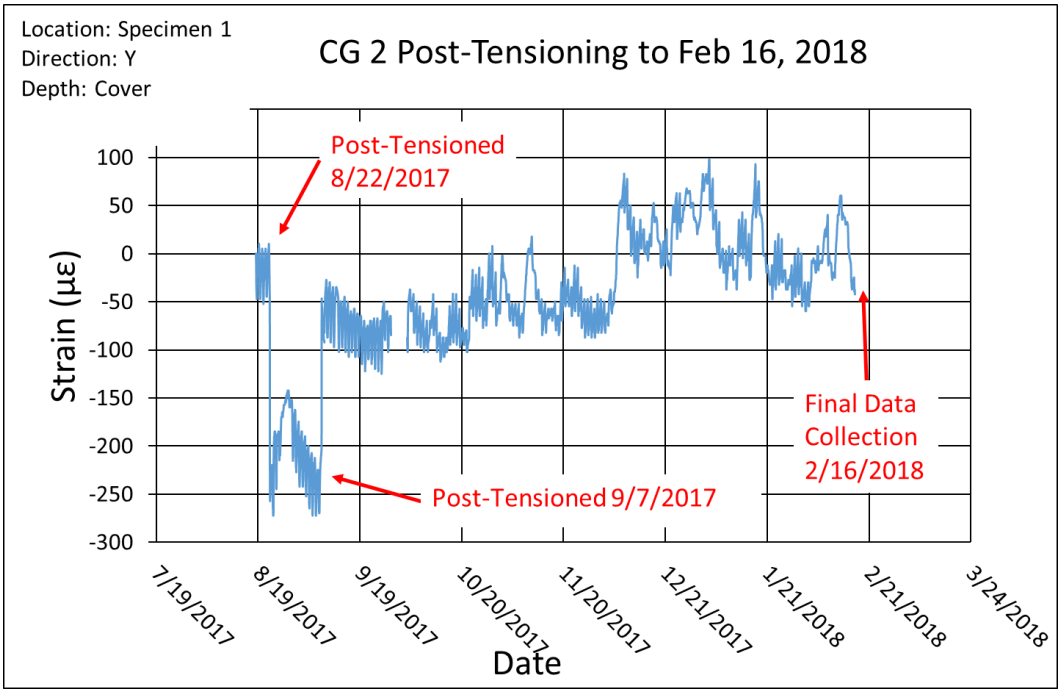

Figure 224 Concrete Gage 2 Strain Data from Post-Tensioning to February 16, 2018

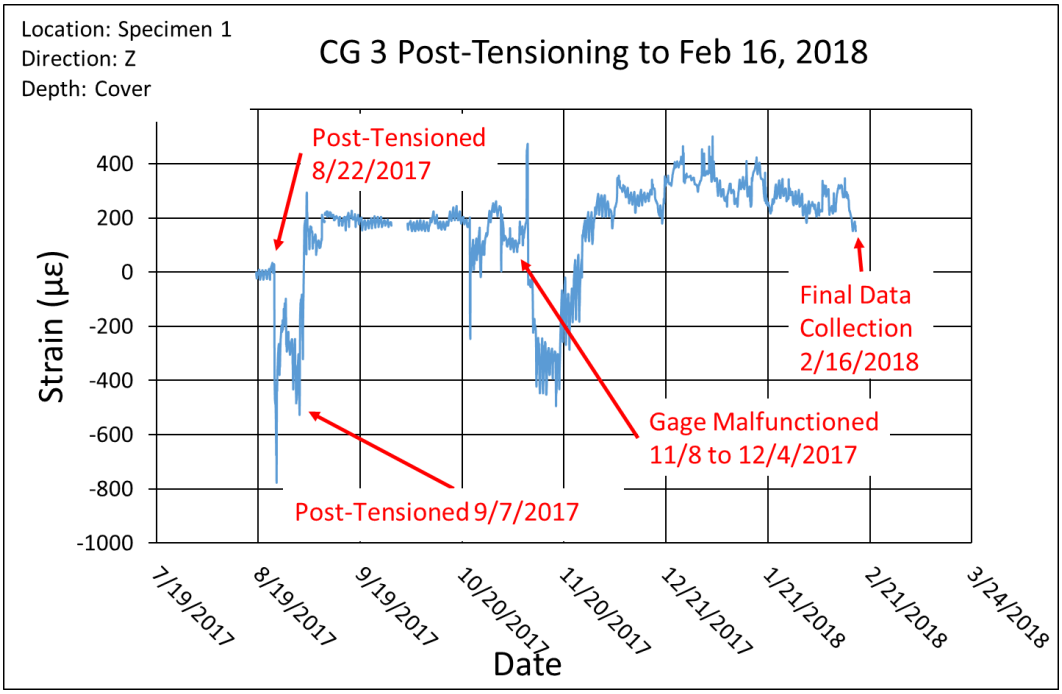

Figure 225 Concrete Gage 3 Strain Data from Post-Tensioning to February 16, 2018

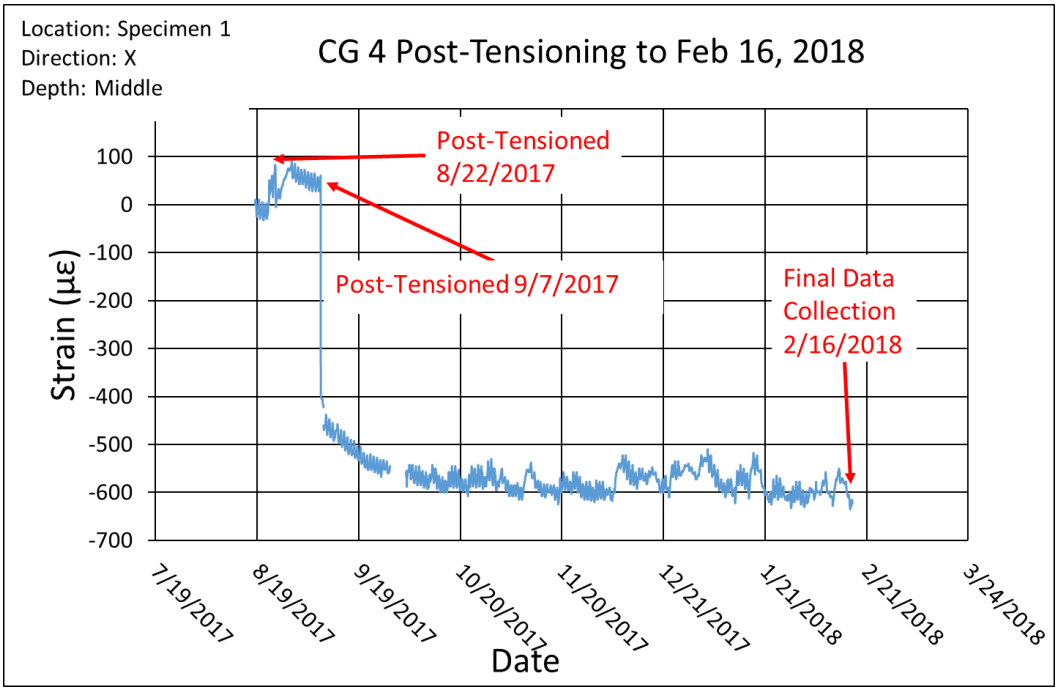

Figure 226 Concrete Gage 4 Strain Data from Post-Tensioning to February 16, 2018

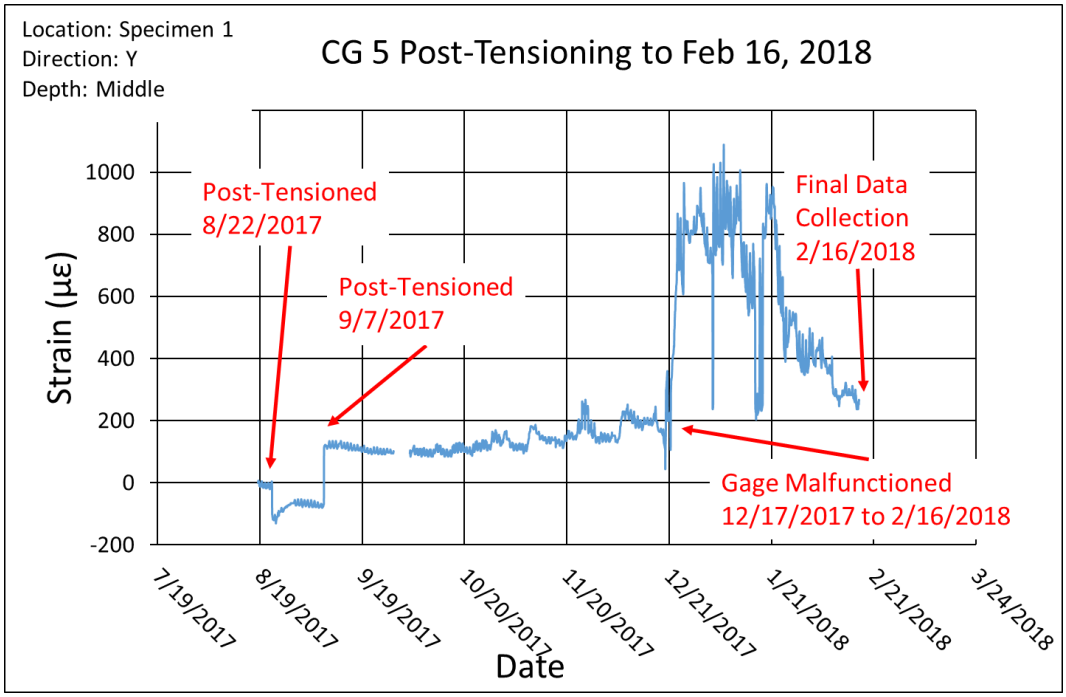

Figure 227 Concrete Gage 5 Strain Data from Post-Tensioning to February 16, 2018

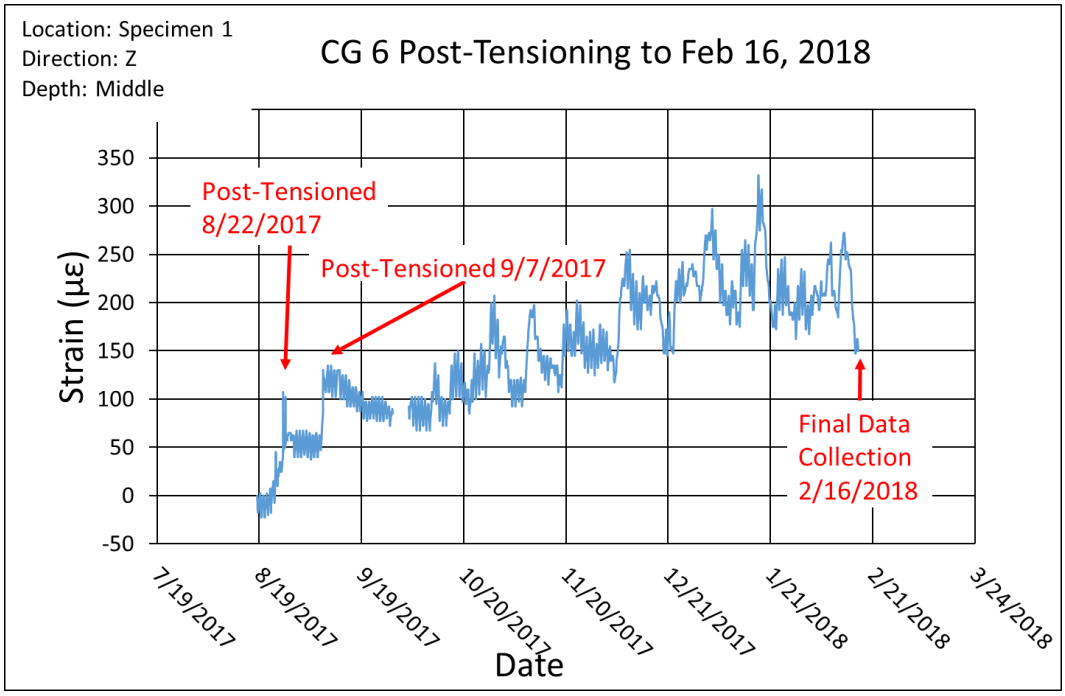

Figure 228 Concrete Gage 6 Strain Data from Post-Tensioning to February 16, 2018

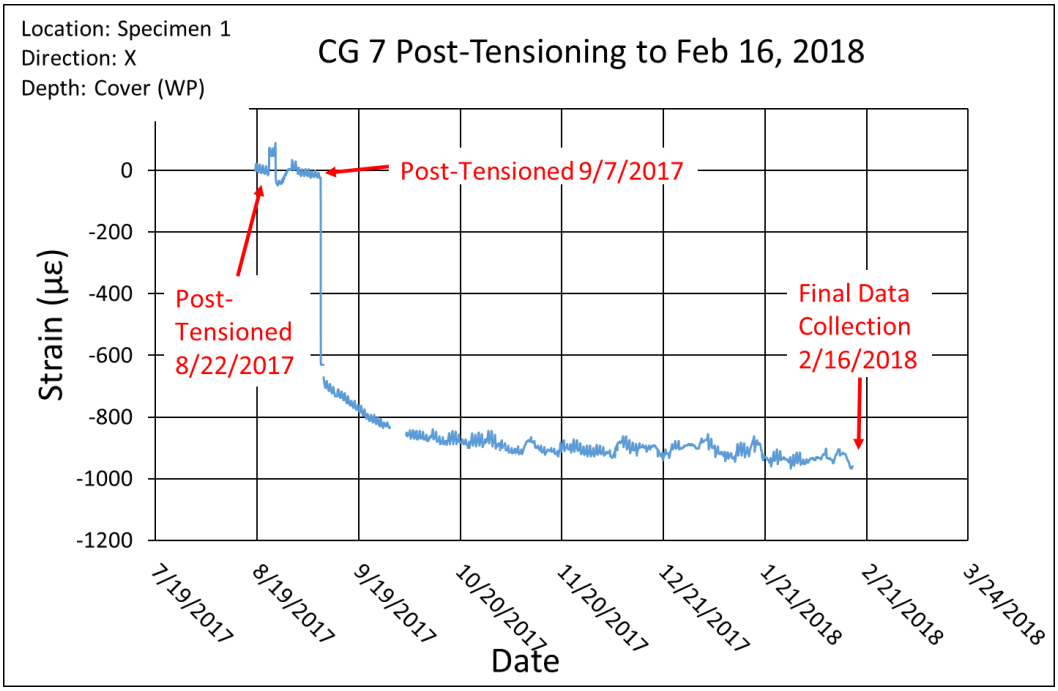

Figure 229 Concrete Gage 7 Strain Data from Post-Tensioning to February 16, 2018

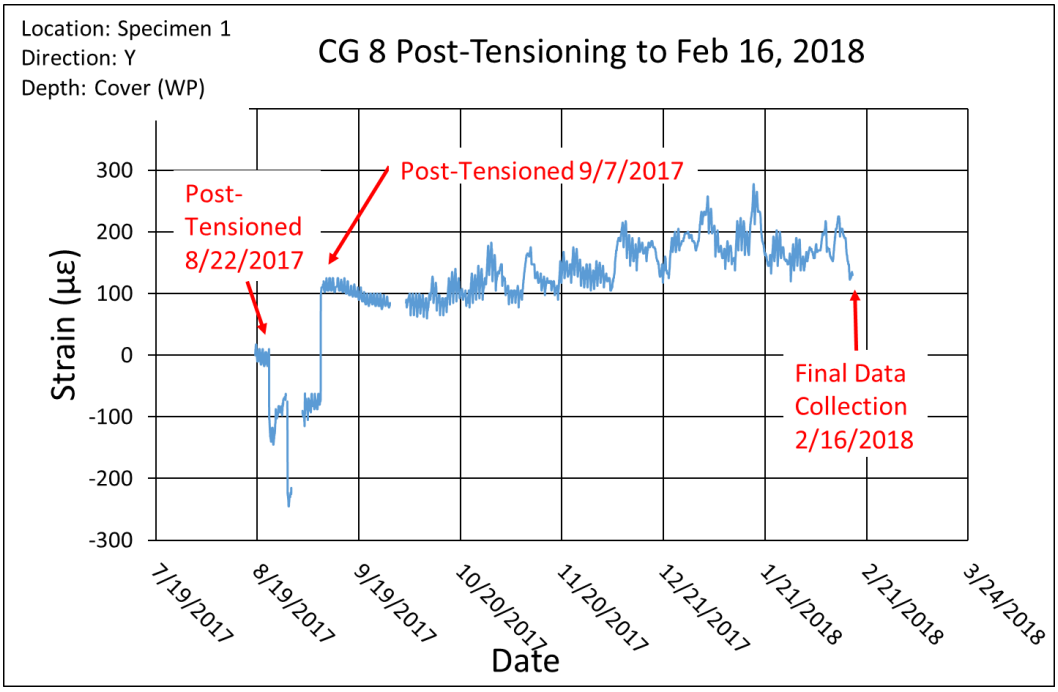

Figure 230 Concrete Gage 8 Strain Data from Post-Tensioning to February 16, 2018

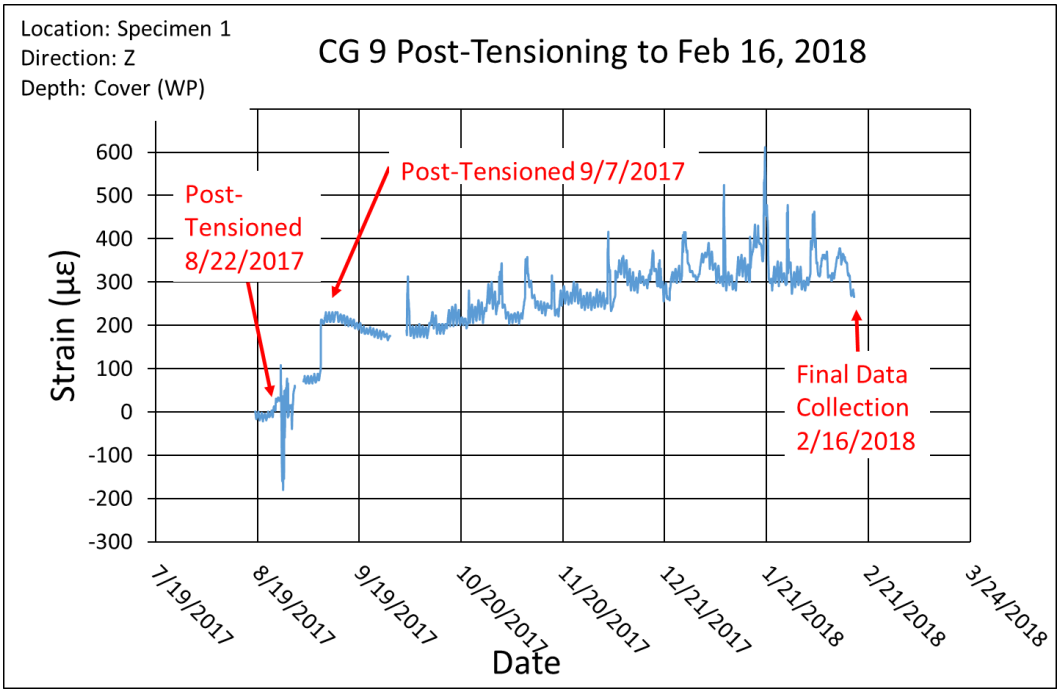

Figure 231 Concrete Gage 9 Strain Data from Post-Tensioning to February 16, 2018

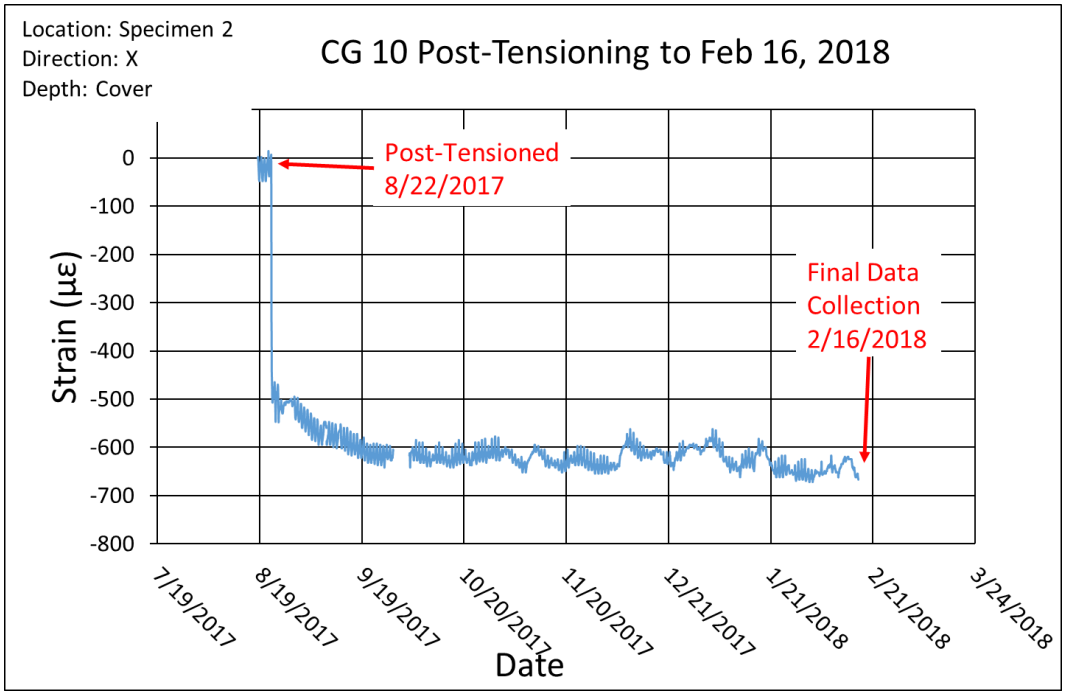

Figure 232 Concrete Gage 10 Strain Data from Post-Tensioning to February 16, 2018

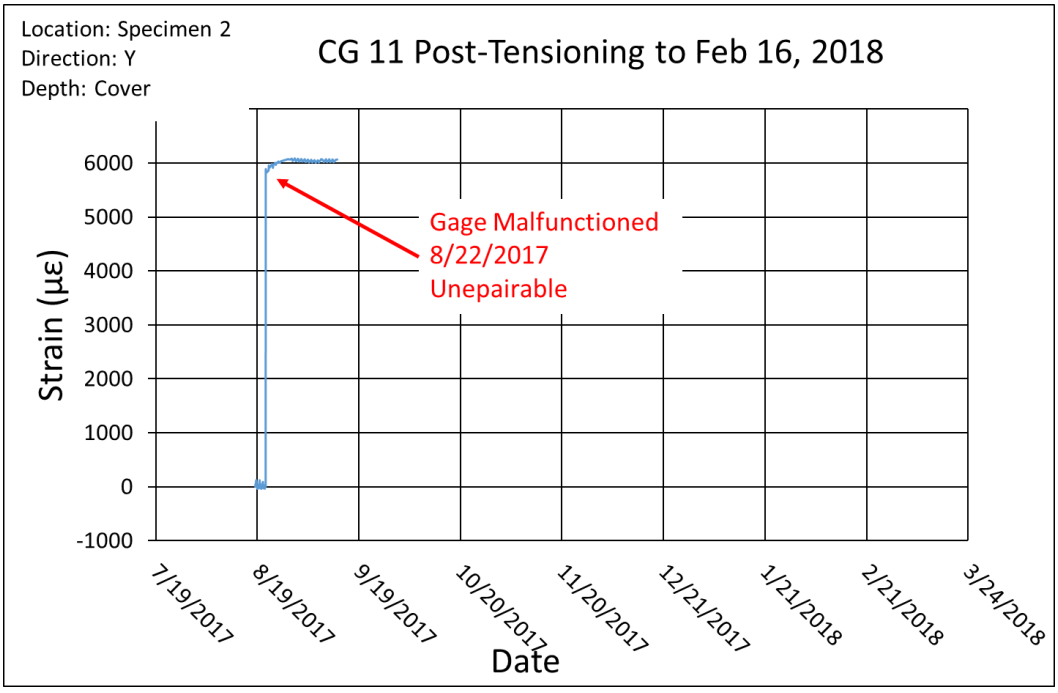

Figure 233 Concrete Gage 11 Strain Data from Post-Tensioning to February 16, 2018

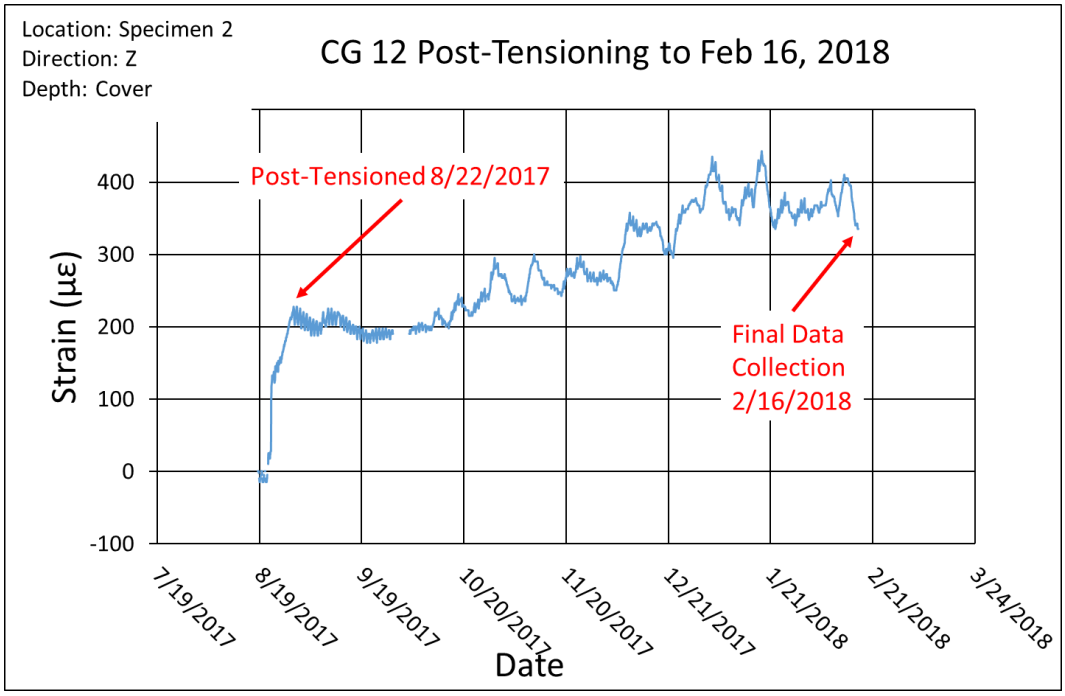

Figure 234 Concrete Gage 12 Strain Data from Post-Tensioning to February 16, 2018

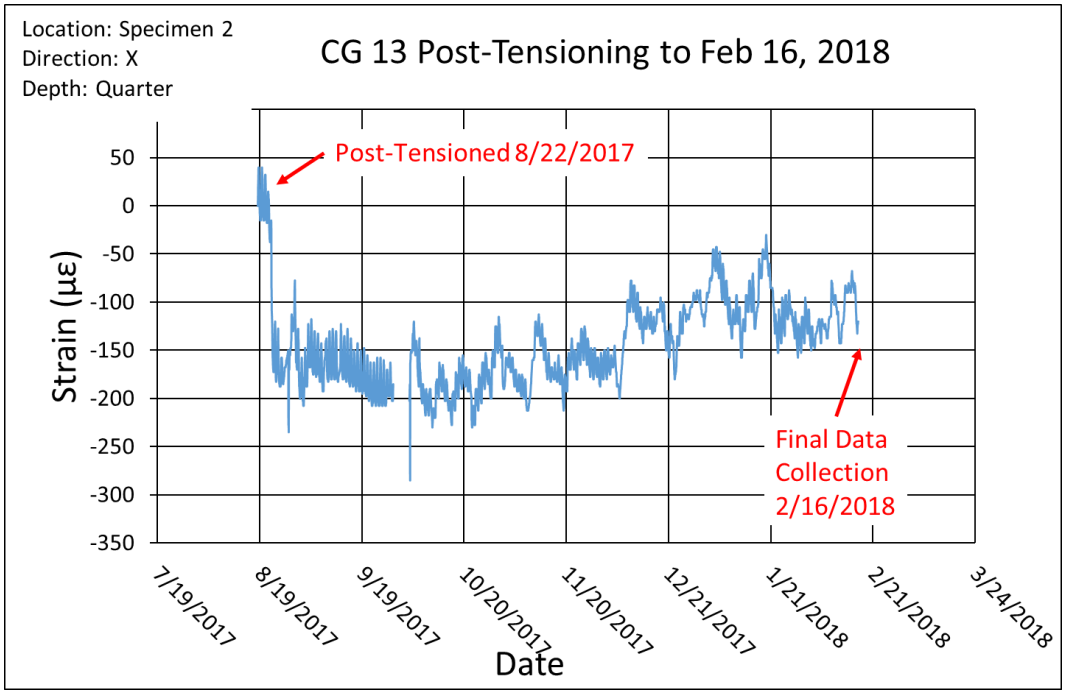

Figure 235 Concrete Gage 13 Strain Data from Post-Tensioning to February 16, 2018

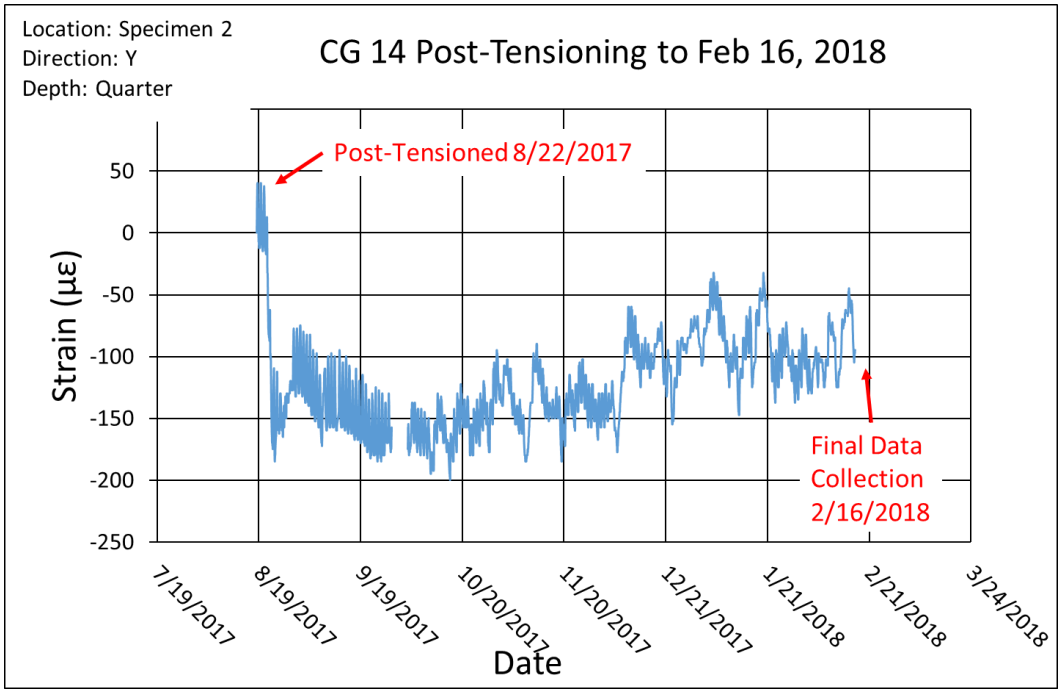

Figure 236 Concrete Gage 14 Strain Data from Post-Tensioning to February 16, 2018

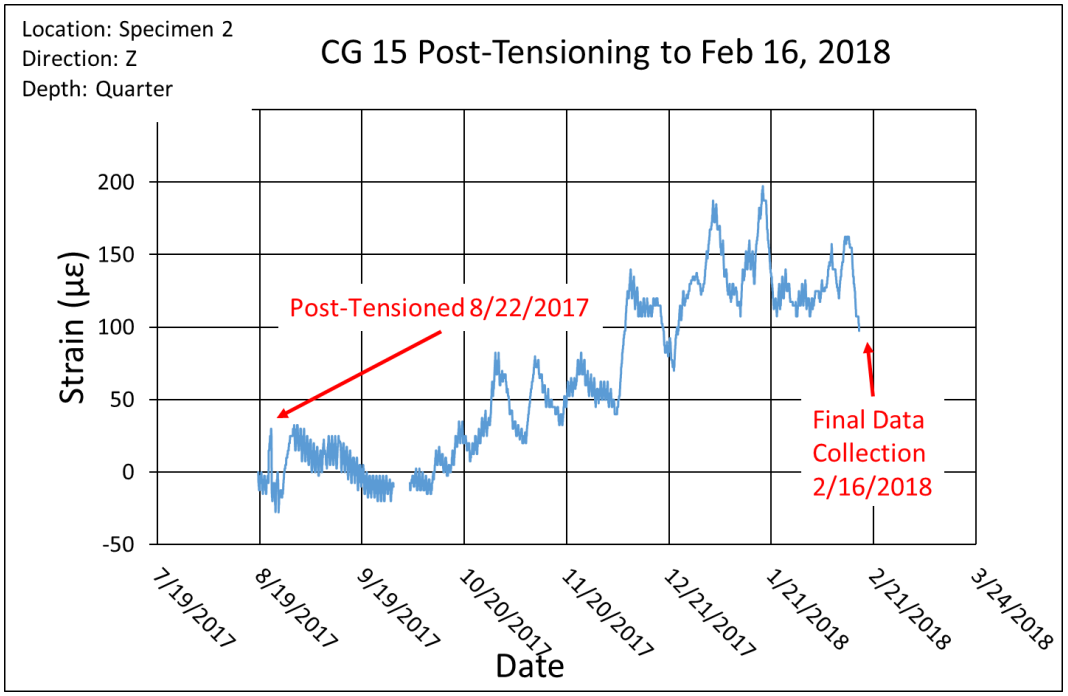

Figure 237 Concrete Gage 15 Strain Data from Post-Tensioning to February 16, 2018

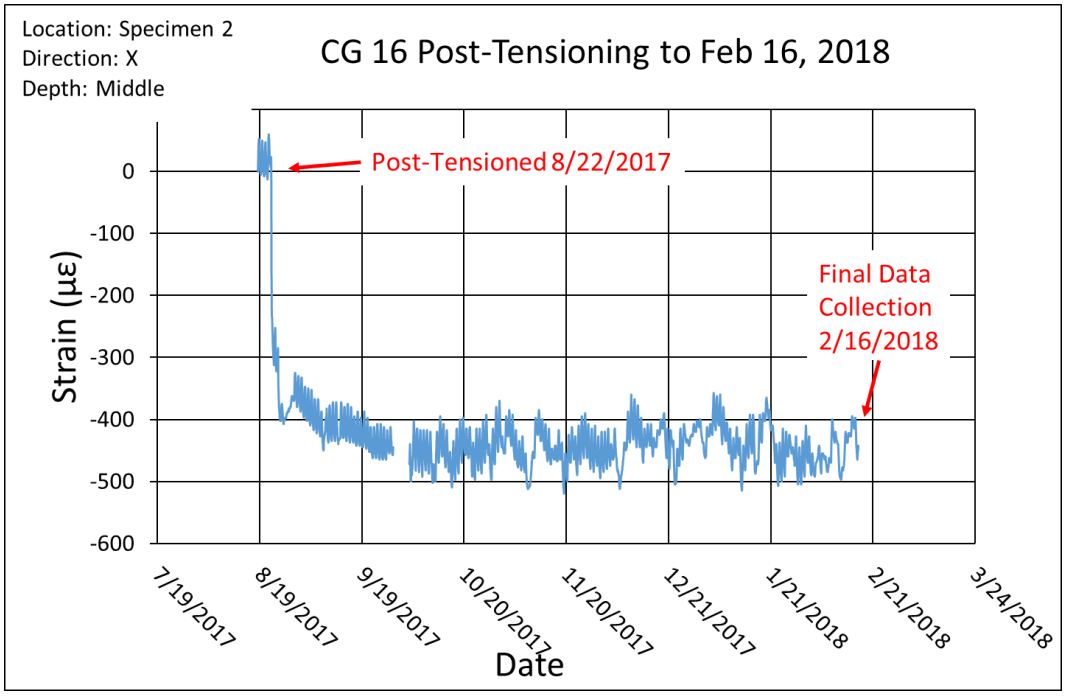

Figure 238 Concrete Gage 16 Strain Data from Post-Tensioning to February 16, 2018

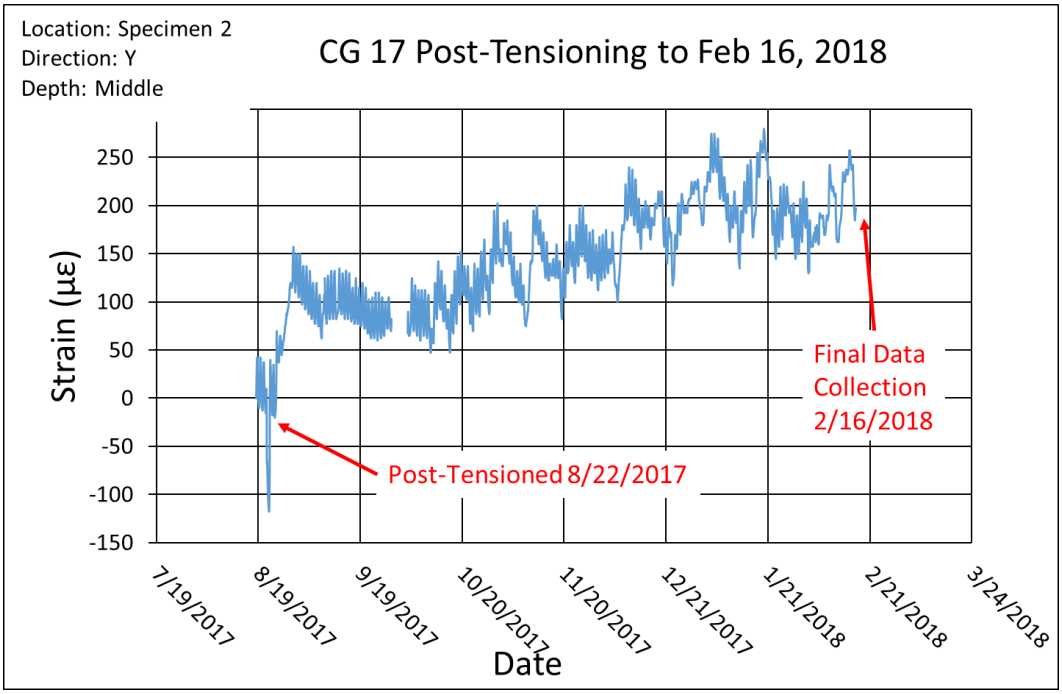

Figure 239 Concrete Gage 17 Strain Data from Post-Tensioning to February 16, 2018

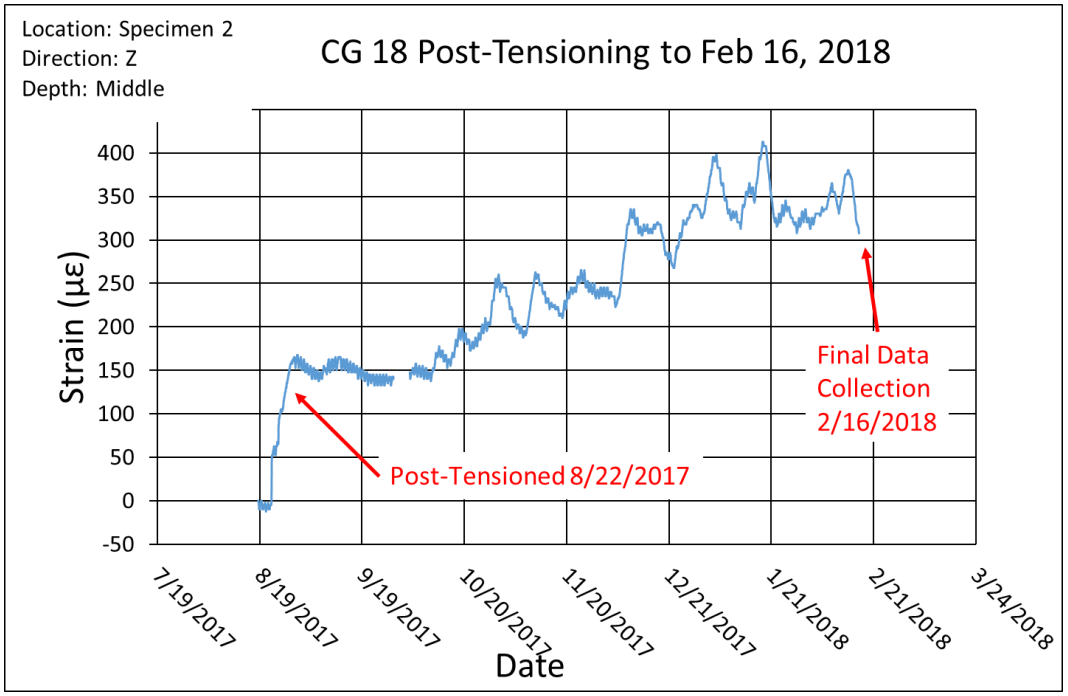

Figure 240 Concrete Gage 18 Strain Data from Post-Tensioning to February 16, 2018

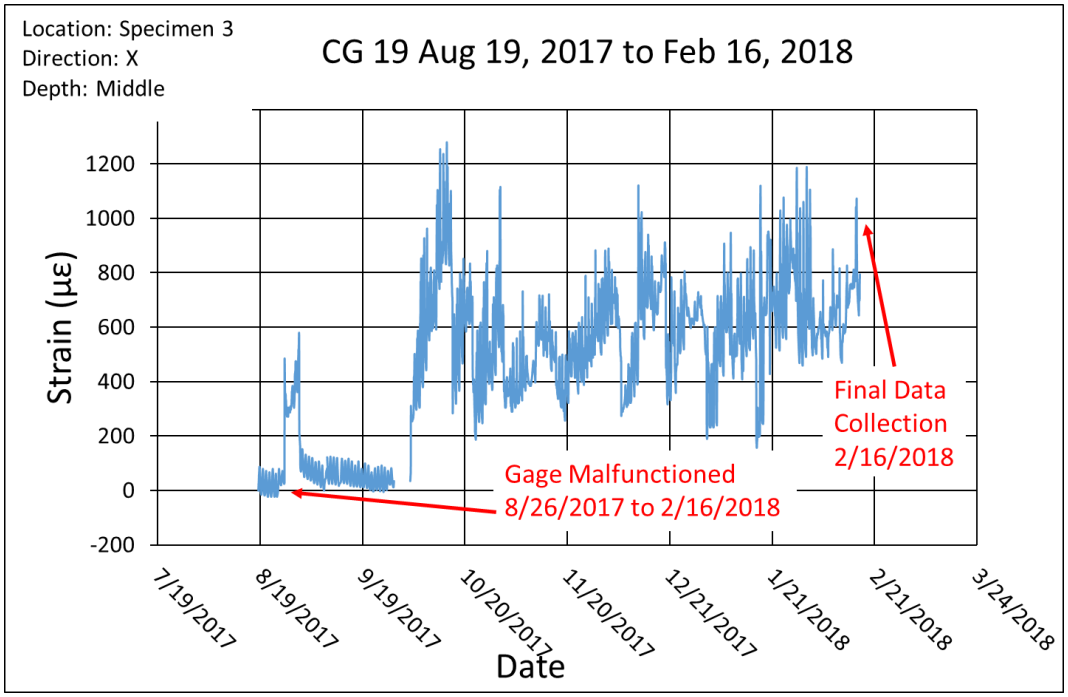

Figure 241 Concrete Gage 19 Strain Data from August 19, 2017 to February 16, 2018

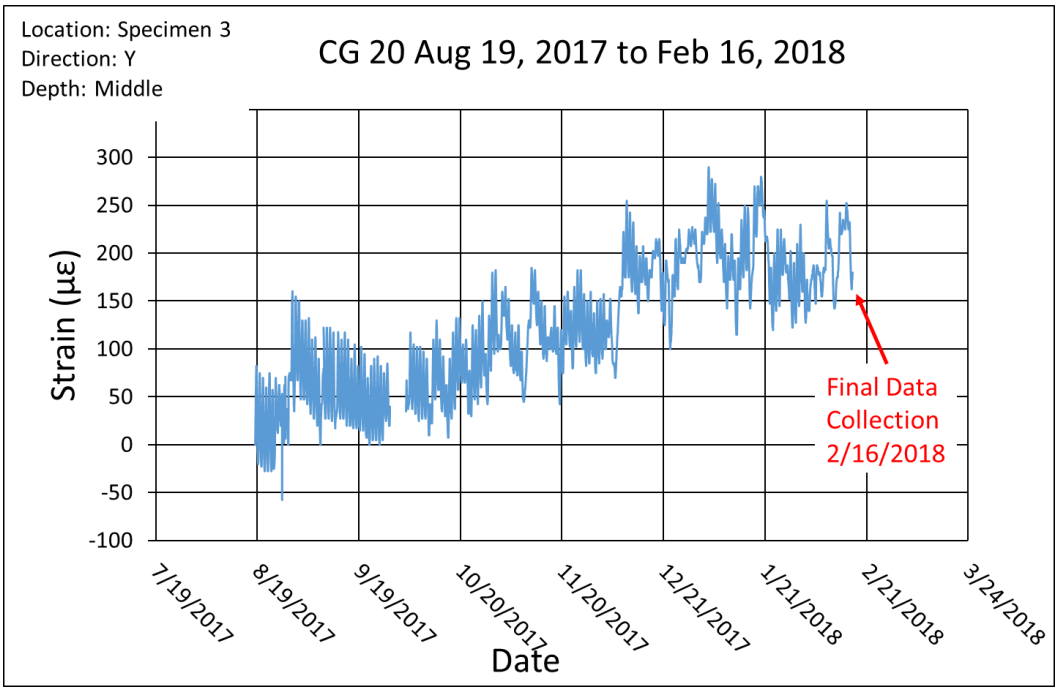

Figure 242 Concrete Gage 20 Strain Data from August 19, 2017 to February 16, 2018

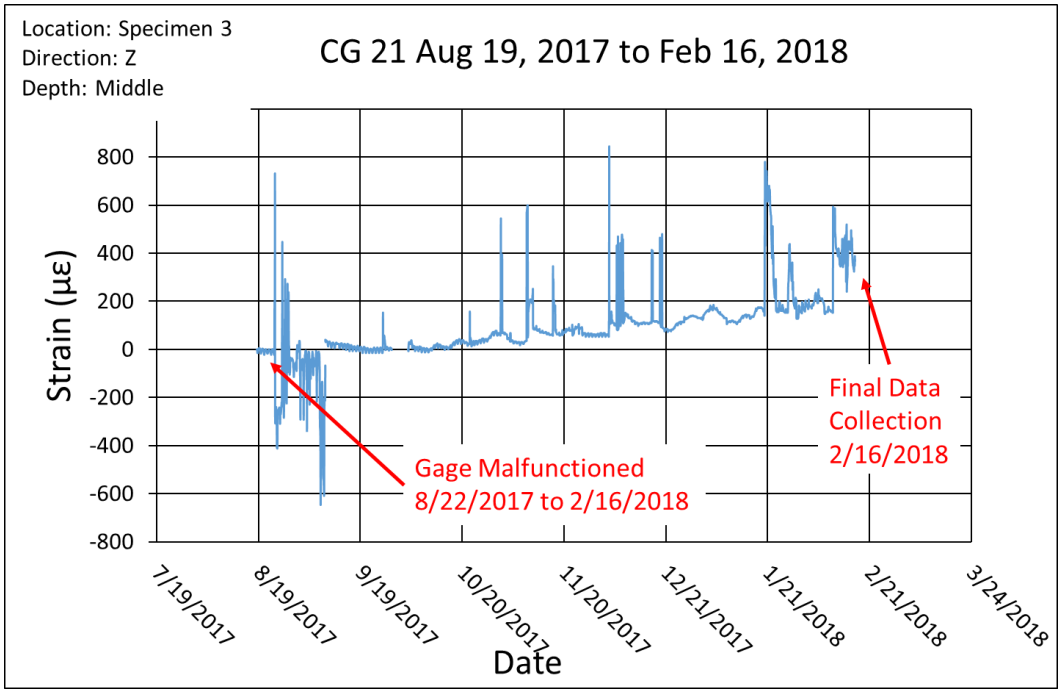

Figure 243 Concrete Gage 21 Strain Data from August 19, 2017 to February 16, 2018

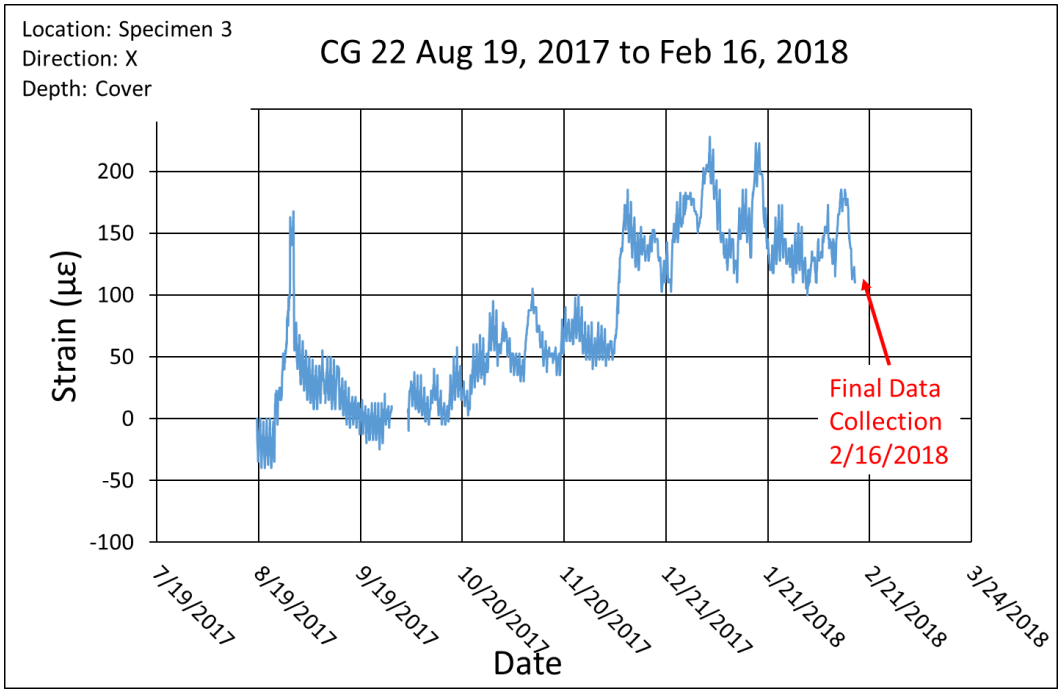

Figure 244 Concrete Gage 22 Strain Data from August 19, 2017 to February 16, 2018

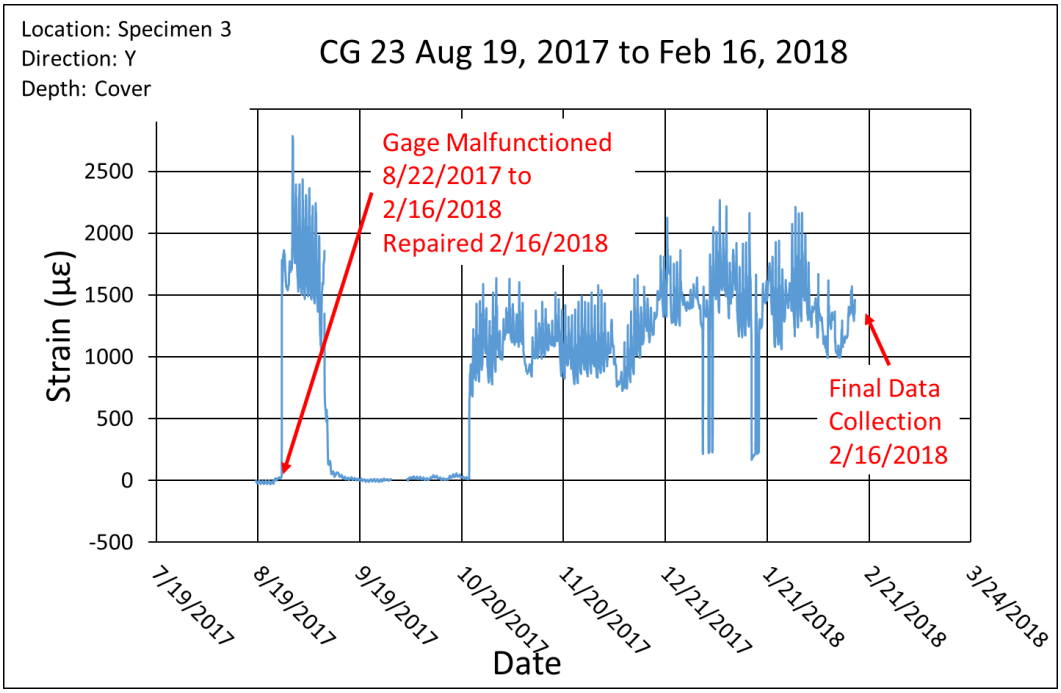

Figure 245 Concrete Gage 23 Strain Data from August 19, 2017 to February 16, 2018

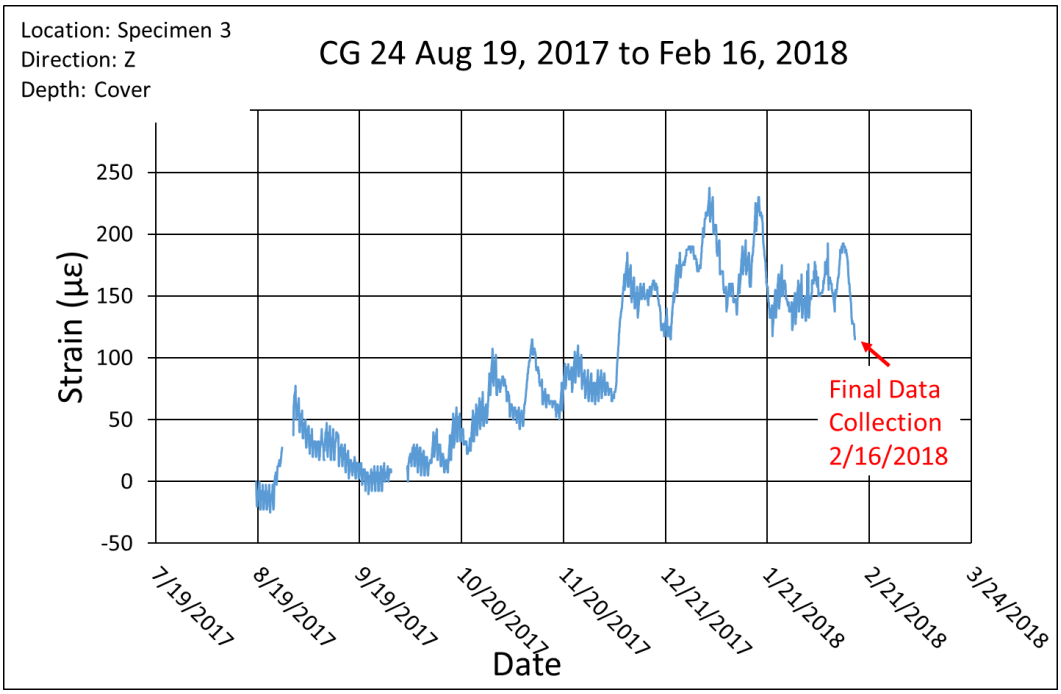

Figure 246 Concrete Gage 24 Strain Data from August 19, 2017 to February 16, 2018

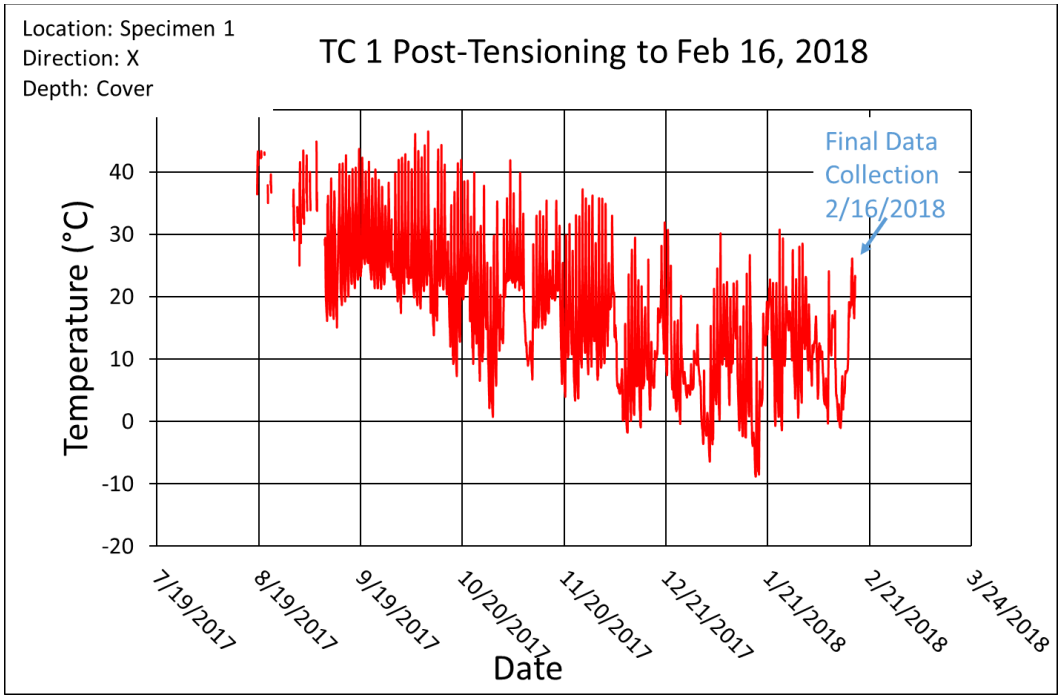

Figure 247 Thermocouple 1 Temperature Data from Post-Tensioning to February 16, 2018

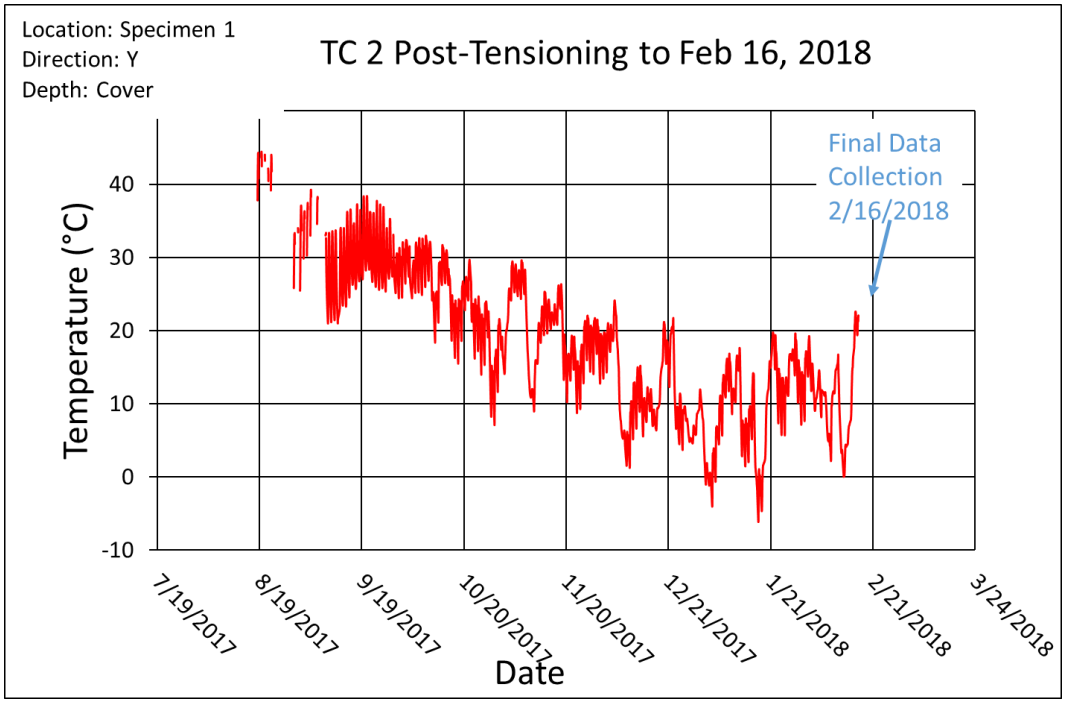

Figure 248 Thermocouple 2 Temperature Data from Post-Tensioning to February 16, 2018

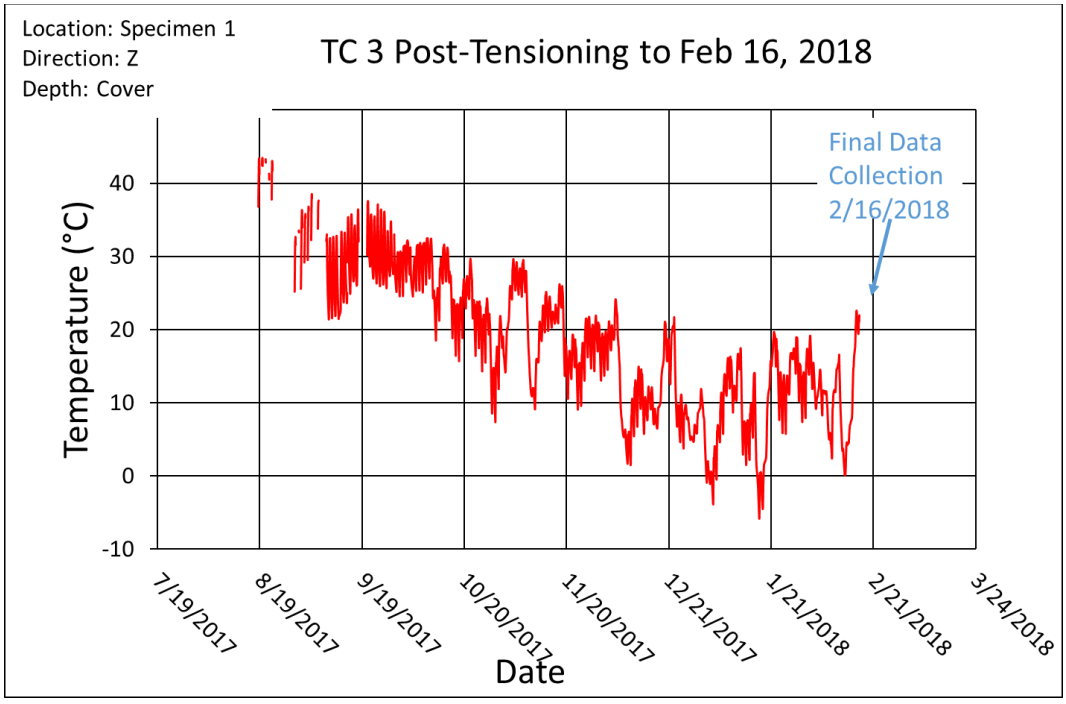

Figure 249 Thermocouple 3 Temperature Data from Post-Tensioning to February 16, 2018

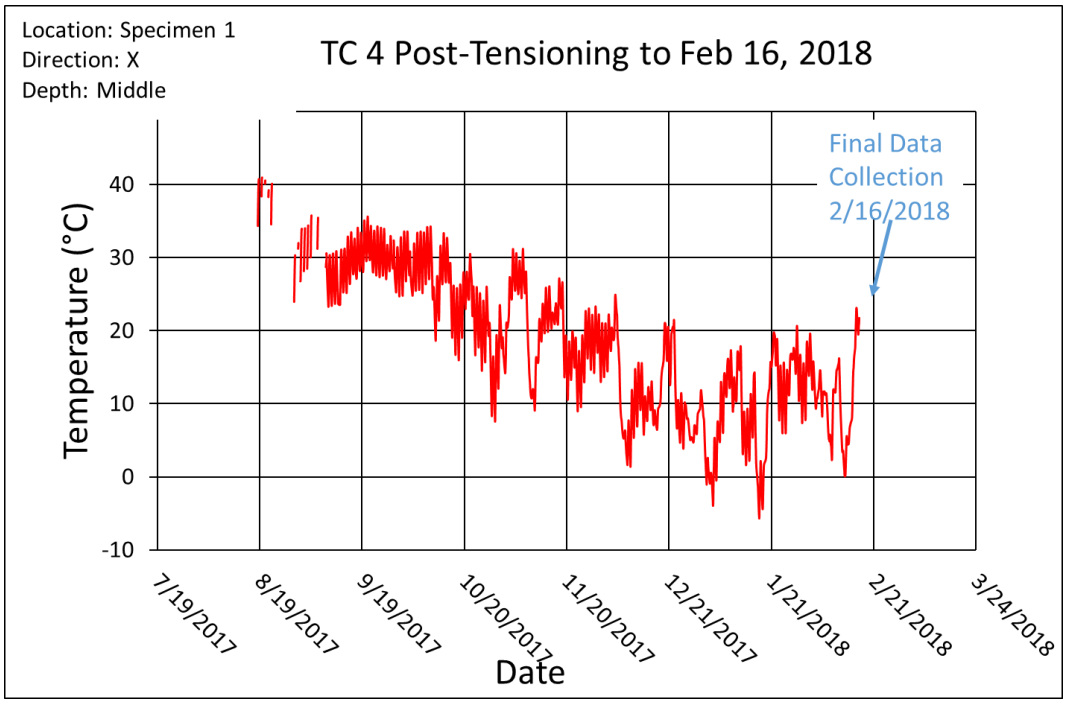

Figure 250 Thermocouple 4 Temperature Data from Post-Tensioning to February 16, 2018

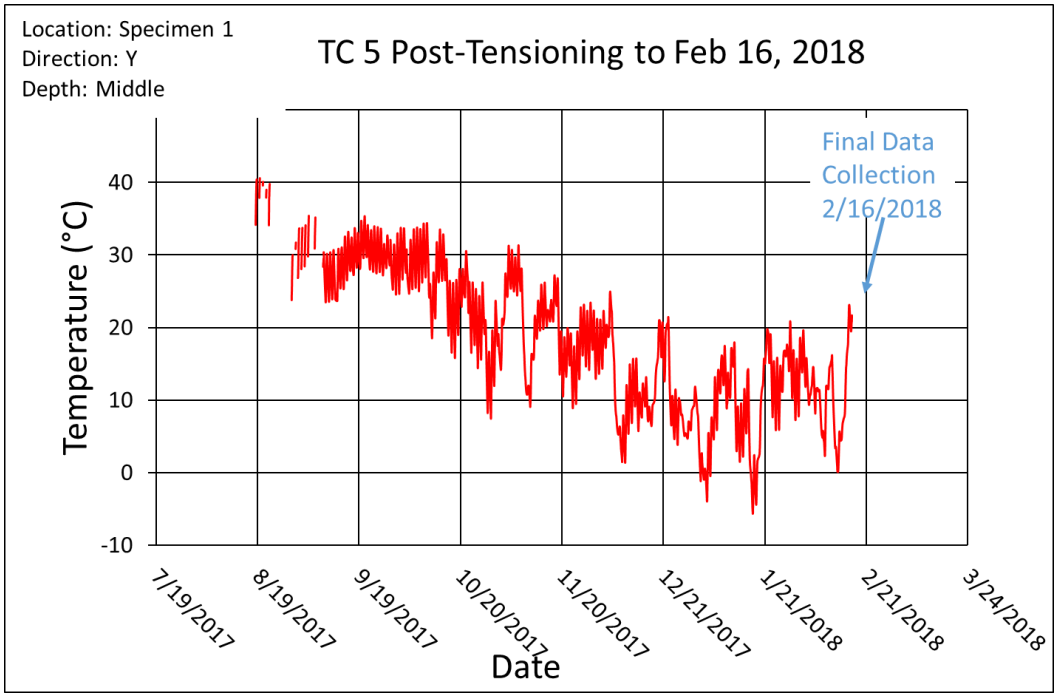

Figure 251 Thermocouple 5 Temperature Data from Post-Tensioning to February 16, 2018

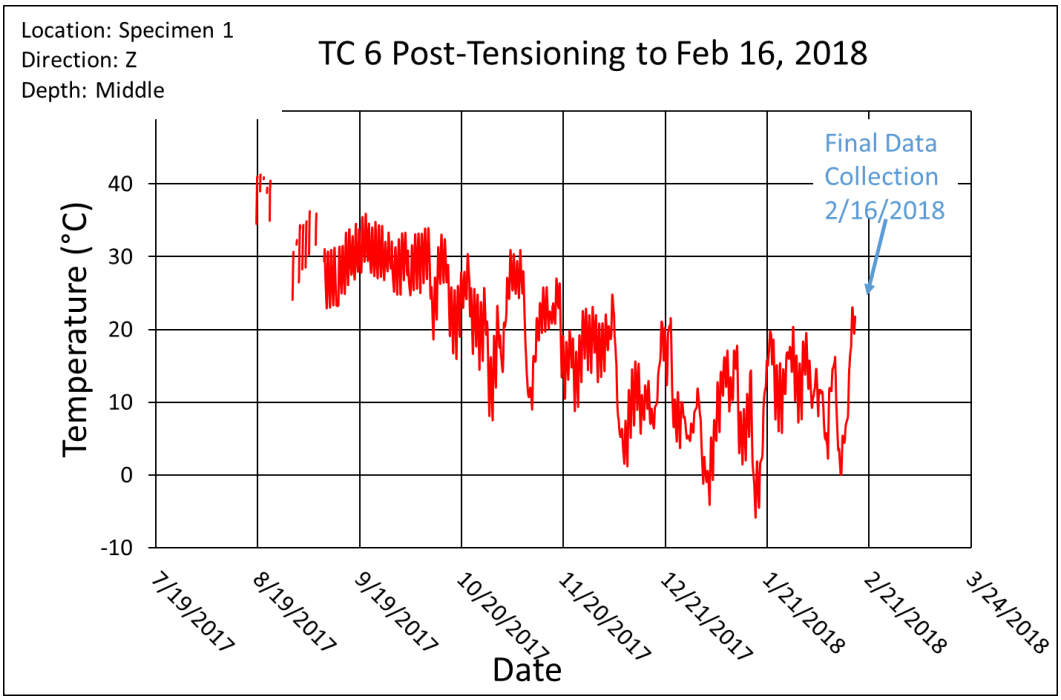

Figure 252 Thermocouple 6 Temperature Data from Post-Tensioning to February 16, 2018

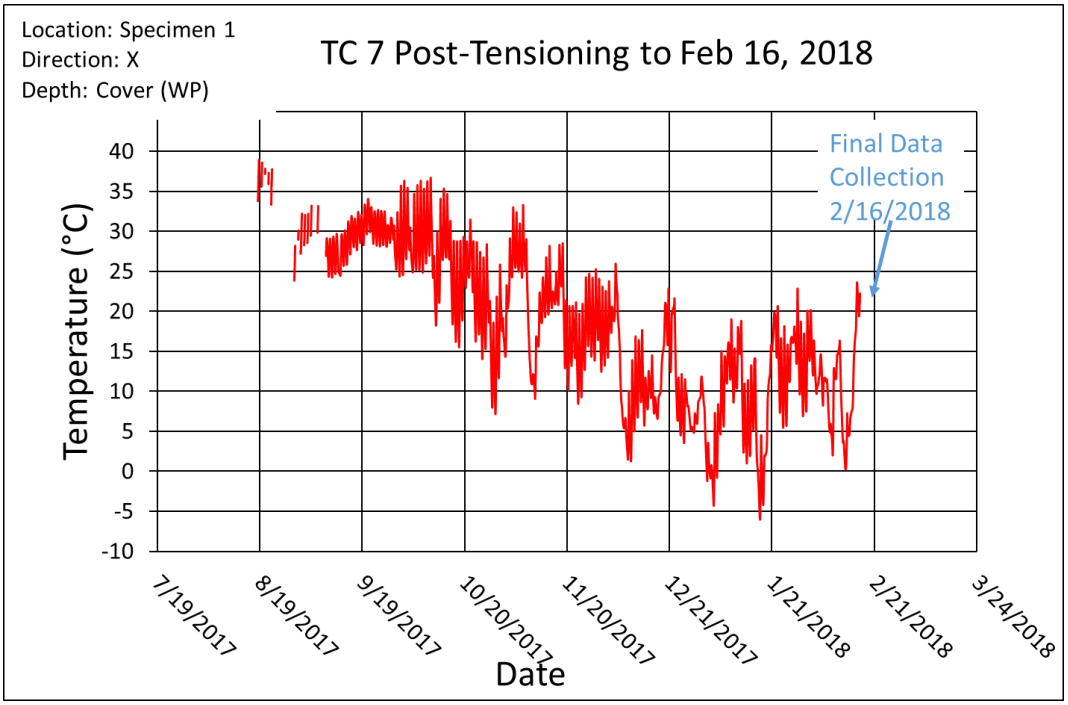

Figure 253 Thermocouple 7 Temperature Data from Post-Tensioning to February 16, 2018

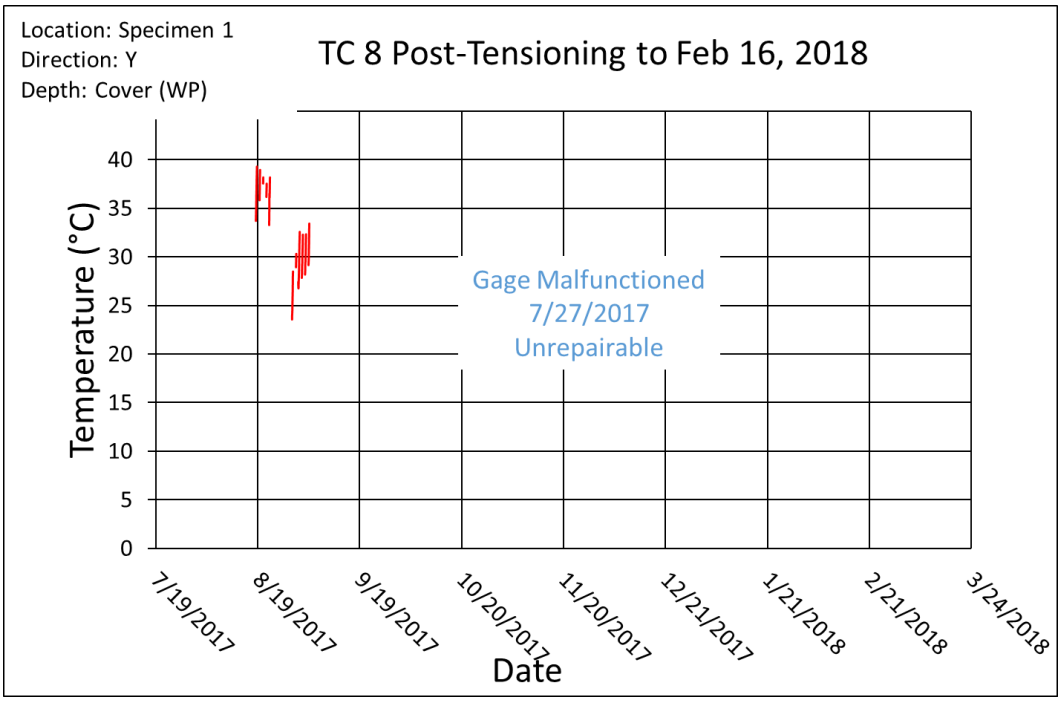

Figure 254 Thermocouple 8 Temperature Data from Post-Tensioning to February 16, 2018

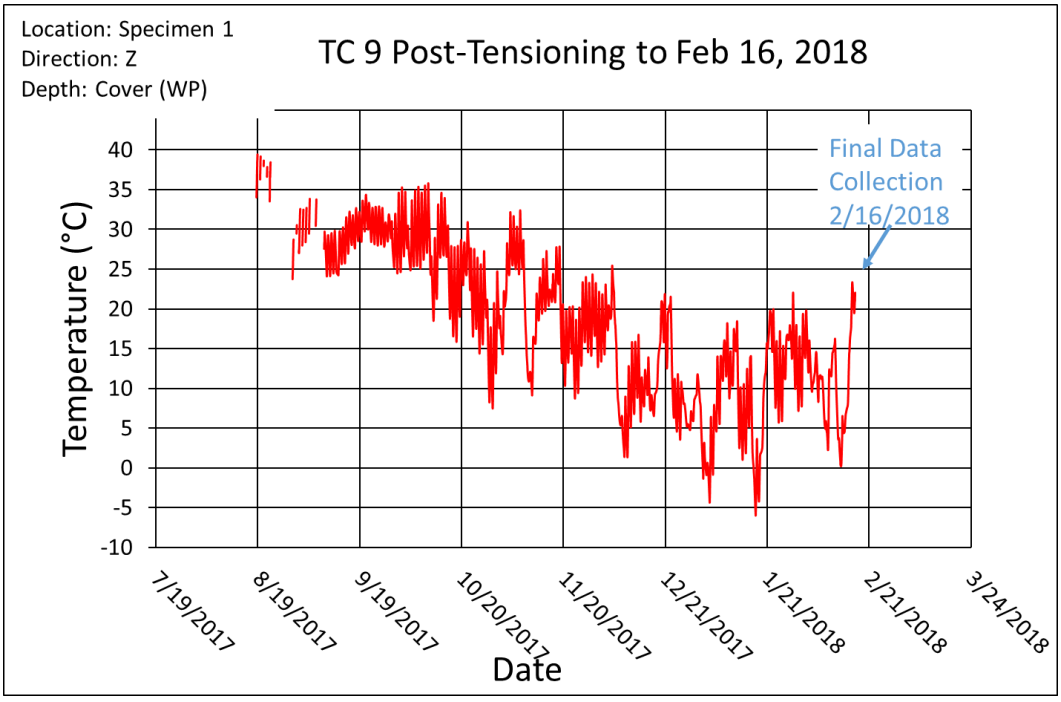

Figure 255 Thermocouple 9 Temperature Data from Post-Tensioning to February 16, 2018

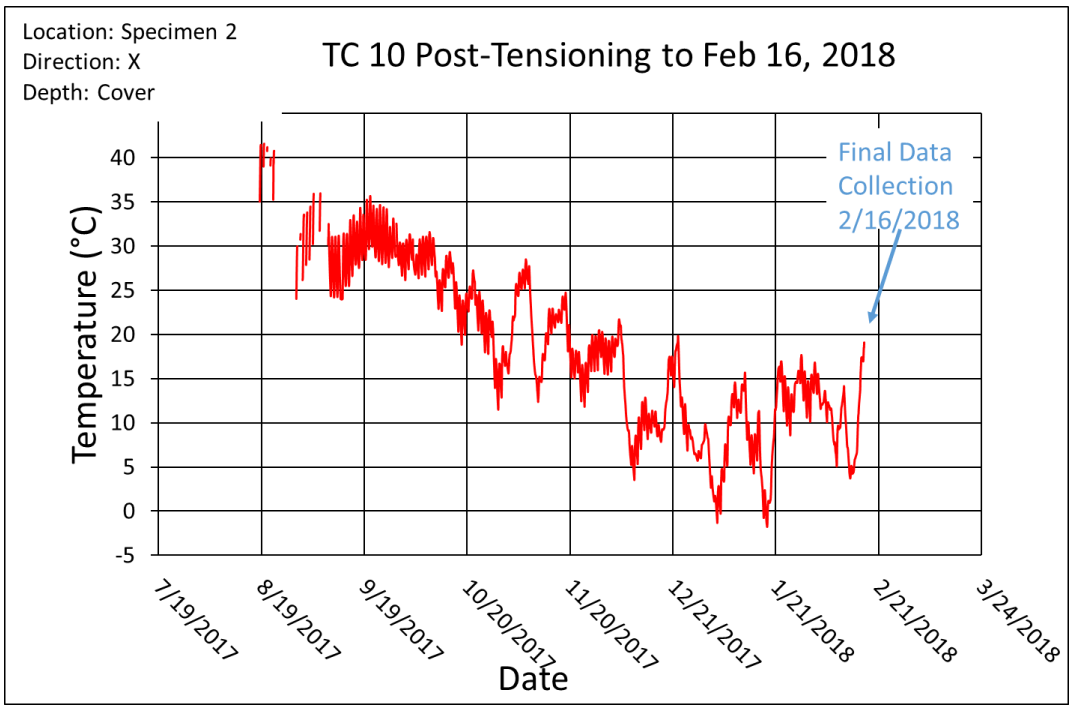

Figure 256 Thermocouple 10 Temperature Data from Post-Tensioning to February 16, 2018

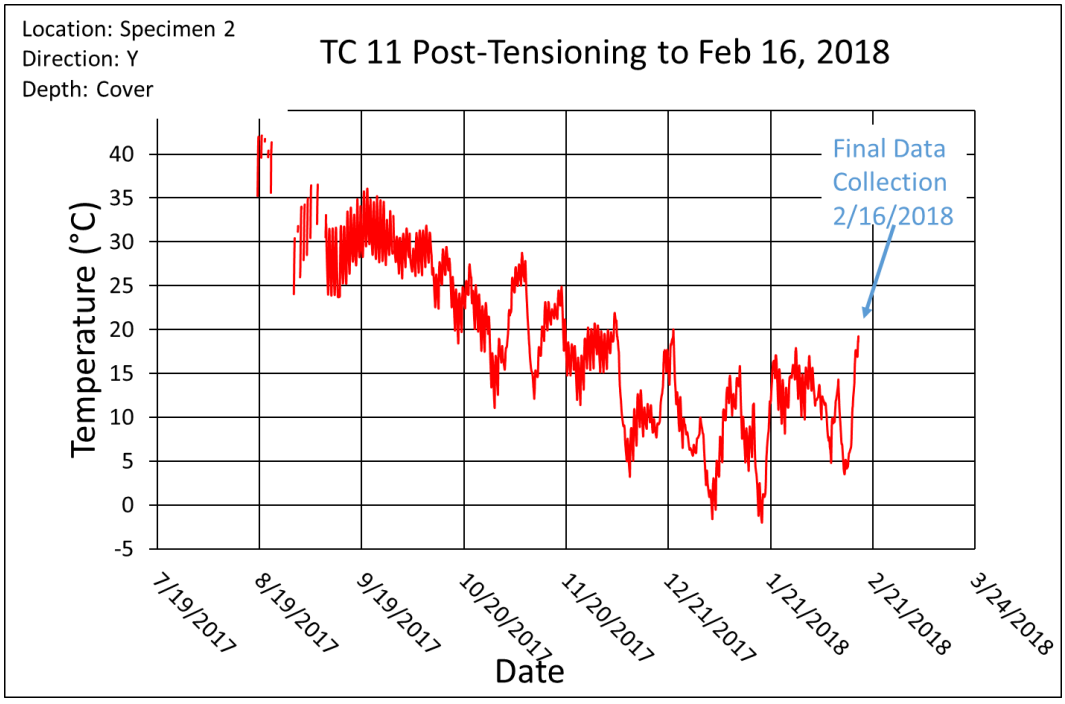

Figure 257 Thermocouple 11 Temperature Data from Post-Tensioning to February 16, 2018

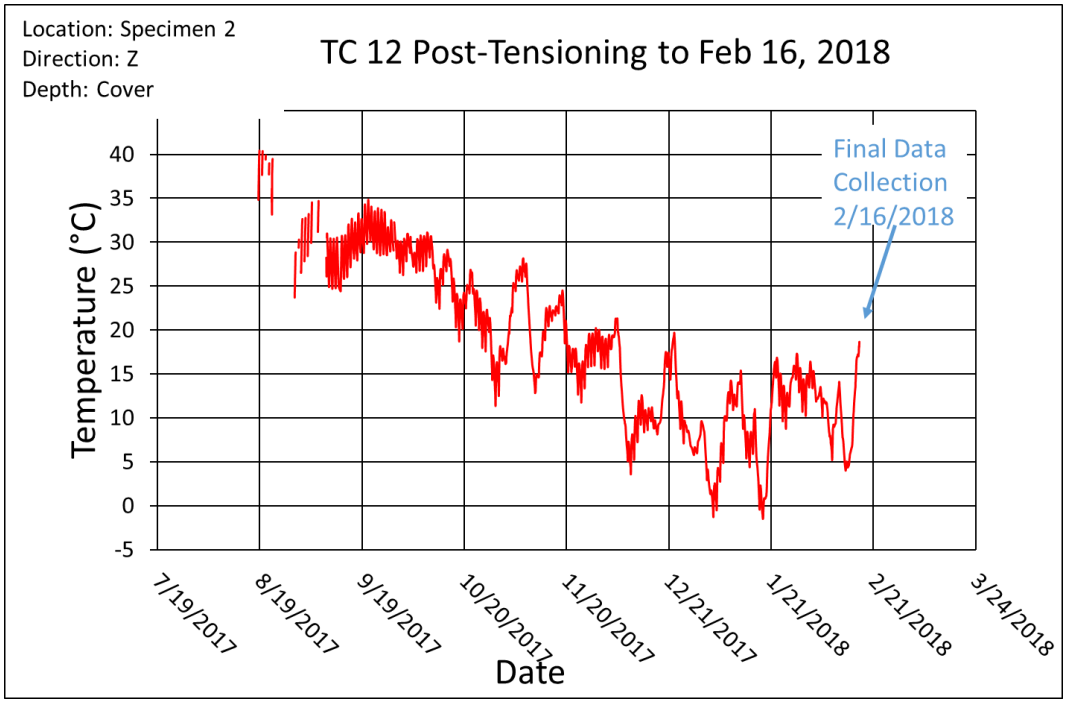

Figure 258 Thermocouple 12 Temperature Data from Post-Tensioning to February 16, 2018

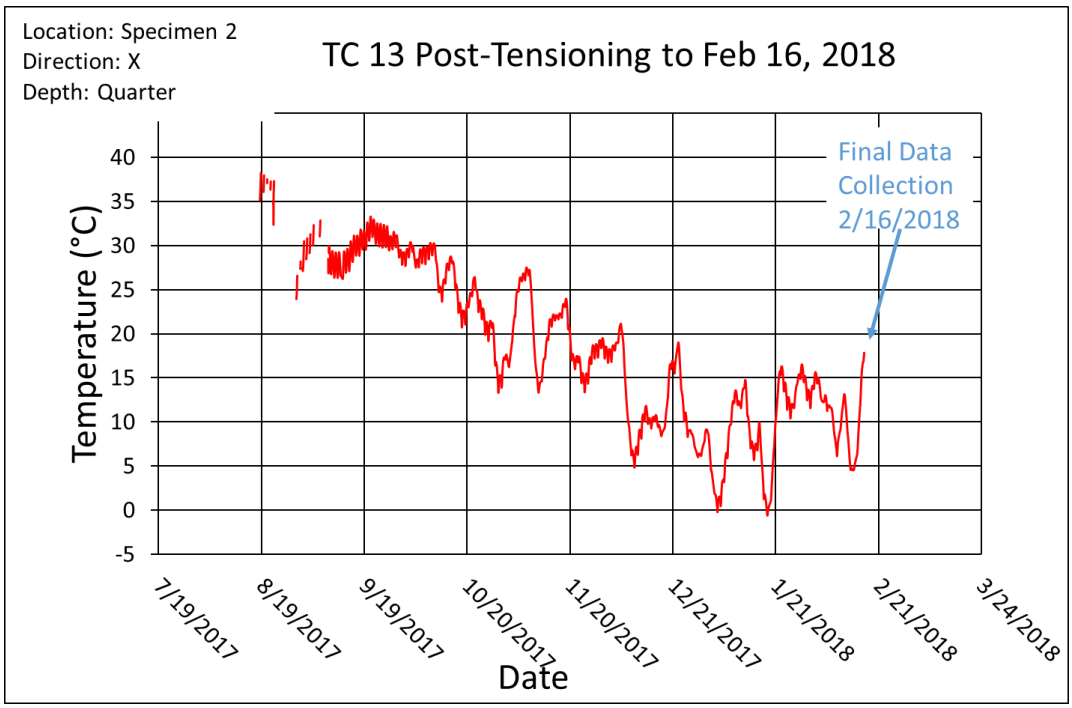

Figure 259 Thermocouple 13 Temperature Data from Post-Tensioning to February 16, 2018

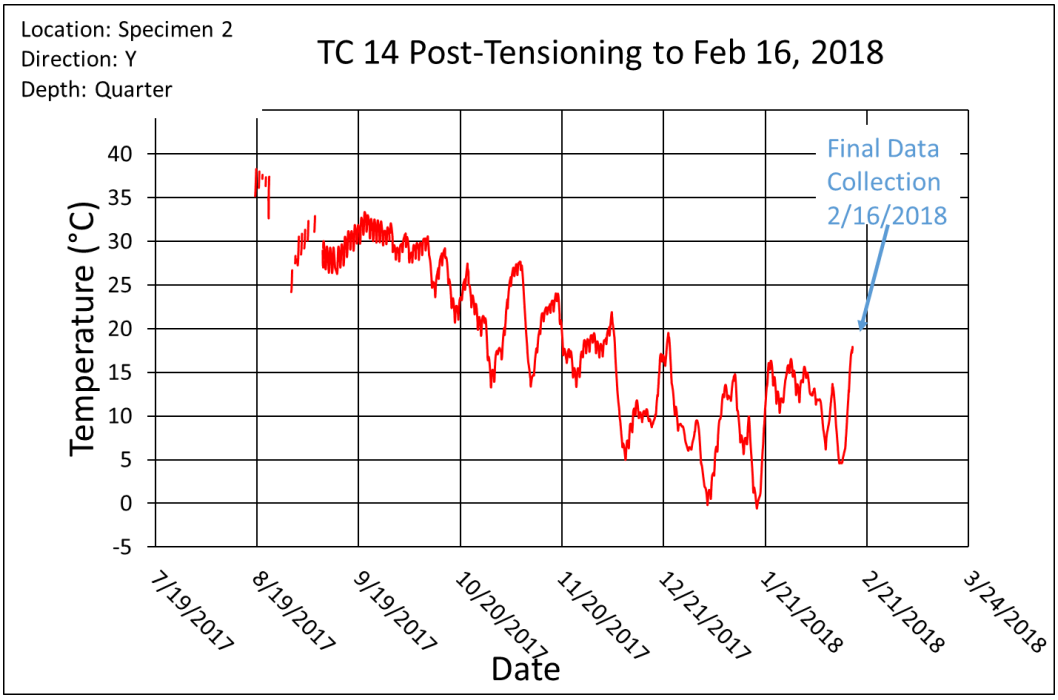

Figure 260 Thermocouple 14 Temperature Data from Post-Tensioning to February 16, 2018

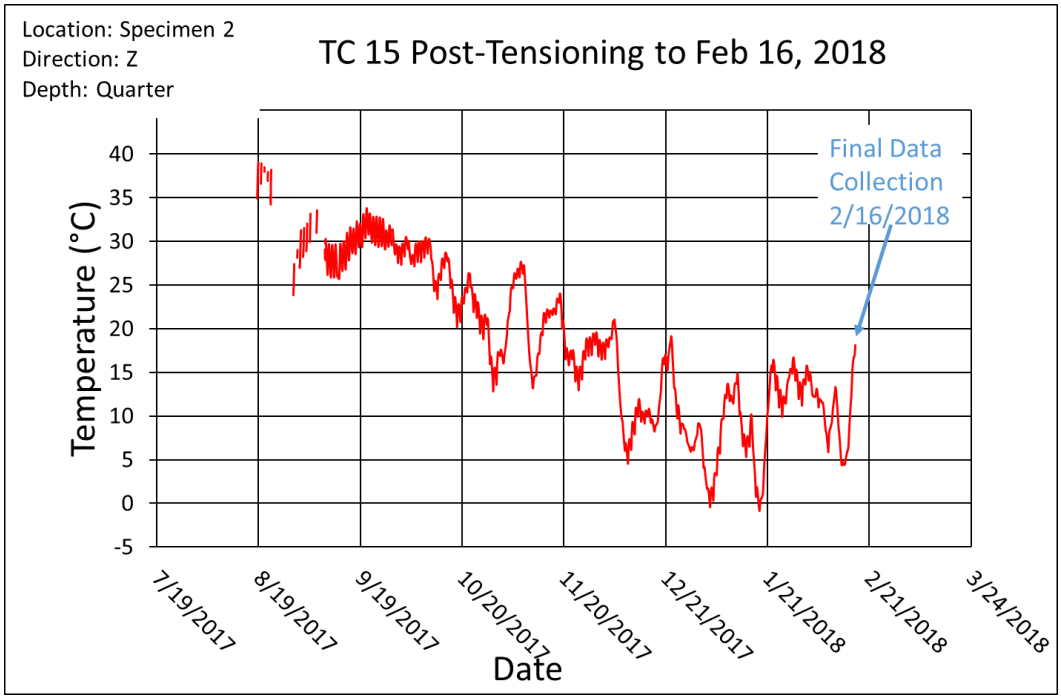

Figure 261 Thermocouple 15 Temperature Data from Post-Tensioning to February 16, 2018

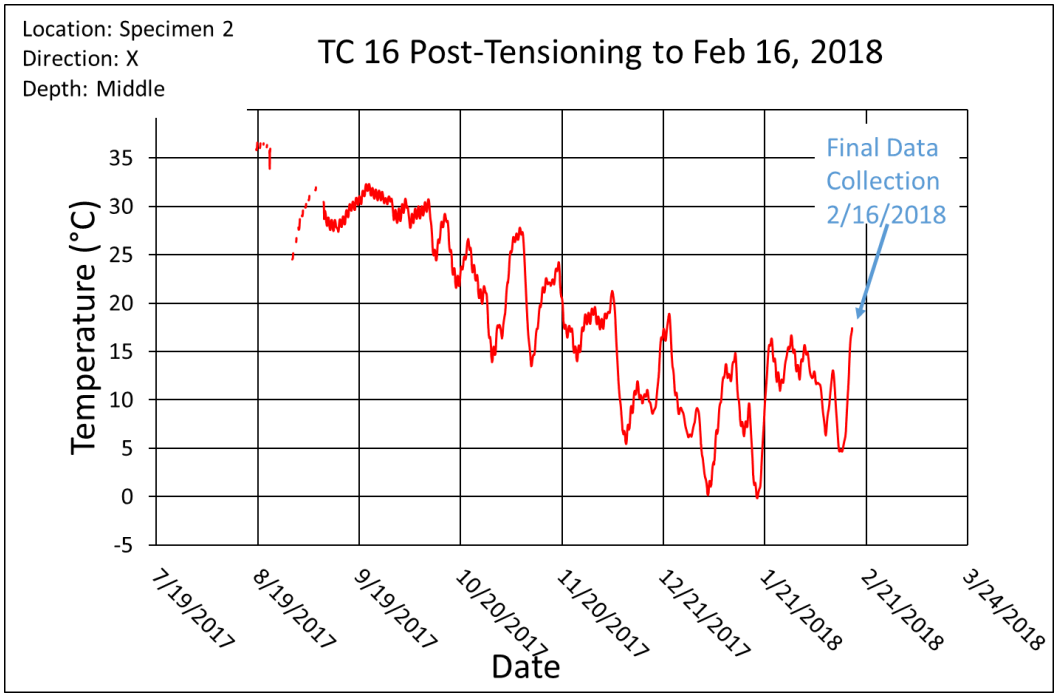

Figure 262 Thermocouple 16 Temperature Data from Post-Tensioning to February 16, 2018

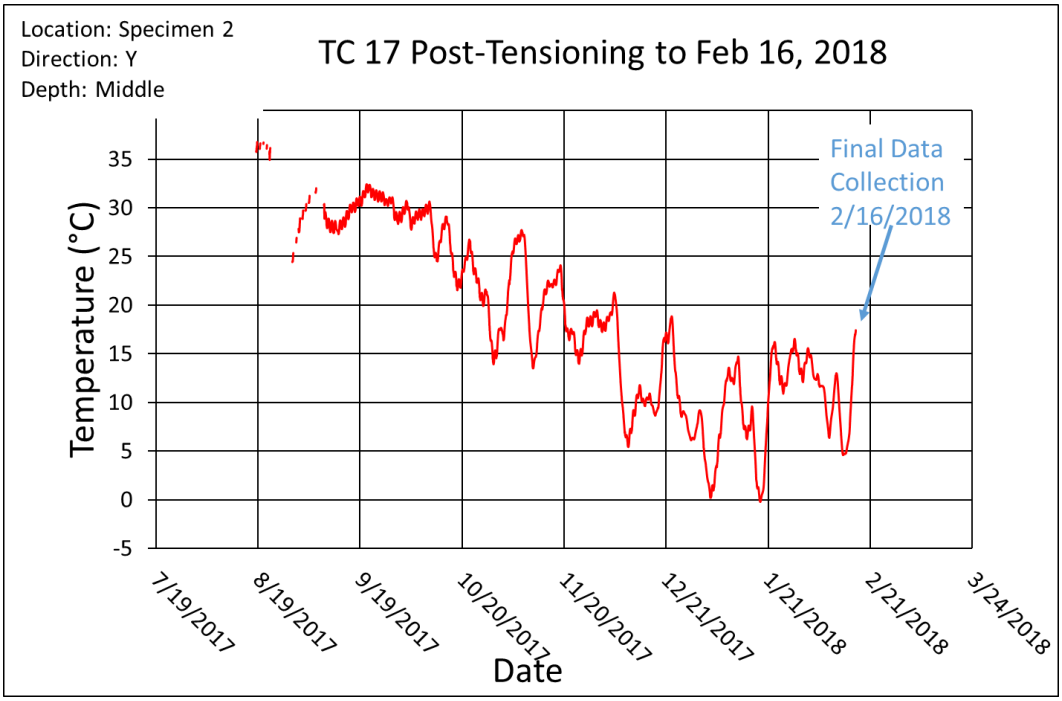

Figure 263 Thermocouple 17 Temperature Data from Post-Tensioning to February 16, 2018

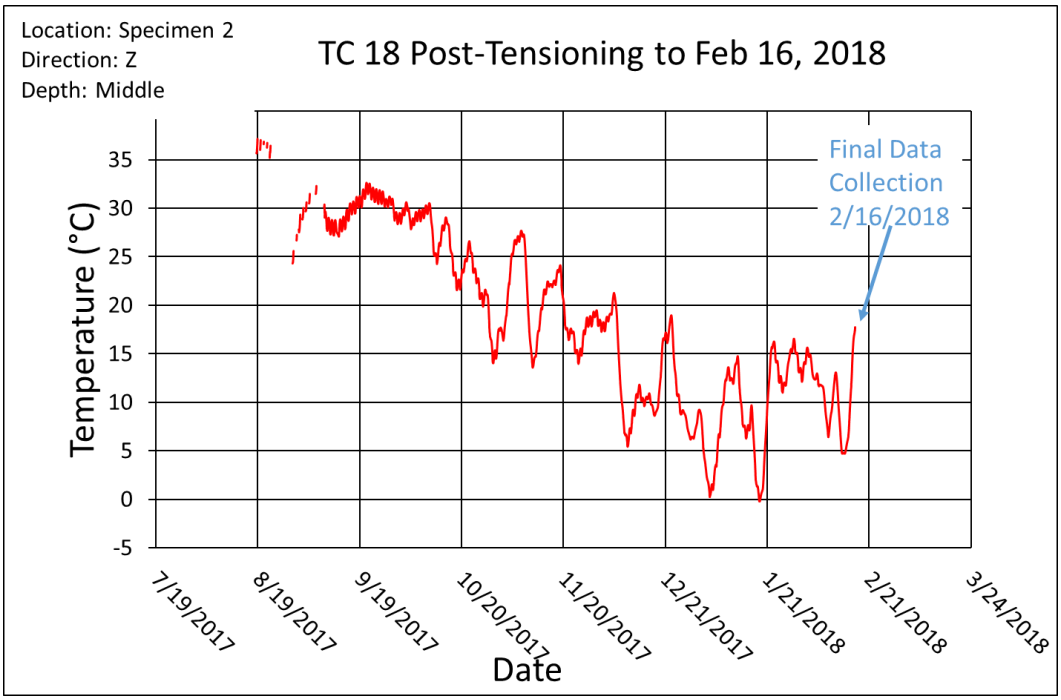

Figure 264 Thermocouple 18 Temperature Data from Post-Tensioning to February 16, 2018

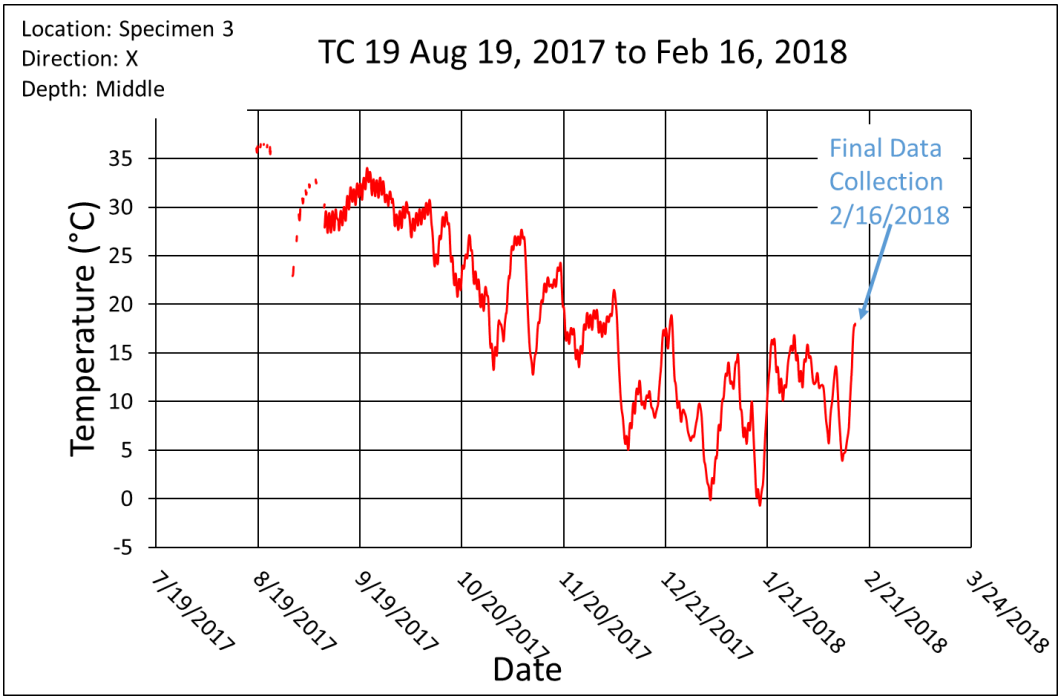

Figure 265 Thermocouple 19 Temperature Data from August 19, 2017 to February 16, 2018

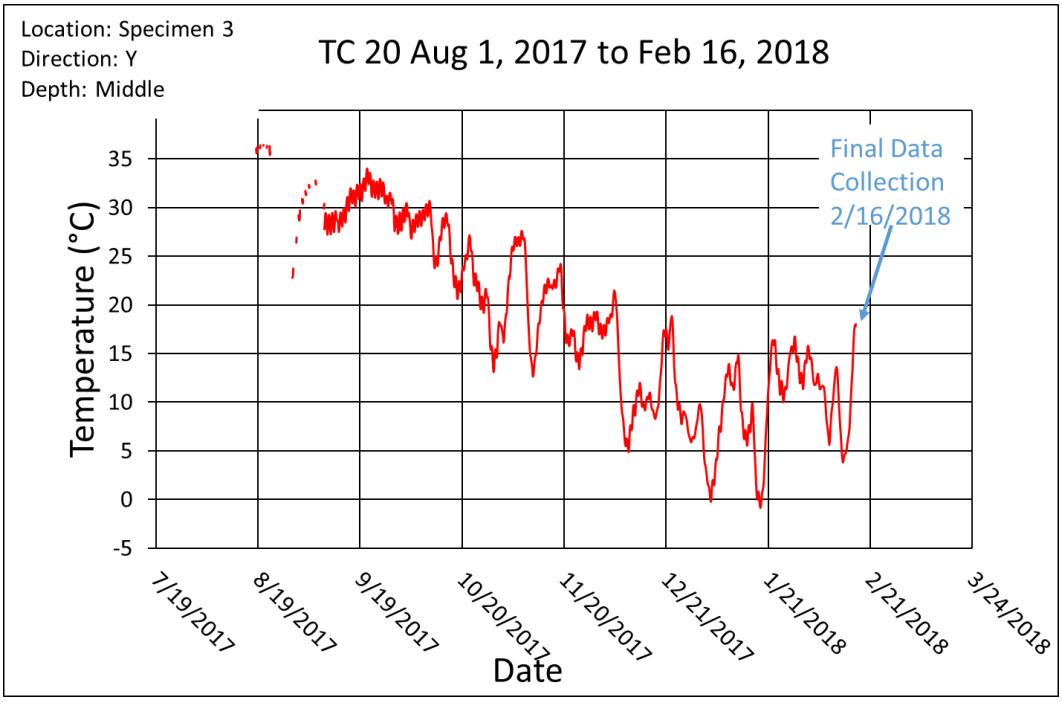

Figure 266 Thermocouple 20 Temperature Data from August 19, 2017 to February 16, 2018

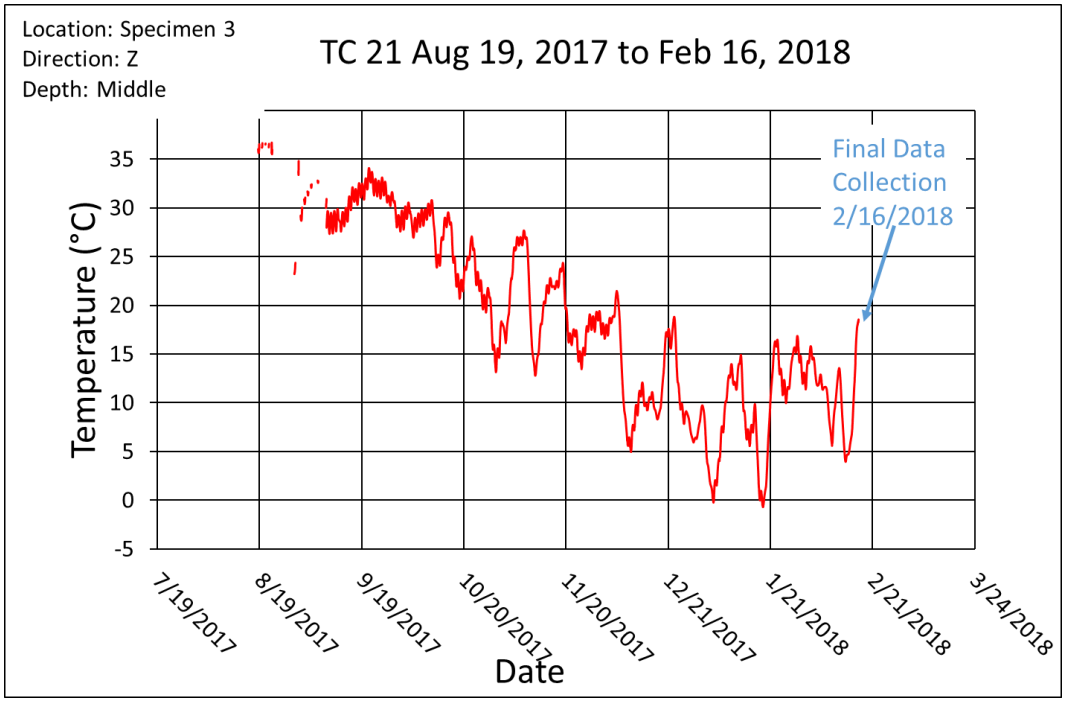

Figure 267 Thermocouple 21 Temperature Data from August 19, 2017 to February 16, 2018

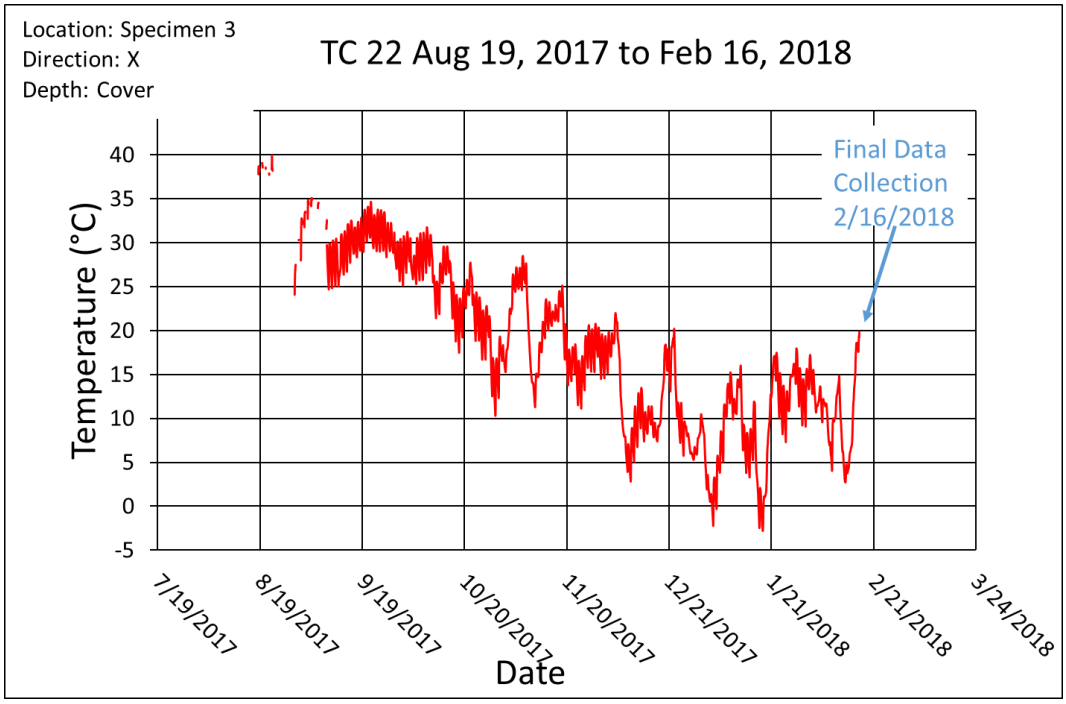

Figure 268 Thermocouple 22 Temperature Data from August 19, 2017 to February 16, 2018

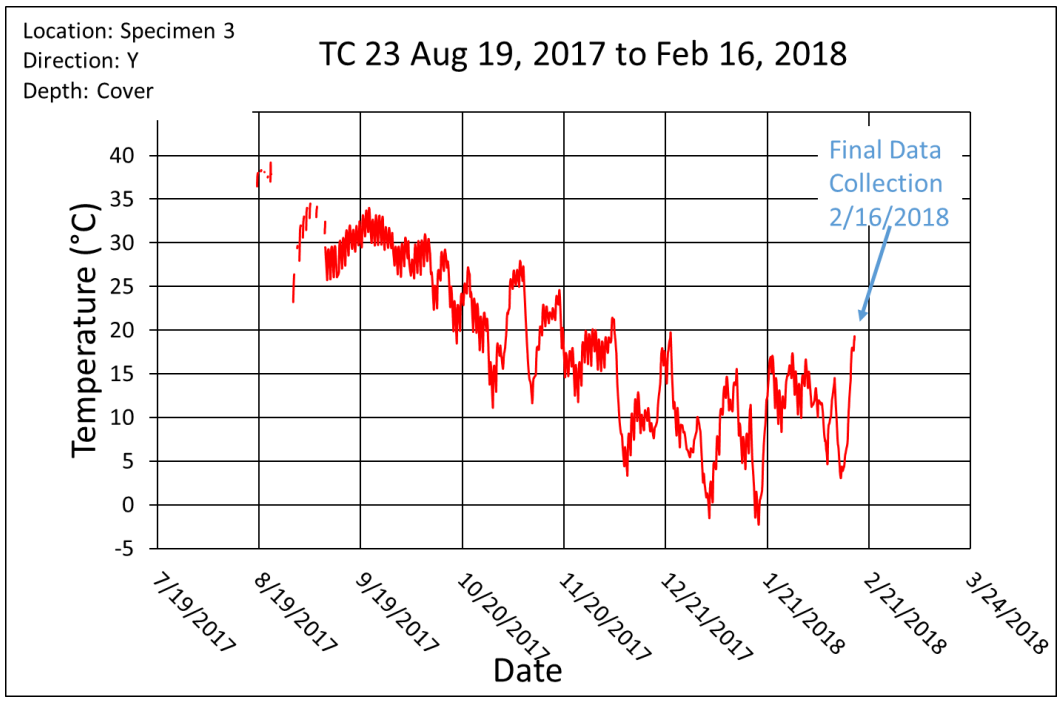

Figure 269 Thermocouple 23 Temperature Data from August 19, 2017 to February 16, 2018

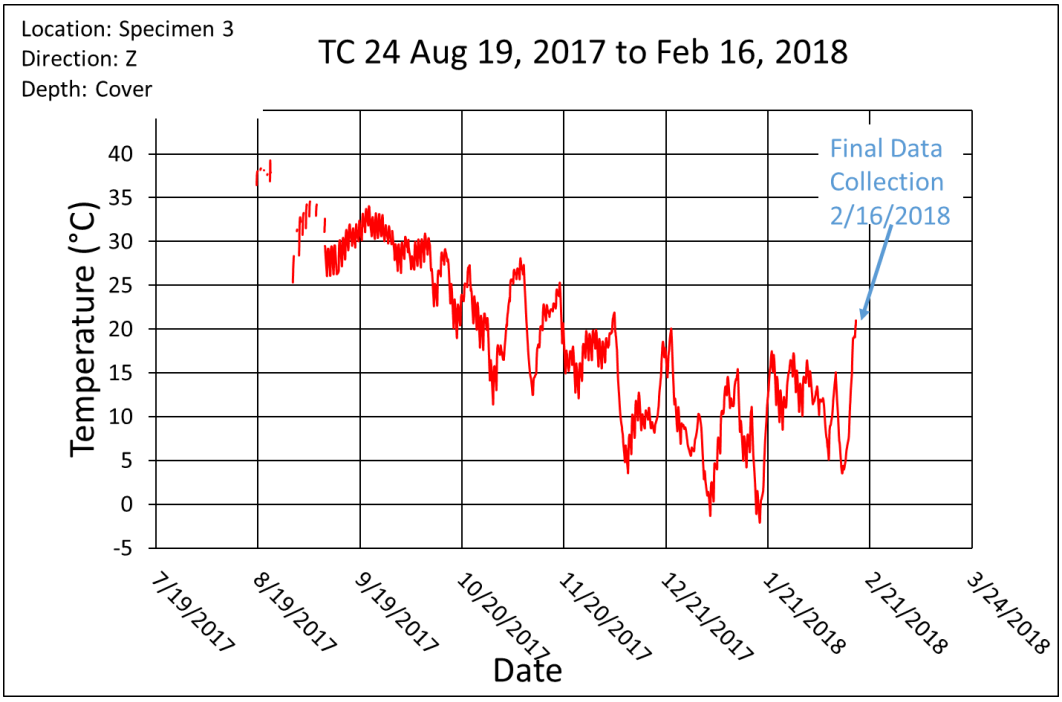

Figure 270 Thermocouple 24 Temperature Data from August 19, 2017 to February 16, 2018

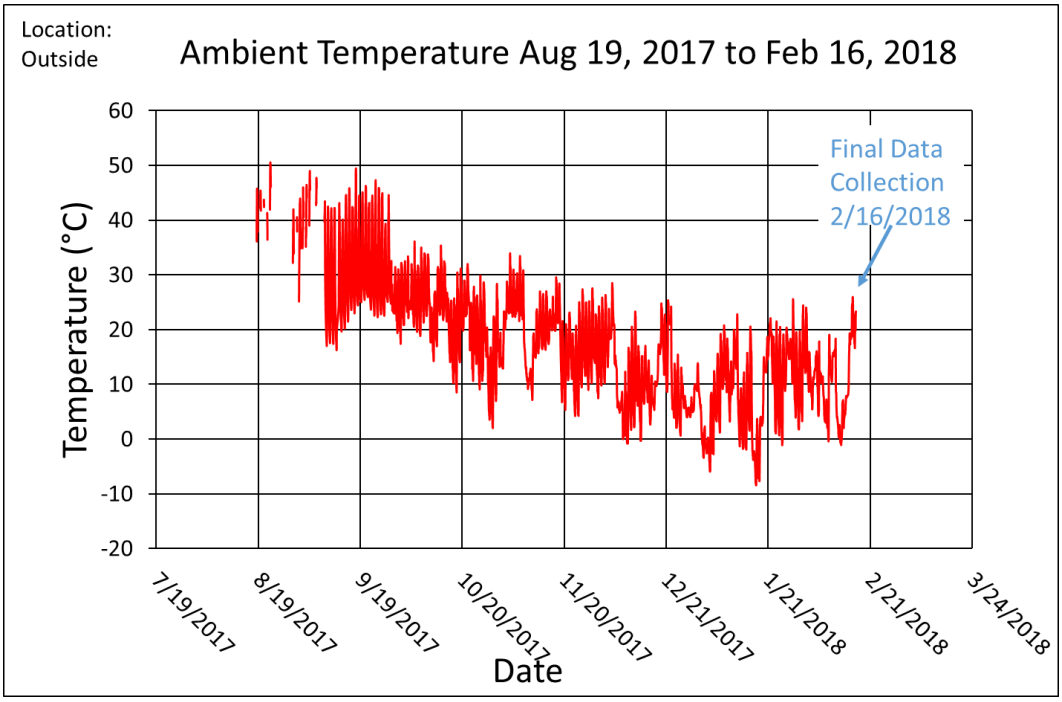

Figure 271 Ambient Temperature Data from August 19, 2017 to February 16, 2018

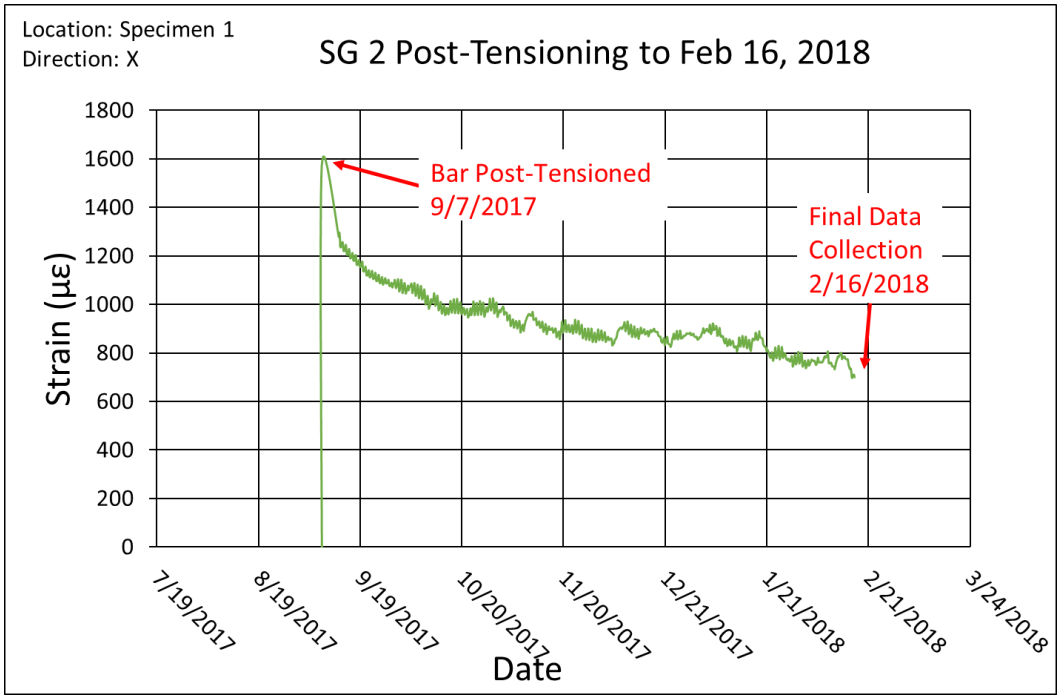

Figure 272 Post-Tensioning Bar Strain Gage 2 Strain Data from Post-Tensioning to February 16, 2018

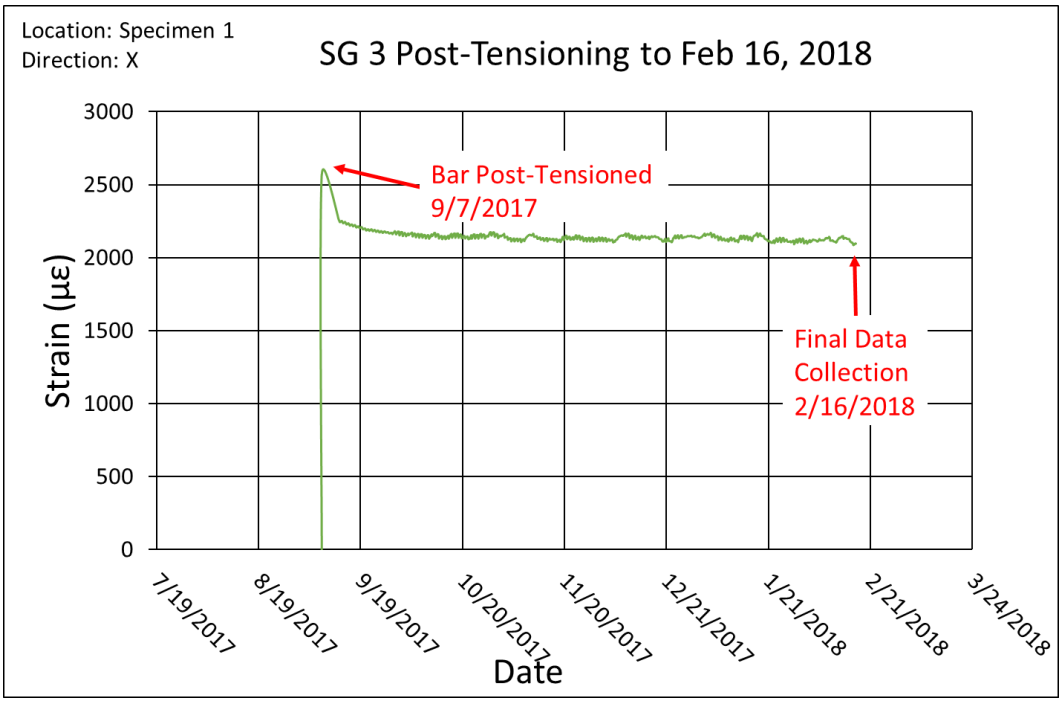

Figure 273 Post-Tensioning Bar Strain Gage 3 Strain Data from Post-Tensioning to February 16, 2018

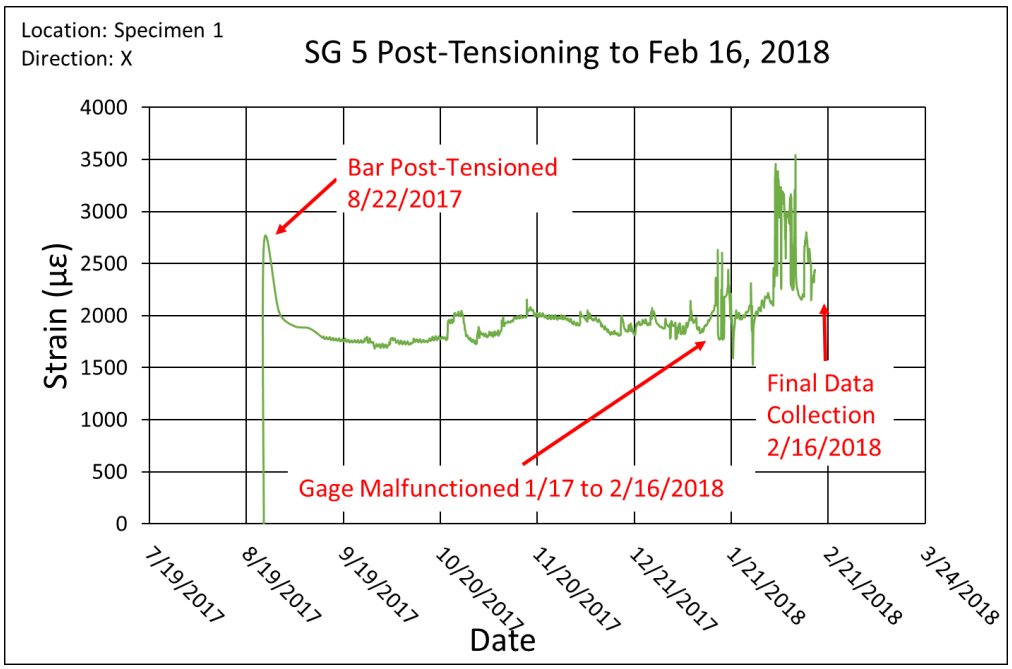

Figure 274 Post-Tensioning Bar Strain Gage 5 Strain Data from Post-Tensioning to February 16, 2018

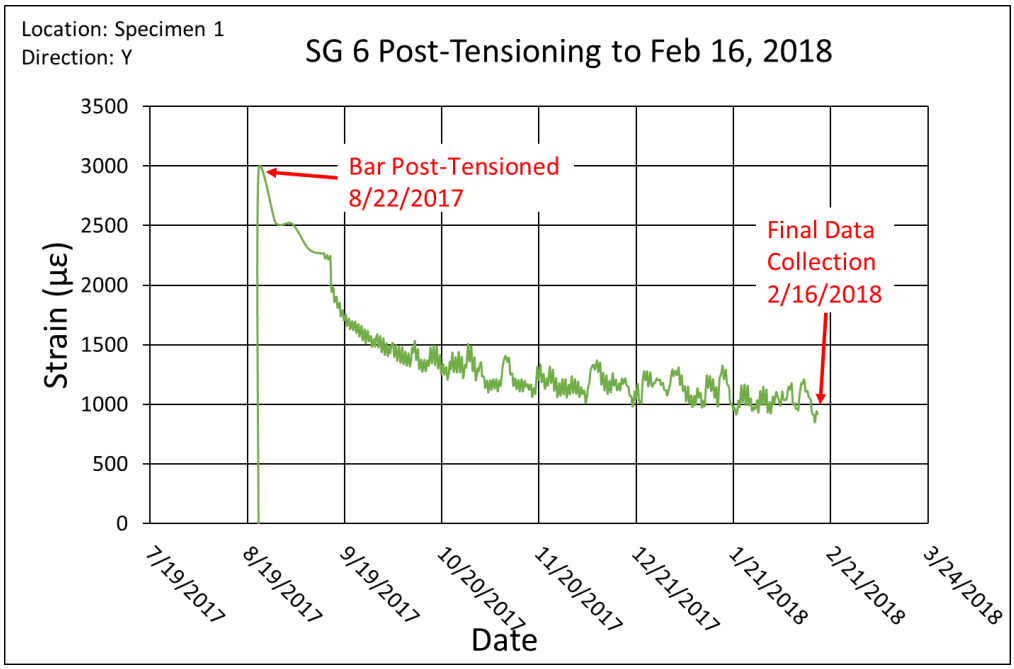

Figure 275 Post-Tensioning Bar Strain Gage 6 Strain Data from Post-Tensioning to February 16, 2018

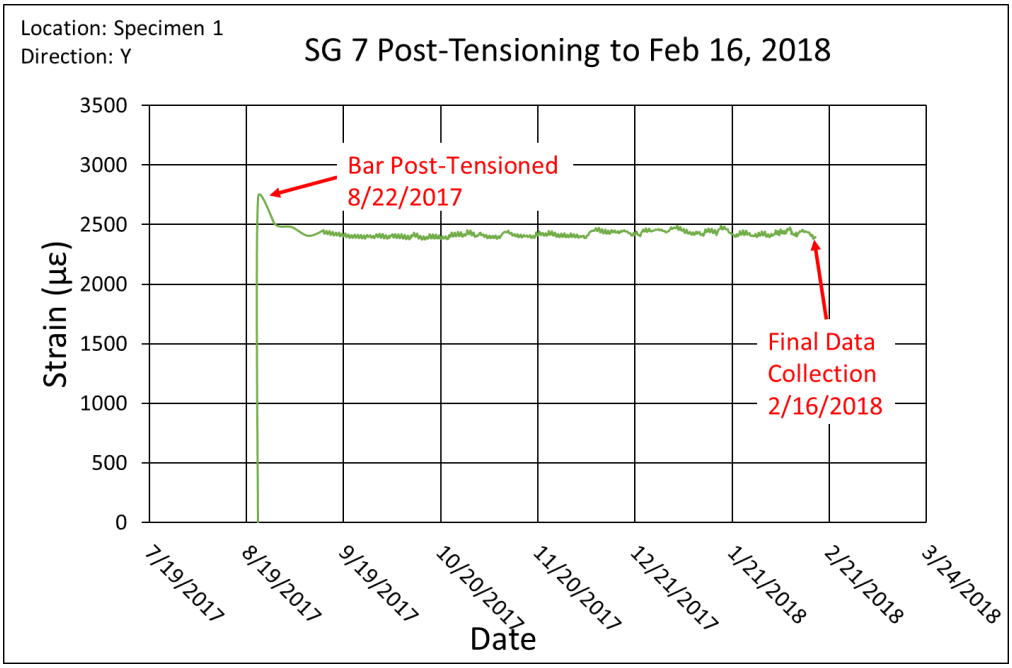

Figure 276 Post-Tensioning Bar Strain Gage 7 Strain Data from Post-Tensioning to February 16, 2018

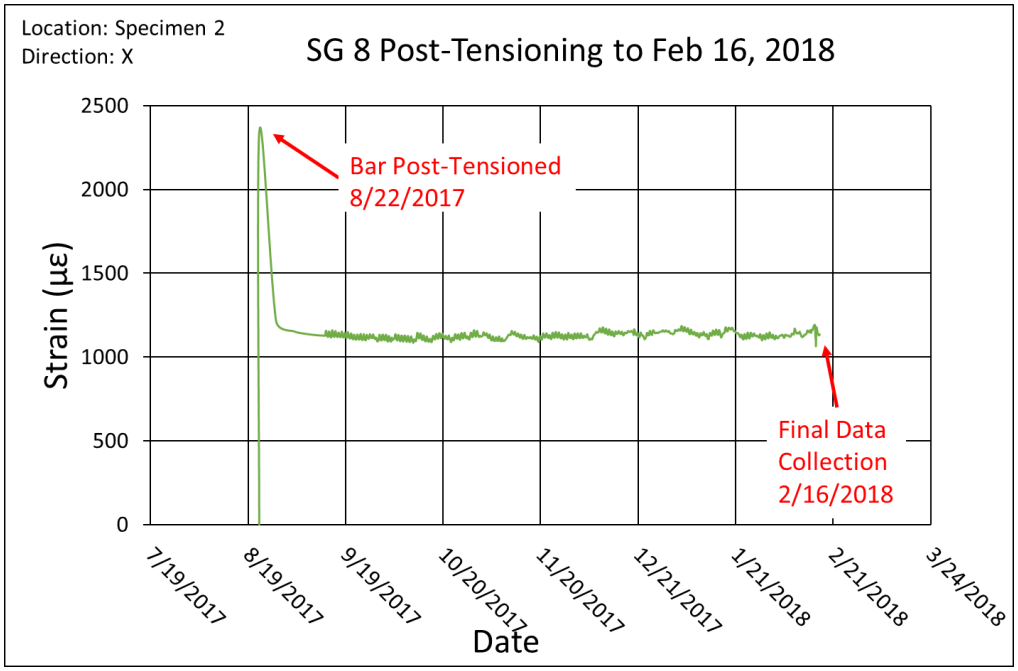

Figure 277 Post-Tensioning Bar Strain Gage 8 Strain Data from Post-Tensioning to February 16, 2018

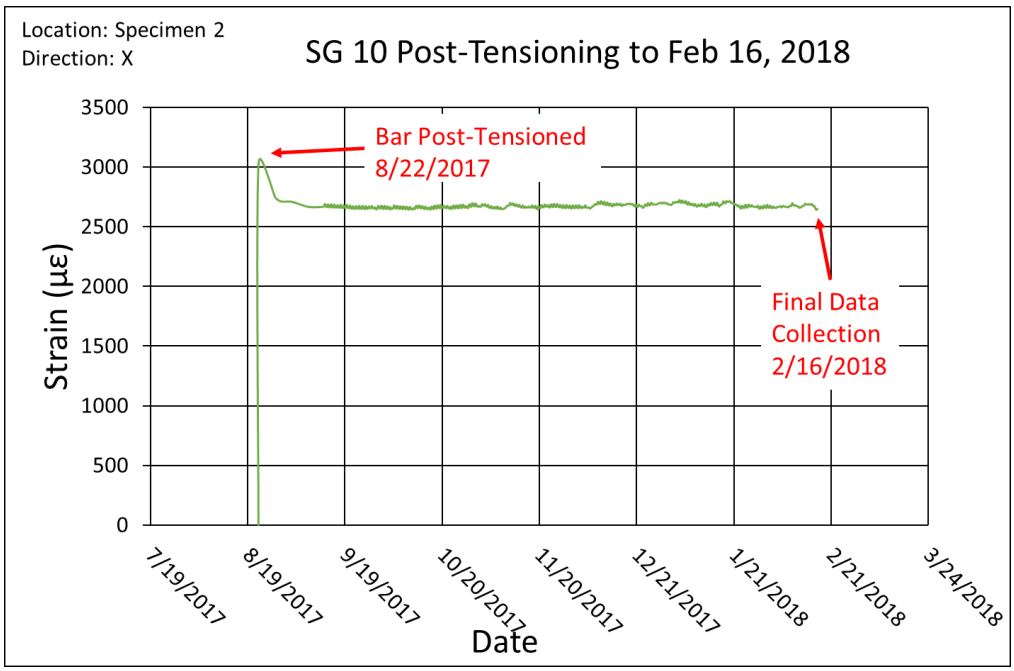

Figure 278 Post-Tensioning Bar Strain Gage 10 Strain Data from Post-Tensioning to February 16, 2018

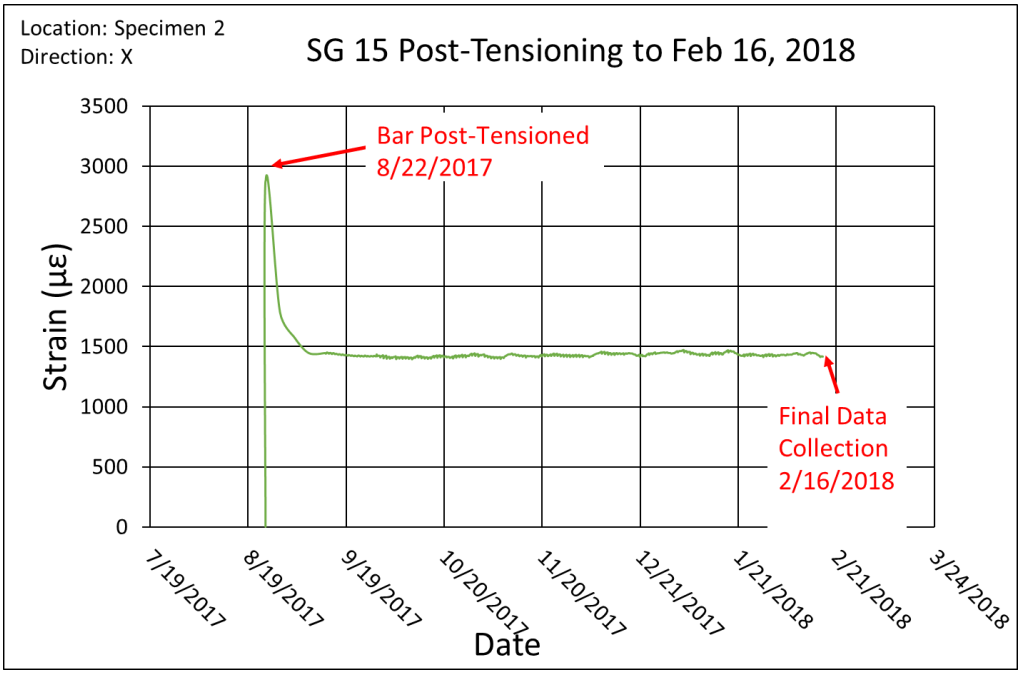

Figure 279 Post-Tensioning Bar Strain Gage 15 Strain Data from Post-Tensioning to February 16, 2018

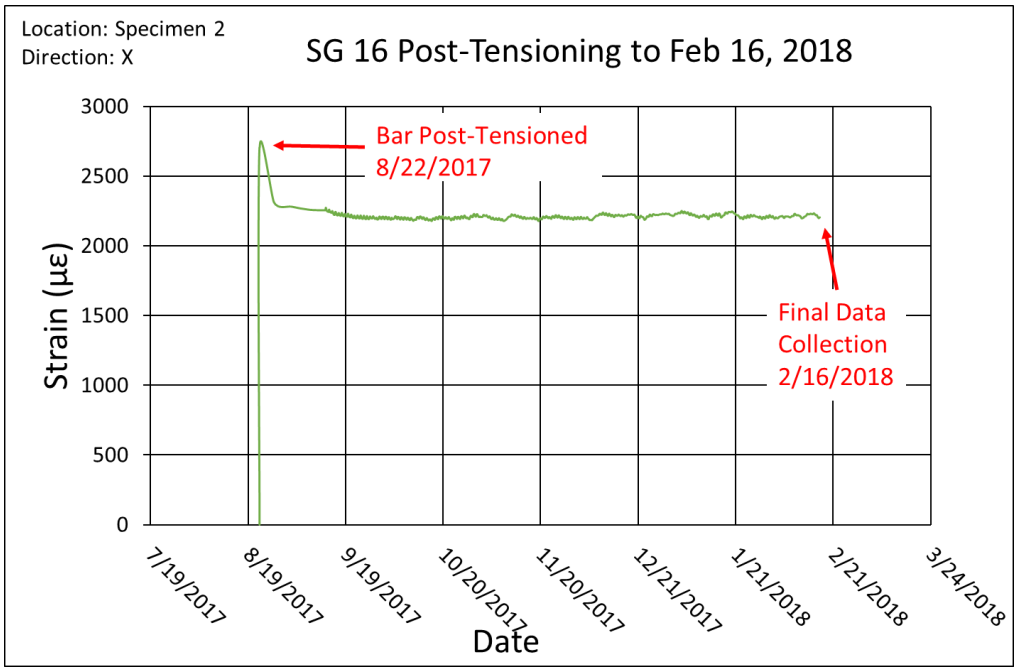

Figure 280 Post-Tensioning Bar Strain Gage 16 Strain Data from Post-Tensioning to February 16, 2018

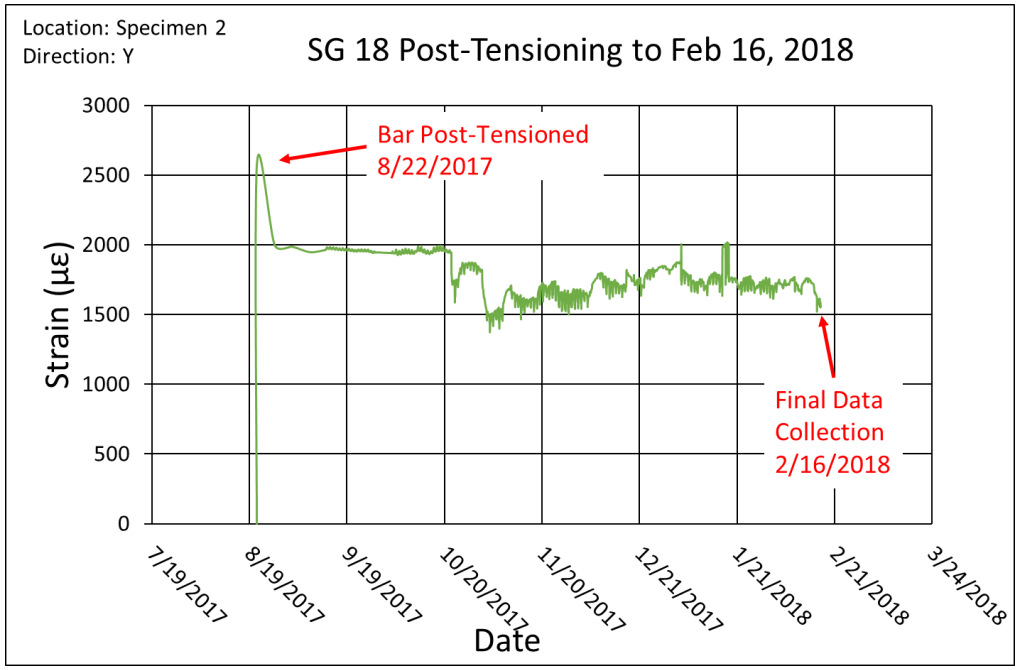

Figure 281 Post-Tensioning Bar Strain Gage 18 Strain Data from Post-Tensioning to February 16, 2018

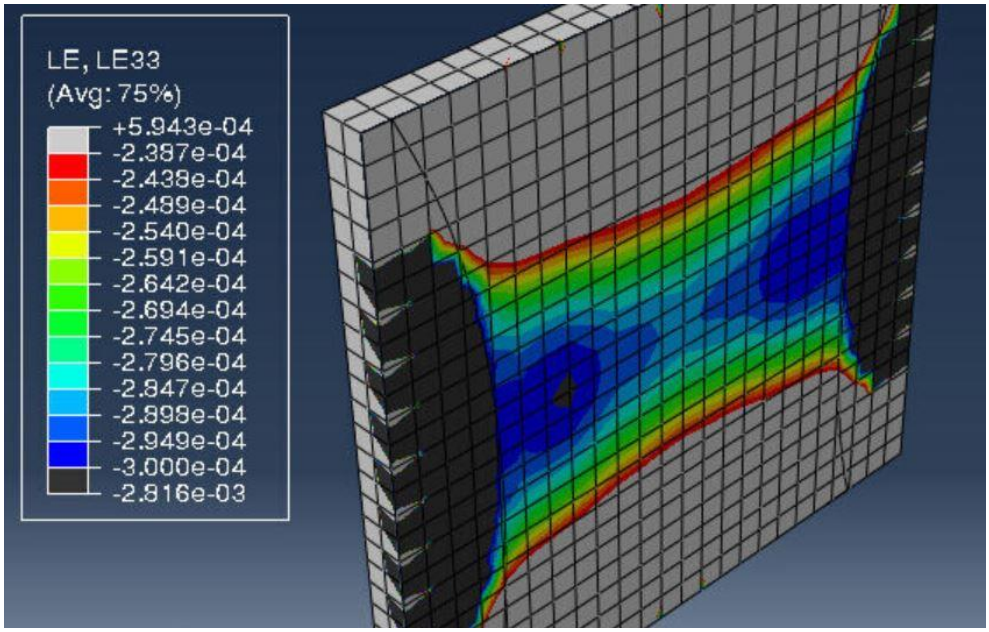

Figure 282 Model 1- Maximum Strains in X-Direction as a Result of Concentrated Compressive Loads

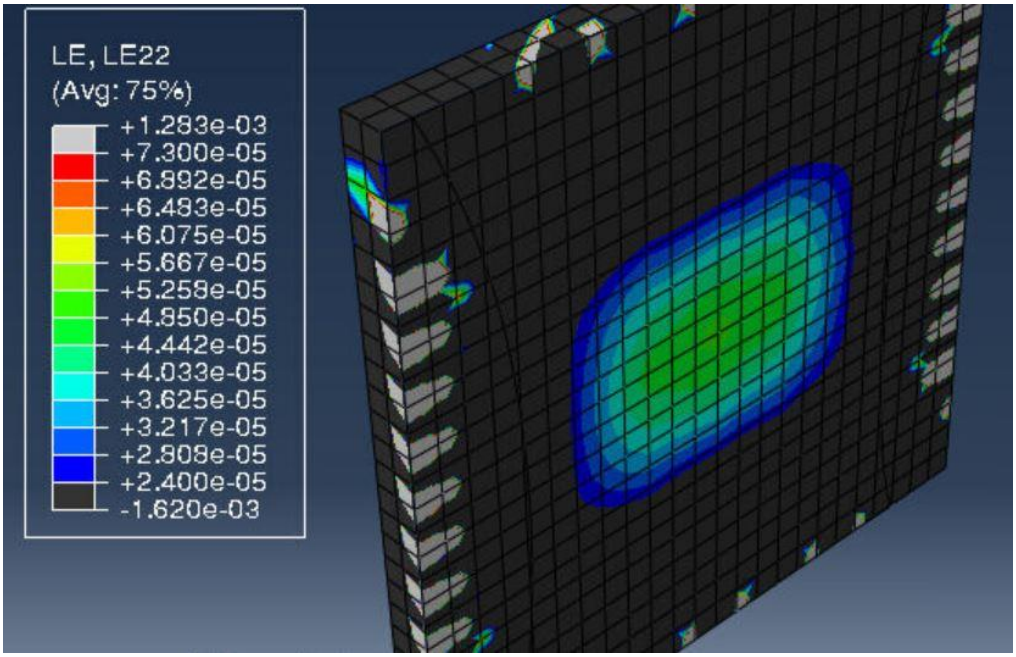

Figure 283 Model 1- Maximum Strains in Y-Direction as a Result of Concentrated Compressive Loads

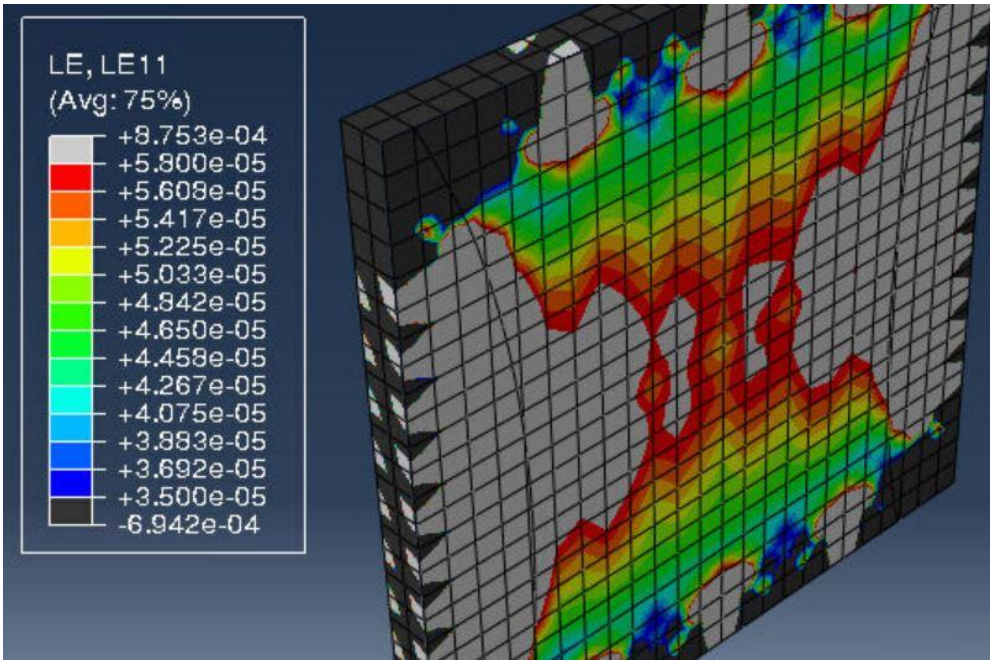

Figure 284 Model 1- Maximum Strains in Z-Direction as a Result of Concentrated Compressive Loads

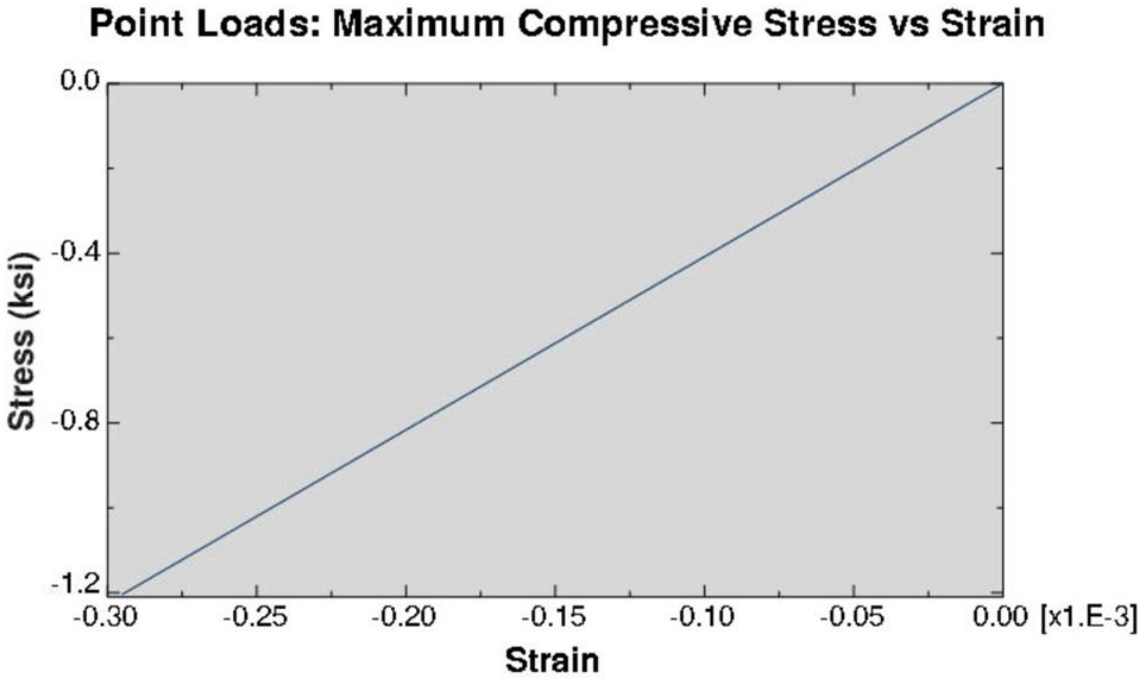

Figure 285 Model 1- Minimum Principal Stress Versus Minimum Principal Strain in Center Element Under Concentrated Compressive Loads

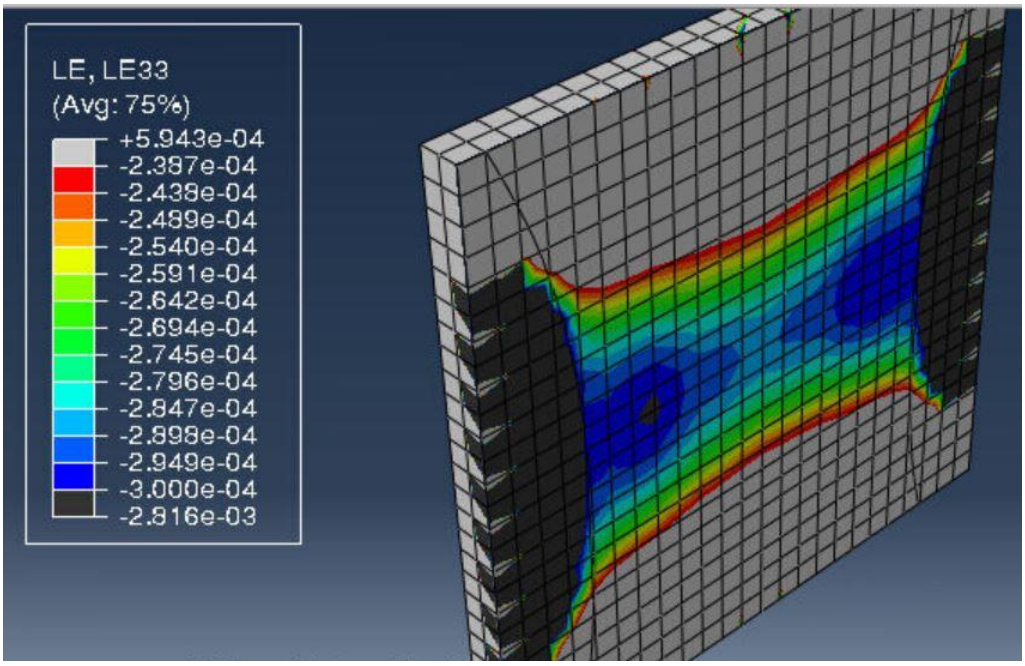

Figure 286 Model 2- Maximum Strains in X-Direction as a Result of Distributed Compressive Loads

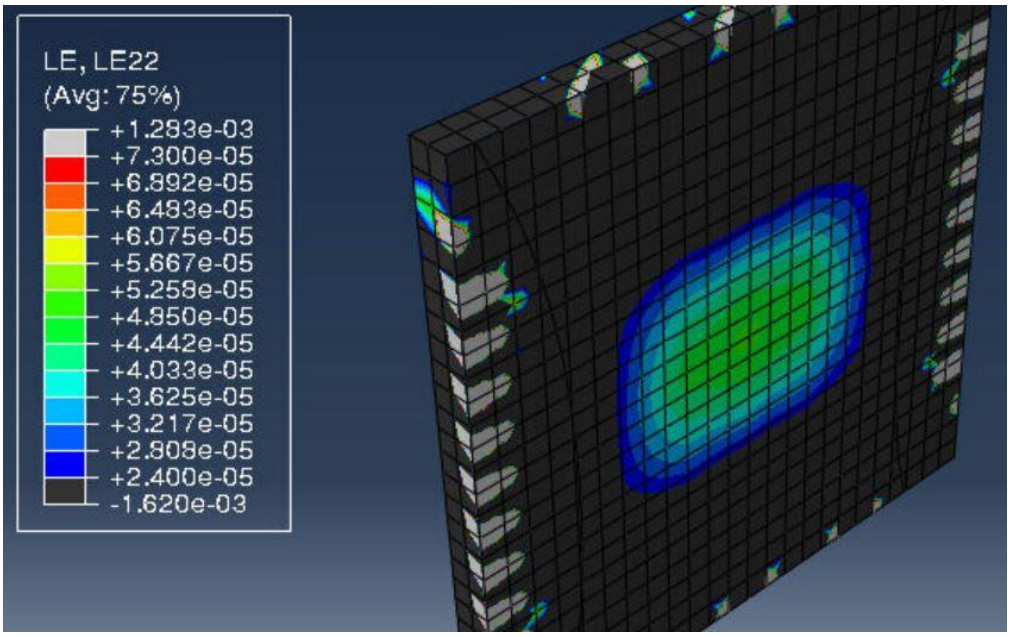

Figure 287 Model 2- Maximum Strains in Y-Direction as a Result of Distributive Compressive Loads

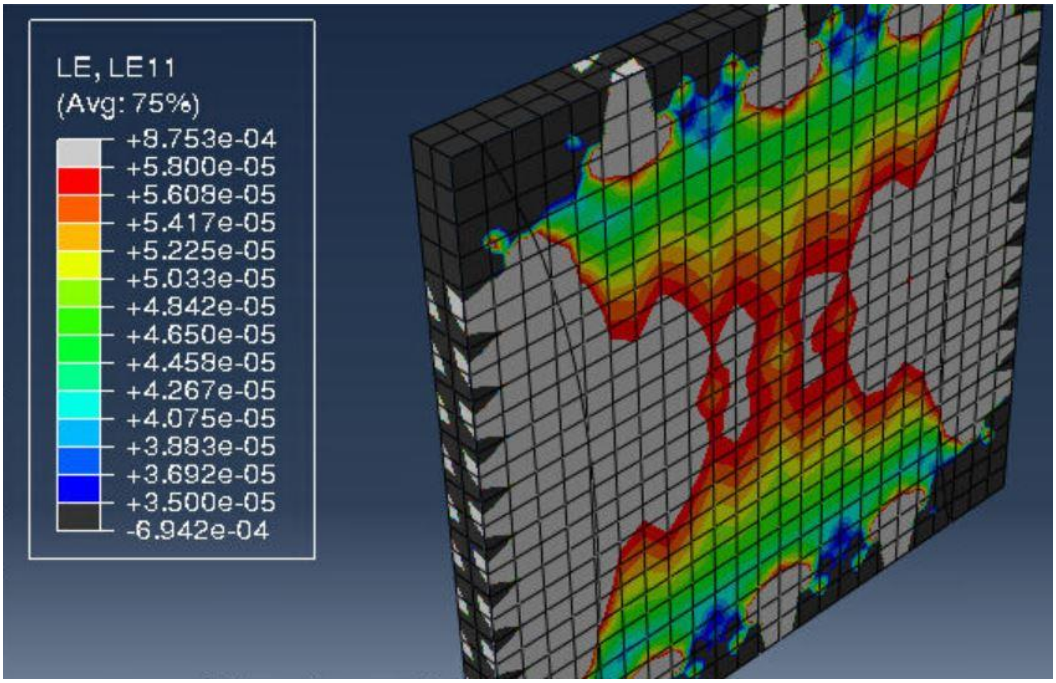

Figure 288 Model 2- Maximum Strains in Z-Direction as a Result of Distributive Compressive Loads

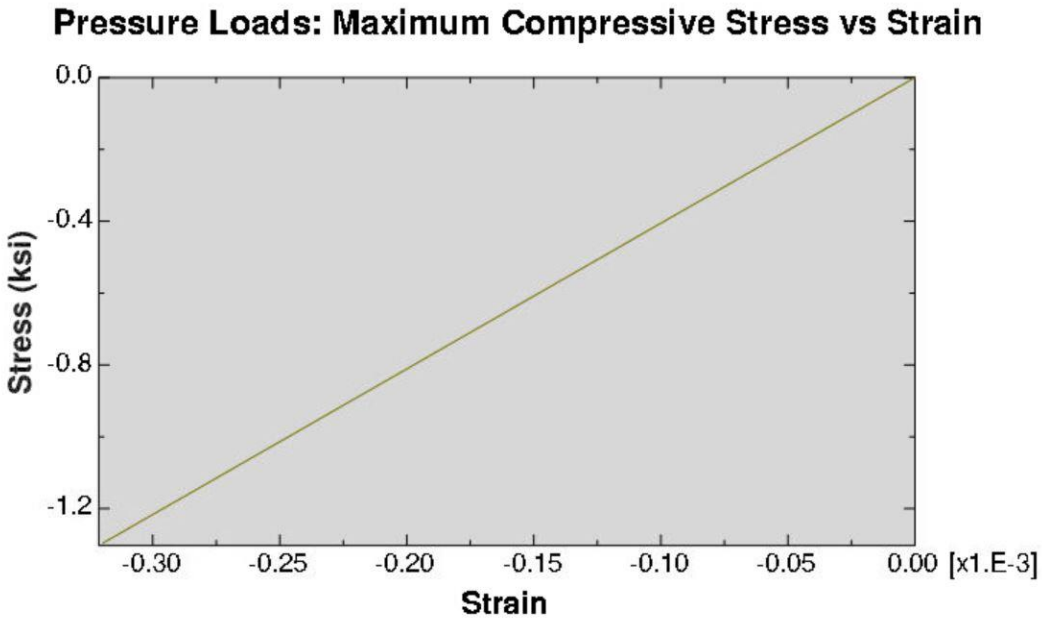

Figure 289 Model 2- Minimum Principal Stress Versus Minimum Principal Strain on Center Element Under Distributed Compressive Loads

APPENDIX B TABLES

Table 1 Concrete Gage Labels, Offsets, Locations in Specimens, and Wiring Location in DAQ

Concrete Gage Labels, Offsets, and Locations				
Gage Label	**Gage Number (Manufacturer Product Data)**	**Offset, με (Manufacturer Product Data)**	**Location in Specimens (Specimen # - Direction - Depth)**	**Location on DAQ**
CG1	1157	220	Specimen 1 - X - Cover	MUX2-1
CG2	1158	1980	Specimen 1 - Y - Cover	MUX2-2
CG3	1241	-1410	Specimen 1 - Z - Cover	MUX2-3
CG4	1239	357.5	Specimen 1 - X - Middle	MUX2-4
CG5	1240	1560	Specimen 1 - Y - Middle	MUX2-5
CG6	1243	-930	Specimen 1 - Z - Middle	MUX2-6
CG7	1242	-320	Specimen 1 - X - Cover - Weatherproof	MUX2-7
CG8	1244	660	Specimen 1 - Y - Cover - Weatherproof	MUX2-8
CG9	1246	-3060	Specimen 1 - Z - Cover - Weatherproof	MUX2-9
CG10	1245	860	Specimen 2 - X - Cover	MUX2-10
CG11	1250	-360	Specimen 2 - Y - Cover	MUX2-11
CG12	1247	-1700	Specimen 2 - Z - Cover	MUX2-12
CG13	1251	810	Specimen 2 - X - Quarter	MUX2-13
CG14	1252	610	Specimen 2 - Y - Quarter	MUX2-14
CG15	1248	-2180	Specimen 2 - Z - Quarter	MUX2-15
CG16	1254	900	Specimen 2 - X - Middle	MUX2-16
CG17	1255	110	Specimen 2 - Y - Middle	MUX3-1
CG18	1249	-910	Specimen 2 - Z - Middle	MUX3-2
CG19	1256	1470	Specimen 3 - X - Cover	MUX2-3
CG20	1257	270	Specimen 3 - Y - Cover	MUX2-4
CG21	1253	-1110	Specimen 3 - Z - Cover	MUX2-5
CG22	1259	870	Specimen 3 - X - Middle	MUX2-6
CG23	1260	1580	Specimen 3 - Y- Middle	MUX2-7
CG24	1258	-3560	Specimen 3 - Z - Middle	MUX2-8

Table 2 Concrete Gage Initial Strain Values After Concrete Pour on 7/7/2017

Concrete Gage Induced Strain from Concrete Pour on 7/7/2017	
Gage Label	**Approx. Strain, με**
CG1	220
CG2	425
CG3	-215
CG4	375
CG5	-775
CG6	-75
CG7	500
CG8	-100
CG9	-815
CG10	120
CG11	Malfunctioned
CG12	-175
CG13	75
CG14	100
CG15	-100
CG16	150
CG17	1600
CG18	-140
CG19	1100
CG20	-500
CG21	Malfunctioned
CG22	950
CG23	-100
CG24	-100

Table 3 Post-Tensioning Bar Strain Gage Box Values, DAQ Initial Values, and Calibration Constant

Post-Tensioning Bar Strain Gage Box Values and DAQ Initial Values on 9/12/2017				
Gage Label	**Box Initial Strain, με**	**DAQ Initial Strain, με**	**Calibration Constant (Box - DAQ)**	**Calibrated Strain, με (DAQ + Calibration Constant)**
SG2	1279	911.7577	367.2423	1279
SG3	2260	1858.542	401.458	2260
SG5	1789	1395.897	393.103	1789
SG6	2266	1892.348	373.652	2266
SG7	2450	2108.986	341.014	2450
SG8	1128	772.8551	355.1449	1128
SG10	2670	2311.323	358.677	2670
SG12	2732	2363.714	368.286	2732
SG15	1447	1100.89	346.11	1447
SG16	2254	1895.938	358.062	2254
SG18	1966	1611.779	354.221	1966

Table 4 Concrete Gage Strain Changes as a Result of Post-Tensioning

Concrete Gage Changes as a Result of Post-Tensioning	
Gage Label	**Approx. Change in Strain, με**
CG1	-575
CG2	-50
CG3	200
CG4	-500
CG5	125
CG6	120
CG7	-725
CG8	115
CG9	215
CG10	-515
CG11	Malfunctioned
CG12	215
CG13	-150
CG14	-125
CG15	10
CG16	-400
CG17	105
CG18	150

Table 5 Concrete Gage Strain Differences between Post-Tensioning and February 16, 2018

Concrete Gage Strain Changes between Post-Tensioning and February 16, 2018			
Gage Label	**Approx. Strain as a Result of Post-Tensioning, με**	**Approx. Strain Reading on February 16, 2018, με**	**Approx. Difference (February reading - Post-Tensioning Strain), με**
CG1	-575	-600	-25
CG2	-50	-25	25
CG3	200	175	-25
CG4	-500	-600	-100
CG5	125	250	125
CG6	120	150	30
CG7	-725	-900	-175
CG8	115	125	10
CG9	215	300	85
CG10	-515	-650	-135
CG11	Malfunctioned	Malfunctioned	Malfunctioned
CG12	215	350	135
CG13	-150	-125	25
CG14	-125	-100	25
CG15	10	100	90
CG16	-400	-450	-50
CG17	105	200	95
CG18	150	325	175
CG19	0	Malfunctioned	Malfunctioned
CG20	0	175	175
CG21	0	Malfunctioned	Malfunctioned
CG22	0	125	125
CG23	0	Malfunctioned	Malfunctioned
CG24	0	125	125

Table 6 Post-Tensioning Bar Strain Gage Strain Differences Between Post-Tensioning and February 16, 2018

PT Bar Strain Gage Strain Changes between September 12, 2017 and February 16, 2018			
Gage Label	**Approx. Strain as a Result of Post-Tensioning, με**	**Approx. Strain Reading on February 16, 2018, με**	**Approx. Difference (February reading – Post-Tensioning Strain), με**
SG2	1279	700	-579
SG3	2260	2100	-160
SG5	1789	Malfunctioned	Malfunctioned
SG6	2266	925	-1341
SG7	2450	2400	-50
SG8	1128	1135	7
SG10	2670	2650	-20
SG15	1447	1415	-32
SG16	2254	2200	-54
SG18	1966	1565	-401

APPENDIX C DATA ACQUISITION PROGRAM

```
'CR1000
'WIRING
'================================================================================
'MULTIPLEXER 1 (4X16 MODE) - QTY. 16 of 21 Half Bridge Strain Gages
'CR1000 ---------- MULTIPLEXER ----------- 4WFBS120 -------- HALF BRIDGE STRAIN GAGE
'    C2 ---------- RES
'    C1 ---------- CLK
'   12V ---------- 12V
'     G ---------- G

'   SE1 ---------- COM OH
'   SE2 ---------- COM OL
'Shield ---------- COM Shield
'Shield ---------- COM EH
'   VX2 ---------- COM EL

'               1H          ----------- 4WFBS120 -------- Sensor High
'               1L          ----------- 4WFBS120 -------- Sensor Low
'               Shield      ----------- 4WFBS120 -------- Sensor Shield
'               2H          -----------
'               2L          ----------- 4WFBS120 -------- Sensor Excitation


'               3H          ----------- 4WFBS120 -------- Sensor High
'               3L          ----------- 4WFBS120 -------- Sensor Low
'               Shield      ----------- 4WFBS120 -------- Sensor Shield
```

```
'               4H          -----------
'               4L          ----------- 4WFBS120 -------- Sensor Excitation
'               .
'               .
'               .
'               31H         ----------- 4WFBS120 -------- Sensor High
'               31L         ----------- 4WFBS120 -------- Sensor Low
'               Shield      ----------- 4WFBS120 -------- Sensor Shield
'               32H         -----------
'               32L         ----------- 4WFBS120 -------- Sensor Excitation
'=================================================================
===========
'MULTIPLEXER 2 (4X16 MODE) - QTY. 16 of 24 Full Bridge Strain Gages
'CR1000 ---------- MULTIPLEXER -------- FULL BRIDGE STRAIN GAGE
'    C3 ---------- RES
'    C1 ---------- CLK
'   12V ---------- 12V
'     G ---------- G

'   SE3 ---------- COM OH
'   SE4 ---------- COM OL
'Shield ---------- COM Shield
'Shield ---------- COM EH
'   VX2 ---------- COM EL

'               1H          -------- Sensor High
'               1L          -------- Sensor Low
'               Shield      -------- Sensor Shield
'               2H          -------- Sensor Excitation -
'               2L          -------- Sensor Excitation +
```

```
'               3H          -------- Sensor High
'               3L          -------- Sensor Low
'               Shield      -------- Sensor Shield
'               4H          -------- Sensor Excitation -
'               4L          -------- Sensor Excitation +
'               .
'               .
'               .
'               31H         -------- Sensor High
'               31L         -------- Sensor Low
'               Shield      -------- Sensor Shield
'               32H         -------- Sensor Excitation -
'               32L         -------- Sensor Excitation +
'================================================================================
'MULTIPLEXER 3 (4X16 MODE) - #17-24 Full Bridge Strain Gages, #17-21 Half Bridge
'CR1000 ---------- MULTIPLEXER ---------- FULL BRIDGE STRAIN GAGE
'    C4 ---------- RES
'    C1 ---------- CLK
'   12V ---------- 12V
'     G ---------- G

'   SE5 ---------- COM OH
'   SE6 ---------- COM OL
'Shield ---------- COM Shield
'Shield ---------- COM EH
'   VX3 ---------- COM EL
```

```
'   FULL BRIDGE SENSORS
'               1H          -------- Sensor High
'               1L          -------- Sensor Low
'               Shield      -------- Sensor Shield
'               2H          -------- Sensor Excitation -
'               2L          -------- Sensor Excitation +

'               3H          -------- Sensor High
'               3L          -------- Sensor Low
'               Shield      -------- Sensor Shield
'               4H          -------- Sensor Excitation -
'               4L          -------- Sensor Excitation +
'               .
'               .
'               .
'               15H         -------- Sensor High
'               15L         -------- Sensor Low
'               Shield      -------- Sensor Shield
'               16H         -------- Sensor Excitation -
'               16L         -------- Sensor Excitation +

'   HALF BRIDGE SENSORS
'               17H         ---------- 4WFBS120 -------- Sensor High
'               17L         ---------- 4WFBS120 -------- Sensor Low
'               Shield      ---------- 4WFBS120 -------- Sensor Shield
'               18H         ----------
'               18L         ---------- 4WFBS120 -------- Sensor Excitation

'               19H         ---------- 4WFBS120 -------- Sensor High
'               19L         ---------- 4WFBS120 -------- Sensor Low
```

```
'              Shield      ---------- 4WFBS120 -------- Sensor Shield
'              20H         ----------
'              20L         ---------- 4WFBS120 -------- Sensor Excitation
'              .
'              .
'              .
'              25H         ---------- 4WFBS120 -------- Sensor High
'              25L         ---------- 4WFBS120 -------- Sensor Low
'              Shield      ---------- 4WFBS120 -------- Sensor Shield
'              26H         ----------
'              26L         ---------- 4WFBS120 -------- Sensor Excitation

'================================================================================
'AM25T - Qty. 24 Type T Thermocouples
'CR1000 ---------- AM25T ---------- TYPE T THERMOCOUPLES
'    C5 ---------- RES
'    C1 ---------- CLK
'   12V ---------- 12V
'     G ---------- G

'   SE7 ---------- HI
'   SE8 ---------- LO
'     G ---------- GROUND
'    AG ---------- SHIELD
'   VX1 ---------- EX

'Declare Variables and Units
Public BattV
Public FCLoaded
```

```
Public PTemp_C
Public CReps
Public ZMode
Public CIndex
Public CAvg
Public LCount, LCount_2, LCount_3, LCount_4

Public SG(21)
Public Vr1000(21)
Public BrZero(21)

Public CG(24)

Public RTempC
Public TC(25)
Public
GFsRaw(21)={2.1,2.1,2.1,2.1,2.1,2.1,2.1,2.1,2.1,2.1,2.1,2.1,2.1,2.1,2.1,2.1,2.1,2.1,2.1,2.1,2.1}
Public Mult(24)={1,1,1,1,1,1,1,1,1,1,1,1,1,1,1,1,1,1,1,1,1,1,1,1}
Public Offs(24)={0,0,0,0,0,0,0,0,0,0,0,0,0,0,0,0,0,0,0,0,0,0,0,0}

Units BattV=Volts
Units PTemp_C=Deg C
Units SG=microstrain
Units Vr1000=mV/V
Units BrZero=mV/V
Units CG=mV/V
Units RTempC=Deg C
Units TC=Deg C

'Define Data Tables
```

```
DataTable(Table1,True,-1)
  DataInterval(0,1,Hr,10)
  Sample(21,SG(),IEEE4)
  Sample(24,CG(),FP2)
  Sample(25,TC(),FP2)
  Sample(1,RTempC,FP2)
EndTable

DataTable(Table2,True,-1)
  DataInterval(0,1440,Min,10)
  Minimum(1,BattV,FP2,False,False)
EndTable

'Calibration history table
DataTable(CalHist,NewFieldCal,10)
  SampleFieldCal
EndTable

DataTable (Raw_HalfBridge,True,-1 )
  Sample (1,Vr1000(),FP2)
EndTable

'Main Program
BeginProg
  'Initialize calibration variables for
  'Half Bridge Strain, 120 ohm with 4WFBS TIM measurement 'Vr1000()'
  CIndex=1 : CAvg=1 : CReps=21     'Load the most recent calibration values from the CalHist table
  FCLoaded=LoadFieldCal(True)
  'Main Scan
```

```
  Scan(1,Hr,1,0)
    'Default CR1000 Datalogger Battery Voltage measurement 'BattV'
    Battery(BattV)
    'Default CR1000 Datalogger Wiring Panel Temperature measurement 'PTemp_C'
    PanelTemp(PTemp_C,_60Hz)

    'Turn AM16/32 Multiplexer On - This multiplexer contains 16 out of 21 Half Bridge Strain gages
    PortSet(2,1)
    Delay(0,150,mSec)
    LCount=1
    SubScan(0,uSec,16)
      'Switch to next AM16/32 Multiplexer channel
      PulsePort(1,10000)
      'Half Bridge Strain, 120 ohm with 4WFBS TIM measurement 'Vr1000()'
      BrFull(Vr1000(LCount),1,mV7_5,1,2,1,2500,True,True,0,_60Hz,1,0)
      LCount=LCount+1
    NextSubScan

    'Turn AM16/32 Multiplexer Off
    PortSet(2,0)
    Delay(0,150,mSec)

    'Turn AM16/32 Multiplexer On - This multiplexer contains 16 out of 24 Concrete gages
    PortSet(3,1)
    Delay(0,150,mSec)
    LCount_2=1
    SubScan(0,uSec,16)
      'Switch to next AM16/32 Multiplexer channel
      PulsePort(1,10000)
```

```
    'Generic Full Bridge measurements 'CG()' on the AM16/32 Multiplexer

BrFull(CG(LCount_2),1,mV25,2,Vx2,1,2500,True,True,0,_60Hz,Mult(LCount_2),Offs(LCount
_2))
     LCount_2=LCount_2+1
   NextSubScan
   'Turn AM16/32 Multiplexer Off
   PortSet(3,0)
   Delay(0,150,mSec)

   'Turn AM16/32 Multiplexer On - This multiplexer contains
   'the remaining 5 half bridge strain gages and the remaining 8 full bridge concrete gages
   PortSet(4,1)
   Delay(0,150,mSec)
 'MEASURE QTY. 8 X FULL BRIDGE STRAIN GAGES (STARTING WITH #17 OF 24)
 LCount_3=17
   SubScan(0,uSec,8)
     'Switch to next AM16/32 Multiplexer channel
     PulsePort(1,10000)
     'Generic Full Bridge measurements 'CG()' on the AM16/32 Multiplexer

BrFull(CG(LCount_3),1,mV25,3,Vx3,1,2500,True,True,0,_60Hz,Mult(LCount_3),Offs(LCount
_3))
     LCount_3=LCount_3+1
   NextSubScan

   Delay(0,150,mSec)
   'MEASURE QTY. 5 X HALF BRIDGE STRAIN GAGES (STARTING WITH #17 OF 21)
   LCount_4=17
   SubScan(0,uSec,5)
     'Switch to next AM16/32 Multiplexer channel
```

```
    PulsePort(1,10000)
    'Half Bridge Strain, 120 ohm with 4WFBS TIM measurement 'Vr1000()'
    BrFull(Vr1000(LCount_4),1,mV7_5,3,3,1,2500,True,True,0,_60Hz,1,0)
    LCount_4=LCount_4+1
  NextSubScan
  'Calculated strain result 'SG()' for
  'Half Bridge Strain, 120 ohm with 4WFBS TIM measurement 'Vr1000()'
  StrainCalc(SG(),21,Vr1000(),BrZero(),2,GFsRaw(),.3)
  'Zeroing calibration for
  'Half Bridge Strain, 120 ohm with 4WFBS TIM measurement 'Vr1000()'
  FieldCalStrain(10,Vr1000(),CReps,0,BrZero(),ZMode,0,CIndex,CAvg,0,SG())

  'Turn AM16/32 Multiplexer Off
  PortSet(4,0)
  Delay(0,150,mSec)

  'Type T (copper-constantan) Thermocouple measurements 'TC()' on the AM25T Multiplexer
  AM25T(TC(),25,mV2_5C,1,4,TypeT,RTempC,1,5,1,True,0,_60Hz,1,0)

  'Call Data Tables and Store Data
  CallTable Table1
  CallTable Table2
  CallTable CalHist
  CallTable Raw_HalfBridge
 NextScan
EndProg
```